



PHD

Nanocellulose Assembly In Aqueous Media: towards hybrid functional materials

Calabrese, Vincenzo

Award date:
2020

Awarding institution:
University of Bath

[Link to publication](#)

Alternative formats

If you require this document in an alternative format, please contact:
openaccess@bath.ac.uk

General rights

Copyright and moral rights for the publications made accessible in the public portal are retained by the authors and/or other copyright owners and it is a condition of accessing publications that users recognise and abide by the legal requirements associated with these rights.

- Users may download and print one copy of any publication from the public portal for the purpose of private study or research.
- You may not further distribute the material or use it for any profit-making activity or commercial gain
- You may freely distribute the URL identifying the publication in the public portal ?

Take down policy

If you believe that this document breaches copyright please contact us providing details, and we will remove access to the work immediately and investigate your claim.

Nanocellulose Assembly In Aqueous Media: towards hybrid functional materials

Vincenzo Calabrese
University of Bath



Submitted in fulfilment of the requirements for the degree of Doctor of Philosophy
September 2019

Supervised by
Prof. Karen J. Edler, Prof. Janet L. Scott

Department of Chemistry
University of Bath
United Kingdom

Copyright

Attention is drawn to the fact that copyright of this thesis rests with the author. A copy of this thesis has been supplied on condition that anyone who consults it is understood to recognise that its copyright rests with the author and that they must not copy it or use material from it except as permitted by law or with the consent of the author.

This thesis may be made available for consultation within the University Library and may be photocopied or lent to other libraries for the purposes of consultation.

Publication List

- [1] Calabrese, V.; Da Silva, M. A.; Schmitt, J.; Zakir Hossain, K. M.; Scott, J. L.; Edler, K. J. Charge-driven interfacial gelation of cellulose nanofibrils across the water/oil interface. *Soft Matter* 2019.
- [2] Calabrese, V.; Muoz-Garca, J. C.; Schmitt, J.; da Silva, M. A.; Scott, J. L.; Angulo, J.; Khimyak, Y. Z.; Edler, K. J. Understanding Heat Driven Gelation of Anionic Cellulose Nanofibrils: Combining Saturation Transfer Difference (STD) NMR, Small Angle X-Ray Scattering (SAXS) and Rheology. *J. Colloid Interface Sci.* 2019, 535, 205–213.
- [3] Calabrese, V.; Da Silva, M. A.; Schmitt, J.; Muoz-Garcia, J. C.; Gabrielli, V.; Scott, J. L.; Angulo, J.; Khimyak, Y. Z.; Edler, K. J. Surfactant Controlled Zwitterionic Cellulose Nanofibril Dispersions. *Soft Matter* 2018, 14 (38), 77937800.
- [4] Calabrese, V.; Courtenay, J. C.; Edler, K. J.; Scott, J. L. Pickering Emulsions Stabilized by Naturally Derived or Biodegradable Particles. *Curr. Opin. Green Sustain. Chem.* 2018, 12, 83–90.
- [5] da Silva, M. A.; Calabrese, V.; Schmitt, J.; Celebi, D.; Scott, J. L.; Edler, K. J. Alcohol Induced Gelation of TEMPO-Oxidized Cellulose Nanofibril Dispersions. *Soft Matter* 2018, 14 (45), 9243–9249.
- [6] Schmitt, J.; Calabrese, V.; Da Silva, M. A.; Lindhoud, S.; Alfredsson, V.; Scott, J. L.; Edler, K. J. TEMPO-Oxidised Cellulose Nanofibrils; Probing the Mechanisms of Gelation: Via Small Angle X-Ray Scattering. *Phys. Chem. Chem. Phys.* 2018, 20 (23), 16012–16020.

Abstract

In the last decade, raising awareness towards the use of sustainable materials resulted in fast-expanding research on cellulose nanoparticles (CNP). The abundance of cellulose and the versatility of CNP to assemble in a myriad of different structures made CNP an interesting building block for a variety of soft materials. To enable the use of CNP in day-to-day soft materials, a fundamental understanding of the CNP assembly coupled with exploratory research, aimed to propose new strategies of assembly, is demanded. Thus, prediction and control of the structure-to-property relationship of CNP-based material can be achieved in industrially relevant conditions. This work aimed to extend the understanding of the structure-property relationship of the CNP assembly required for the production of capsules and hydrogels able to incorporate targeted components. As a starting point, oxidised cellulose nanofibrils (OCNF) and cationic cellulose nanofibrils (CCNF) dispersions were investigated as a function of time and temperature; crucial parameters to account for shelf-life and processing of materials. To ensure heat insensitivity while gaining rheological control upon addition of secondary species, zwitterionic cellulose nanofibrils (ZCNF) were produced through covalent grafting of a quaternary ammonium moiety onto OCNF. The assembly and the flow behaviour of the ZCNF dispersions were found to be strongly responsive upon addition of ionic surfactants due to electrostatic interactions. On the other side, the addition of non-interacting colloids into OCNF-based hydrogels was pursued with the aim to preserve charge accessibility of the OCNF surface whilst modulating mechanical properties of the dispersion. This enabled the formation of long-living millimetre-sized spheroidal hydrogels in water, able to incorporate coordination polymers.

Using the complexation of CCNF and an oppositely charged polymer, spheroidal hydrogels were further developed to have a core-shell structure, from which a proof-of-concept application in biocatalysis is provided. By analogy to the core-shell spheroidal hydrogels, the charge-driven complexation between OCNF and an oppositely charged surfactant was used to target the OCNF assembly, and gelation, at the interface between two immiscible fluids (water/oil). The interfacial gelation of OCNF and its mechanical properties were investigated to provide solid knowledge for the production of capsules.

This work combines individual investigations regarding the structure-property relationship of CNP in aqueous media, providing an insightful contribution towards the production of functional materials.

Acknowledgements

Here we are! Writing this last bit trying to make sure everyone will be properly acknowledged.

First of all, I would like to express my immense gratitude to Karen and Janet - a great synergistic team. Thanks for broadening my perspective of science, boosting my curiosity = knowledge. As part of the team, I also need to acknowledge Karen Edler's group. I would like to thank Marcelo for his constant and resolute help - there has not been, literally, a day without me asking you a question, so this is the list I can say. Julien, Zakir, Saffron thanks for your help. I must thank Julien for introducing me to the *fun* of Board Games, especially at 3 am on Saturday whilst doing experiments somewhere. Special thanks to Andi and a former member Cecilia for the laughing sessions.

Since i am writing this acknowledgements just before lunch, i can not forget to acknowledge the lunch crew: Kamran, Hui, Giuseppe Andrea, Davide, HannaH (maybe not in campus), and Emile. A special thank goes to Andrea for her constant help and support; late at night listening to my research-based issues or questions can be tough, I know, thus it needs recognition. I would like to thank Davide for his engaging spirit and passion (there is not been a lunch break without talking about science). I want to thank Emile, a good friend and a good scientist. A global thank to Daniele, Clelia, Margherita, Raffaele, Luca, Diletta, Deborah, Elisa and Enrico.

A special thank to my family, which may appreciate better Italian.

Un profondo e sentitissimo grazie va' alla mia famiglia che mi ha aiutato giorno dopo giorno. Nonostante le distanze ho ricevuto sempre conforto e sostegno, ma soprattutto la vostra fiducia. Alla fine, questa tesi e' frutto del mio e del vostro lavoro. Un ringraziamento speciale va' a zio Jack per il suo supporto.

To conclude, i would like to thank the soundtrack of this thesis, powered by *tool*.

1	Introduction	1
1.1	Outlook	1
1.2	Cellulose nanoparticle (CNP)	2
1.3	Assembly in bulk - 3D	5
1.3.1	Ion induced assembly	6
1.3.2	Modulating CNP assembly <i>via</i> addition of secondary components	7
1.3.3	CNP-surfactant interactions	7
1.3.4	CNP-polymer interactions	8
1.4	Assembly at interfaces - 2D	10
1.4.1	CNP adsorption at liquid-liquid interfaces: Outlook	11
1.4.2	CNP at planar liquid-liquid interfaces	12
1.4.3	CNP at liquid-liquid interfaces of microscopic droplets: Pickering emulsions	13
1.5	Aims and objectives	13
2	Techniques	15
2.1	Small angle scattering	15
2.1.1	Radiation types: Neutron and X-ray	17
2.1.2	Probing colloidal systems	18
2.1.3	SANS and SAXS instruments	20
2.2	Rheology of soft materials and complex fluids	21
2.2.1	Steady-state shear flow	21
	Viscosity as function of shear rate	22
	Viscosity as function of time	23
	Viscosity as function of the volume fraction	24
2.2.2	Viscoelasticity	24
	Strain sweep	26
	Frequency sweep	28
2.2.3	Setup	28
2.3	Other techniques	29
2.3.1	Dynamic Interfacial Tension	29
2.3.2	Dynamic light scattering (DLS)	29
2.3.3	ζ -potential	30
2.3.4	Confocal microscopy	32

3	Understanding heat driven gelation of anionic cellulose nanofibrils: Combining saturation transfer difference (STD) NMR, small angle X-ray scattering (SAXS) and rheology	33
4	Surfactant controlled zwitterionic cellulose nanofibril dispersions	45
5	Filler size effect in an attractive fibrillated network: a structural and rheological perspective	57
6	Composite hydrogel spheroids incorporating cellulose nanofibrils and chiral coordination polymer nanofibres	77
7	Core-shell spheroidal hydrogels produced via charge-driven interfacial complexation	85
8	Charge-driven interfacial gelation of cellulose nanofibrils across the water/oil interface	107
9	Conclusions and Future Work	119
10	Appendix	133
10.1	Supporting information for Chapter 3	133
10.2	Supporting information for Chapter 4	147
10.3	Supporting information for Chapter 5	151
10.4	Supporting information for Chapter 6	155
10.5	Supporting information for Chapter 7	161
10.6	Supporting information for Chapter 8	164

1.1 Outlook

Soft materials are systems which easily deform upon perturbation due to the relative weak interactions between building blocks composing the material.^[1] These materials include complex liquids, colloidal dispersions, gels, emulsions and many other systems. Pierre-Gilles de Gennes has been considered the founder of soft matter, receiving the Nobel Prize in physics in 1991.^[2,3] Since then, soft matter research has inflated exponentially. Interest in soft matter has been mainly given towards the fundamental understanding of model systems, the design of new functional materials and a combination of both.

Soft materials such hand-creams, paints, detergents, sponges and toothpastes are ubiquitous in day-to-day life. Although very different from each other, all these materials have in common a complex structure. Such structure is often composed of multiple types of polymers and/or particles to achieve a specific structure-property relationship. In the past decades, attention has been given towards the use of petrochemically-derived polymers due to cheap manufacture and the ability to tune their properties rather simply, allowing a large scale production of many types of soft materials. The poor recyclability of such materials has been addressed only recently, due to the increasing awareness regarding plastic pollution and waste management. As such, soft matter research has shifted towards bio-derived systems to improve the understanding required to manufacture biodegradable materials - which decompose into smaller molecules such as H_2O and CO_2 by microorganisms under specific conditions.^[4] Many biodegradable polymers could replace totally or partially the petrochemically-derived polymers in formulated consumer products.

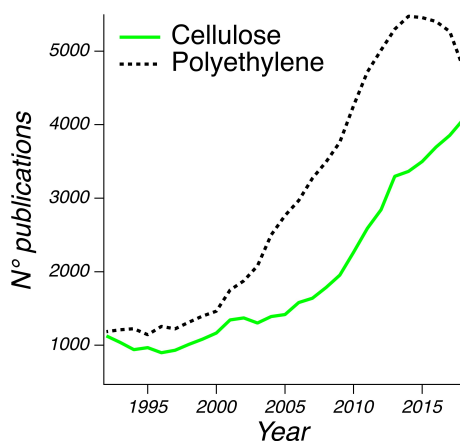


Figure 1.1 Number of publications per year containing the word "cellulose" and "polyethylene" as obtained by *pubmed*^[5].

Starch, cellulose, chitosan, casein, whey proteins, fatty acids and waxes are only a few examples of biodegradable matrices which could be used. However, each of these components is suitable for specific targeted application with their pro and cons. For instance, chitosan is known for its antimicrobial activity due to the strong electrostatic interactions with the negatively charged cell wall, making it suitable in the biomedical field and as food preservative.^[6] Milk proteins have been broadly used in the food industry to structure food (e.g. as rheological modifiers), while unsaturated fatty acids have been used in combination with organogelators to produce solid-like structures as replacement of saturated fats in food products.^[7] One of the main concern related to the use of biodegradable components in non-edible products is, quite often, their nutritional value which conflicts with the growing global demand of food.^[8] In this context, proteins which are highly demanded for their nutritional value and recognition in healthy diets are solely used in food products. Moreover, biodegradable components should be available in large quantities and avoid undesired effects such as allergies; milk proteins are, for example, common allergens in childhood.^[9] In this context, cellulose is a versatile building block for a variety of soft materials since does not directly compete with the human food chain, can be extracted from waste materials, it is present in large quantities and has a specific chemical composition which makes it suitable in formulated products as a substitute to less or non-degradable polymers. For this reason, in the last decade, the research regarding cellulose has been growing at the expense of non-biodegradable polymers. This is shown by an instance provided in Figure 1.1 where the number of publications per year containing the word "cellulose" and "polyethylene", the most common plastic, are compared. However, the whole picture of how cellulose assembles with itself and with other (macro)molecules is still incomplete and further research is required to achieve structures (materials) with the desired functional properties.

In section 1.2, the main avenues for the preparation of cellulose nanoparticles (CNP), including cellulose nanofibrils (CNF) and cellulose nanorods (CNR), are discussed with the focus on the CNP assembly in bulk, 3D, (section 1.3) and at the interface, 2D, (section 1.4).

1.2 Cellulose nanoparticle (CNP)

Cellulose is an unbranched polymer of β -1,4 linked D-glucose units with a high degree of polymerization.^[10] The long polymer chains are assembled through associative van der Waals, intra- and inter-molecular (hydrogen bonds) forces.^[10] Cellulose is the main component of the plant cell walls. As such, plants constitute one of the greatest cellulose sources on the planet. Some bacteria can also produce cellulose (e.g. *Acetobacter xylinus*), identified as bacterial cellulose. One of the advantages of bacterial cellulose compared to plant-derived cellulose is the higher degree of purity. For this reason, bacterial cellulose is used as a food ingredient; *Nata de Coco* is an instance of a low calorie bacterial cellulose-based dessert.^[11,12] In woody plant cells, the supramolecular assembly of cellulose chains is referred to as microfibrils which have a cross-section of *ca.* 350 nm and a length up to μm .^[10] When dispersed in aqueous media, microfibrils undergo flocculation at low concentrations due to net interfibrillar attractive forces (hydrogen bonds and van der Waals).^[12] Nevertheless, at greater microfibril concentrations, the formation of an interconnected fibrillar network can be used to avoid flocculation and sedimentation.^[12] To produce stable cellulose dispersions in aqueous media, cellulose nanoparticles (CNP) are often produced via chemical modification, introducing charged moieties (at specific pHs) and followed by mechanical treatment. These procedures lead to the formation of charge stabilized colloidal CNP. Common procedures for CNP productions are (Figure 1.2):

(i) Sulfuric acid hydrolysis, which yields CNP with negatively charged sulfate groups on the surface. This hydrolysis occurs in the presence of 64% H_2SO_4 at 45°C for a few hours followed by mechanical treatment.^[13] This procedure leads to cellulose nanocrystals (CNC) with a length

of a few hundred *nm* and a cross-section in the order of 2-6 *nm*.^[14,15]

(ii) The 2,2,6,6-tetramethylpiperidine-1-oxyl radical (TEMPO)-mediated oxidation of the primary OH groups.^[13,16,17] TEMPO-oxidation uses catalytic amounts of TEMPO/NaBr/NaClO to selectively introduce charged carboxylate groups at the C6 position of the glucose rings of cellulose, yielding negatively charged oxidised cellulose nanofibrils (OCNF). OCNF belong to the colloidal domain, with a size of few hundreds of *nm* in length and *ca.* 4 *nm* in cross-section.

(iii) Glycidyltrimethylammonium chloride (GTMAC) grafting of cellulose has been shown to lead the formation of cationic cellulose nanofibrils (CCNF) with a large aspect ratio (similar to OCNF).^[18-20] This reaction is conducted in alkaline conditions and, a higher yield is obtained in semi-dry conditions due to undesired side reactions occurring with water molecules - such as the hydrolysis of GTMAC.^[18]

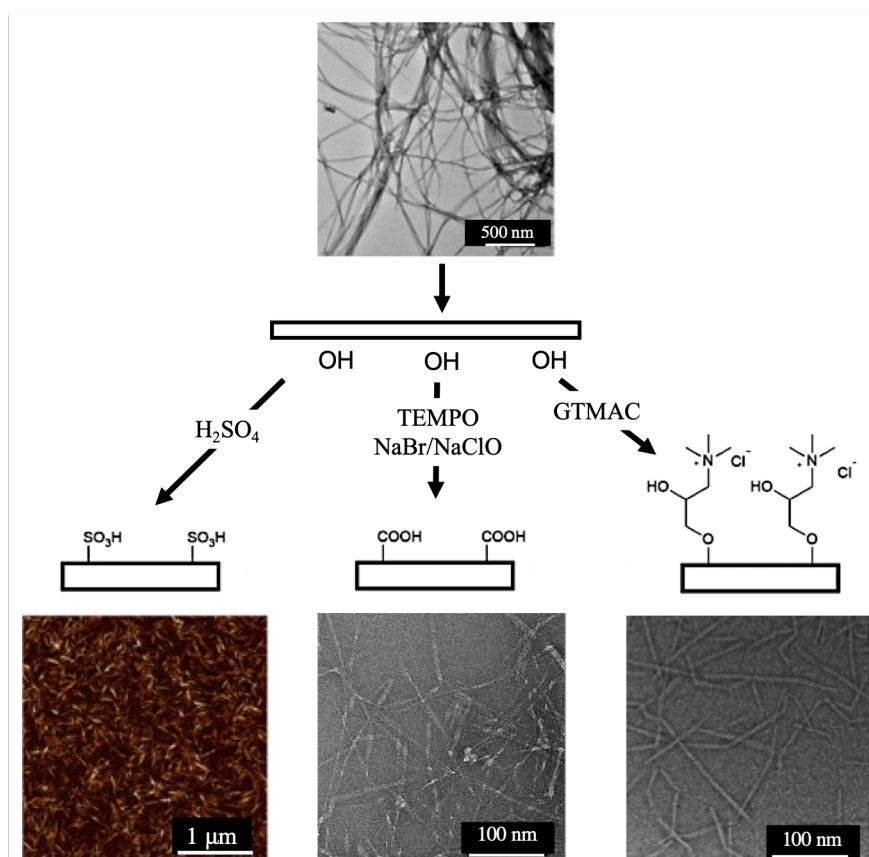


Figure 1.2 Schematic diagram of the methodologies employed for the production of CNP with different dimensions and surface chemistry. Top picture adapted from^[12] with permission from Elsevier. Bottom left picture adapted from^[14] with permission from the American Chemical Society. Bottom central picture adapted from^[21] - Published by the PCCP Owner society. Bottom right picture adapted from^[20] - Published by the Royal Society of Chemistry.

On the base of diffraction techniques (e.g. X-ray diffraction)^[22,23] and Nuclear Magnetic Resonance (NMR) spectroscopy^[24] it is generally accepted that CNP consist of glucose chains which arrange in amorphous (disordered) and crystalline (ordered) domains. Although the amorphous *vs* crystalline ratio is quantitatively accessible by these techniques, unrevealing the spatial distribution of such domains is, to date, challenging and controversial.^[22-26] Two different models have been proposed, at the nanofibril level, based on the spatial arrangements of the crystalline and amorphous domains: (i) amorphous patches interposed between crystalline domains along the fibril direction^[23,25] and (ii) amorphous patches covering the outer layer of a crystalline core^[24].

Importantly, the amorphous *vs* crystalline ratio has been found to diverge between cellulose source (e.g. cotton *vs* softwood) inducing distinct CNP sizes.^[24]

Remarks regarding OCNF and CCNF The OCNF described in the experimental chapters is produced using the TEMPO-mediated oxidation of wood pulp followed by high-pressure homogenisation.^[13,16,17] The OCNF was provided as a ≈ 8 wt% paste in water with a degree of oxidation of $\approx 25\%$ as determined by conductometric titration and solid state NMR (described in section 10.2). Although the introduction of the carboxylate group is selective to the C6 position of the glucose unit, the spatial distribution of the glucose unit containing carboxylate group is expected to be stochastically distributed onto the fibril. For the CCNF, the GTMAC grafting is not selective to a specific hydroxyl group of the glucose unit, hence, the GTMAC grafting is expected to occur stochastically at the glucose unit and fibril level. To date, a detailed study regarding the distribution of functionalised glucose units within the CNP has not been described in the literature. In addition, for OCNF, the ratio between crystalline and amorphous domains has generally been found between 0.7 and 0.9, as determined by X-ray diffraction, and this variation assigned to the different cellulose source.^[13,27] For CCNF, the ratio between crystalline and amorphous domains has been determined via NMR to be ≈ 0.4 for the same cellulose source (α -cellulose) and grafting procedure described in the experimental chapters.^[20]

Although OCNF and CCNF own a similar degree of functionalisation, they could not be considered as mirror particles with opposite charge due to the chemical difference between functional groups. Specifically, the quaternary ammonium group, from the GTMAC grafting, has less charge accessibility compared to the carboxylate group. As such, CCNF is less susceptible to ion-induced charge screening compared to OCNF.^[28]

1.3 Assembly in bulk - 3D

Controlling CNP assembly is pivotal for the production of functional materials with targeted properties. For instance, large aspect ratio CNP are of great interest due to their ability to form hydrogels and Volume-spanning Arrested States (VAS) with up to 99.9 wt% water.^[29,30] It is noted that although both gels and VAS show solid like properties at rest ($G' > G''$ in the linear viscoelastic region), they are differentiated by the presence of attractive and repulsive colloidal particles, respectively.^[31] The effect of CNP concentration in aqueous media is a crucial parameter, leading to a sol-gel transition upon increasing CNP concentration.^[21] Gelation is often associated to the formation of a percolated network due to the long range connectivity of CNP. Nordenstrom et al. obtained an estimate of the minimum amount of CNP required to form a percolated gel (ϕ_{min}) from the inverted cuvette test.^[30] It is noted that this methodology accesses the minimum amount of CNP required to form a network which does not yield upon the gravitational stress. Nordenstrom et al. found that the CNP concentration required to form VAS and gels decreases upon increasing CNP aspect ratio, making CNP with high aspect ratios more efficient rheological modifiers.^[30] A rough estimation of the percolation threshold of isotropically oriented CNP can be obtained using a volume excluded approach where each CNP is considered as a perfect rigid rod with radius, a , length, L , and a radius of gyration, R_g , as:^[32]

$$R_g^2 = \frac{a^2}{2} + \frac{L^2}{12} \quad (1.1)$$

From here it is possible to calculate the volume excluded by a single CNP as the volume of a sphere of radius equal to R_g (V_{R_g}) and, consequently, the number of V_{R_g} that can be contained in a specific volume (v). The maximum number of V_{R_g} contained in v will roughly correspond to the number of CNP at the ϕ_{min} . From here it is possible to track back the CNP wt% at the ϕ_{min} as discussed in section 10.6. For CNP with $a = 3$ and $L = 170$ nm, representative of the OCNF dimensions presented in the following experimental chapters and in the work of Schmit et al.^[21], $\phi_{min} \approx 1.4$ wt%. Although the calculation herein proposed does not account for anisotropic configurations of the rods and CNP-CNP interactions, the ϕ_{min} here predicted find good agreement with the OCNF concentration where the onset of elasticity and attractive interactions are reported in the work of Schmit et al.^[21] It is indeed generally accepted that at the ϕ_{min} rheological parameters as toughness, viscosity and elasticity increase significantly. However, in the work of Nordenstrom et al. for fibrils with similar aspect ratio a $\phi_{min} \approx 5.5$ wt% was reported.^[30] The source of large discrepancy can be associated to the inverted cuvet test employed in their study which does not probe the minimum CNP concentration required to undergo the sol-gel transition but rather the minimum CNP concentration to achieve a gel which is able to hold its shape, avoiding yielding, along the experimental time frame. Overall, the large aspect ratio of CNP allows for the sol-to-gel transition in a concentration range between 1 - 6 wt% in absence of extra additives such as surfactants and salt. As such, in the following experimental chapters, CNP concentrations below the one required to induce the sol-to-gel transition are generally used to better relate rheological and structural changes to specific phenomena (e.g. temperature, addition of additives).

Increase in CNP concentration has also been shown to induce the formation of nematic domains.^[33-35] This isotropic-to-nematic transition was, at first, suggested by Uhlig et al., via the formation of a structure peak in small angle neutron scattering experiments upon the increase in CNP concentration - the structure peak associated with a preferential assembly of CNP (discussed in 2.1.2). The isotropic-to-nematic transition has been further validated through polarized optical microscopy and associated with sharp rheological changes, such as increase in viscosity and elasticity.^[34,35] Shear induced nematic ordering has also been shown to be strongly dependent on the CNP concentration as elucidated by rheo-SANS experiments.^[36] In particular, the greater

CNP alignment at a specific shear rate (elucidated by the degree of anisotropy of two-dimensional scattering data) has been correlated to the shear thinning behaviour (decrease in viscosity with the shear rate).^[36] Shear thinning behaviour of CNP hydrogels has been shown to be comparable with commercially available creams and gels for topical drug delivery.^[37] As such, shear thinning has been often considered an exploitable feature of CNP in formulations for personal care products.^[38] A further advantage of the shear induced CNP alignment has been demonstrated in wet-spun fiber formations where fibers of μm range in diameter and mm in length are produced through the extrusion of CNP hydrogels in a coagulation bath (e.g. ethanol).^[39,40] The degree of CNP alignment in the extrusion capillary was found to strongly affect mechanical properties. In particular, toughness and elasticity increased with the CNP alignment.^[39,40]

1.3.1 Ion induced assembly

Since the development of the Derjaguin–Landau–Verwey–Overbeek (DLVO) theory, colloidal stability has been often described as the balance of long range repulsive electrostatic forces (V_r) and short range attractive forces (V_a) (e.g. van der Waals and hydrogen bonds) as:

$$V = V_r + V_a \quad (1.2)$$

Where V is the interaction potential energy, often expressed in kT (k being the Boltzmann constant, and T the temperature in Kelvin). Fukuzumi et al. employed experimental methodology (rheology and turbidity measurements) to prove the validity of the DLVO theory for CNP dispersions.^[41] CNP were treated as cylindrical rods, where the repulsive and attractive potential for two parallel CNP, V_r^p and V_a^p respectively, were calculated as^[41]

$$V_r^p = 64\pi^{0.5} \frac{(\kappa a)^{0.5}}{\kappa^2} n k T \gamma^2 L \exp(-\kappa H) \quad (1.3)$$

$$V_a^p = \frac{-ALa^{0.5}}{24H^{1.5}} \quad (1.4)$$

whilst the repulsive and attractive potential for two crossed CNP, V_r^c and V_a^c respectively, calculated as

$$V_r^c = 128\pi \frac{a}{\kappa^2} n k T \gamma^2 \exp(-\kappa H) \quad (1.5)$$

$$V_a^c = \frac{-Aa}{6H} \quad (1.6)$$

where,

$$\gamma = \tanh\left(\frac{e|\zeta|}{4kT}\right) \quad (1.7)$$

$$\kappa = \sqrt{\frac{2\rho e^2}{\epsilon_0 \epsilon kT}} \quad (1.8)$$

For simplicity, symbols and respective descriptions are shown in Table 1.1. This theory is based on the concept that the electrolyte concentration decreases the Debye length ($\frac{1}{\kappa}$), associated with the repulsive forces, until a threshold where associative forces dominate.^[41] For instance, for OCNF, presented in the following experimental chapters, the Debye length (equation 1.8) decreases from a few nm to sub- nm length scales upon an increase of the ionic strength (Figure 1.3 insert), leading attractive interactions to dominate. This is depicted by the interaction potential energy profiles shown in Figure 1.3. For parallel interactions of OCNF (considered as a cylinder with a radius (a) of 3 nm and length (L) of 170 nm) the maximum energy potential (V_{max}) decreases from $\approx 400 kT$ to $\approx 100 kT$ upon an increase of the ionic strength (Figure 1.3 a, b). Such decrease in V_{max} allows a reduction in the average inter-particle distance, although

Table 1.1 Symbols from equation 1.3, 1.4, 1.5, 1.6, 1.7, 1.8 with description and unit as described by reference^[41]

Symbol	Description	Unit
A	Hamaker constant	J
n	number density of ions	m^{-3}
κ	Reciprocal Debye length	m^{-1}
k	Boltzmann constant	$J \cdot K^{-1}$
ρ	Bulk concentration electrolytes	m^{-3}
H	Distance between particles	m
a	Radius of cylinder	m
L	Length of cylinder	m
e	Electron charge	C
ζ	Surface charge	V
ϵ_0	Vacuum permittivity	$F \cdot m^{-1}$
ϵ	Relative permittivity of the media	-

the positive and large value of kT denotes that parallel assembly is not favourable even at high salt concentrations. Nevertheless, the interaction potentials for crossed OCNF (Figure 1.3 c, d) display much lower values of kT , compared to the parallel interaction potential. Specifically, at greater ionic strength, V_{max} is of the order of the thermal energy (few kT) allowing spontaneous aggregation. Similar interaction potential profiles were found by Fukuzumi et al. for OCNF with a similar size to that herein reported.^[41]

As shown by Fukuzumi et al., the favourable interactions between crossed cylinders displayed by the DLVO prediction, were well correlated with an increase in viscosity, and an increase in turbidity.^[41] Further investigations conducted via small angle scattering has shown that a transition from repulsive to attractive interfibrillar interactions occurs upon the increase of ionic strength; this was well associated with a sol-to-gel transition.^[21] Divalent and trivalent ions have been shown to be more effective gelators than monovalent ions.^[34,42,43] This related to the fact that ions with greater valency are more effective towards charge screening of CNP.^[34] Moreover, Bertsch et al. proved through a combination of scattering, rheological and imaging techniques that careful tuning of repulsive *vs* attractive interactions leads to the formation of ordered nematic domains.^[34,35] Similarly to the ionic strength, it has been found that tuning of the pH leads to a different state of aggregation of CNP. For instance, for OCNF, which bear a carboxyl group on the surface, it has been shown that at pH values similar to the pKa of the carboxyl group, protonation of the charged moieties occurs, leading to a reduction in surface charge and strong aggregation.^[27,44,45]

1.3.2 Modulating CNP assembly *via* addition of secondary components

As previously discussed, CNP can form hydrogels at low concentrations. The shear thinning behaviour of these hydrogels makes CNP appealing for specific industrial applications as bio-based rheological modifiers, for instance, in formulations for personal care products, where a shear thinning behaviour is desired. However, the interactions of CNP with a variety of surfactants and/or polymers present in formulated products also needs to be accounted for.

1.3.3 CNP-surfactant interactions

CNP assembly in presence of negative, positive and neutral surfactants revealed that positively charged surfactants (oppositely charged compared to OCNF) were the most efficient to induce destabilization of the dispersions as shown through a combination of optical and rheological analysis. The presence of anionic surfactants, such as sodium dodecylsulfate (SDS) or sodium lauryl ether sulfate (SLES), has been shown to strongly influence the rheology of the CNP suspensions,

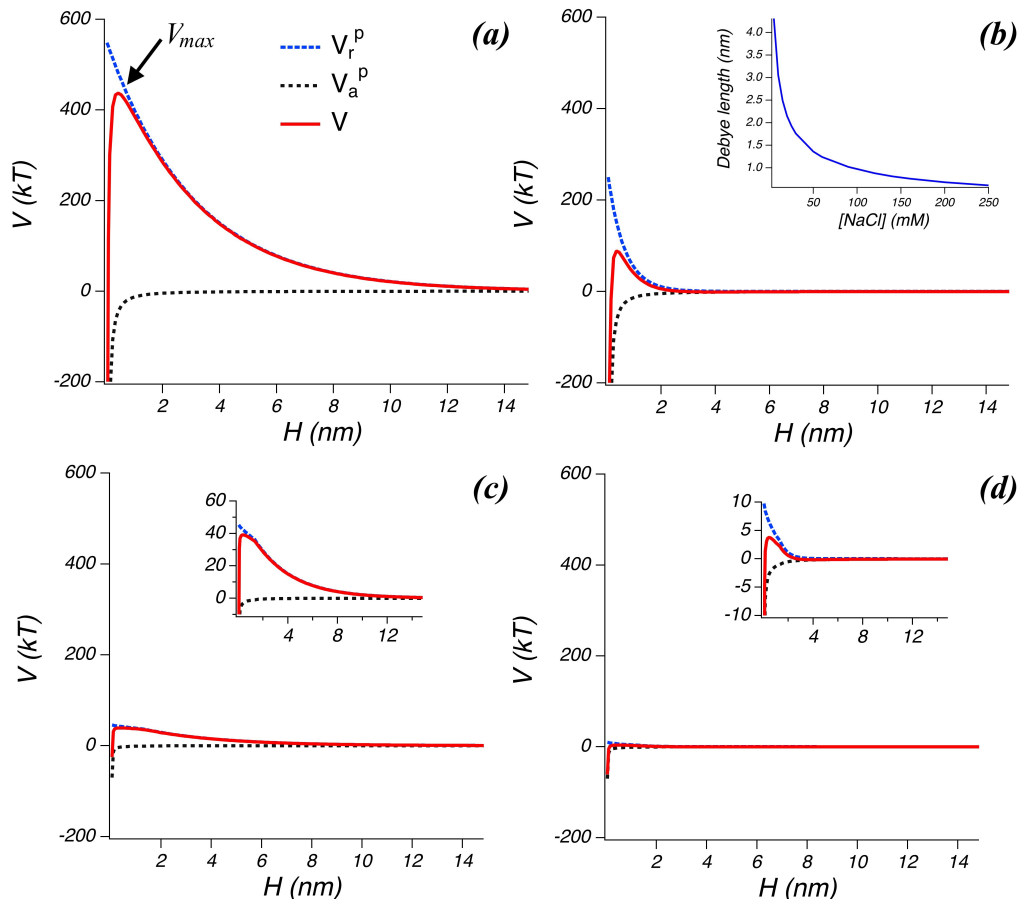


Figure 1.3 Interaction potential energy (V), expressed in kT , between two parallel (a, b) and crossed (c, d) cylindrical rods of radius 3 nm and length of 170 nm at low ionic strength, 10 mM NaCl at $|\zeta| = 50 \text{ mV}$ (a, c), and high ionic strength, 250 mM NaCl at $|\zeta| = 22 \text{ mV}$ (b, d). Cylinder dimensions and values of $|\zeta|$ at specific ionic strength are representative of OCNF presented in the following experimental chapters.

leading to the formation of gel-like materials with pronounced thinning upon shear.^[38] These strong associative interfibrillar interactions have been hypothesized to arise from either micellar cross-linking or a depletion flocculation mechanism.^[38] Contrarily, the presence of neutral surfactants in CNP dispersions kept the suspension stability unchanged up to a surfactant concentration of 8 wt\% .^[46] An instance of the different optical appearance for OCNF dispersions in presence of differently charged surfactants is presented in Figure 1.4a.^[46] Further work on CNP-oppositely charged surfactant interactions acknowledged electrostatic interactions as the driving force of surfactant adsorption onto the oppositely charged CNP surface.^[47–50] Increase of the ionic strength was shown to retard the adsorption of the surfactant onto the CNP surface, whilst increasing the charge density of the CNP lead to an opposite trend.^[50] On the application side, the combination of CNP and surfactant has recently been proposed as a greener alternative for enhanced oil recovery, where CNP and surfactants allow tuning of viscosity and surface activity, respectively.^[51]

1.3.4 CNP-polymer interactions

Due to the hydrophilic nature of CNP, many of the potential applications will likely be in aqueous media, hence, understanding CNP interactions with water-soluble species such as water-soluble polymers is pivotal.^[52] CNP-polymer interactions have been shown to be strongly polymer-type dependent; hindering any structural and rheological prediction prior to experimental proofs. CNC

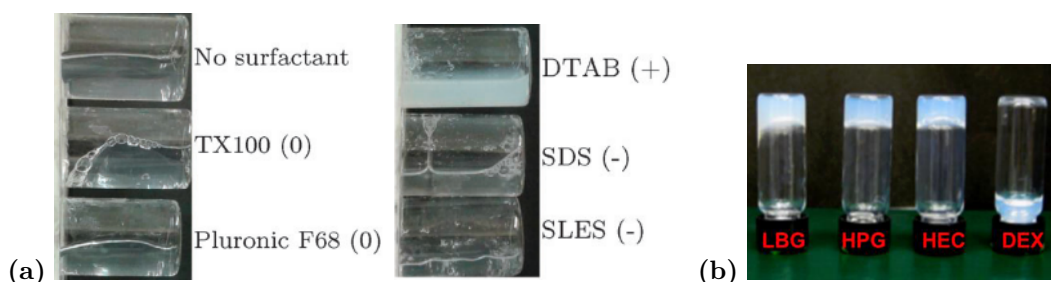


Figure 1.4 (a) CNP dispersions containing non-ionic, cationic and anionic surfactants as indicated by (0), (+), and (-), respectively. Reprinted from^[46] with permission of the Royal Society of Chemistry. (b) CNP dispersions containing locust bean gum (LBG), CNP-hydroxypropyl guar (HPG), CNP-hydroxyethyl cellulose (HEC) and CNP-dextran (DEX). Reprinted from^[57] with permission of the American Chemical Society.

in the presence of the negatively charged carboxymethyl cellulose (CMC) was found by Oguzlu et al.^[53] to induce depletion flocculation of the CNC alongside a sol-to-gel transition whilst Chen et al.^[54] reported on the formation of stable colloidal CNC dispersions in the presence of CMC; this latest report found little or no interactions of CMC with CNC. Interestingly, the presence of CMC has been shown to promote the formation of nematic domains in CNC dispersions, in a similar fashion as recently described by Bertsch et al.^[34,35] upon NaCl addition.^[53] The presence of non-ionic polymers in CNP dispersions has been shown to lead to divergent results in terms of CNP-polymer interactions and rheological behaviour. For instance, poly(vinyl alcohol) (PVA) has been shown to adsorb onto the CNC surface, leading to stronger interfibrillar interactions; as shown by a weak strain overshoot in an oscillatory strain sweep experiment discussed in section 2.2.2.^[54] Nevertheless, another non-ionic polymer, poly(ethylene oxide) (PEO), has been shown to weakly adsorb onto the CNC surface, although the rheological properties of the hydrogel were unchanged.^[53] Non-ionic polyethylene glycol (PEG) was found to not adsorb onto CNC surfaces whilst inducing gelation through a depletion flocculation mechanism.^[55] Similarly, the addition of high molecular weight dextran (DEX) caused demixing due to depletion flocculation, altering the nematic ordering of CNC.^[56] Further investigation revealed that dextran did not adsorb onto the CNC surfaces, so did not change the rheological properties of the hydrogels.^[57] Other non-ionic polymers such as hydroxyethyl cellulose (HEC),^[58] hydroxypropyl guar (HPG) and locust bean gum (LBG) adsorbed onto CNC surfaces, leading to a sol-gel transition when added to a liquid-like CNC dispersion as displayed in Figure 1.4b.^[57] Overall, two distinct phenomena can be discerned for CNP-polymers systems: (i) polymer adsorption onto CNP and (ii) depletion flocculation induced by the polymer. However, a clear understanding of the structure-to-mechanical property relationship of these systems is still lacking.

1.4 Assembly at interfaces - 2D

Surface active species, such as amphiphilic surfactants, are well known to adsorb at the interface of two immiscible phases such as water/air (W/A) or water/oil (W/O). This is associated with the affinity of the hydrophilic segments with the polar phase, coupled with the affinity of the hydrophobic segments with the more hydrophobic phase. For surfactants, the partitioning of the hydrophobic chain towards the affine phase (e.g. oil) has been shown to increase the mobility of the molecules constituting the counter-phase (e.g. water), leading to an augmented entropic contribution (ΔS).^[59] The favourable surfactant adsorption across two immiscible phases is often described by a negative Gibbs free energy of adsorption, ΔG , given as

$$\Delta G = \Delta H - T\Delta S < 0 \quad (1.9)$$

where ΔH is the adsorption enthalpy, and T the temperature. ΔG is also expressed as

$$\Delta G = \gamma\Delta A - T\Delta S \quad (1.10)$$

where γ is the surface tension, defined as the work required to increase the area of a surface isothermally, and ΔA is the surface area between the two phases.^[60] It is consequently possible to relate surfactant adsorption at interfaces *via* surface tension measurements.

Differently from amphiphilic (macro)molecules, the adsorption of non-amphiphilic particles is still not well understood. At the present, it is unclear whether there is a generalized rule which links particle adsorption to a decrease in γ as for the case of surfactants. This is displayed by scattered opinions and contradictory results in the scientific community.^[61] For instance, Vatanparast et al.^[62] reported that hydrophilic silica nanoparticles alone are not surface active, similarly to the previous report of Vignati et al.^[63] However, Du et al. reported on the decrease in γ with particle adsorption at W/O interfaces, employing different types of particles.^[64] Although it is unclear whether particle adsorption is driven by a decrease in γ , adsorbed particles would displace the contact area between the two phases, ΔA in equation 1.10, leading to a favourable energy of adsorption.^[61]

The understanding of particles adsorbed at the interface has been exploited in the context of emulsion stabilization. Emulsions are multiphasic systems, typically formed by an aqueous and an organic phase where one of the phases is present in the form of droplets (dispersed phase) and the second phase as the continuous phase. In the case of water and oil as the two immiscible phases, water-in-oil (water droplets in the continuous oil phase) and oil-in-water emulsions (oil droplets in the continuous aqueous phase) can be formed when energy is provided to the system. The energy input is usually induced through mechanical forces, such as shaking or homogenization, and in most cases it is required to overcome the thermodynamically unfavourable increase in surface area (ΔA in equation 1.10) achieved with the formation of droplets.^[65,66]

In the context of emulsions, the role of particles at the interface was first reported by Ramsden in 1903^[68] and Pickering in 1907^[69]. This type of emulsion has been, since then, identified as a Ramsden-Pickering or more frequently a Pickering emulsion. The stability of the particle-stabilized emulsions has been associated with the large energy of adsorption of the particles at the interface as described by the surface free energy, G , given as

$$G = \gamma_{1S}A_{1S} + \gamma_{2S}A_{2S} + \gamma_{12}A_{12} \quad (1.11)$$

where γ_{1S} , γ_{2S} and γ_{12} are the values of surface tension at the phase 1-particle, phase 2-particle and phase 1-phase 2 interface, respectively, whilst, A_{1S} , A_{2S} and A_{12} are the values of the contact area between phase 1-particle, phase 2-particle and the area eliminated by the adsorption of the particle at the interface, respectively.^[70] For spherical particles, equation 1.11 can be expressed

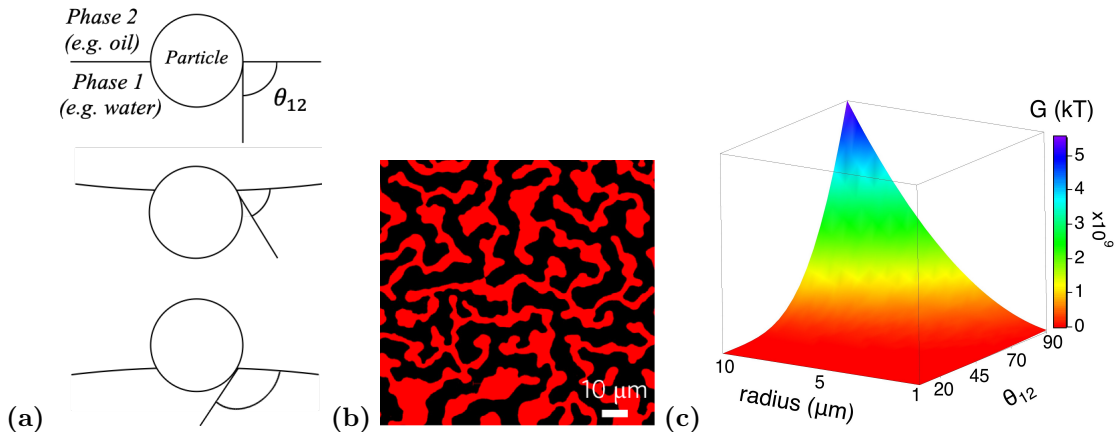


Figure 1.5 (a) Schematic illustration of the three phase contact angle, θ_{12} . (b) Micrograph of a bicontinuous interfacially jammed emulsion gel (or Bijel). Reprinted from^[67] with permission of Springer Nature. The red and black area corresponds to the oil and the aqueous phase, respectively. (c) Energy of adsorption (G) expressed in kT of spherical particles across the W/A interface ($\gamma_{w/a} = 72.2 \text{ mN} \cdot \text{m}^{-1}$) as function of particle radius and three phase contact angle, θ_{12} , at $T = 300 \text{ K}$, as calculated from equation 1.12

as

$$G = \pi r^2 \gamma_{12} (1 - |\cos \theta_{12}|)^2 \quad (1.12)$$

where r is the radius of the particle and θ_{12} is the three phase contact angle which is defined as the angle between the tangent to the particle surface at the three-phase contact line.^[71] The θ_{12} is conventionally measured from the aqueous phase and particles that adsorb with $\theta_{12} < 90^\circ$ and $\theta_{12} > 90^\circ$ are considered as hydrophilic and hydrophobic respectively (Figure 1.5a).^[71] When particles adsorb at the interface with $\theta_{12} \neq 90^\circ$ they will impose a curvature of the interface as schematically illustrated in Figure 1.5a.^[72] The type of curvature (concave or convex) depends on the hydrophilicity of the particles (hence θ_{12}). For instance, hydrophilic particles will partition a greater surface area towards the aqueous phase whilst hydrophobic particles towards the oil phase. Such curvature of the interface determines the formation of oil-in-water or water-in-oil emulsions in accord with $\theta_{12} < 90^\circ$ and $\theta_{12} > 90^\circ$, respectively. Interestingly, when the surface chemistry of the particle is tuned such as particles sit exactly at $\theta_{12} = 90^\circ$, the particles do not impose any curvature of the interface and the formation of an interconnected liquid network is achieved as shown in Figure 1.5b. The formation of this structure has been suggested for the first time through computer simulations in 2005 and named as bicontinuous interfacially jammed emulsion gel (or Bijel).^[73] An experimental follow up in 2007 provided evidence of the Bijel formation.^[74] As shown by equation 1.12, the energy of adsorption of a particle scales with r^2 and predicts the maximum energy of adsorption when a particle is exactly partitioned between the two phases, hence with $\theta_{12} = 90^\circ$, as depicted by Figure 1.5c. For instance, for a spherical particle sitting across the W/A interface ($\gamma_{w/a} = 72.2 \text{ mN} \cdot \text{m}^{-1}$) of $r = 10 \mu\text{m}$ with a $\theta_{12} = 90^\circ$ the energy of adsorption is in the order of $\approx 10^9 kT$, a value far greater than the energy provided by Brownian motion, resulting in an irreversible attachment of the particle at the interface under quiescent conditions.^[75]

1.4.1 CNP adsorption at liquid-liquid interfaces: Outlook

Since the first report, in 2011, of Kalashnikova and coauthors^[76] on CNP-stabilized emulsions, CNP adsorption at liquid-liquid interfaces has been broadly explored in the context of emulsions.^[70,77] Curiously, since the work of Kalashnikova et al. considerable research has been con-

ducted regarding the use of CNP as emulsion stabilizers without prior reports on CNP assembly across quiescent planar liquid-liquid interfaces via for instance surface shear rheology, reflectometry, or pendant drop tensiometric measurements. Experiments conducted on planar interfaces allow exploration of the assembly at the interface, which is still challenging to measure or purely qualitative (e.g. microscopy) for interfaces of microscopic droplets. In addition, experiments on quiescent planar liquid-liquid interfaces remove the variable of the energy input employed to generate the emulsions, allowing studies of the spontaneous CNP adsorption at the interface.

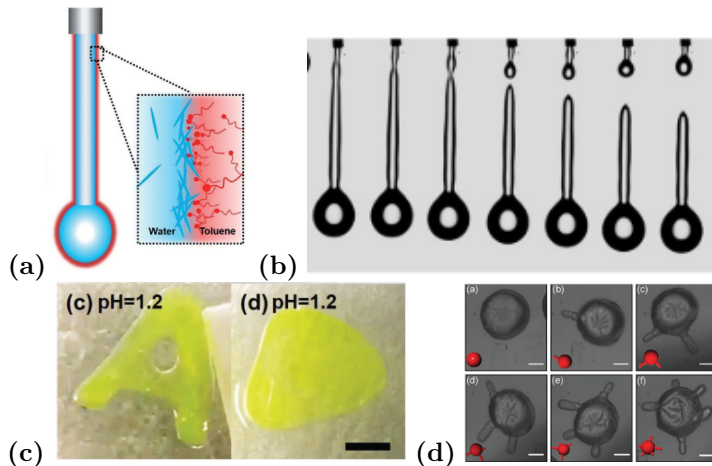


Figure 1.6 (a) Schematic illustration of the charge-driven interfacial assembly of negatively charged CNP and oppositely charged surfactants in the organic phase. Adapted from^[78] with permission of Angewandte Chemie International Edition. (b) Liquid tubules formed using an aqueous CNC dispersion and an organic phase rich in oil-soluble and oppositely charged species as presented in (a). Adapted from^[78] with permission of Angewandte Chemie International Edition. (c) Liquid letter formed using an aqueous CNC dispersion and an organic phase rich in oil-soluble oppositely charged polymer (left) and in absence of the oppositely charged polymer (right). Reprinted from^[79] with permission of Advanced Materials. (d) Microcapsules obtained through charge-driven interfacial complexation. Reprinted from^[80] with permission of the Royal Society of Chemistry.

1.4.2 CNP at planar liquid-liquid interfaces

The first instance of unmodified-CNP adsorption across liquid-liquid has been reported only recently by Bertsch et al.^[14] However, amphiphilicity tuning of CNP has been broadly employed to promote the CNP adsorption across planar interfaces. Such amphiphilicity tuning of CNP has been mainly achieved through (i) covalent grafting of hydrophobic moieties (e.g. carbon chains)^[81,82] or (ii) electrostatic binding of surfactants.^[78,79,83]

Regarding approach (i), it has been shown, for instance, that increasing the grafting of a C_{16} chain onto CNC, the contact angle increased to values $> 90^\circ$, pinpointing the hydrophobic character of the particles. Such interfacial CNC-layers were found to form weak interfacial networks, able to reform after breakage.^[81,82] For approach (ii), the main focus has been towards the coupled use of negatively charged CNP and oppositely charged oil-soluble surfactants (or polymers). This approach relies on the use of two oppositely-charged species with opposite phase affinity, which direct the assembly across the liquid-liquid interface as shown in Figure 1.6a. The charge-driven interfacial complexation follows a similar mechanism as proposed for the broadly studied complex coacervates (assembly driven by oppositely charged species) where adsorption is promoted through the favourable interactions between the oppositely charged moieties and due to the increased entropic contribution (ΔS) through counterion release.^[84] This charge-driven interfacial complexation has been shown to yield strong interfaces able to form well-defined and long-living liquid structures such as liquid-tubules,^[78] liquid-letters,^[79] and capsules^[80] as shown in Figure 1.6b, c and d respectively. Although qualitative proofs of the strong interfacial binding

have been pinpointed, the rheological properties of the interface that allow trapping of the liquid in long-living nonequilibrium shapes have not yet been defined. In such regard, rheological insights into the charge-driven interfacial assembly of OCNF at W/O interface are presented in Chapter 8 .

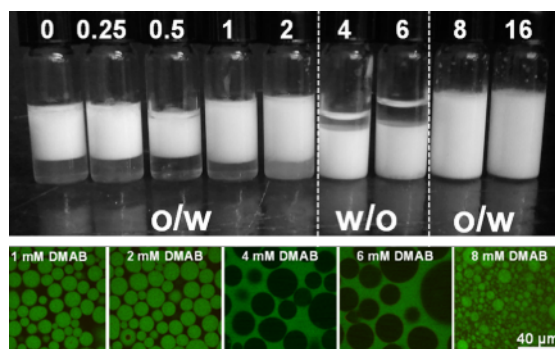


Figure 1.7 Top: emulsion produced using 50 vol% water and oil. The water phase with a fixed 0.25 wt% CNC and the surfactant didecyldimethylammonium bromide (DMAB) at concentrations (mM) indicated in the photograph. Bottom: confocal laser scanning microscopy (CLSM) photographs of the emulsions as shown in the top picture. The green areas in the CLSM pictures indicate the presence of oil. Adapted from^[85] with permission of Elsevier.

1.4.3 CNP at liquid-liquid interfaces of microscopic droplets: Pickering emulsions

The use of CNP as an emulsion stabilizer represents a low cost and sustainable alternative to conventional petrochemically-derived emulsion stabilizers. As such, since the first work of Kalashnikova and coauthors^[76] in 2011, the research on this area has increased drastically. Unmodified-CNP have been generally recognized as good Pickering stabilizers for oil-in-water emulsions due to the dominant hydrophilic character of the unmodified-particles.^[76,85–92] The good stability of the CNP-based emulsions has been mainly assigned to the coupled physical CNP barrier at the W/O interface and the CNP surface charge, hindering aggregation and coalescence of the droplets.^[76,89] Typical CNP (of nanometer size) produce droplets with a mean size in the order of $\approx 1 \mu\text{m}$ when full coverage of the W/O interface is achieved.^[89] As shown by small angle neutron scattering (SANS), charged CNC were shown to form, roughly, a monolayer around the oil droplets, in agreement with previous microscopy investigations.^[76,86] Contrarily, uncharged CNC showed a thicker layer, suggesting multiple CNC stacking at the interface^[86] and strong flocculation of the oil droplets due to charge screening.^[89] However, the fibrillar network formed at higher CNP concentrations was found to increase viscosity and reduce flocculation and creaming of the oil droplets.^[91] The use of oppositely charged surfactants, which adsorb onto the CNP surface, has also been shown to be a powerful strategy to modify the three phase contact angle, θ_{12} , of the particles, allowing the formation of water-in-oil or oil-in-water emulsions in according to the amount of used surfactant, as displayed in Figure 1.7.^[85] Alternatively, covalent grafting of hydrophobic moieties onto the CNP surface has also been shown to improve the emulsion stability compared to unmodified-CNP.^[93]

1.5 Aims and objectives

It can be concluded that CNP assembly can be tuned using different strategies, each of which will lead to a specific structure-property relationship. However, to exploit the full potential of CNP, unexplored strategies of assembly need investigation. This can be achieved by addressing industrially relevant research questions (e.g. *how do we make a product with a specific property?*) with more fundamental research questions (e.g. *why is this phenomenon happening?*). In such regard, this project aims to explore new avenues for CNP assembly in aqueous media leading to fabrication of capsules and hydrogels which could incorporate and deliver targeted components. To achieve this goal, the CNP assembly must be controllable and compatible with common industrial

processes and conditions. For instance, industrial operating temperatures can go up to *ca.* 150°C for common sterilization procedures and this could impact on the final material properties. The effects of heat are described in Chapter 3 which presents the heat-induced sol-to-gel transition occurring in aqueous OCNF dispersions.^[94] Moreover, the incorporation of CNP in formulated products must account for the presence of components, such as surfactants and polymers, which could interfere with (or aid) the CNP assembly. In this context, Chapter 4 describes the role of electrostatic interactions between zwitterionic cellulose nanofibrils (ZCNF) and surfactants, aiming to control the rheological behaviour of the dispersion. However, charge-driven complexation between CNP and oppositely charged surfactants reduces the charge accessibility of CNP; an useful feature for adsorption of charged species (e.g. ionic drugs) and/or further reactions. On this basis, the addition of non-interacting species, usually named fillers for the case of colloidal particles, in a CNP dispersion could enable rheological tuning while preserving the charge accessibility of the CNP. This is described in Chapter 5 which discusses how the filler size affects the structure and the rheological properties of a fibrillated network composed of OCNF. The understanding provided in Chapter 5 enabled the production of composite spheroidal hydrogels containing coordination polymers (in Chapter 6). Specifically, Chapter 6 describes key parameters that enable retention of coordination polymers into the gel structure. With the aim to form capsules characterized by a core-shell type of structures, Chapters 7 and 8, focus on the assembly of CNP across interfaces. Specifically, Chapter 7 presents the production of core-shell spheroidal hydrogels using CNP and an oppositely charged polymer. In the end, Chapter 8 focuses on the CNP assembly across the W/O interface, revealing key requirements to produce capsules with a solid-like shell.

Overall this work aims to bridge and broaden the understanding related to CNP assembly in bulk (3D) and across interfaces (2D); two crucial aspects to account for the production of capsules and hydrogels incorporating targeted components. This work begins with the principle of the characterization techniques (Chapter 2) used to establish the structure-property relationship of the CNP assembly. Experimental Chapters follow as summarised in Figure 1.8 and Chapter 9 draws conclusions from the experimental work and gives suggestions for future research directions.

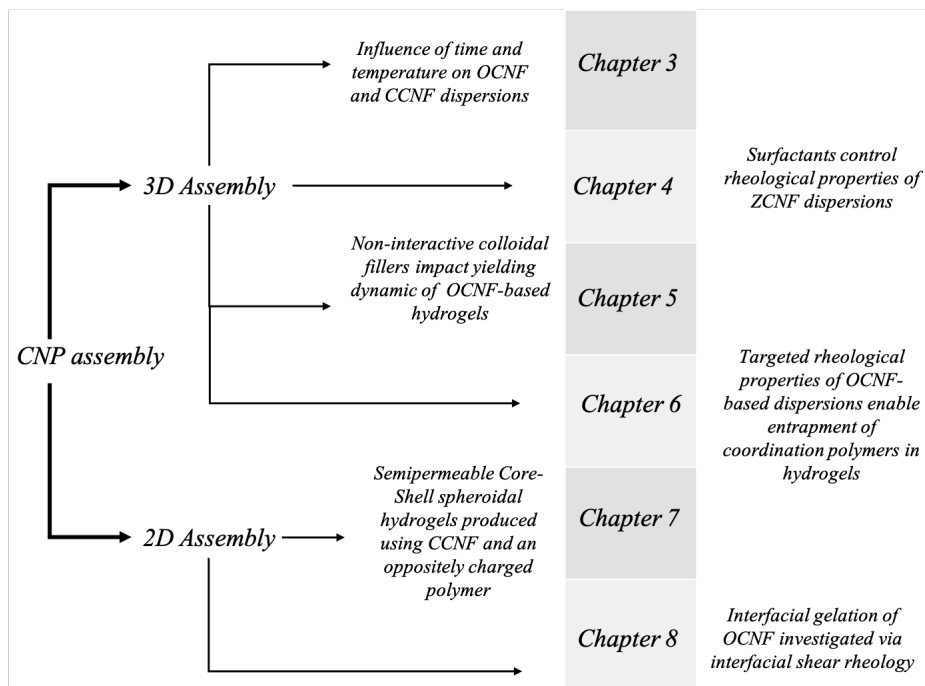


Figure 1.8 Schematic branching of the experimental chapters. For each Chapter a brief description is added to highlight the main topic.

Nowadays many techniques are available to study size, shape and assembly of colloidal particles. Scattering and rheology are powerful and versatile techniques which allow to establish the structure-to-mechanical properties relationship of materials. Scattering techniques are non-invasive and allow to probe the material architecture, whilst rheology determines how a material responds to deformations. As for every structural characterization method, scattering techniques often allows answers to questions as "*what is the structure?*", whilst rheology "*how does it flow?*". Although these are not trivial questions, the coupling of information obtained by scattering and rheology enables to further extend the scientific interest, and answer the question "*why does it flow?*". In the following sections, the principles of small angle scattering (SAS) and rheology are discussed with a focus on colloidal systems.

2.1 Small angle scattering

Most common scattering techniques rely on an incident monochromatic radiation of wavelength λ shone onto the sample which is then scattered by an angle θ and detected by a detector (Figure 2.1).^[95,96] Nevertheless, part of the radiation will be also transmitted, absorbed and reflected by the sample. Scattering events are classified as elastic and inelastic. In the case of elastic scattering, as displayed in Figure 2.1, the incident radiation is scattered without energy loss, whereas for the inelastic case, some energy is lost with the collision. The following sections will focus on elastic scattering only. In the case of elastic scattering, the incident wave vector, k , and the scattering wave vector, k' , have the same magnitude and they are defined by λ as^[32,95]

$$|k| = |k'| = \frac{2\pi}{\lambda} \quad (2.1)$$

The scattering vector, q , is defined as

$$q = \vec{k}' - \vec{k} \quad (2.2)$$

it follows that the scattering vector, q , is calculated as^[95]

$$q = \sin\left(\frac{\theta}{2}\right)(2k) = \sin\left(\frac{\theta}{2}\right)\left(\frac{4\pi}{\lambda}\right) \quad (2.3)$$

The q vector is particularly important to determine the probed length scale in the experiment and to compare scattering data produced by radiation with different λ (*e.g.* X-ray, light). It must be noticed that the q vector is in reciprocal space and the real space distance d is obtained by $d = 2\pi/q$. Therefore, at high angle or high- q , smaller structures are probed compared to low

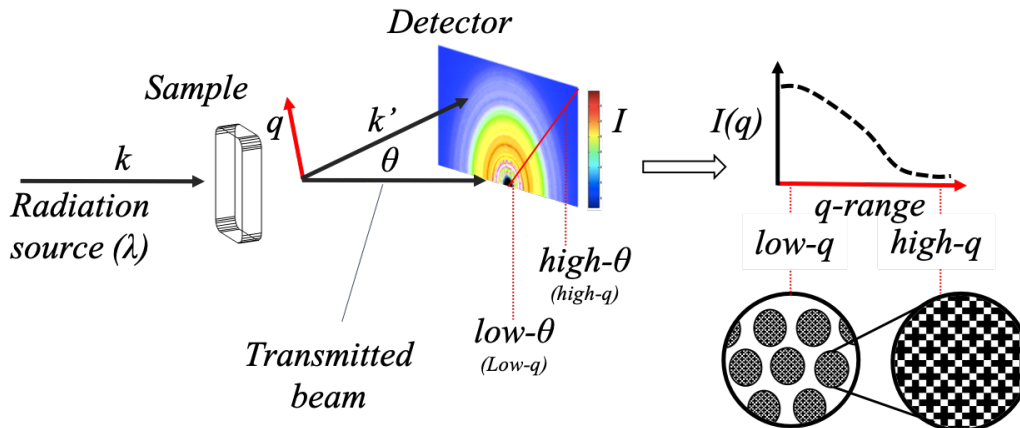


Figure 2.1 Schematic representation of the incident radiation (k), with wavelength (λ), scattered by the sample through an angle θ as indicated by the wave vector k' . q indicates the scattering vector. Conversion from a 2D scattering intensity profile to 1D scattering curves is shown on the right.

angles or low- q as schematically depicted in Figure 2.1.

The measured scattered intensity $I(q)(cm^{-1})$ is defined, for dilute isotropic suspensions of centrosymmetric particles as^[95]

$$I(q) = \phi V_p (\Delta SLD)^2 P(Q) S(Q) + Background \quad (2.4)$$

Where ϕ is the volume fraction occupied by the particles, V_p is the volume of a single particle (in cm^3), ΔSLD is the difference in scattering length density between the dispersed particles and the solvent (in cm^{-2}), $P(q)$ is the normalized form factor which describes the shape and size of the particles and $S(q)$ is the structure factor and describes interference of the radiation with multiple objects, thus usually associated with particle-particle interactions.^[95] The scattered intensity profile is collected by the detector as a 2D pattern (Figure 2.1). Isotropic 2D patterns are an indication of homogeneous and isotropic suspensions, whilst anisotropic 2D patterns arise from materials which exhibit ordered domains. To allow better comparison between samples, it is common practice for isotropic 2D patterns, to calculate the radial intensity average, as function of q , leading to characteristic 1D $I(q)$ vs q patterns as depicted in Figure 2.1. A further contribution to the scattered intensity arises from the air, sample holder (usually glass, or quartz for liquid samples) and solvent which has to be subtracted from the overall scattered intensity $I(q)$.

Scattering techniques have been widely employed to resolve particle morphologies, hence, focusing on the $P(q)$. To pinpoint the contribution arising from $P(q)$ to the scattering intensity, samples are usually prepared in the dilute regime; where the wavelength of the radiation is smaller than the distance between the particles. Therefore, each scattered wave vector will contain information regarding a single particle. For colloidal systems, this concentration is usually at $\phi < 0.01$. When the volume fraction increases, the mean particle distance becomes similar or smaller than the wavelength of the radiation source. The scattering wave vector will, therefore, contain contributions from neighbouring particles, pinpointed by $S(q)$ in equation 2.4.

$I(q)$ can be normalised for standard values (*e.g.* water or vanadium) in order to obtain values in absolute intensity.^[97] Data on an absolute scale are important to gain information regarding the total volume fraction or for instance the volume fractions of interacting objects. Nevertheless, the absolute intensity is not a requirement for the calculation of $P(q)$ and related information.

2.1.1 Radiation types: Neutron and X-ray

As described by equation 2.1 and 2.3, the λ of the incident radiation is crucial, together with the sample-to-detector distance, to specify the q -range of interest, therefore, to probe the desired features of the samples. For instance, visible light with λ in the range 390-700 nm is used as incident radiation, to probe length scales in the μm -range.^[98] As such, due to the shorter wavelength, X-rays and neutrons have been used to investigate objects from atomistic to nm scales (λ in the order of \AA). Nevertheless, X-rays and neutrons interact differently with matter and this needs to be accounted for.^[95] To describe how strongly radiations interact with atoms, the concept of scattering cross section, σ , has been introduced. The σ is measured in barns (1 barn = $10^{-28}m^2$) and is equivalent to the area of the atom *visible* to the radiation.^[99] X-rays are an electromagnetic radiation (usually $\lambda < 30\text{\AA}$) which strongly interact with the electron cloud of atoms. As such, strong X-rays scatterers have large values of atomic number.^[96] X-ray can be produced in laboratories, although, the poor flux (the number of incident neutrons or X-rays per unit area per second), the constrained sample-to-detector distance and the sample environment could often be limiting factors. To overcome these limitations, the use of large-scale facilities is often necessary. Such large-scale facilities produce a flux of X-rays orders of magnitude greater than bench-instruments and provide the opportunity to reach larger sample to detector distances allowing to probe larger length scales. Neutrons are neutral subatomic particles with a mass equal to 1839 electrons.^[98] They are more penetrating than X-rays since they are uncharged and interact with the nucleus of the atoms, a small portion of the whole atom.^[95] It is noted that as an estimate, the $I(q)$ decreases in relation with the sample thickness of 99% per mm for X-rays, compared to 1% per mm for neutrons.^[98] The specific interactions of neutrons with nuclei and X-rays with the electron cloud results in different SLD for the same component as captured by different equations needed to calculate the SLD. For neutrons, the SLD is calculated as the sum of the scattering properties of multiple atoms (b_i) normalised by the occupied volume, V (equation 2.5). For X-rays it is calculated as indicated by equation 2.6, accounting for the atomic number (Z_i) and the electron radius (r_e).

$$SLD = \frac{\sum_i^n b_i}{V} \quad (2.5)$$

$$SLD = \frac{\sum_i^n Z_i r_e}{V} \quad (2.6)$$

Considering a neutron beam, water and deuterated water (D_2O) provide an instance of molecules with different SLD ($SLD_{H_2O} = -0.56 \cdot 10^{-6} \text{\AA}^{-2}$, $SLD_{D_2O} = 6.34 \cdot 10^{-6} \text{\AA}^{-2}$), contrarily to X-rays, where the SLD for water and D_2O are unchanged.^[95] As such, the mixing of H_2O and D_2O at different ratios can be employed to tune the SLD of aqueous media. Therefore, SANS allows us to perform experiments where two or more components have equal SLD. These type of experiments are often referred as contrast matching experiments, where two or more components that have equal SLD are contrast matched, hence $\Delta SLD = 0$, and as indicated by equation 2.4, $I(q) = \textit{Background}$.^[32,95] In order to extrapolate, experimentally, the contrast match of a component in an aqueous media, it is common practice to measure samples prepared at equal concentration but different $D_2O\%$. Plotting the scattering intensity at low- q as $\sqrt{I(q_0)}$ vs $D_2O\%$ a linear trend is established. From the line crossover at $\sqrt{I(q_0)} = 0$ it is possible to extrapolate the $D_2O\%$ required to contrast match solvent and component.^[97] In Figure 2.2a, an example is provided. This information is extremely useful to deconvolute structural information in bi-component systems (e.g. A + B + Solvent). For instance, at the contrast match point $SLD_{\textit{solvent}} = SLD_A \neq SLD_B$ it is possible to obtain structural information of component B, without scattering contribution from A. In practice, this is the case when the components, A and B, are different in nature (e.g. lipid tails and DNA). For components with similar atomic composition, like starch and cellulose, this methodology fails. Nevertheless, tuning

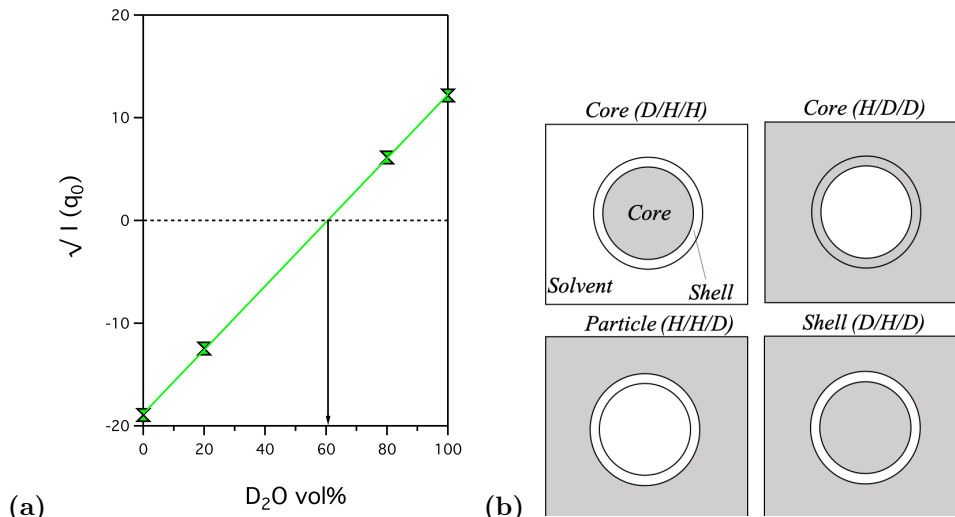


Figure 2.2 (a) Determination of the contrast match for an aqueous silica nanoparticle dispersion. The scattering Intensity at low- q ($I(q_0)$) for samples at different concentration of D_2O is plotted as the $\sqrt{I(q_0)}$ vs $\%D_2O$. A linear fit, indicated by the green line, was used to extrapolate the point where $\sqrt{I(q_0)} = 0$. (b) Schematic representation of the contrast matching experiment. H and D indicates hydrogenated and deuterated components.

of the ΔSLD between components can also be executed through the employment of deuterated components. An instance is provided for core-shell particles in Figure 2.2b. To highlight the scattering contribution from the core, a combination of deuterated core (D-core), hydrogenated shell (H-shell) and hydrogenated solvent (H-solvent) can be employed. Alternatively, H-core, D-shell and D-solvent. In both cases, the solvent and the shell are contrasted matched. Combinations of deuterated/hydrogenated components to highlight the scattering from the whole particle or the shell are depicted in Figure 2.2 (b). Although a simple concept, contrast-matching experiments employing deuterated components are not always possible. The main issues are the high cost and the difficulty to produce deuterated compounds. Moreover, the samples could change properties in the presence of D-solvents (e.g. D_2O) or other D-components, due to different inter-particle and intra-particle interactions. Therefore, such differences need considerations.

2.1.2 Probing colloidal systems

SAS has been broadly used in colloidal science to obtain specific structural information about particles and their assembly. To perform such characterization, model fitting of SAS data has become a must. The data fitting relies on the fact that objects scatter in according to their shape, volume and interactions as indicated in equation 2.4. Nevertheless, prior to data fitting, an in-depth knowledge regarding the system, coupled with a solid understanding of the scattering pattern is required. These prerequisites are pivotal to ensure a *real* physical interpretation of the system. Imaging techniques provide a way to obtain insights on the size and shape of the objects, although invasive sample preparation for sub- μm imaging techniques is often a hurdle. Once an indicative object size and shape is obtained, it is possible to use an appropriate fitting model for SAS data. At this stage, SAS over imaging techniques provide a much more, statistically meaningful information. Besides, SAS allows extrapolation of the interaction potentials between objects ($S(q)$) *in-situ*, without invasive sample preparation. Instances of scattering patterns of monodisperse hard spheres and cylinders in dilute conditions, $S(q) = 1$, are shown in Figure 2.3. At high- q , the linear trend (in a log-log plot), often referred to the Porod region, indicates that the characteristic length scale of the object is probed. At the end of the Porod region, towards lower q , a new characteristic dimension is probed or the onset of a plateau region, called the Guinier

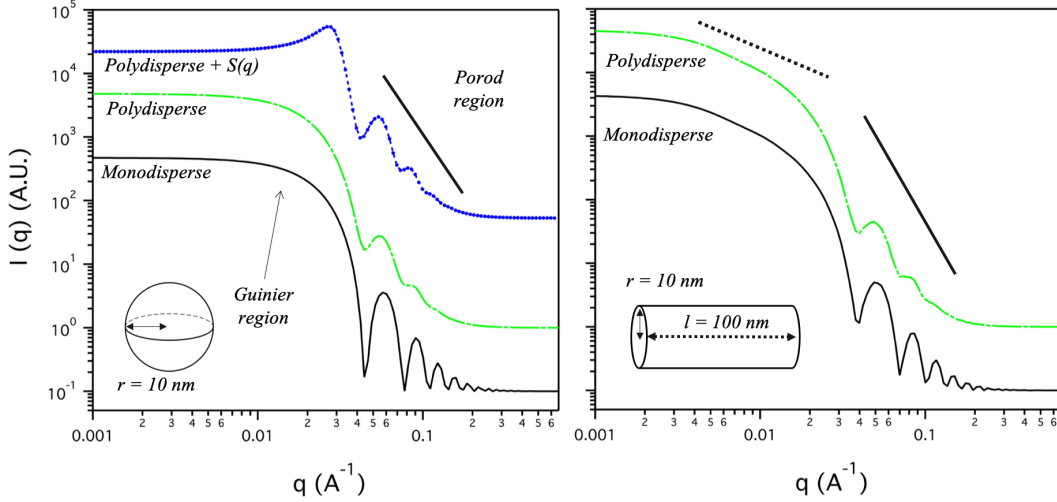


Figure 2.3 Scattering patterns for (left) spheres and (right) cylindrical objects. For both, spheres and cylinders, the effect of radius polydispersity is shown. For the concentrated polydisperse spheres, the structure factor ($S(q)$) is shown.

region, occurs. For spheres, since only one characteristic dimension is present (the radius, r), the Guinier region follows the Porod, indicating that the object size is fully probed. As such, the point where the Guinier region onsets allows estimation of the radius of gyration of the probed object as $d = 2\pi/q$. On the contrary, for cylinders, two different slopes are visible; at high- q the radius and at lower q values the overall length of the cylinder. Increasing polydispersity of the radius for the scattering patterns showed in Figure 2.3 results in smoother curves due to the averaged form factor between objects of different size.^[96] When the particle concentration is increased above a certain threshold, interparticle interactions begin to be detectable. For instances, particles interactions for polydisperse hard sphere are displayed in Figure 2.3 by a sharp peak occurring in the proximity of the Guinier region.

The ability to probe structures at different length scales made SAS techniques pioneering in the characterization of the colloidal assembly in terms of fractal dimension (D).^[100] The concept of fractal aggregation relies on the structure self-similarity at different length scales as displayed in Figure 2.4.^[100] With a focus on colloidal science, fractals can be defined as objects formed by a number of primary particles (i) which scales with the radius of gyration (R_g) of the cluster and the radius of the single particle (R_p) as described in equation 2.7 (Figure 2.4).^[100]

$$i \propto \left(\frac{R_g}{R_p} \right)^D \quad (2.7)$$

Assuming constant R_g and R_p , aggregates with a large value of D have more primary particles, i , than aggregates with smaller D . Hence, greater values of D correspond to denser aggregates. The D is obtained by the exponent of the power law ($I(q) \propto q^n$) in the Porod region, hence, often referred to the fractal Porod exponent. At low- q , when the exponent of the power law (n) follows a constant trend, the presence of a fractal-like aggregate is referred to the mass fractal D_m ; associated to the number or mass of the particles per unit volume.^[32] On the contrary, at high- q , the object surface is probed. Therefore, the fractal scaling obtained from the high- q region is indicative of the surface fractal, D_f . The surface fractal is a number from 3 to 4, where 3 corresponds to a rough surface and 4 to a completely smooth surface. The D_f is obtained by the power law at high- q and follows the power law exponent as $D_f = 6 - |n|$.^[32]

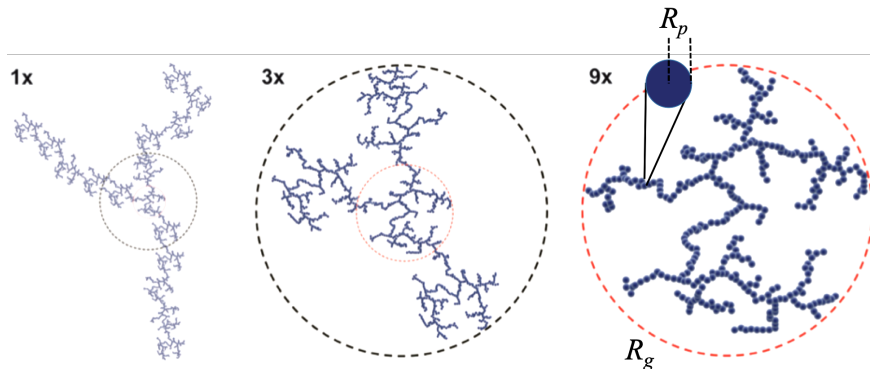


Figure 2.4 Fractal objects observed at different magnification (1, 3 and 9x). R_g and R_p indicate the radius of gyration of the cluster and the particle, respectively. Reprinted from^[101]
 - Published by the PCCP Owner Society.

2.1.3 SANS and SAXS instruments

In the following experimental sections, the data presented from SANS and SAXS experiments have been obtained from different facilities, each with specific characteristics.

(i) SANS2d (ISIS, Rutherford Appleton Laboratory, Didcot, UK). This is a time-of-flight SANS (ToF-SANS) instrument which uses multiple wavelength ($2.0 \leq \lambda \leq 14.0 \text{ \AA}$) instead of a monochromatic beam (with a single wavelength). In ToF-SANS instruments the λ is calculated by the time that a single neutron uses to cover the source-to-detector distance. ToF is common for SANS instruments which use neutron produced by spallation sources, where a proton beam collides with an heavy metal target generating a pulsed neutron beam. ToF-SANS allows the best use of the incoming neutrons, yielding an high flux and the widest possible q-range for a fixed sample-to-detector distance. For ToF-SANS, the frequency of the neutron pulse is pivotal, together with the length of the instrument, to avoid overtaking of the slowest neutrons by the fastest neutrons (with small λ).^[102]

(ii) D22 (ILL, Institut Laue Langevin (FR)). This is a SANS instrument which uses a continuous neutron beam generated by a nuclear reactor. This instrument uses a single wavelength ($4.5 \leq \lambda \leq 40 \text{ \AA}$) selected by a monochromator. The detector is placed in a vacuum chamber and the operating sample-to-detector is in the range 1.1 - 17.6 m. For this instrument, it is often the case to acquire data in 2 different sample-to-detector positions when a wider q-range is required.

(iii) I22 is a SAXS instrument (Diamond Light Source, Rutherford Appleton Laboratory, Didcot, UK) which uses a monochromatic X-ray beam of $\lambda = 1 \text{ \AA}$ accelerated by a synchrotron. The 2D data are collected by a SAXS and a WAXS detector with adaptable sample-to-detector distance. For this beamline, only the length between the sample and the SAXS detector is in vacuum. The large sample area allows specific sample environments to be installed (e.g. Rheo-SAXS).

(iv) Anton-Paar SAXSpoint 2.0 is an in-house SAXS instrument equipped with a copper source (Cu K- α , $\lambda = 1.542 \text{ \AA}$) and a 2D EIGER R series Hybrid Photon Counting (HPC) detector. The sample-to-detector distance can be tuned to cover a q-range of ($0.01 \leq q \leq 2 \text{ \AA}^{-1}$). Samples are loaded in sealed quartz capillaries and placed in a vacuum chamber.

2.2 Rheology of soft materials and complex fluids

The name rheology derives from the Greek *rheo* "flow" and *logia* "study", hence, it is defined as the study of deformation and flow of matter. The assessment of rheological properties is important for day-to-day materials (*e.g.* personal care, food, cleaning agents), therefore highly interesting for industrial purposes. From a more fundamental point of view, the accurate evaluation of the rheological properties is of great importance to assess interactions in soft materials and complex fluids.^[103,104] Shear rheology has been, for more than one century, one of the most employed technique to probe bulk properties. This technique is based on the concept of shear flow, which identifies a uniform flow which follows the direction of the shear.^[105] Specifically, a fluid between two parallel plates at distance, h , flows when the top plate slides with velocity V in the x direction over the stationary bottom plate (Figure 2.5). The nearest fluid layer to the moving plate will move at a velocity equal to V , whilst the subsequent fluid layers will move at a local velocity of V_x , following a constant V_x gradient with h . As such, the shear rate, $\dot{\gamma}$, can be defined as^[105]

$$\dot{\gamma} = \frac{dV_x}{dh} = \frac{V}{h} \quad (2.8)$$

To generate the flow, the top plate has to slide in the x plane with a force which is proportional to the surface area of the plate. Therefore the characteristic force is expressed as stress, σ , which corresponds to the force applied per unit area. From here the proportionality between $\dot{\gamma}$ and σ can be related to the proportionality factor, viscosity (η) as

$$\sigma = \eta \dot{\gamma} \quad (2.9)$$

From equation 2.9, it is possible to categorize two main type of fluids: Newtonian, which η is independent of $\dot{\gamma}$ and non-Newtonian, where η is dependent on $\dot{\gamma}$. It must be noticed that in order to ensure a well-defined velocity gradient, shear of the plate should be slow enough to avoid turbulent flows and care must be taken to avoid slippage of the sliding plate with the nearest fluid layer (often referred to as wall slippage). Since rheological measurement relies on a defined $\dot{\gamma}$, the choice of the right geometry is helpful to avoid undesired phenomena (*e.g.* turbulence and slippage) and to obtain meaningful data in a broader range of $\dot{\gamma}$. Low viscosity liquid samples are measured in concentric cylinder types of geometry (Figure 2.5b), where the large surface area of the geometry increases the sensitivity of the measurements at low $\dot{\gamma}$. For solid-like materials such as gels and pastes, cone and plate and parallel plate geometries are advised (Figure 2.5b). Geometries with special refinements, as sandblasted geometries, are also available in order to avoid wall slippage between the probe and the sample.^[106]

2.2.1 Steady-state shear flow

From day-to-day experience, we know that increasing the concentration of particles in a liquid phase (*e.g.* adding flour in water) would increase the overall viscosity up to the formation of a paste or a solid-like material (the dough is ready!). Hence, a general relation between η and the particle volume fraction ϕ can be generally postulated as

$$\eta = f(\phi) \quad (2.10)$$

where ϕ is the volume of the particles over the the total volume of the suspension.

The theoretical prediction of η in complex fluids has interested scientists for more than one century and yet, the complete theoretical understanding has not been achieved. One of the complications arises especially for non-Newtonian fluids, where η is a function of $\dot{\gamma}$ (equation 2.9), ϕ (equation 2.10) and often also dependent on the characteristic time scale of the measurement.

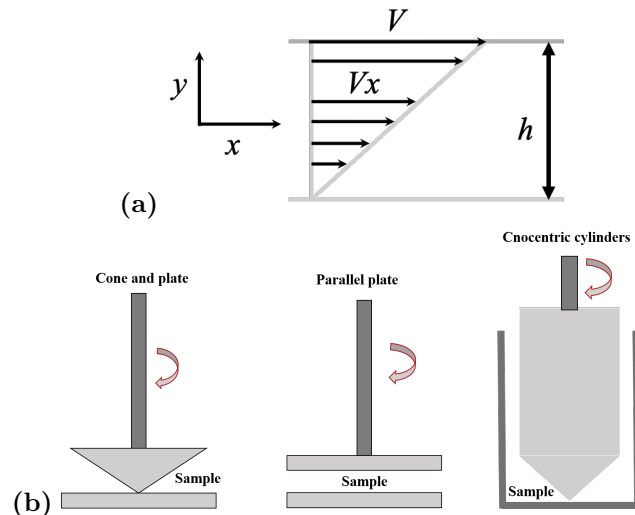


Figure 2.5 (a) Velocity gradient of a fluid in between a stationary (bottom) and a sliding plate (top). The distance between the plates is indicated by h . The velocity of the moving plate is V whilst the velocity of the fluid V_x . (b) Common geometries employed for rheological measurements.

Viscosity as function of shear rate

Laun^[107] described well this complex relationship using the gradual concentration increase of charge-stabilized latex particles in water (Figure 2.6a). At low concentration, the fluid is Newtonian, whilst at greater concentrations, non-Newtonian behaviour is observed. Specifically, a pronounced decrease in η with $\dot{\gamma}$ occurs in the low- $\dot{\gamma}$ region; this is referred to as shear thinning. Contrarily, in the high- $\dot{\gamma}$ region, η increases as function of $\dot{\gamma}$; this phenomenon is known as shear thickening. Shear thinning is a ubiquitous phenomenon occurring in dispersions at moderate values of ϕ . The origin of shear thinning is strongly system dependent. For instance, shear thinning of colloidal particles with a large aspect ratio (e.g. fibrils), has mainly been associated to the alignment of the particles in the direction of the flow.^[108–110] Contrarily, for strongly heterogeneous and aggregated systems, this phenomenon has mainly been attributed to the breakage of the aggregates upon shear.^[44,111] Different rheo-optic techniques have been developed to better understand the origin of shear thinning, mainly flow birefringence and rheo-SAS (small angle scattering).^[112]

Shear thickening usually occurs at high values of volume fractions $\phi \geq 0.40$ and in the high- $\dot{\gamma}$ region. Although the specific origin of shear thickening is system-dependent, the general cause has been associated with the restricted motion of particles in suspensions, causing a strong energy dissipation and an increase in viscosity.^[113] The most famous example of shear thickening material is corn starch in water at concentrations greater than 55wt%.^[114] In shear thinning materials it is often possible to distinguish two viscosity plateaus: a Newtonian region at low- $\dot{\gamma}$ and high- $\dot{\gamma}$, indicated by η_0 and η_∞ , respectively. (Figure 2.6b). At low- $\dot{\gamma}$, the applied stress is not enough to disrupt the interparticle equilibrium, whilst, at intermediate- $\dot{\gamma}$ the particles rearrange as function of $\dot{\gamma}$, leading to a decrease in η . At high- $\dot{\gamma}$ the dispersed particles could not further change arrangement (e.g. alignment) upon increase in $\dot{\gamma}$. Commonly employed empirical models which describe shear thinning fluids are the power law and the Cross model. The power law model is useful to describe the viscosity profile at intermediate- $\dot{\gamma}$ (equation 2.11).

$$\eta = k\dot{\gamma}^m \quad (2.11)$$

The severity of the viscosity decay is captured by the power law exponent, m , whilst k is the proportionality factor. Based on the magnitude of m , it is possible to describe phenomena such as dispersion stability and flocculation.^[116] The Cross model described in equation 2.12 allows extrapolation of the limiting viscosities, η_0 and η_∞ , which correspond to the viscosity at $\dot{\gamma} = 0$ and $\dot{\gamma} = \infty$, respectively.^[113] It is important to notice that this model describes the viscosity

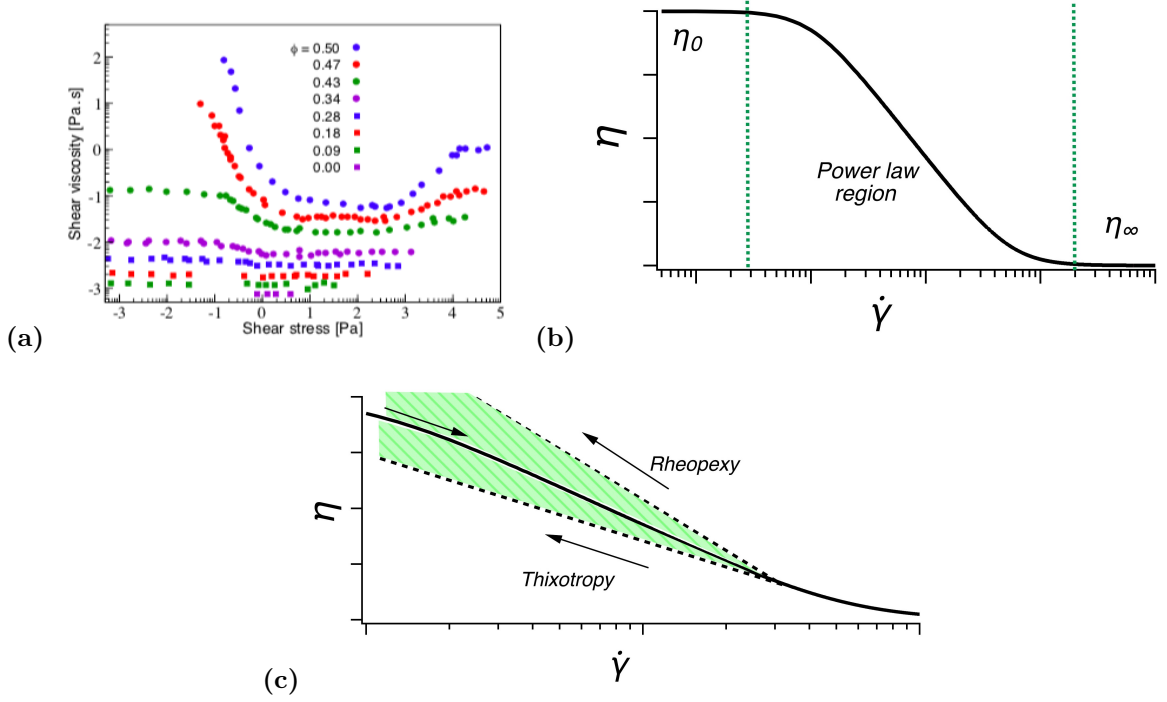


Figure 2.6 (a) Viscosity (η) vs shear stress (σ) of stable latex particles in water as function of concentration. Reprinted from^[115] with permission of IOP publishing, from the the original work by Laun^[107]. (b) The Cross model plot (equation 2.12), displaying a classical shear thinning material with Newtonian regions at low and high shear rates ($\dot{\gamma}$), respectively indicated by the limiting viscosities η_0 and η_∞ . (c) Illustrative graph displaying a common shear loop experiment. Arrows indicate the increasing (left to right) and decreasing (right to left) of the magnitude of $\dot{\gamma}$.

decrease at intermediate- $\dot{\gamma}$ by the power law as displayed in equation 2.11.

$$\frac{\eta - \eta_\infty}{\eta_0 - \eta_\infty} = \frac{1}{1 + k\dot{\gamma}^m} \quad (2.12)$$

Viscosity as function of time

Non-Newtonian materials experience a structural change upon shear, leading to phenomena as shear thinning or thickening. As such, most soft materials as gels and pastes will recover over time the structural conformation that existed prior to shear. The ability to recover the original structure after cessation of the shear was reported for the first time by Peterfi in 1927 and the term *thixotropy* coined to describe this phenomenon.^[117] Now, thixotropy is defined as the viscosity decrease with time upon constant $\dot{\gamma}$, which recovers the original viscosity upon cessation of the flow.^[118] This phenomenon is associated with flow-induced structural changes and often observed in pastes and gels.^[118,119] Although different methodologies have been proposed, thixotropy is commonly assessed by performing a shear loop where $\dot{\gamma}$ is increased and decreased in the same manner (Figure 2.6c). When the viscosity curves obtained by increasing and decreasing $\dot{\gamma}$ are superimposed, the material is time independent, and non-thixotropic.^[118] On the contrary, the material is defined to be thixotropic and work softening if η has lower values upon decreasing $\dot{\gamma}$.^[118] When the viscosity further increases with the decrease in $\dot{\gamma}$, the phenomenon is known as rheopexy.^[118] This phenomenon is more scarcely observed compared to thixotropy, but reported to occur in concentrated suspensions.^[118,120] It is noted that the results of the shear loop are strictly dependent on the time frame in which the increase and decrease of the shear rate occurs.^[118] Fast thixotropic loops could have a different $\dot{\gamma}$ outcome than slow loops. Nevertheless, applying identical time frames, the thixotropy loop provides comparable information about the

time dependency of the material.

Viscosity as function of the volume fraction

Particles in suspension under shear, distort the flow field, leading to an increase in dissipated energy and an increase in viscosity. In the dilute regime ($\phi \leq 0.05$), interparticle interactions can often be neglected, hence the viscosity can be captured accounting only for the energy dissipated by each particle.^[121] In 1906, Einstein attempted to calculate the size of large molecules from viscosity measurements in the dilute regime, based on the assumption that the molecules behaved as rigid spheres.^[122] Although the concept was correct, a mistake was found in the calculation, and in the 1911 the corrected version was published, which established the relationship between viscosity and particle volume fraction as^[123]

$$\eta_r = 1 + [\eta]\phi \quad (2.13)$$

Where η_r is the relative viscosity, defined as η of the dispersion normalised by η of the continuous phase. In the dilute regime, particles do not disturb each other and particle interactions can be neglected.^[121] Therefore, the viscosity arises from the cumulative contribution of individual particles, following a linear trend with the volume fraction (Figure 2.7a). The $[\eta]$ corresponds to the intrinsic viscosity and is dependent on the particle morphology including roughness and shape;^[121] For hard spheres, Einstein obtained $[\eta] = 2.5$.^[123] Values of $[\eta]$ can be used to calculate the molecular weight of polymers.^[124]

Batchelor extended the Einstein relation (Equation 2.13) in the semi-dilute regime $\phi \cong 0.1$. At these concentrations, the flow distortion caused by a single particle under flow is not independent but is strongly affected by the neighbouring particles and the distorted flow field surrounding the particles.^[121] Such far-field hydrodynamic interactions, K_H , have been accounted for in 1972 by Batchelor and Green, by the commonly known Batchelor equation (2.14)(plot shown in Figure 2.7a).^[125]

$$\eta_r = 1 + [\eta]\phi + K_H\phi^2 \quad (2.14)$$

Batchelor and Green obtained a value of $K_H = 7.6$, for hard spheres.^[125]

Concentrated dispersions having $\phi > 0.1$ have been described, for the first time, by an empirical relation proposed by Krieger and Dougherty (equation 2.15).^[126]

$$\eta_r = \left(1 - \frac{\phi}{\phi_{max}}\right)^{-1[\eta]\phi_{max}} \quad (2.15)$$

Where ϕ_{max} is the maximum packing fraction, corresponding to the point where insufficient interstitial fluid is present between particles and the viscosity asymptotes to infinity.^[113,121] The ϕ_{max} depends on factors as size distribution, shape, and rigidity of the particles. For instance, increasing polydispersity of the system has been shown to shift the ϕ_{max} towards greater values as schematically illustrated in Figure 2.7b. In the concentrated regime, viscosity is also a function of $\dot{\gamma}$ (Figure 2.6a), hence, differently than for equation 2.13 and 2.14, for the Krieger and Dougherty equation (2.15) distinct results can be obtained according to the employed $\dot{\gamma}$.^[113] Nonetheless, the values of viscosity for a specific shear rate follow, in good agreement, equation 2.15. For instance, plotting values of viscosity from low to high $\dot{\gamma}$ (or η_0 to η_∞) for a shear thinning fluid, results in a ϕ_{max} shift towards greater values as schematically illustrated in Figure 2.7b.^[127]

2.2.2 Viscoelasticity

Materials under deformation will experience a stress, which could be dissipated, stored or a combination of both. Purely elastic materials store the energy acquired through the deformation, and

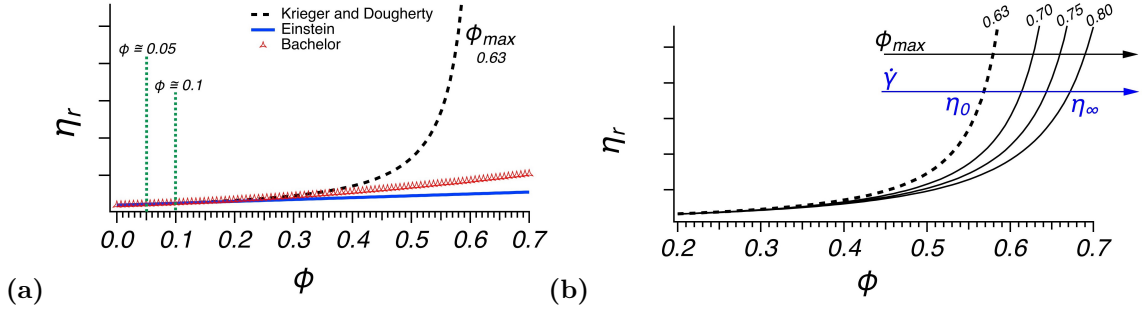


Figure 2.7 (a) Relative viscosity (η_r) vs volume fraction (ϕ) plotted using equation 2.13, 2.14 and 2.15. Equation 2.15 was plotted using $[\eta] = 2$ and $\phi_{max} = 0.63$. Lines are used to separate the region of validity of each equation. (b) Relative viscosity (η_r) vs volume fraction (ϕ) plotted using equation 2.15 with fixed $[\eta] = 2$ at different values of ϕ_{max} . Arrows indicate the direction of the trend upon change of $\dot{\gamma}$ and ϕ_{max} .

upon removal of the deformation always return to their conformation as it was prior to deformation. Contrarily, purely viscous materials dissipate the energy acquired with the deformation, stopping the material from recovering its shape and structure upon removal of the deformation. A large span of materials are classified as viscoelastic, identifying materials which own both elastic and viscous features. Among other types of rheological assessments (e.g. shear rheology), the most employed technique to study viscoelasticity in soft materials is oscillatory rheology. This technique allows to study a broad range of material responses, resulting in a powerful tool to study material transitions occurring upon specific stimuli (e.g. liquid-gel upon heating). Oscillatory shear rheology is based on the analysis of the material response to an imposed sinusoidal shear strain (for a strain controlled rheometer) as

$$\gamma(t) = \gamma_0 \sin(\omega t) \quad (2.16)$$

where ω is the oscillation frequency, t the time and $\gamma_0 = s/h$, s being the top plate displacement and h the sample thickness interposed between the stationary bottom plate and the sliding top plate (Figure 2.8a). The material response, to the applied sinusoidal deformation, is measured as stress, $\sigma = F/A$ where F is the force and A the surface area. For small deformations, the material response is sinusoidal and the stress is described as

$$\sigma(t) = \sigma_0 \sin(\omega t + \delta) \quad (2.17)$$

where σ_0 is the stress amplitude and δ the phase angle between the applied strain and the measured stress response. For purely elastic and viscous materials, the strain and stress are in phase, $\delta = 0^\circ$ and out of phase $\delta = 90^\circ$, respectively. For viscoelastic materials, $0^\circ < \delta < 90^\circ$ (Figure 2.8b). Although material properties can be described by σ_0 and δ , the stress response is described by the shear modulus G^* and further decomposed into the storage modulus G' and the loss modulus G'' as

$$G^* = \left(\frac{\sigma_0}{\gamma_0} \right) = \sqrt{(G')^2 + (G'')^2} \quad (2.18)$$

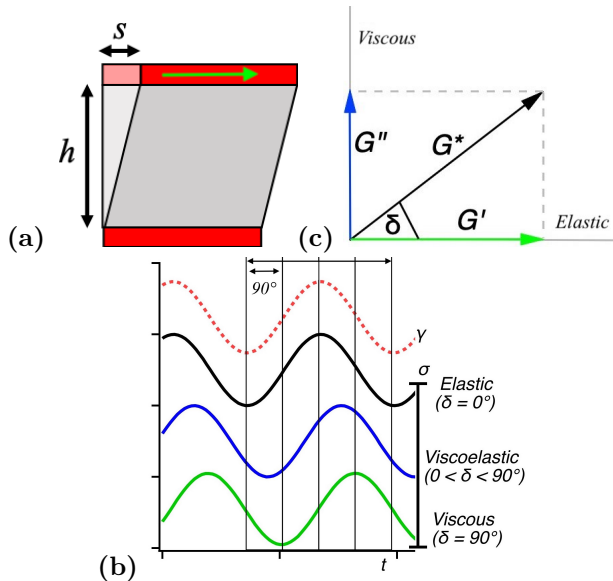
Where G' and G'' can be expressed in terms of phase shift as

$$G' = \left(\frac{\sigma_0}{\gamma_0} \right) \cos(\delta) \quad (2.19)$$

and

$$G'' = \left(\frac{\sigma_0}{\gamma_0} \right) \sin(\delta) \quad (2.20)$$

Figure 2.8 (a) A sample of thickness, h , undergoing oscillatory deformation imposed by the top plate sliding of a deformation s . (b) Characteristic sinusoidal shear strain $\gamma(t)$, as shown in equation (2.16), applied to a sample during a small amplitude oscillatory experiment. The material response, to the deformation $\gamma(t)$, displayed as stress, $\sigma(t)$. Characteristic materials responses are displayed by a phase shift, δ , between 0° and 90° . (c) Vector diagram for the shear modulus, G^* , and the derived storage and loss modulus G' and G'' , respectively as displayed in equation 2.19 and 2.20



as illustrated in the vector diagram in Figure 2.8c. G' is associated with the elastic component of the material response, whilst, G'' with the viscous component of the material response. Hence, materials are usually defined as solid-like when $G' > G''$, whilst, it is liquid-like when $G'' > G'$.

Strain sweep

Oscillatory rheology provides insightful information regarding the structure of soft materials. It is common to perform a strain sweep experiment, at a constant frequency (ω), as displayed in Figure 2.9a for a commercial hand cream, in order to identify specific mechanical properties of the materials. At small amplitude oscillatory shear (SAOS), soft materials respond in a sinusoidal fashion, as described by equation 2.17, and their mechanical response is independent of the magnitude of the applied deformation (G' and G'' constant). When such conditions hold, the material is probed in the linear viscoelastic region (LVR). In the LVR, the experiment is not destructive, probing the material properties at rest.^[105] In the LVR, the material response is sinusoidal, and the moduli, G' and G'' , are fully descriptive of the material properties as displayed in Figure 2.9b, where the sinusoidal fit entirely captures the $\sigma(t)$. When further strain is applied, soft materials show a transition from a solid-like, $G' > G''$, to a liquid-like $G'' > G'$. The stress at which $G' = G''$ defines the yield stress, σ_y whilst, the strain at which $G' = G''$ is the yield strain. Modulation of the yield stress is of great importance for targeting specific applications. For instance, high yield stress is desired for a toothpaste $\sigma_y \sim 100$ Pa^[129] which should firmly stand on the toothbrush. Contrarily, a shower gel would require lower yield stress $\sigma_y \sim 10$ Pa^[129], allowing prompt squeezing from the bottle and moderate flowing on the hands. Yielding and flowing of soft materials occur upon large amplitude oscillatory shear (LAOS), where the material response depends on the magnitude of the applied strain. In addition, in the LAOS regime, the stress response is not fully captured by a sinusoidal fit, as displayed in Figure 2.9c, due to the presence of higher harmonics, hence, the non linear viscoelastic region (NLVR) of the material is probed.^[130] Although the NLVR has received less attention compared to the LVR, mainly due to the lack of an established framework of analysis, its understanding is fundamental to tune mechanical phenomena occurring upon large deformations (e.g. the spreading of hand cream onto the skin). Rheological properties such as structural breakage (yielding), flow, structural recoverability and plasticity are instances of non-linear mechanical properties. Although G' and G'' lose their rigorous mathematical support in the NLVR, they have still been employed to characterize the material response upon large deformations.^[104] Hyun et al. showed that, if care is taken, the analysis of G' and G'' upon structural breakage can reveal information regarding

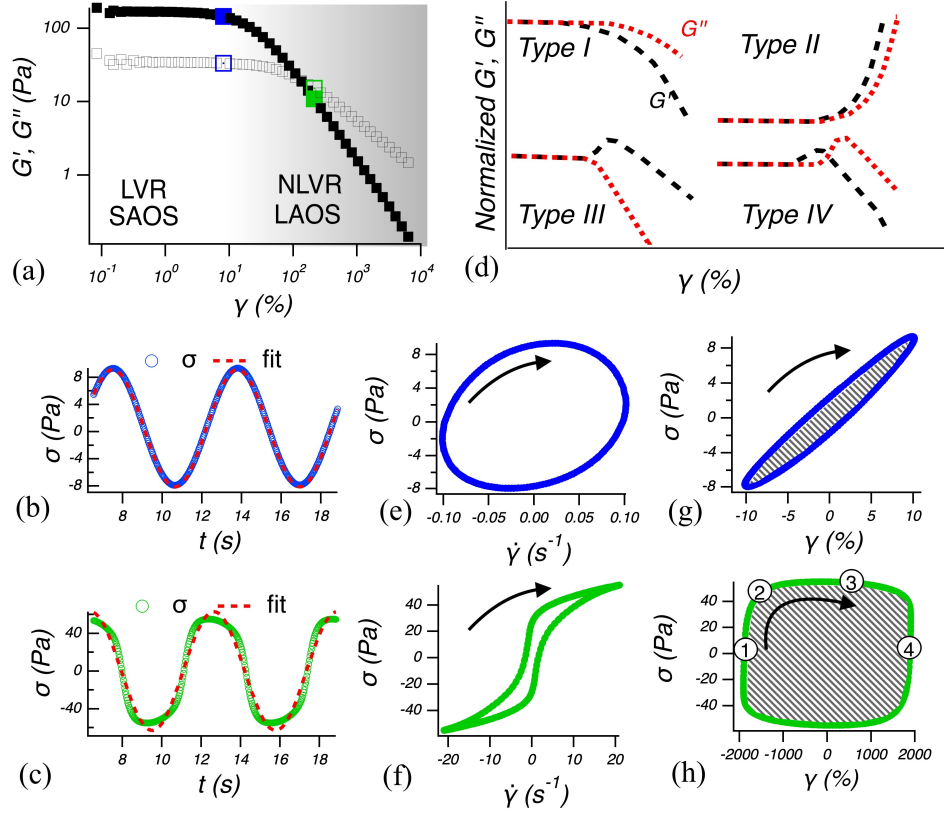


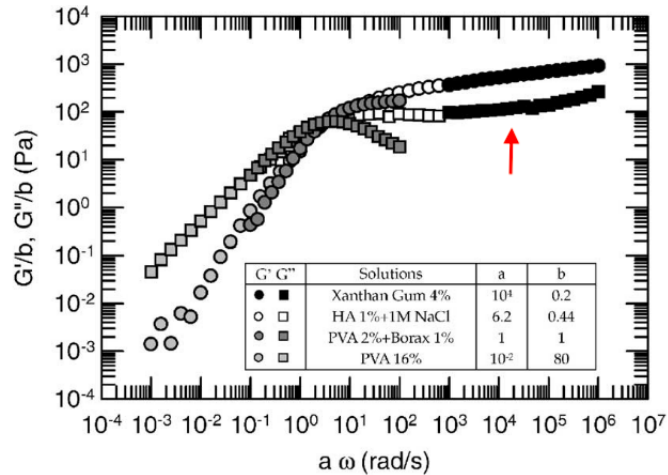
Figure 2.9 (a) Strain sweep from small amplitude oscillatory shear (SAOS) (in the linear viscoelastic region (LVR)) up to large amplitude oscillatory shear (LAOS). The grey area indicates the LAOS and the non linear viscoelastic region (NLVR). The blue and green dot indicate the strain point where waveform analysis was conducted (b, c, e, f, g, h). (b) and (c) display the stress response, $\sigma(t)$ to SAOS and LAOS as indicated in (a). The red dotted line indicates the sinusoidal fit to $\sigma(t)$. (d) Schematic diagram of the four types of G' and G'' trends. Adapted version from [128] with permission of Elsevier, after the original work of [104]. (e) and (f) show the viscous representation (σ vs $\dot{\gamma}$) of the Lissajous plot, constructed from the $\sigma(t)$ as displayed in (b) and (c), respectively. (g) and (h) show the viscous representation (σ vs γ) of the Lissajous plot, constructed from the $\sigma(t)$ as displayed in (b) and (c), respectively. The sequence of events suggested by Rogers et al. [103] are indicated as (1) straining, (2) yielding, (3) flowing and (3) regeneration. The arrows indicate the direction of σ as function of $\dot{\gamma}$ or γ .

the microstructure of soft materials. [104] Hyun et al. identified, experimentally, four different mechanical fingerprints upon strain sweep experiment based on the trends of G' and G'' : (*Type I*) strain thinning, (*Type II*) strain hardening, (*Type III*) weak strain overshoot, and (*Type IV*) strong strain overshoot (Figure 2.9d). [104] These rheological fingerprints were interpreted based on the strength of the associative interaction between building blocks; the strongest associative forces were associated with *Type II*, followed by *Type IV*, *Type III* and *Type I*. The following theoretical prediction, [131] well established the framework of Hyun et al.

To achieve a more in-depth understanding, Rogers et al. proposed a direct analysis of the waveform, omitting assumptions required for G' and G'' . [103] In this analysis, the waveform presented in Figure 2.9b, c, is plotted as Bowditch-Lissajous plot (commonly known as Lissajous plot), where the stress, σ , is plotted as function of shear rate, $\dot{\gamma}$, (Figure 2.9e, f) or strain γ (Figure 2.9g, h). The σ vs $\dot{\gamma}$ Lissajous plot is known as the viscous representation, whilst the σ vs γ Lissajous plot is the elastic representation. For the elastic representation, the area enclosed in the Lissajous plot corresponds to the dissipated energy. As such, the liquid-like behaviour of a sample is observable by Lissajous plots with a rhomboidal shape which enclose more area (Figure 2.9g, h). This is captured in Figure 2.9g, h, where at larger strains the Lissajous plot displays

an evident increase of the enclosed area. To better interpret the non-linear behaviour, Rogers et al., decomposed the elastic representation of the Lissajous plot into separate sequences of events. Where, starting from $\sigma = 0$, a sequence of straining, yielding, flowing and structural reformation (labelled in Figure 2.9h by 1, 2, 3 and 4, respectively) occur.^[103] The mechanical fingerprints observable in the Lissajous plot have been clearly related to specific structural properties, as confirmed via Rheo-SANS.^[132,133]

Figure 2.10 Frequency sweep curves of various polymer solutions. G' and G'' are scaled by the factor b , and the frequency (ω) scaled by the factor a . The arrow indicates the Xanthan Gum 4% sample. Adapted from^[104] with permission of Elsevier.



Frequency sweep

Once the LVR is determined, frequency sweep experiments can be performed to gain information regarding the time-dependent behaviour of the sample. Frequency sweeps are executed using a constant oscillatory strain (within the LVR) upon increasing the rate of oscillation; frequency (ω). Liquid-like materials show G' and G'' dependent on the frequency, and, if within an accessible frequency range, it is possible to observe the moduli crossover $G' = G''$ corresponding to the relaxation time, τ as^[105]

$$\tau = \frac{1}{\omega} \quad (2.21)$$

Contrarily, solid-like materials, show frequency independence. However, scaling of the frequency sweep has been shown to lead a unified trend (Figure 2.10), highlighting the fact that soft materials have a dominant liquid or solid-like behaviour in according to the characteristic time frame of the experiment. In practice, only limited frequency ranges are accessible, constraining the characteristic time scale of the experiment. This often results in inaccessible information regarding the relaxation time of the material as for the case of Xanthan Gum 4% in Figure 2.10) which lack of the $G' - G''$ crossover, hence an accessible relaxation time.

2.2.3 Setup

Rheological measurements were performed using a stress-controlled rheometer (Discovery HR-3, TA instruments) equipped with a Peltier unit for temperature control (± 0.1 °C). Bulk rheology was conducted with plate-plate geometries, whilst interfacial rheology was conducted using the double wall-ring (DWR) geometry as shown in Figure 2.11. Detailed information regarding the specific rheological setup are annexed to each experimental chapter.

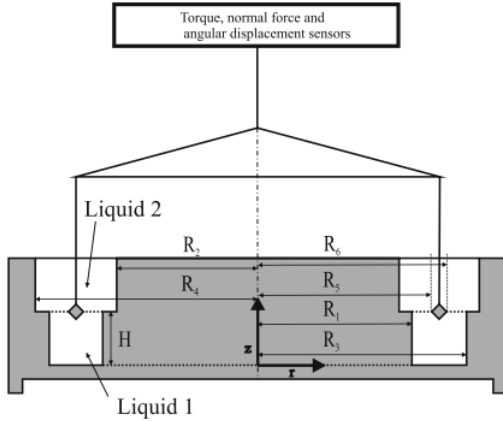


Figure 2.11 . Double wall ring geometry as used in the following experiment sections. $R_1 = 31 \text{ mm}$, $R_2 = 30 \text{ mm}$, $R_3 = 39.5 \text{ mm}$, $R_4 = 40.5 \text{ mm}$, $R_5 = 34.5 \text{ mm}$, $R_6 = 35.5 \text{ mm}$, $H = 10 \text{ mm}$. Reprinted from^[134] with permission of Springer Nature.

2.3 Other techniques

2.3.1 Dynamic Interfacial Tension

Surface tension, γ , has been mainly characterized using the Du Noüy method. This method relies on the force required to raise a ring (similar in shape to one described in Figure 2.11) immersed in a solution. This force (F) depends on the geometry of the ring and by the surface tension of the solution as^[135]

$$\gamma = \frac{F}{2\pi(r_i + r_o)} \quad (2.22)$$

where r_i and r_o are respectively the inner and outer radius of the ring. Particular care is needed to achieve excellent cleaning of the ring (through washing and flaming) and the vessel containing the liquid.

2.3.2 Dynamic light scattering (DLS)

Dynamic light scattering is one of the most commonly used methodologies to promptly obtain particle size distributions of colloidal particles. This methodology relies on the Brownian motion of the particles in a media. Specifically, the speed of a particle is inversely proportional to the size of the particle - larger particles move slower compared to smaller particles. This is depicted by the translational diffusion coefficient (D_t in m^2/s) in the Stokes-Einstein equation as^[136]

$$D_t = \frac{kT}{6\pi\eta R_H} \quad (2.23)$$

where k is Boltzmann constant (JK^{-1}), T the temperature (K), η the zero shear viscosity ($Pa \cdot s$) and R_H is the hydrodynamic radius of the particle (m). In a classical DLS measurement, monochromatic light is scattered by the sample and recorded for a single scattering angle (θ) over time as $I(t)$. A correlation function $g(\tau)$ is then computed to extract the time dependence of $I(t)$ as^[137,138]

$$g(\tau) = \frac{\langle I(t_0)I(t_0 + \tau) \rangle}{\langle I(t_0) \rangle^2} \quad (2.24)$$

where τ is the time delay which is added to scattering intensity at $t = 0$ ($I(t_0)$) and the brackets indicate the average of multiple measurements. Since $g(\tau)$ is an exponential process, when $g(\tau)$ vs τ is plotted on a log-log scale, at short times, particles are correlated so $g(\tau)$ is constant. The point where $g(\tau)$ lose correlation (decreases) is defined as τ^* which is the characteristic decay time. For instance, small particles show smaller values of τ^* compared to larger particles. A

relation between the translation diffusion coefficient and τ^* is expressed as

$$\tau^* = \frac{1}{2D_t q^2} \quad (2.25)$$

where q is the scattering vector defined in 2.3 (in m^{-1}). From D_t , the hydrodynamic radius can be obtained from equation 2.23.

It is important to note that this technique measures how quickly a particle moves in a media under Brownian motion, hence, it measures the hydrodynamic radius of a particle. For instance, the hydration shell is accounted as part of the particle since it moves with the particle. However, a complication arises from the measurement of anisotropic particles which undergo translation and, a not negligible rotational diffusion, D_r . Since equation 2.23 accounts only for D_t , other techniques are necessary to deconvolute the two main diffusion coefficients (D_t and D_r) allowing extrapolation of the particle dimensions. For instance, dynamic depolarized light scattering (DDLS) has been proposed as a suitable methodology for this objective.^[139] Regarding rod-shaped particles, de la Torre and Bloomfiel^[140] proposed a modified Stokes-Einstein equation to access the length or the width of rod-shaped particles from DLS measurements. Importantly, to use such equation one of the dimensions (length or width) needs to be known.^[30] For spherical particles, sophisticated models have been developed to relate the correlation function with polydispersity and distribution of polydispersity (e.g. monomodal, bimodal).

Typical samples are prepared in a diluted regime (e.g. < 0.5 wt%) to avoid strong interparticle interactions and in low viscosity media. In the following experimental chapters a Malvern Zetasizer Nano equipped with a He-Ne laser beam with wavelength of 633 nm is used and the scattered light acquired at $\theta = 173^\circ$.

2.3.3 ζ -potential

The charge at the interface of the particle affects the ion distribution in the continuous phase. Specifically, particles are surrounded by a primary dense counterion layer (closer to the particle surface) named the *Stern layer* and by a secondary *diffuse layer* where counterions are less densely packed (Figure 2.12).^[141,142] The *Stern layer* and the *diffuse layer* are usually referred to as the electrical double layer. ζ -potential measurements rely on the movement of the particles when an electric field is applied across the dispersion, referred to as electrophoretic mobility (U_e). The closer layer of counterions to the particle core will act as part of the particle and will migrate with it under the applied electric field - constituting the hydrodynamic radius of the particle -. Contrarily, the layer of counterions positioned further away won't migrate with the particle. The potential at the boundary where counterions won't contribute to the hydrodynamic radius of the particle is the ζ -potential as shown in Figure 2.12. The electrophoretic mobility (U_e in $m^2 s^{-1} V^{-1}$) is defined as the electrophoretic speed (v in (m/s)) of a solute over an applied potential ($E = V/L$, where V is the applied potential (V) and L is the length of the capillary tube (m)) and correlates with ζ -proportional as^[141,142]

$$U_e = \frac{v}{E} = \frac{2\epsilon\epsilon_0\zeta F(\kappa a)}{3\eta} \quad (2.26)$$

where ϵ is the relative permittivity of the media, ϵ_0 the vacuum permittivity ($F m^{-1}$), ζ is the ζ -potential (V) and η is the zero shear viscosity ($Pa s$). $F(\kappa a)$ is the Henry's function where κ is the Debye length (m^{-1}) displayed in equation 1.8 and a is the particle radius (m). A simple form of the Henry's function is given by the commonly used Smoluchowski approximation $F(\kappa a) = 1.5$, implying that the double layer is thin compared to the particle radius. In practice, the U_e is measured using a technique called Laser Doppler Electrophoresis (LDE) which utilizes the frequency shift of the scattered light associated to the electrophoretic motion of the particles, known as the Doppler effect.^[143] Factors as ionic strength and pH are pivotal to the ζ -potential,

determining, as described in 1.3.1, the colloidal stability. ζ -potential measurements were carried out on the Malvern Zetasizer Nano described above.

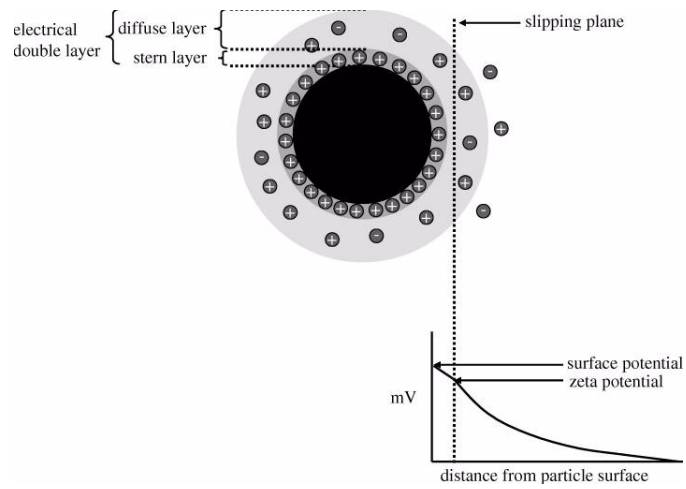


Figure 2.12 Schematic double layer surrounding a particle dispersed in an aqueous media. Reprinted from^[141].

2.3.4 Confocal microscopy

Confocal microscopy is a widespread technique in biomedical and soft matter science for the imaging of materials (e.g. tissues) containing fluorescent probes (fluorophores). The confocal laser scanning microscope (CLSM or LSCM) has the same working principle as a conventional light microscope using a laser with a specific wavelength (λ) rather than a light containing multiple wavelengths.^[144,145] The presence of fluorophores in the specimen improves the signal-to-noise ratio and the detection of the targeted materials is based on the affinity between a target and the specific fluorophore. The affinity between target and fluorophore is often based on hydrophobic and electrostatic interactions. In soft matter, fluorophores are often used to highlight particles or particular features of particles.^[144,145] Specifically, the use of two fluorophores with separate emission wavelength and different target affinity, allows a different part of the sample to be distinguished. Although easy in principle, the affinity of a fluorophore with a target is not necessarily unique, hence the choice of the right fluorophore is pivotal to avoid misleading information. In practice, a laser beam (high-energy) is reflected by a dichroic mirror and hits the sample. The dichroic mirror allows the low-energy wavelength emitted by the samples to pass through the pinhole, discarding the contribution from the scattered light, and the photo detector from which the image is reconstructed.^[144,145] One of the limitations of this technique is the photobleaching of the fluorophores which fade irreversibly upon a long exposure time at high laser intensity.^[144] It is also important to highlight that fluorophores, although often used in μM quantities, can strongly interfere with the investigated system. CLSM analysis were carried out on a Zeiss LSM880 microscope (Zeiss, Germany).

CHAPTER 3

UNDERSTANDING HEAT DRIVEN GELATION OF ANIONIC CELLULOSE NANOFIBRILS: COMBINING SATURATION TRANSFER DIFFERENCE (STD) NMR, SMALL ANGLE X-RAY SCATTERING (SAXS) AND RHEOLOGY

Before exploring assembly strategies which enable the formation of capsules and composite hydrogels, this study aims to determine the fundamental insights into interfibrillar interactions. Specifically, how do heat and time affect the structure and mechanical properties of hydrogels composed by cellulose nanofibrils (CNF)? Establishing the link between these two parameters and the material properties is crucial to ensure long term stability of a material. It is indeed common practice to evaluate the shelf-life of a product under the required market conditions.^[146] However, tackling this problem at a fundamental level (on a single component rather than a composite end product) allows to control the ageing and heat sensitivity of a material. For instance, heat responsiveness could be an advantageous characteristic suitable for specific applications whilst detrimental for others. In the past few years, CNF have been broadly employed to form hydrogels with industrially relevant applications such as the delivery of active components^[37] and thickening matrices in formulated products.^[38] Despite the promising proof-of-concept, the evaluation of the structural changes occurring upon ageing and heat have been neglected; crucial factors determining a product shelf-life. As such, in this study, we evaluate the effect of these factors using a combination of techniques and comparing two types of CNF with similar sizes. Contrarily to the cationic cellulose nanofibrils (CCNF) the structural and rheological properties of the hydrogels composed by the oxidised cellulose nanofibrils (OCNF) are dramatically affected by time and heat. In the following study, we pinpoint the transient nature of the OCNF network. Specifically, this work demonstrates that the OCNF network evolves with time (age) and heat but can reversibly regenerate its initial structure through a mechanical input such as vigorous shaking. These pieces of knowledge are crucial to enable large scale processing of CNF-based materials such as the flow control of CNF dispersions in pipelines and the prediction of the properties of the CNF-based material under common sterilization procedures (up to *ca.* 150°C).^[146] Moreover, this work establishes the link between the network structure, water confinement and the resulting rheological properties. Since the publication of this work, the ageing and the temperature effect of CNF dispersions has been considered in a few publications using a set of methodologies similar to the one described in the following Chapter. For instance, the combination of hydrophobized cellulose nanocrystals with hydroxypropyl methylcellulose has been shown to produce thermosensitive hydrogels based on the interplay between hydrophobic moieties of the two components.^[147] Besides the augmented gel elasticity and viscosity with the increase in

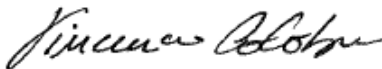
3. UNDERSTANDING HEAT DRIVEN GELATION OF ANIONIC CELLULOSE NANOFIBRILS: COMBINING SATURATION TRANSFER DIFFERENCE (STD) NMR, SMALL ANGLE X-RAY SCATTERING (SAXS) AND RHEOLOGY

temperature, the amount of the constrained water increased correspondingly, similarly to that described in the following Chapter. The link between network, water and rheological properties has been further exploited to produce hydrogels with targeted mechanical and hydration properties.^[148] Prior to this publication only a few publications have focused on how heat and time affect the structure-property relationship of cellulose-based gels, although using water-soluble cellulose rather than CNF.^[149-151] For water-soluble cellulose containing hydrophobic moieties, hydrophobic interactions have often been invoked as the main driving force leading to gelation and/or increase in viscosity upon heat.^[149,151] For the case of water-dispersible OCNF, the underlying mechanism leading to a heat-induced sol-to-gel transition could be a complex interplay between different type of interactions (e.g. hydrophobic, hydrogen bonds, electrostatics). As such, the difficulty of the system enabled us only to propose a mechanism of heat-induced gelation. To confirm or disprove the hypothesis further investigation is demanded.

Supporting information available in section 10.1.

The publication included here is reproduced under the Creative Commons License.^[119]



This declaration concerns the article entitled:			
Understanding Heat Driven Gelation of Anionic Cellulose Nanofibrils: Combining Saturation Transfer Difference (STD) NMR, Small Angle X-Ray Scattering (SAXS) and Rheology.			
Publication status (tick one)			
draft manuscript	<input type="checkbox"/>	Submitted	<input type="checkbox"/>
		In review	<input type="checkbox"/>
		Accepted	<input type="checkbox"/>
		Published	<input checked="" type="checkbox"/>
Publication details	Calabrese, V.; Muñoz-García, J. C.; Schmitt, J.; da Silva, M. A.; Scott, J. L.; Angulo, J.; Khimyak, Y. Z.; Edler, K. J. Understanding Heat Driven Gelation of Anionic Cellulose Nanofibrils: Combining Saturation Transfer Difference (STD) NMR, Small Angle X-Ray Scattering (SAXS) and Rheology. <i>J. Colloid Interface Sci.</i> 2019 , <i>535</i> , 205–213.		
Candidate's contribution to the paper (detailed, and also given as a percentage).	<p>The candidate contributed to/ considerably contributed to/predominantly executed the...</p> <p>Formulation of ideas: -The initial idea was formulated by VC based on preliminary rheological data. 85%</p> <p>Design of methodology: -All the measurements were designed by VC with exception of NMR. The NMR experiments were designed by JMG based on concentrations and temperature ranges indicated by VC. 75%</p> <p>Experimental work: - The experimental work was conducted by VC exception made for NMR. The ready to be measured samples for NMR were provide by VC to JMC whom performed the NMR experiments and elaborated the data. Help in scattering data analysis was provided by JS. -75% of the experimental work and data analysis was carried out by VC.</p> <p>Presentation of data in journal format: -The first draft was written by VC with contribution of JMG to the writing of the NMR related sections. Subsequent drafts were reworked by VC following feedback from KJE, JLS, JS, MAS and YK. 85%</p>		
Statement from Candidate	This paper reports on original research I conducted during the period of my Higher Degree by Research candidature.		
Signed			Date 27/09/19

Regular Article

Understanding heat driven gelation of anionic cellulose nanofibrils: Combining saturation transfer difference (STD) NMR, small angle X-ray scattering (SAXS) and rheology [☆]



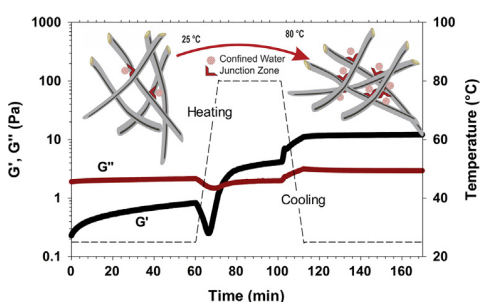
Vincenzo Calabrese ^{a,1}, Juan C. Muñoz-García ^{b,1}, Julien Schmitt ^a, Marcelo A. da Silva ^a, Janet L. Scott ^{a,c}, Jesús Angulo ^b, Yaroslav Z. Khimyak ^{b,*}, Karen J. Edler ^{a,*}

^a Department of Chemistry, University of Bath, Claverton Down, Bath BA2 7AY, UK

^b School of Pharmacy, University of East Anglia, Norwich Research Park, Norwich NR4 7TJ, UK

^c Centre for Sustainable Chemical Technology, University of Bath, Claverton Down, Bath BA2 7AY, UK

GRAPHICAL ABSTRACT



ARTICLE INFO

Article history:

Received 11 June 2018

Revised 21 September 2018

Accepted 24 September 2018

Available online 25 September 2018

Keywords:

Water confinement

Hydrogel

TEMPO oxidised cellulose

Heat induced gelation

Saturation transfer difference NMR

SAXS

Rheology

ABSTRACT

A novel mechanism of heat-triggered gelation for oxidised cellulose nanofibrils (OCNF) is reported. We demonstrate that a synergistic approach combining rheology, small-angle X-ray scattering (SAXS) and saturation transfer difference NMR (STD NMR) experiments enables a detailed characterisation of gelation at different length scales. OCNF dispersions experience an increase in solid-like behaviour upon heating as evidenced by rheological studies, associated with enhanced interfibrillar interactions measured using SAXS. Interactions result in an increased fibrillar overlap and increased population of confined water molecules monitored by STD NMR. In comparison, cationic cellulose nanofibrils (produced by reaction of cellulose with trimethylglycidylammonium chloride) were found to be heat-unresponsive.

© 2018 The Authors. Published by Elsevier Inc. This is an open access article under the CC BY license (<http://creativecommons.org/licenses/by/4.0/>).

[☆] Electronic Supplementary Information (ESI) available: STD and reference NMR spectra, rheological data for other OCNF and CCNF dispersion concentrations, ¹H ¹³C HSQC spectra and NOESY build up curves for OCNF before and after heating, fluorescence data, contributions to STD signal, temperature evolution of STD signal, and further NMR characterisation data. See DOI: <https://doi.org/10.1039/x0xx00000x>.

* Corresponding authors.

E-mail addresses: j.l.scott@bath.ac.uk (J.L. Scott), j.angulo@uea.ac.uk (J. Angulo), y.khimyak@uea.ac.uk (Y.Z. Khimyak), k.edler@bath.ac.uk (K.J. Edler).

¹ The authors contributed equally to the work.

1. Introduction

There is an enormous interest in cellulose based hydrogels as inexpensive and biodegradable gels, for their industrial and sustainable applications. Cellulose naturally occurs in plant cell walls as a hierarchical assembly of fibrils, tightly bonded via multiple hydrogen bonds [1,2]. Cellulose and cellulose derivatives are becoming of great importance for the production of a wide range of biodegradable materials, as their rheological properties have gained great importance for several applications ranging from drug release [3], microbeads [4], to functional ingredients in food (e.g. thickeners, stabilizers, gelling agents) [5–7].

Due to strong attractive forces between fibrils, cellulose aqueous dispersions have poor stability, which can be improved by the introduction of repulsive interactions [8]. For instance, the 2,2,6,6-tetramethylpiperidine-1-oxyl radical (TEMPO)-mediated oxidation of the primary OH groups is one of the most commonly used surface modifications, which selectively introduces negatively charged carboxylate groups at the C6 position of the glucose rings of cellulose [9–11]. The TEMPO-mediated oxidation yields stable anionic oxidised cellulose nanofibrils (OCNF) with high surface charge (ζ -potential < -30 mV) [12]. The large aspect ratio of OCNF (5 nm diameter, up to few μ m length) leads to a low overlap concentration (i.e., the minimum volume fraction of particle necessary for particle-particle interactions to occur) and hydrogels can form with a water content up to 99.9% [8,13,14]. The gelation properties of OCNF aqueous dispersions have been widely investigated under different conditions by varying pH [8], electrolyte [12,15] and surfactant [6,14] concentrations, showing a wide span of rheological properties. In several studies, cation-induced gelation of OCNF, due to screening of the negative charges, has been reported [12,15,16]. Crawford et al. first demonstrated a surfactant-induced gelation, proposing either a depletion flocculation mechanism or a micellar crosslinking between fibrils [6]. More recently, stable shear thinning dispersions have been also reported using cationic cellulose nanofibrils (CCNF) [17,18]. However, to the best of our knowledge, the gelation of OCNF dispersions triggered only by temperature has never been reported before. Previous gelation processes have required addition of acids, oppositely charged ions or surfactants.

In this work, we investigate a yet unreported reversible physical gelation induced by temperature alone without any structural or chemical change in the OCNF. By raising the temperature, weak physical gels were obtained from OCNF dispersions. Further rheological investigations revealed the reversibility of the process. Since the only input to this system was the increased temperature, we hypothesised that the interactions between the OCNF and water could be important to understand the mechanism of gelation. Studies of the structure and dynamics of water by NMR have so far largely relied on the determination of ^1H T_1 and T_2 relaxation times [19,20]. However, while the former can be misinterpreted due to its symmetric behaviour at short and long correlation times (i.e. high T_1 times might indicate either very fast or very slow dynamics), the latter is strongly affected by the kinetics of chemical exchange, thus hindering the real impact of molecular motion on T_2 relaxation. On these grounds, we have instead used an NMR approach based on the saturation transfer difference (STD) experiment on D_2O hydrogel samples which overcomes the drawbacks of NMR relaxation measurements. It is based on monitoring the STD signal of the residually protonated water (HDO) in hydrogel samples prepared in D_2O . It should be noted that STD NMR has been applied before to the study of small molecule gelators focusing on the NMR signals of the gelator, but the technique is restricted to relatively small molecules even using high field NMR [21]. Here, we demonstrate that STD NMR can be used to

easily follow the changes in water confinement in systems constituted by nanoparticulate gelators (cellulose derivatives) undergoing a sol-to-gel transition. Hence, herein we describe the reversible heat-induced gelation of OCNF aqueous dispersion. Coupling STD-NMR with rheology measurements and small angle x-ray scattering to determine network structures, provides detailed structural insights into the gelation mechanisms upon increased temperature, both at the mesoscale level and at the molecular level.

2. Materials and methods

2.1. Sample preparation

OCNF, prepared as described previously using a TEMPO/NaOCl/NaBr oxidation [13] followed by high pressure homogenization, were provided by Croda, as a solid paste in water (ca. 8 wt% OCNF). The degree of oxidation was determined to be 25% (ζ -potential ~ -55 mV), measured by conductometric titration [13,22,23].

CCNF with a degree of substitution of 26% (ζ -potential $\sim +50$ mV) were obtained treating α -cellulose (product number C8002) powder with glycidyltrimethylammonium chloride ($\geq 90\%$) (GTMAC), both purchased from Sigma-Aldrich[®]. Ethanol ($>95\%$), NaOH ($\geq 97\%$) and HCl (37%) were purchased from Sigma-Aldrich[®]. Ultrapure deionized water, DI, (18.2 M Ω -cm) was used throughout.

OCNF were purified by dialysis to remove residual salts and preservatives [24]. Approximately 20 g of OCNF were suspended in 100 mL of DI and stirred at room temperature for 30 min, the dispersion acidified to pH 3 using 1 M HCl (aq) and dialysed against DI (Sigma-Aldrich[®] cellulose dialysis tubing, molecular weight cut-off of 12,400 Da) for 3 days with daily replacement of DI. The dialysed OCNF were processed via mechanical shear (ULTRA TURRAX, IKA T25 digital, 30 min at 6500 rpm) and the pH adjusted to 7 using 0.1 M NaOH (aq). After a second dialysis step (as previously reported) the dispersion was diluted to ca 2 wt% (dry basis) and dispersed by sonication: Ultrasonic Processor FB-505, Fisher, 200 W \cdot cm $^{-2}$, equipped with a 1 cm probe, using a series of 1 s on 1 s off in pulse mode for a net time of 5 mins at 60% amplitude on ca 45 mL dispersion contained in an ice bath. The GTMAC grafting of α -cellulose was carried out following the semi-dry protocol suggested by Zaman et al. [18]. The functionalization was performed using 1 g of NaOH, 20 g of α -cellulose, 7.2 g of DI and 36.4 g of GTMAC. The CCNF dispersion was dialysed and dispersed as previously described for OCNF. The solid contents (wt%) of the OCNF and CCNF dispersions were obtained by drying approximately 10 g of the dispersion in an oven at 60 $^\circ\text{C}$ until constant mass was achieved. The final concentration was calculated based on the average of three measurements. Specific concentrations of OCNF and CCNF dispersions were obtained via dilution of the stock dispersions.

2.2. Rheology

The rheological measurements were performed using a stress-controlled rheometer (Discovery HR3, TA instruments[®]) equipped with a sandblasted plate-plate geometry (40 mm). The samples were used without any further processing and the edge of the sample was covered with a thin layer of mineral oil to prevent evaporation and further covered with a solvent trap to ensure homogeneity of temperature within the chamber. Two types of experiments were conducted. Small amplitude oscillatory shear (SAOS) experiments at 0.1% strain and 10 rad s $^{-1}$ angular frequency and steady state flow curves. The SAOS rheology experi-

ments were performed within the linear viscoelastic region as determined by amplitude and frequency sweeps experiments. To establish the same deformational history for all the samples, 1 min of rotational pre-shear at constant shear of 1 s^{-1} was applied, afterwards, the samples were subject to the following sequence of experiments: (i) thixotropy loop with increase in shear rate from 0.1 to 100 s^{-1} in 161 s, then reversed; (ii) SAOS-time ramp of 60 min; (iii) SAOS-heating ramp, from 25 to $80 \text{ }^\circ\text{C}$ with a heating rate of $5 \text{ }^\circ\text{C min}^{-1}$; (iv) SAOS-time ramp of 30 min; (v) SAOS-cooling ramp, from 80 to $25 \text{ }^\circ\text{C}$ with a heating rate of $5 \text{ }^\circ\text{C min}^{-1}$; (vi) SAOS-time ramp of 60 min and (vii) thixotropy loop as described in (i).

The percentage recoverable energy, $RE\%$, derived from the thixotropy loop was obtained by Eq. (1), where A_i is the area under the shear viscosity curve upon increase of shear rate ($0.1\text{--}100 \text{ s}^{-1}$) and A_d is the area under the shear viscosity curve upon decrease of shear rate ($100\text{--}0.1 \text{ s}^{-1}$).

$$RE\% = \left(\frac{A_d}{A_i} \right) 100 \quad (1)$$

In addition, a power law model [25], Eq. (2), for the shear viscosity from 0.1 to 100 s^{-1} was used to describe the magnitude of the shear-thinning behaviour.

$$\eta \propto \dot{\gamma}^n \quad (2)$$

where $\dot{\gamma}$ is the shear rate and n is the power law exponent, which can be derived from the slope of the curve in the logarithmic representation.

2.3. Fluorescent probe

Surface hydrophobicity of OCNF was probed using the fluorescent probe 6-propionyl-2-(*N,N*-dimethylamino)- naphthalene (PRODAN, $\geq 98.0\%$ Sigma-Aldrich®). A PRODAN in methanol ($\geq 98.0\%$ Sigma-Aldrich®) stock solution of 0.32% [w/v] was prepared and stored in the dark at $15 \text{ }^\circ\text{C}$. $10 \mu\text{L}$ of the PRODAN stock solution was added to 2 mL OCNF dispersions at 0.012, 0.05 and 0.1 wt% before and after heating ($80 \text{ }^\circ\text{C}$ for 30 min) followed by gentle shaking. The measurements were performed in the dark after the samples were kept in the dark for at least 2 h prior to measurement. The relative fluorescence intensity (RFI) was measured in a spectrofluorometer (Perkin Elmer LS 50B) as a function of the emission scan. The excitation wavelength used was 365 nm and the emission scanned from 400 to 650 nm with excitation slit widths at 5 nm as reported by Haskard et al. [26].

2.4. UV-visible spectrophotometry

Measurement of transmitted light (%) was used to detect interfibrillar aggregation using a UV-Vis spectrophotometer (Agilent®/HP 8453). Dispersions were degassed (in a sonicating bath), and loaded into a quartz cuvette (Hellma Analytics®, $1 \times 1 \times 5 \text{ cm}$). Subsequently, a layer of mineral oil was placed on the top of the dispersions to prevent solvent evaporation during the heating process. The cuvette was immersed for 2/3 of its height in a water bath at $80 \text{ }^\circ\text{C}$ for 30 min, ensuring that the dispersion was completely immersed below the water-bath level. The samples were equilibrated at room temperature for at least 2 h before measurements. The transmittance spectrum was obtained between 500 and 800 nm and plotted as function of wavelength (nm).

2.5. Small angle X-ray scattering (SAXS)

Small angle X-ray scattering (SAXS) measurements were performed at Diamond light source (Didcot, Oxfordshire), on the I22

beamline with a beam energy $E = 12.4 \text{ keV}$ and wavelength $\lambda = 1 \text{ \AA}$. The data were collected using a Pilatus P3-2M (Silicon hybrid pixel detector, DECTRIS) with a total acquisition time of 7 s (as an average of multiple frames of 100 ms). The probed q -range was $0.005\text{--}0.75 \text{ \AA}^{-1}$ where q is the scattering vector. The samples were loaded into glass capillary tubes (Capillary tube supplies Ltd®) of 1.5 mm external diameter. To avoid solvent evaporation, heated samples were sealed with mineral oil and prepared in a water bath at $80 \text{ }^\circ\text{C}$ for 30 min followed by cooling at room temperature. The measured scattered intensity $I(q) (\text{cm}^{-1})$ is defined for dilute isotropic suspensions as follows [27]

$$I(q) = \varphi V_p (\Delta\rho)^2 P(q) S(q) + bkg \quad (3)$$

where φ is the volume fraction occupied by the particles, V_p is the volume of the particles (in cm^3), $\Delta\rho$ is the difference in scattering length density between the dispersed particles and the solvent (in cm^{-2}), $P(q)$ is the normalized form factor which describes the shape and size of the particles, $S(q)$ is the structure factor and describes interference of the X-ray beam with multiple objects, usually associated with particle-particle interactions, and bkg is the background. The scattering data were background subtracted, and, in agreement with the particle morphology observed in transmission electron microscopy (TEM) measurements [13,18], cellulose fibrils were modelled as rigid cylinders with an elliptical cross section and a uniform scattering length density. As such, the major radius of the cross-section (r_a) and radius axial ratio (ρ) were fitted variables while the value of the fibril length (L) was kept fixed in agreement with previous TEM measurements, 300 and 1000 nm respectively for CCNF [18,28] and OCNF [13]. The interactions between the rigid fibrils were modelled using the Random Phase Approximation (RPA) [27,29,30], with the parameter v_{RPA} describing the strength of the interactions. Positive values of v_{RPA} are associated with repulsive interaction between rods, while negative values are associated with attractive interactions. This model, based on mean-field theory has been studied extensively in the literature and recently applied for oxidised cellulose nanofibrils [31].

2.6. Nuclear magnetic resonance spectroscopy

All the solution state NMR experiments were carried out using a Bruker Avance I spectrometer operating at a ^1H frequency of 499.69 MHz equipped with a 5 mm probe. Around $700 \mu\text{L}$ of dispersion (4 and 1 wt%) in 99.9% D_2O (Sigma-Aldrich®) was pipetted into a 5 mm NMR tube at room temperature. It should be noted that the cellulose dispersions (OCNF and CCNF) were not solvent exchanged in D_2O beforehand; therefore, the final concentration of exchangeable protons (hence HDO) in the gels was proportional to the OCNF and CCNF concentrations used (1 and 4 wt%). Variable temperature (VT) experiments were performed from 25 to $80 \text{ }^\circ\text{C}$, at different intervals, allowing thermal stabilisation of the sample for 20 min before acquisition. All the experiments were carried out using a 5 s relaxation delay. The analysis of the NMR spectra was focused on the HDO residual signal.

$^1\text{H}\text{--}^{13}\text{C}$ HSQC and NOESY experiments were carried out for the characterisation of OCNF 1 wt%, before and after heating the sample at $80 \text{ }^\circ\text{C}$ (^1H spectrum of CCNF 1 wt% showed very large broadening precluding further characterisation). A coaxial tube containing toluene- d_8 was used within the 5 mm NMR tube for chemical shift referencing at different temperatures. Thus, ^1H and $^1\text{H}\text{--}^{13}\text{C}$ HSQC experiments were referenced to the chemical shift values of the residual methyl peak of toluene- d_8 (2.08 ppm) [5]. Phase-sensitive HSQC experiments with $^1\text{H}\text{--}^{13}\text{C}$ correlation via double inept transfer were acquired with 256 increments in the F1 dimension. Phase-sensitive NOESY experiments with water

suppression with gradients were carried out at 100, 200, 300, 400 and 500 ms mixing time with 128 increments in F1.

Saturation Transfer Difference (STD) NMR experiments [32] were performed by selective ^1H saturation of the OCNF and CCNF networks (resonances below 0 ppm), employing a spoil sequence to remove unwanted magnetization. Cascades of 49 ms Gaussian-shaped pulses at a field strength of 50 Hz were employed, with a delay of $4 \mu\text{s}$ between successive pulses, for a total saturation time of 4 s. The *on*-resonance and *off*-resonance frequencies were set to -1 and 50 ppm, respectively, and a recycle delay of 5 s was used. The STD spectra were obtained by subtracting the *on*- from the *off*-resonance spectrum (I_{sat} and I_0 , respectively, †ESI, Figs. S1 and S2). To determine the STD response (η_{STD}) of the HDO peak (which is proportional to the fraction of bound HDO), its signal intensity in the difference spectrum (I_{STD}) was integrated relative to the signal intensity in the *off*-resonance spectrum (I_0) [33].

$$\eta_{\text{STD}} = \left(\frac{I_0 - I_{\text{sat}}}{I_0} \right) 100 = \left(\frac{I_{\text{STD}}}{I_0} \right) 100 \quad (4)$$

3. Results and discussion

Examination of the rheological behaviour of CCNF dispersions showed no effect of temperature. However, OCNF dispersions revealed a striking sol-to-gel transition upon heating, never observed before, to our knowledge, for a cellulose-based dispersion (Fig. 1).

3.1. Evidencing the heat-induced gelation of OCNF dispersions: rheology

The 1.25 wt% OCNF dispersion sol-to-gel transition was analysed using measurements of storage (G') and loss (G'') moduli of the dispersion as a function of temperature and compared with a 1 wt% CCNF dispersion (Fig. 1, †ESI, Fig. S3 for OCNF at 1, 1.5, 1.75 and 4 wt%). In the first time ramp, the OCNF dispersion showed a time dependent G' similar to the behaviour observed by Veen et al. [34] for bacterial cellulose dispersions, associated with the reformation of the cellulose fibrillar contacts after disruption of the network induced by the loading of the sample in the rheometer. During the temperature ramp, G' sharply increased with temperature rise from 25 to 80 °C, then reached equilibration at 80 °C. Surprisingly, G' continued to increase upon cooling (from 80 to 25 °C). The evolution of G' and G'' upon heating, with $G' < G''$ before heating and $G' > G''$ after heating, indicates that the OCNF dispersion underwent a heat-induced sol-to-gel transition. It is noted that the OCNF dispersion showed an increase in G' of one order of magnitude upon heating, while the value of G'' remains constant. As such, the system increased in overall elasticity (G'), while the viscous component (G'') remained constant. After cooling down to room temperature, G' and G'' remained constant. For CCNF dispersions a slight increase in G' was observed upon equilibration at 80 °C, but neither G' nor G'' changed significantly upon heating, indicating that, unlike OCNF, the rheological properties of the CCNF dispersions are insensitive to the heating process at this concentration.

In order to gain information regarding the rearrangement of the network upon shear of the non-heated OCNF and heated OCNF (OCNF*), we carried out thixotropy loop experiments, before and after the heating loop previously described (*in situ* heating). It is noted that the results of the thixotropy loop are strictly dependent on the time frame in which the increase and decrease of the shear rate occurs. Due to this, a faster thixotropic loop could produce a different outcome than a slower loop. Regardless, as the conditions

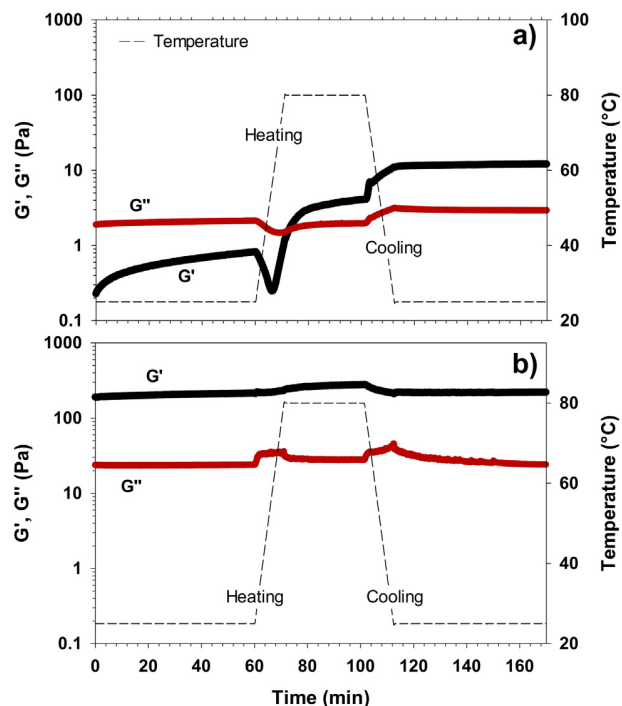


Fig. 1. Storage (G') and loss (G'') moduli as function of temperature and time, (a) 1.25 wt% OCNF dispersion and (b) 1 wt% CCNF dispersion. The OCNF solid content of 1.25 wt% was selected over 1 wt% as the heat-induced gelation effect is more pronounced at this concentration (†ESI, Fig. S3 for OCNF at 1, 1.5 and 1.75 wt%). (ii) The concentration of the fibrils used in all experiments is well above the overlap concentration, calculated to be substantially less than 0.1 wt% [6]. Error for intrinsic limitation of sample loading and equipment of ca. 5%. This is within the size of the symbols used on the graphs.

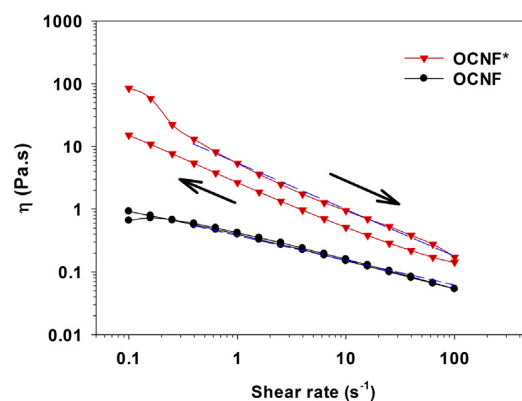


Fig. 2. Shear viscosity loop (Pa.s) of OCNF and OCNF* (heated) 1.25 wt% dispersions. The increase and decrease of the shear (s^{-1}) is indicated by the arrows. The dashed line corresponds to the fitted power law model (Eq. (2), for shear rate from 0.39 to 100 s^{-1} , $R^2 > 0.99$). Error for intrinsic limitation of sample loading and equipment of ca. 5%. This is within the size of the symbols used on the graphs.

for each loop remain the same, the thixotropy loop provides comparable information about the material.

At first the shear viscosity of the OCNF* dispersion had a value almost two orders of magnitude greater than that of the OCNF dispersion (at 0.1 s^{-1}), confirming that the OCNF forms a stronger network upon heating (Fig. 2). The OCNF dispersion is a non-thixotropic fluid, indicating that particle interactions are quickly restored after disruption induced by shear flow [35]. On the contrary, the OCNF* dispersion showed a considerable work softening behaviour [36] characteristic of gel-like materials, where a slow

regeneration of the colloidal aggregates occurs [25]. Similar trends have been observed for cellulose nanocrystals [35], CCNF [17] and bacterial cellulose [37] dispersions at concentrations beyond the gelation threshold [17,35,37] but never a heat-induced change in thixotropy as for the 1.25 wt% OCNF dispersion. In addition, the non-thixotropic OCNF and the work softening OCNF^{*} dispersions were underlined by a significant difference in recoverable energy, RE%, 97% and 51% respectively (Eq. (1)). The intensity of the shear-thinning behaviour described by the exponent n of a power law model (Eq. (2)) resulted in greater values for OCNF^{*} compared to OCNF, 0.74 and 0.15 respectively, indicating the presence of a stronger network, which decays more significantly upon shearing [24].

Further rheological measurements performed on OCNF^{*} dispersions showed a complete loss of gel-like properties when the heating loop was made prior to the loading of the sample into the rheometer. In this situation, the OCNF^{*} dispersion showed similar rheological properties compared to the OCNF dispersions, indicating that the perturbation occurring during loading is enough to induce a complete gel-to-sol transition. Nevertheless, the thixotropy loop of the *in situ* prepared OCNF^{*} dispersion showed only partial breakage of the network, with incomplete restoration of the viscosity observed prior to heating. Thus, the difference in rheological properties between the water bath and the *in situ* heated OCNF dispersions indicates that a complete gel-to-sol transition is obtained either at higher shear rates ($>100 \text{ s}^{-1}$), or upon other forms of perturbation (e.g. shaking) prior to measurements.

To better understand the heat induced gelation mechanism of OCNF dispersions, we combined SAXS and UV-Vis measurements to investigate the aggregation state of fibrils at the mesoscale level, and NMR spectroscopy to probe molecular scale changes of water confinement in the OCNF hydrogel.

3.2. Structural information at the mesoscale level: UV-Vis and SAXS

The strong influence of the deformational history on the gel properties of OCNF dispersions, as observed in the thixotropy loops (Fig. 2), required non-invasive, *in situ*, techniques to better understand the sol-to-gel transition. To that aim, SAXS and UV-Vis experiments were carried out to track the impact of temperature on the aggregation state of the fibrils at the mesoscale level. In particular, SAXS experiments allow a quantitative description of the aggregation state of the fibrils.

The UV-Vis spectra clearly showed a lower transmittance for the 1 wt% OCNF^{*} compared to the OCNF, indicating that the aggregation of the OCNF fibrils is enhanced upon heating (Fig. 3) [15].

The microstructure of the 1 wt% OCNF and CCNF dispersion were probed using SAXS (Fig. 4). In all the SAXS curves, the Guinier region was not observed in the low q -range, showing that the overall fibril length is greater than the length scale probed in this experiment ($> 125 \text{ nm}$) [38]. Nevertheless, the SAXS patterns showed two clear regions for the OCNF dispersions: a high q -range for $q > 0.1 \text{ \AA}^{-1}$ associated with the fibril cross-section and a low q -range for $q < 0.1 \text{ \AA}^{-1}$ linked to the elongated aspect of the fibrils. In the high q -range, the intensities $I(q)$ of OCNF and OCNF^{*} were superimposable in absolute scaling, indicating that the cross-section of the fibrils is not influenced by the heating process. On the contrary, in the low q -range, a significant difference in signal intensity was observed between the OCNF and OCNF^{*} dispersions. In the low q -range the signal intensity of the OCNF dispersion followed a q^{-1} slope (dashed line on Fig. 4a) which is characteristic of rigid rods [38] and in agreement with the SAXS [39] and small angle neutron scattering (SANS) [40,41] data previously reported. After heating, the intensity increased and followed a $q^{-1.67}$ slope. In agreement with rheological data, the CCNF did not show strong variations between the non-heated CCNF and the

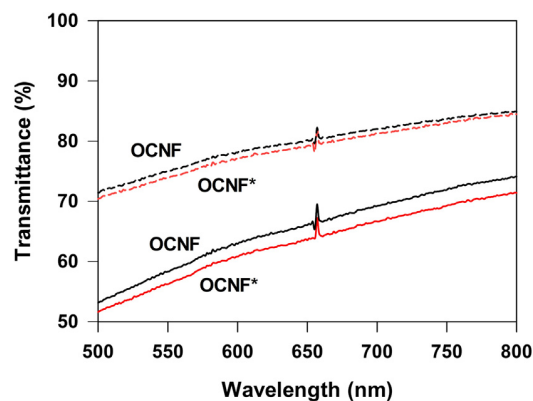


Fig. 3. UV-Vis transmittance spectra of the OCNF and OCNF^{*} dispersions at 0.5 and 1 wt%, dashed and solid line respectively. Error for intrinsic limitation of the equipment of ca. 1% is within the width of the line.

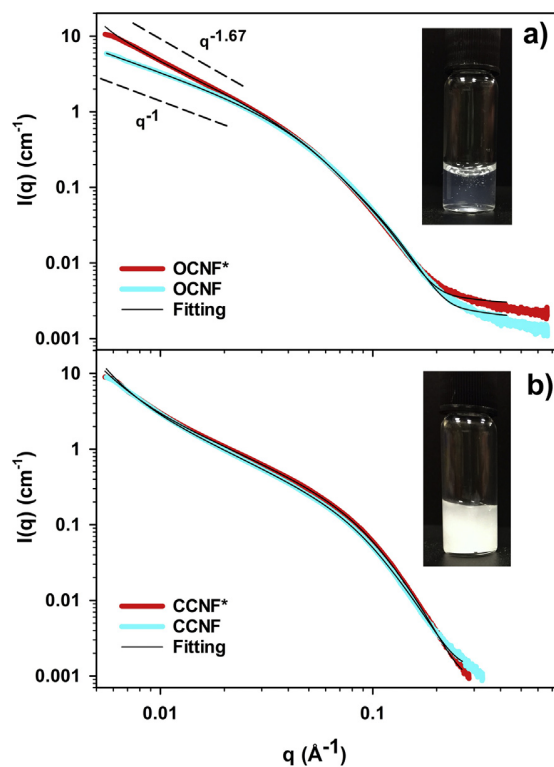


Fig. 4. SAXS patterns for (a) 1 wt% OCNF (in blue) and OCNF^{*} (in red) dispersions and (b) 1 wt% CCNF (in blue) and CCNF^{*} (in red) dispersions. Intensity is given in absolute scaling (cm^{-1}), errors in the value of the intensity are given on the graph. The black lines are the fits given by a model of interacting rigid cylinders with an elliptical cross-section. Dashed lines indicate the slopes where D_m is obtained. For CCNF and CCNF^{*}, the slope in the q -range $0.02\text{--}0.06 \text{ \AA}^{-1}$ is $\sim q^{-1}$ as expected for fibrillar objects. Images of 1 wt% OCNF and CCNF dispersions are shown as insets.

heated CCNF (CCNF^{*}), the two curves being almost completely superimposable. It can be noted concerning the slope in the low q -range, that the patterns deviate from the q^{-1} slope, indicating that the fibrils are already aggregated before heating, in agreement with the gel state observed for CCNF in rheology before heating.

The best data fitting for both OCNF and CCNF was obtained using a model of interacting rigid cylinders, with interactions modelled using the Random Phase Approximation (Table 1) [27,29,30]. The parameter ν_{RPA} describes, from the aggregation state of the cellulose fibrils, information regarding the interfibrillar interactions.

Table 1Values of the fitted SAXS data for 1 wt% OCNF, OCNF⁺, CCNF and CCNF⁺ dispersions.

	Length (nm) ^a	Major radius (nm) ^b	Radius axial ratio	$v_{\text{RPA}}^{\text{c}}$	D_m
OCNF	1000	4.3 ± 0.1	0.30 ± 0.03	0	1.00
OCNF ⁺	1000	4.3 ± 0.1	0.31 ± 0.03	-19.8 ± 0.5	1.67
CCNF	300	2.6 ± 0.1	0.46 ± 0.03	-5.1 ± 0.5	\
CCNF ⁺	300	2.7 ± 0.1	0.45 ± 0.03	-7.4 ± 0.5	\

^a The length of the fibrils was kept fixed at the values given by the literature for the CCNF [18,28] and OCNF [13].^b The polydispersity over the cross-section was found to be 20%.^c For OCNF, interactions were not needed to fit the data, hence v_{RPA} was fixed at 0.

For OCNF, v_{RPA} was null due to non-interacting behaviour of the fibrils. On the contrary, the v_{RPA} parameter was found to be -19.8 for OCNF⁺, suggesting interfibrillar attractive interactions as indicated by the negative value of v_{RPA} . For CCNF, the signal can be modelled well by interacting rigid fibrils before and after heating, in both cases with the addition of a q^{-4} signal at very low q -range to describe the presence of larger aggregates as suggested by a more turbid dispersion (Fig. 4b inset) and gel-like behaviour. In that case as well, heating seemed to further decrease the v_{RPA} value, although the change is less pronounced and in the low- q region the two curves superimposed. The strong interactions between CCNF explains, therefore, the minimal CCNF rearrangement upon heating.

It is noted that, in the model of fibril-fibril interaction employed herein, the actual value of v_{RPA} will be dependent on the length of the nanofibrils (fixed at 300 and 1000 nm for CCNF and OCNF respectively). Nonetheless, assuming the fibril form-factor is unchanged with changes in temperature, the trends observed in the variation of v_{RPA} upon heating are valid. The SAXS results suggest that non-attractive OCNF experience a change in fibril-fibril interaction upon heating, leading to gelation. A similar phenomenon was previously observed upon addition of salt, where reduction of the electrostatic repulsion between OCNF led to gelation [31].

The aggregation of OCNF was also evaluated in terms of fractal theory. The mass fractal dimension (D_m), obtained from the slope in the low- q power law region, showed a noteworthy increase in D_m upon heating, indicating the formation of a more space spanning network [41,42]. In a recent study, Wu et al. [43] showed the primary importance of the particle shape over the material properties and that the assembly of elongated particles diverge significantly from the reaction-limited cluster aggregation (RLCA) and diffusion-limited cluster aggregation (DLCA) previously proposed for spherical colloidal particles [44]. Interestingly, Wu et al. [43] reported values of D_m for asbestos and glass rod-like particles nearly equal to the D_m values of OCNF⁺ shown here (Table 1).

3.3. Monitoring changes in water confinement during gelation: NMR relaxation and saturation transfer difference (STD NMR) of residually protonated water (HDO)

While UV-Vis and SAXS yielded a mesoscopic picture of OCNF heat-induced gelation, providing information about changes in fibril-fibril interactions, solution NMR spectroscopy could be used to probe the gelation at the molecular level in terms of water dynamics. It is well known that NMR not only provides information on the chemical nature and conformation of molecules but also allows the investigation of the dynamics of the individual components (molecular motions) [45,46]. Importantly, solution-state NMR has already been employed to provide direct surface characterisation of nanocellulose and TEMPO-oxidised nanocellulose in aqueous colloidal suspensions [47]. Only the nuclei at the surface of cellulose fibres are visible by solution NMR, as those in the core are not detected due to their very short T_2 relaxation time (large signal broadening).

In this work, we have focused on the analysis of the residually protonated water peak (HDO) in the dispersions prepared in D₂O, which originates from the ¹H-²H(D) exchange due to fibril-D₂O interactions. In this regard, it is important to note that O'Neill et al. recently demonstrated by deuterium labelling, neutron scattering and molecular dynamics simulations that there exist two well differentiated populations of water associated with cellulose [48]. One is more mobile and can be associated with surface water, and the second population is consistent with confined water that can be attributed to water present in the narrow spaces between fibrils. Importantly, ¹H-¹³C HSQC and NOESY experiments carried out before and after heating of the OCNF gels at 80 °C showed no change in the chemical environment or conformation, respectively, at the surface of OCNF fibrils upon heat-induced gelation (†ESI, Figs. S4 and S5), in agreement with fluorescent spectroscopy which confirmed the unchanged hydrophobicity of the fibrils after heating (†ESI, Fig. S6). As neither the dimensions of OCNF nanofibrils, nor the conformation of the surface moieties changed upon heating, as shown by SAXS (Fig. 4, Table 1) and NMR (†ESI, Figs. S4 and S5) respectively, we can reasonably assume that the fraction of surface water is not affected significantly by heating. On these grounds, we have focused our NMR discussion on the role of water in terms of changes in the fraction of confined water, as presented below.

Due to the intrinsic limitations of T_1 and T_2 relaxation measurements, we developed a new methodology based on Saturation Transfer Difference NMR (STD NMR) spectroscopy [49] to monitor the behaviour of water in the gels upon heating and to correlate with our rheological observations. STD NMR is a very well-known ligand-based NMR technique for the characterisation of binding of small molecules to macromolecular receptors, and it has already been applied to study the exchange phenomena of small organo- and hydrogelators between the free state, in the isotropic phase of the gel, and the bound state, in the anisotropic network [21,50]. To the best of our knowledge, it has never been employed to study the evolution of the state of water during the gelation process. Here, we focus on monitoring the residually protonated water molecules (HDO) during the process of gelation. Briefly, by irradiating ¹H resonances corresponding to the core of the cellulose network (1 ppm), we can observe the binding of water to the surface of cellulose fibrils. Importantly, the measured STD factor is directly proportional to the fraction of OCNF-confined water (f_{BW}) when the experiments are carried out in D₂O gels. Under these conditions we can safely discard any significant contribution from direct saturation transfer through chemical exchange of HDO with the hydroxyl groups of cellulose, as the majority of them will be deuterated, compared to the enormous network of non-exchangeable sugar protons available to transfer magnetization to bound HDO molecules by inter-molecular NOE (schematic representation †ESI, Fig. S7).

On these grounds, we measured the STD factors of the residual HDO water peak for OCNF and CCNF gels prepared in D₂O at different temperatures (Fig. 5, for non-normalised data †ESI, Fig. S8). Notably, the results showed a striking difference between OCNF and CCNF dispersions. While in OCNF dispersion the STD factors

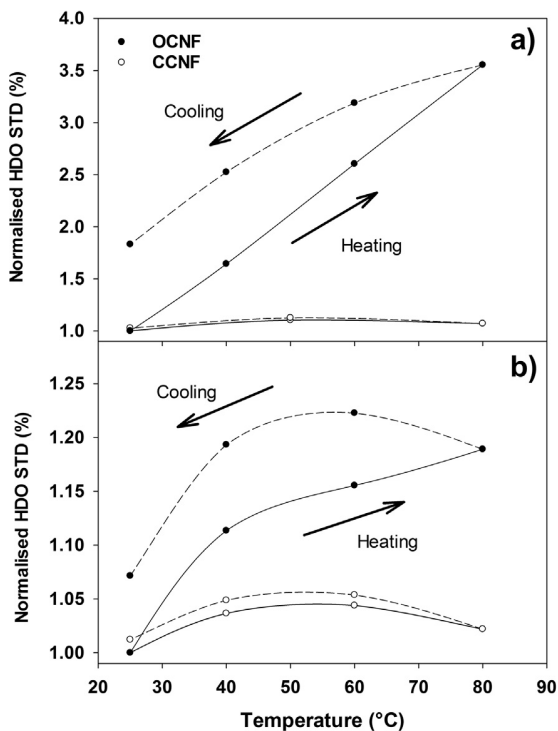


Fig. 5. Temperature evolution of the ^1H HDO STD factor for OCNF (solid circles) and CCNF (empty circles) dispersions (a) 1 wt% and (b) 4 wt%, during heating (solid line) and cooling (dashed line) cycles. An *on-resonance* frequency of -1 ppm was used to saturate the OCNF and CCNF networks. The STD values are normalised against the value obtained at 25°C for each dispersion (the lowest value in both cases). The error of the measurement of STD factors is ca. 10%, in line with the previous reports [21].

increased significantly with temperature up to 80°C , in CCNF dispersions it showed only a small enhancement up to 60°C and a slight decrease at 80°C (Fig. 5). The latter is probably due to the lower efficiency of intramolecular ^1H - ^1H spin diffusion (cellulose saturation intrinsically lower) and intermolecular nuclear Overhauser effect (cellulose – HDO) at high temperature. It should be noted the hysteretic evolution of the STD factor of HDO in OCNF dispersions during the heat-cooling cycle (Fig. 5), is thus in agreement with the observed temperature-dependent rheological behaviour (Fig. 1). Notably, the increase in the STD factor of water in OCNF gels upon heating was found to be significantly higher at a lower concentration of OCNF (Fig. 5, †ESI, Fig. S8), in very good

agreement with rheology where the highest concentration tested (4 wt%) showed only a small increase in G' after the heating protocol (†ESI, Fig. S3d). Thus, the STD NMR experiments are directly reporting an increase in the fraction of OCNF-confined water molecules in the dispersion upon heating, which is not observed in the case of the CCNF dispersion. The increased fraction of OCNF-confined water observed upon heat-induced gelation is not due to conformational changes at the surface of OCNF fibrils (e.g. changes in the glycosidic bond torsion angles, or reorientation of the hydroxymethyl group in non-oxidised residues), but to changes at the mesoscale level, i.e. higher fibril-fibril overlap, in excellent agreement with the rheological and SAXS data.

In this way, we have demonstrated that STD NMR with observation of the residually protonated water molecules (HDO) is a simple powerful tool to study the hydration features of gels constituted by high molecular weight gelators (cellulose), reporting on changes in water confinement during gelation, and demonstrated the excellent correlation of the STD factor of the HDO peak to the rheological data of hydrogels prepared in D_2O .

3.4. Proposed mechanism of heat induced gelation of OCNF dispersions

The gelation of OCNF with increased temperature is the result of a delicate interplay of electrostatic and hydrophobic interactions in this system. As water is heated, the dielectric constant decreases, from 78.57 at 25°C to 62.33 at 80°C [51]. Decreased dielectric constant indicates a decreased polarizability of the fluid, which effectively acts as increased charge screening for electrostatic interactions. From our work on OCNF with added monovalent salt, increased charge screening causes the local aggregation of the fibrils, resulting in gelation [31] – only a small amount of added electrolyte is required to cross from repulsive interactions to attractive ones, as measured by SAXS [31]. Similarly, here heating causes some degree of flocculation in the OCNF suspensions, reducing light transmission, and a weak gel forms. This corresponds to the SAXS data which show no change in fibril cross section, but a change in the interaction parameter ν_{RPA} which indicates an increase in attractive interactions between the fibrils at higher temperatures. Gel formation is associated with an increase in confined water, seen by the STD NMR, since increased contact between fibrils will constrain water at the interfaces between the two surfaces (schematically depicted in Fig. 6). Once formed, after cooling the gel is in a metastable state, which is easily disrupted and returned to the dispersed state by agitation-induced shear. Increased charge screening would not alter the apparent hydrophobicity of the fibrils, so this is consistent with the fluores-

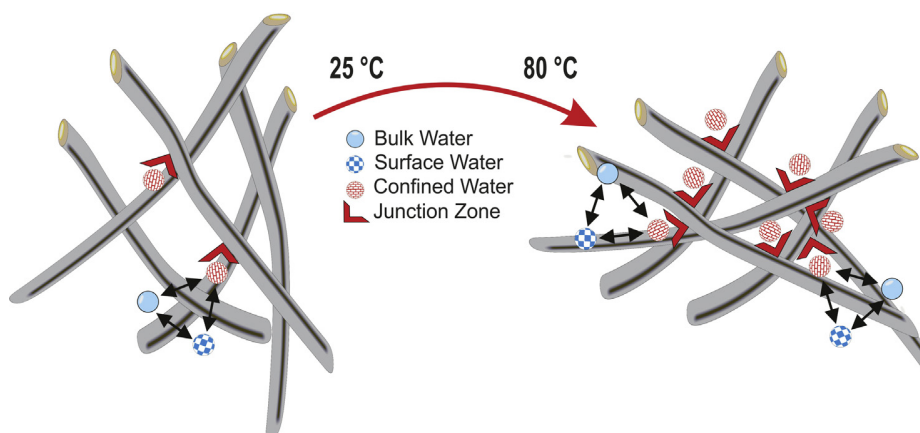


Fig. 6. Schematic representation of the increased overlap of the oxidised cellulose nanofibrils (OCNF) upon heating. After heating, the number of junction zones (highlighted in red) between fibrils increase, increasing the amount of confined water, without strong densification of the cluster. Note: cellulose fibrils and water molecules are not to scale.

cence data (†ESI, Fig. S6). CCNF is less responsive to electrostatic screening effects [52] due to the presence of stronger interfibrillar interactions as shown by SAXS (Fig. 4b) and by greater moduli (G' and G'') in oscillatory rheology (Fig. 1b), hindering further fibrillar rearrangement upon heating. Since this suspension is already gelled, changes in dielectric constant and electrostatic screening make little difference to the structure.

4. Conclusion

In this work we describe a novel mechanism of temperature triggered gelation for oxidised nanocellulose hydrogels, along with a thorough study of the process, from the rheological macroscopic behaviour, through nanoscale fibril aggregation, down to the molecular level of the water dynamics within the OCNF network. Rheological measurements revealed that the negatively-charged OCNF forms a metastable physical gel upon heating. The OCNF heat-induced gels were preserved upon cooling, but easily disrupted by mechanical perturbation. However, same behaviour was not observed for the positively-charged CCNF at the same concentrations. This shows the gelation is specific to OCNF and not a general behaviour of nanocelluloses. SAXS analysis of the OCNF gels pointed towards an increase in junction zones between fibrils, indicating a transition from widely dispersed fibrils to closer contact. These junction zones work as crosslinking points creating a connected network that leads to the remarkable increase in the elastic moduli observed. STD NMR experiments detected an increase in the population of confined water with temperature, this behaviour not observed for CCNF, suggesting a correlation between water confinement and gel formation. We proposed that this heat-induced fibril aggregation is mainly driven by changes of the dielectric constant of the dispersing media (water) which alters the fine balance between attractive forces (interfibrillar hydrogen bonding and hydrophobic interactions) and repulsive forces (electrostatic interactions) favouring a closer interaction between the fibrils leading to the formation of a metastable aggregate and gel formation. For the CCNF, the attractive element of this balance is already stronger than for OCNF and the CCNF fibrils are already in a higher level of aggregation, as seen by SAXS, such that heating cannot meaningfully affect the gel structure further. These observations of gelation in OCNF due to heating are significant for proposed applications of these materials in rheology modification, since formulation and industrial processing frequently involve heating steps, which may therefore alter the properties of the suspension. The results outlined here will permit selection of nanocellulose properties and post-processing of suspensions to enhance or avoid this effect and inform further work towards uptake of such materials in real-life applications.

These results also demonstrate the strength of using combined non-invasive, *in situ* techniques to probe the gel properties from nanoscale using SAXS to molecular scale using STD NMR, giving detailed insights into mechanism. In particular the work shows the benefits of using STD NMR on residual HDO in D_2O solvated hydrogel samples of particulate gelators to monitor changes in the populations of surface-confined water molecules with temperature. The ease of the STD NMR methodology, and the solid evidence gathered in this work may allow a future boost in the use of HDO-based STD NMR experiments to correlate changes in confined water populations with rheology, within the hydrogel research community.

Acknowledgements

V.C. thanks University of Bath for supporting his PhD. J.C.M.G. thanks EPSRC for funding (EP/N033337/1). M.A.D.S. and J.S. thank

EPSRC for funding this project (grant EP/N033310/1). The authors would like to thank Valeria Gabrielli for helping with the acquisition of NMR experiments, as well as the Diamond Light Source for the award of beam time (experiment no. SM16364), and Drs Nick Terrill, Andy Smith, and Tim Snow for their assistance with the experiments on beamline I22. We also acknowledge access to UEA Faculty of Science Research Facilities. Additional research data supporting this publication are available as electronic supplementary files at DOI: 10.15125/BATH-00476 and [https://people.uea.ac.uk/en/datasets/data-for-understanding-heat-driven-gelation-of-anionic-cellulose-nanofibrils-combining-saturation-transfer-difference-std-nmr-small-angle-xray-scattering-saxs-and-rheology\(a524288d-b4ac-4b6e-a40a-3a6dd1677d3c\).html](https://people.uea.ac.uk/en/datasets/data-for-understanding-heat-driven-gelation-of-anionic-cellulose-nanofibrils-combining-saturation-transfer-difference-std-nmr-small-angle-xray-scattering-saxs-and-rheology(a524288d-b4ac-4b6e-a40a-3a6dd1677d3c).html).

Conflict of interest

The authors declare no conflicts of interest.

Appendix A. Supplementary material

Supplementary data to this article can be found online at <https://doi.org/10.1016/j.jcis.2018.09.085>.

References

- [1] T. Saito, S. Kimura, Y. Nishiyama, A. Isogai, *Biomacromolecules* 8 (2007) 2485–2491.
- [2] A. Isogai, T. Saito, H. Fukuzumi, *Nanoscale* 3 (2011) 71–85.
- [3] D. Celebi, R.H. Guy, K.J. Edler, J.L. Scott, *Int. J. Pharm.* 514 (2016) 238–243.
- [4] J. Coombs O'Brien, L. Torrente-Murciano, D. Mattia, J.L. Scott, *ACS Sustain. Chem. Eng.* 5 (2017) 5931–5939.
- [5] L. Li, *Macromolecules* 35 (2002) 5990–5998.
- [6] R.J. Crawford, K.J. Edler, S. Lindhoud, J.L. Scott, G. Unali, *Green Chem.* 14 (2012) 300–303.
- [7] K.J. De France, T. Hoare, E.D. Cranston, *Chem. Mater.* 29 (2017) 4609–4631.
- [8] T. Saito, T. Uematsu, S. Kimura, T. Enomae, A. Isogai, *Soft Matter* 7 (2011) 8804–8809.
- [9] D. da Silva Perez, S. Montanari, M.R. Vignon, *Biomacromolecules* 4 (2003) 1417–1425.
- [10] Y. Okita, T. Saito, A. Isogai, *Biomacromolecules* 11 (2010) 1696–1700.
- [11] S. Tsuguyuki, A. Isogai, *Biomacromolecules* 5 (2004) 1983–1989.
- [12] H. Fukuzumi, R. Tanaka, T. Saito, A. Isogai, *Cellulose* 21 (2014) 1553–1559.
- [13] Y. Habibi, H. Chanzy, M.R. Vignon, *Cellulose* 13 (2006) 679–687.
- [14] N. Quennou, S.M. Hashmi, H.S. Choi, J.W. Kim, C.O. Osuji, *Soft Matter* 12 (2015) 157–164.
- [15] H. Dong, J.F. Snyder, K.S. Williams, J.W. Andzelm, *Biomacromolecules* 14 (2013) 3338–3345.
- [16] N. Masruchin, B.D. Park, V. Causin, I.C. Um, *Cellulose* 22 (2015) 1993–2010.
- [17] M. Hasani, E.D. Cranston, G. Westman, D.G. Gray, *Soft Matter* 4 (2008) 2238–2244.
- [18] M. Zaman, H. Xiao, F. Chibante, Y. Ni, *Carbohydr. Polym.* 89 (2012) 163–170.
- [19] Y.E. Shapiro, *Prog. Polym. Sci.* 36 (2011) 1184–1253.
- [20] C.L. Cooper, T. Cosgrove, J.S. van Duijneveldt, M. Murray, S.W. Prescott, *Soft Matter* 9 (2013) 7211.
- [21] S.M. Ramalhethe, K.P. Nartowski, N. Sarathchandra, J.S. Foster, A.N. Round, J. Angulo, G.O. Lloyd, Y.Z. Khimyak, *Chem. – A Eur. J.* 23 (2017) 8014–8024.
- [22] K. Zhang, S. Fischer, A. Geissler, E. Brendler, *Carbohydr. Polym.* 87 (2012) 894–900.
- [23] J.C. Courtenay, M.A. Johns, F. Galembeck, C. Deneke, E.M. Lanzoni, C.A. Costa, J.L. Scott, R.I. Sharma, *Cellulose* 24 (2016) 253–267.
- [24] V. Calabrese, M.A. da Silva, J. Schmitt, J.C. Muñoz-García, V. Gabrielli, J.L. Scott, J. Angulo, Y.Z. Khimyak, K.J. Edler, *Soft Matter* (2018), <https://doi.org/10.1039/c8sm00752g>.
- [25] I.T. Norton, F. Spyropoulos, P. Cox, *Chemical Engineering*, Wiley-Blackwell, 2011, pp. 10–15.
- [26] C.A. Haskard, E.C.Y. Li-Chan, *J. Agric. Food Chem.* 46 (1998) 2671–2677.
- [27] J.S. Pedersen, *Adv. Colloid Interface Sci.* 70 (1997) 171–210.
- [28] J.C. Courtenay, S.M. Ramalhethe, W.J. Skuze, R. Soni, Y.Z. Khimyak, K.J. Edler, J.L. Scott, *Soft Matter* 14 (2018) 255–263.
- [29] S. Manet, J. Schmitt, M. Impéror-Clerc, V. Zholobenko, D. Durand, C.L.P. Oliveira, J.S. Pedersen, C. Gervais, N. Baccile, F. Babonneau, I. Grillo, F. Meneau, C. Rochas, *J. Phys. Chem. B* 115 (2011) 11330–11344.
- [30] T. Shimada, M. Doi, K. Okano, *J. Chem. Phys.* 88 (1988) 2815–2821.
- [31] J. Schmitt, V. Calabrese, M.A. Silva, S. Lindhoud, V. Alfreðsson, J.L. Scott, K.J. Edler, *Phys. Chem. Chem. Phys.* 20 (2018) 16012–16020.
- [32] M. Mayer, B. Meyer, *J. Am. Chem. Soc.* 123 (2001) 6108–6117.
- [33] C.A. Lepre, J.M. Moore, J.W. Peng, *Chem. Rev.* 104 (2004) 3641–3676.
- [34] S.J. Veen, P. Versluis, A. Kuijck, K.P. Velikov, *Soft Matter* 11 (2015) 8907–8912.

-
- [35] J. Araki, M. Wada, S. Kuga, T. Okano, *Colloids Surfaces A Physicochem. Eng. Asp.* 142 (1998) 75–82.
- [36] A.J.M. Nic, J. Jirat, B. Kosata, IUPAC. *Compendium of Chemical Terminology*, 2nd ed. (the 'Gold Book'), Compiled by A. D. McNaught and A. Wilkinson. Blackwell Scientific Publications, Oxford, 1997.
- [37] D. De Kort, S. Veen, H. Van As, D. Bonn, K. Velikov, J. Van Duynhoven, *Soft Matter* 12 (2016) 4739–4744.
- [38] B. Hammouda, in: *Probing Nanoscale Structures - The SANS toolbox*, National Institute of Standards and Technology Center for Neutron Research Gaithersburg, 2010, pp. 211–225.
- [39] Y. Su, C. Burger, B.S. Hsiao, B. Chu, *J. Appl. Crystallogr.* 47 (2014) 788–798.
- [40] Y. Mao, K. Liu, C. Zhan, L. Geng, B. Chu, B.S. Hsiao, *J. Phys. Chem. B* 121 (2017) 1340–1351.
- [41] F. Cherhal, F. Cousin, I. Capron, *Langmuir* 31 (2015) 5596–5602.
- [42] G. Beaucage, *J. Appl. Crystallogr.* 28 (1995) 717–728.
- [43] L. Wu, C.P. Ortiz, D.J. Jerolmack, *Langmuir* 33 (2017) 622–629.
- [44] S. Lazzari, L. Nicoud, B. Jaquet, M. Lattuada, M. Morbidelli, *Adv. Colloid Interface Sci.* 235 (2016) 1–13.
- [45] Y. E. Shapiro, ed. P. Somasundaran, CRC Press, New York, USA, *Encyclopedia*, 2006, p. 1219.
- [46] C. Mayer, *Prog. Nucl. Magn. Reson. Spectrosc.* 40 (2002) 307–366.
- [47] F. Jiang, J.L. Dallas, B.K. Ahn, Y. Lo Hsieh, *Carbohydr. Polym.* 110 (2014) 360–366.
- [48] H. O'Neill, S.V. Pingali, L. Petridis, J. He, E. Mamontov, L. Hong, V. Urban, B. Evans, P. Langan, J.C. Smith, B.H. Davison, *Sci. Rep.* 7 (2017) 1–13.
- [49] M. Mayer, B. Meyer, *Angew. Chemie - Int. Ed.* 38 (1999) 1784–1788.
- [50] M.D. Segarra-Maset, B. Escuder, J.F. Miravet, *Chem. - A Eur. J.* 21 (2015) 13925–13929.
- [51] G.P. Srivastava, Y.P. Varshni, *Physica* 22 (1956) 584–586.
- [52] J.C. Courtenay, Y. Jin, J. Schmitt, K.J. Edler, J.L. Scott, 2018 (in preparation).

CHAPTER 4

SURFACTANT CONTROLLED ZWITTERIONIC CELLULOSE NANOFIBRIL DISPERSIONS

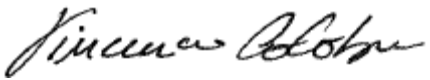
In Chapter 3 the structural and rheological properties of cationic cellulose nanofibrils (CCNF) and oxidised cellulose nanofibrils (OCNF) were investigated as a function of time and temperature. Contrarily to OCNF, the CCNF gels did not display any thermosensitivity. This is an advantageous feature for marketable materials where constant material properties are desired over a wide range of time and temperature.^[146] Since the pronounced aggregation state of CCNF yielded heat insensitive hydrogels, OCNF were covalently grafted with a quaternary ammonium group (the same positive moiety as used in CCNF), to form electrostatically interacting zwitterionic cellulose nanofibrils (ZCNF). Besides the heat insensitivity of ZCNF, the positive and negative moieties on the ZCNF surface enabled tuning of their assembly through electrostatic interplays with other species such as counterions, polymers and surfactants. However, the demand to substitute petrochemically-derived polymers in formulated products, directed us to investigate the potential of ZCNF as a rheological modifier when combined with common surfactants present in commercial products, where surfactants confer essential properties such as cleansing and foaming.^[152] The colloidal stability of ZCNF was investigated in three different scenarios using, commercially available neutral and charged surfactants to seek a more generalized understanding of how ZCNF interact with surfactants. We found that ionic surfactants trigger drastic changes to the ZCNF assembly in aqueous media. Of great interest is the addition of neutrally charged surfactants which, although mild, promote some level of stabilization in the ZCNF dispersion. This mechanism of stabilization could be highly interesting to preserve the charge accessibility of the ZCNF while enhancing its colloidal stability.^[153]

The charge accessibility of zwitterionic polymers has been efficiently used to deliver ionic drugs.^[154] However, the limiting factor related to zwitterionic components is their poor colloidal stability due to electrostatic interactions which lead to aggregation. On this basis, the depletion stabilization mechanism, achieved through the use of soluble polymers in the continuous phase, has been described as a promising stabilization route to preserve charge accessibility.^[153] Moreover, zwitterionic celluloses obtained by various sources and chemical pathways have shown a large span of useful properties such as antifouling properties,^[155,156] antimicrobial activity^[157] and potential applications in drug delivery^[158] and encapsulation^[159]. Specifically, Haitao et al.^[160] demonstrated the efficiency of zwitterionic cellulose acetate as absorbents of Cu^{2+} and Cd^{2+} from aqueous solutions whilst Liu et al.^[156] used zwitterionic cellulose acetate to prepare membranes for protein separation and purification. As such, the simple strategy used to produce ZCNF presented in this work may have impact in multiple fields. After the publication of this Chapter, the grafting of the quaternary ammonium group has used to functionalise acetylated cel-

lulose nanofibrils.^[161] However, information regarding the stability of the zwitterionic acetylated cellulose dispersions was not provided.^[161] In the following Chapter, the production of ZCNF and its colloidal stability in the presence of surfactants is discussed with the aim to understand and control the ZCNF assembly for applications in the delivery of targeted components.

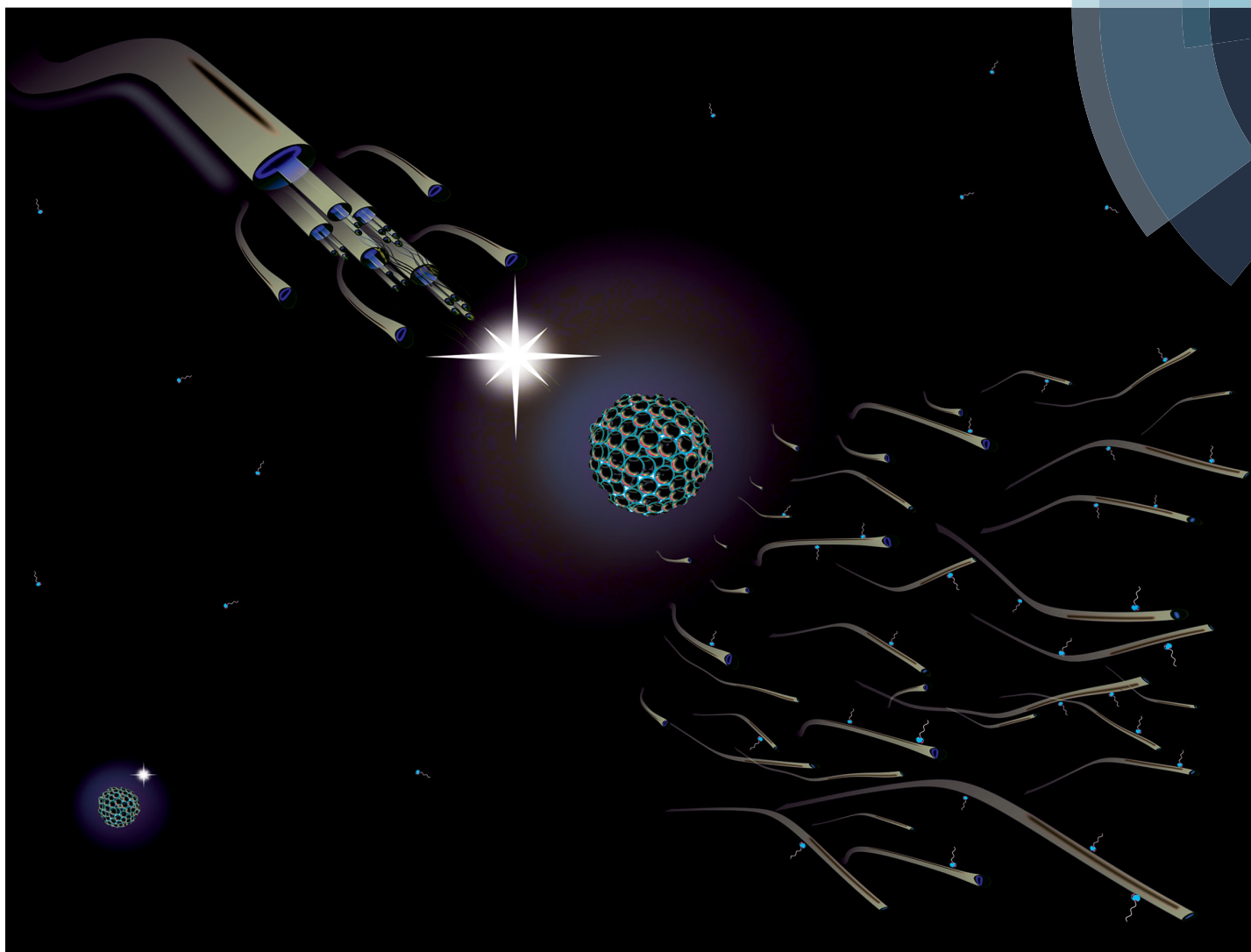
Supporting information available in section 10.2.
The publication included here is reproduced under the Creative Commons License.^[44]



This declaration concerns the article entitled:								
Surfactant Controlled Zwitterionic Cellulose Nanofibril Dispersions								
Publication status (tick one)								
draft manuscript	<input type="checkbox"/>	Submitted	<input type="checkbox"/>	In review	<input type="checkbox"/>	Accepted	<input type="checkbox"/>	Published <input checked="" type="checkbox"/>
Publication details	Calabrese, V.; Da Silva, M. A.; Schmitt, J.; Muñoz-Garcia, J. C.; Gabrielli, V.; Scott, J. L.; Angulo, J.; Khimyak, Y. Z.; Edler, K. J. Surfactant Controlled Zwitterionic Cellulose Nanofibril Dispersions. <i>Soft Matter</i> 2018 , <i>14</i> (38), 7793–7800.							
Candidate's contribution to the paper (detailed, and also given as a percentage).	<p>The candidate contributed to/ considerably contributed to/predominantly executed the...</p> <p>Formulation of ideas: -The initial idea was formulated by VC. 90%</p> <p>Design of methodology: -All the measurements were designed by VC with the exception of NMR. The NMR experiments were designed by VG and JMG based on previous standard characterization procedures. 85%</p> <p>Experimental work: - The experimental work was conducted by VC with the exception of NMR. Ready to be measured samples for NMR were provided by VC to VG whom performed the NMR experiments. KJE contributed to the experimental SANS work. 85% -The 95% of the experimental work and data analysis was carried out by VC.</p> <p>Presentation of data in journal format: -The first draft was handled by VC with contribution of JMG and VG for the materials and method part regarding the NMR related section. The drafted manuscript has been sent within the authors for comments and corrections. 90%</p>							
Statement from Candidate	This paper reports on original research I conducted during the period of my Higher Degree by Research candidature.							
Signed						Date	29/09/19	

Soft Matter

rsc.li/soft-matter-journal



ISSN 1744-6848



PAPER

Karen J. Edler *et al.*

Surfactant controlled zwitterionic cellulose nanofibril dispersions



Surfactant controlled zwitterionic cellulose nanofibril dispersions†

Cite this: *Soft Matter*, 2018, 14, 7793

Vincenzo Calabrese,^a Marcelo A. da Silva,^a Julien Schmitt,^a Juan C. Muñoz-García,^b Valeria Gabrielli,^b Janet L. Scott,^{a,c} Jesus Angulo,^b Yaroslav Z. Khimyak^b and Karen J. Edler^{a,*}

Received 11th April 2018,
Accepted 30th July 2018

DOI: 10.1039/c8sm00752g

rsc.li/soft-matter-journal

Zwitterionic cellulose nanofibrils (ZCNFs) with an isoelectric point of 3.4 were obtained by grafting glycidyltrimethylammonium chloride onto TEMPO/NaBr/NaOCl-oxidised cellulose nanofibrils. The ZCNF aqueous dispersions were characterized *via* transmission electron microscopy, rheology and small angle neutron scattering, revealing a fibril-bundle structure with pronounced aggregation at pH 7. Surfactants were successfully employed to tune the stability of the ZCNF dispersions. Upon addition of the anionic surfactant, sodium dodecyl sulfate, the ZCNF dispersion shows individualized fibrils due to electrostatic stabilization. In contrast, upon addition of the cationic species dodecyltrimethylammonium bromide, the dispersion undergoes charge neutralization, leading to more pronounced flocculation.

Introduction

Zwitterionic polymers are a class of polyampholytes, containing anionic and cationic groups with a neutral net charge at a specific pH.¹ In the last decade, this class of compounds has received attention for metal binding,² antifouling^{3–5} and antimicrobial⁶ properties and their application in drug delivery⁷ and encapsulation.^{8,9}

The self-assembly and the stabilization of zwitterionic moieties depend on pH, ionic strength and temperature;¹⁰ ideal features for the development of responsive materials.^{2,11} At the isoelectric point (IP), polyampholyte polymers (*e.g.* proteins) show charge symmetry between the negatively and positively charged moieties leading to flocculation, whereas electrostatic stabilization dominates at pH values far from the IP.^{10,11} Ionic strength has also been shown to change the conformational arrangement of block polyampholytes and to strongly influence protein solubility, due to a charge screening effect.^{12,13} Although electrostatic stabilization of zwitterionic components is easy to achieve, a drawback is the decreased charge accessibility; a desirable feature for drug delivery. In order to ensure particle stabilization while retaining their surface and charge accessibility,

depletion stabilization has been previously employed to stabilize several colloidal particles, including gold¹⁴ and silica particles.¹⁵ This mechanism occurs when particles, in the presence of non-adsorbing polymers, gain configurational entropy overcoming the attractive osmotic pressure caused by the depletion layer.¹⁶ This phenomenon occurs at polymer concentrations beyond the concentration required to induce depletion flocculation due to the overlapping of the polymer, which decreases the attractive osmotic energy.¹⁶

Zwitterionic components, such as proteins, can compete with food supplies, whereas block polyampholytes are not necessarily biodegradable or derived from renewable sources. Here, we describe a novel route for the production of plant-based zwitterionic cellulose nanofibrils (ZCNFs), based on the reported TEMPO-mediated oxidation^{17–19} and glycidyltrimethylammonium chloride (GTMAC) cationization reactions.^{20,21} This functionalization route involves the selective introduction of negatively charged carboxyl groups^{17,19,22} by oxidation, followed by grafting of quaternary ammonium groups from the GTMAC-cationization.²¹ Although pathways for the production of cellulose nanofibrils (CNFs) bearing oppositely charged moieties have been reported,^{6,7} their self-assembly in aqueous media has not, to the best of our knowledge, been described, although the colloidal properties of oxidised cellulose nanofibrils (OCNFs)^{18,23–25} and quaternary ammonium salt grafted CNF^{21,26,27} aqueous dispersions have been characterized. Here, we describe the functionalization and double-charged nature of ZCNFs revealed by ¹³C nuclear magnetic resonance (NMR) spectroscopy and ζ-potential measurements. The relative stability and structure of dispersions of ampholytic ZCNFs in aqueous media containing the anionic surfactant sodium dodecyl sulfate (SDS), cationic

^a Department of Chemistry, University of Bath, Claverton Down, Bath, BA2 7AY, UK. E-mail: k.edler@bath.ac.uk; Tel: +44 (0)1225 384192

^b School of Pharmacy, University of East Anglia, Norwich Research Park, Norwich, NR4 7TJ, UK. E-mail: j.angulo@uea.ac.uk, y.khimyak@uea.ac.uk

^c Centre for Sustainable Chemical Technology, University of Bath, Claverton Down, Bath, BA2 7AY, UK. E-mail: j.l.scott@bath.ac.uk; Tel: +44 (0)1225 386307

† Electronic supplementary information (ESI) available: Material characterisation, conductimetric titration and attenuated total reflectance Fourier transform infrared (ATR-FTIR) spectra. See DOI: 10.1039/c8sm00752g

surfactant dodecyltrimethylammonium bromide (DTAB) and the non-ionic surfactant TWEEN[®] 80 (TW80) were investigated *via* ζ -potential, transmission electron microscopy (TEM), rheology and small angle neutron scattering (SANS).

Materials

Sample preparation

OCNF, prepared using a TEMPO/NaOCl/NaBr oxidation²⁸ of wood pulp followed by high-pressure homogenization, was provided by Croda[®] International Plc (Goole, UK) as an 8 wt% slurry. The material was purified by dialysis to ensure that any salts or other process related impurities were removed. In brief, 20 g of OCNF was suspended in 100 mL of deionised (DI) water, dispersed by thorough stirring at room temperature, acidified to pH 3 using 1 M HCl (aq.) and dialysed (Sigma-Aldrich[®] cellulose dialysis tubing, molecular weight cut-off 12 400 Da) against DI water, for 3 days with daily replacement of DI water. The dialysed OCNF was processed *via* mechanical shear (Ultra Turrax, IKA T25 digital, 30 min at 6500 rpm) and the pH adjusted to 7 using 0.1 M NaOH (aq.). After a second dialysis step, the dispersion was diluted to *ca.* 2 wt% (dry-basis) and dispersed by sonication (Ultrasonic Processor FB-505, Fisher, 200 W cm⁻², equipped with a 1 cm probe) in a series of 1 s on/1 s off pulses for a net time of 5 min at 60% amplitude in *ca.* 45 mL of dispersion contained in an ice bath. Post-purification, stable OCNF dispersions (degree of oxidation (DO) 25%, relative to the hydroxyl group in C6 of the anhydroglucose units, measured by conductometric titration, ESI,[†] Fig. S1^{17,21}) were prepared. The OCNF dispersion was freeze-dried and used as the substrate for the glycidyltrimethylammonium chloride ($\geq 90\%$) (GTMAC, Sigma-Aldrich[®]) functionalization. NaOH powder (15.7 wt% relative to OCNF dry weight), ultra-pure DI water (18 M Ω cm, weight ratio OCNF/water = 1/23) and GTMAC (20 mol eq. relative to anhydroglucose units (AGUs)) were added to the freeze-dried OCNF. The mixture was stirred for 15 h, heated in a water bath at 65 \pm 1 $^{\circ}$ C for 80 min with constant stirring in a sealed vial, cooled to 25 $^{\circ}$ C and the reaction quenched by addition of EtOH. To purify the resultant ZCNF dispersion, the suspension was centrifuged (5 min at 3600 RCF) and the pellet collected and redispersed in DI water; the process was repeated 10 times. This ZCNF dispersion was treated as the stock from which all others were prepared. ZCNFs were dispersed by sonication (Ultrasonic Processor FB-505, Fisher, 200 W cm⁻², equipped with a 0.63 cm probe), using a series of 1 s on/1 s off pulses for 2 min at 60% amplitude in *ca.* 45 mL of suspension. The pH of the ZCNF stock dispersion was 6.8 and not adjusted except where otherwise stated. The concentration (wt%) of the ZCNF stock dispersion was determined by gravimetric analysis and specific ZCNF concentrations were obtained by dilution of the ZCNF stock dispersion with DI water. The ZCNF dispersions at various pH values were obtained by addition of 1 M HCl (aq.) or 1 M NaOH (aq.) and ZCNF dispersions containing the surfactant were prepared by addition of the previously dissolved surfactant and vortexed thoroughly.

Methods

Rheological analyses were performed using a stress-controlled rheometer (Discovery HR-3, TA instruments[®]) at 25 $^{\circ}$ C equipped with a sandblasted plate–plate geometry (40 mm). The samples were vortexed thoroughly to ensure homogeneity before loading and pre-sheared for 30 s at a shear rate of 1 s⁻¹ prior to measurement of shear viscosity (25 to 100 s⁻¹). The viscosity data are presented as the relative viscosity, η_r , defined as the apparent viscosity, η_{app} , normalized by the viscosity of the continuous phase, η_{cp} .

ζ -Potential measurements were conducted using a Malvern Zetasizer Nano ZSP[®]. The samples were diluted to 0.01 wt% ZCNF by addition of water containing HCl (aq.) or NaOH (aq.) to achieve a specific pH, or surfactant solution, placed in a capillary electrode cell and the ζ -potential was determined as an average of 4 measurements of 100 scans each.

The shape and size of the ZCNFs were investigated using TEM (JEOL JEM-2100, at 200 kV operating voltage). One droplet of the sample (0.01 wt%) was placed on a hydrophilized copper grid (previously glow discharged) and allowed to rest for 30 s, and the excess was removed using filter paper. A droplet of 2% uranyl acetate was added on top of the grid–sample substrate and the excess was removed after 30 s.

The surface tension at the air water interface (γ_{aw}) was measured using the Du Noüy ring method (Sigma 701 instrument, Attension[®], Sweden) using a 9.58 mm platinum ring. ZCNF dispersions at 0.001 wt% were prepared by dilution with DI water and the γ_{aw} measured in a vessel with a diameter of 66 mm. Afterwards, an aliquot of surfactant solution was added to the dispersion (dropwise to the air–water interface) and the evolution of the γ_{wa} in the static solution was monitored for 60 min. It should be noted that the surfactant concentrations (125 μ M SDS, 125 μ M DTAB and 2.5 μ M TW80) were chosen to be below the critical micelle concentration (CMC) of the surfactants.^{29,30} Control samples were prepared using DI water instead of the ZCNF dispersion.

Small angle neutron scattering (SANS) data were collected on SANS2D and Larmor beamlines (Rutherford Appleton Laboratory, Didcot, UK) using wavelengths between 1.5 and 14 \AA to obtain a q -range between 0.004 and 0.6 \AA^{-1} . Freeze-dried ZCNF was dispersed in D₂O by sonication, as described above, and ZCNF dispersions containing surfactant were prepared by addition of the deuterated surfactants, d-SDS and d-DTAB (in dry form, provided by the ISIS Deuteration Facility) and thorough vortex-mixing. Samples were loaded into 1 mm thick quartz cells. Background subtraction and normalization of the scattered intensity $I(q)$ (cm⁻¹) was conducted using the Mantid software routine and data modelling was conducted using the software Sasview 4.0.1.³¹ In agreement with the particle morphology observed by TEM measurements, ZCNFs were modelled as flexible cylinders with elliptical cross sections and uniform scattering length densities, based on the worm-like chain model of Kratky and Porod with the incorporation of the excluded volume effect as described by Pedersen and Schurtenberger.³² The Kuhn length, b_{Kuhn} , (twice the persistence length) and the

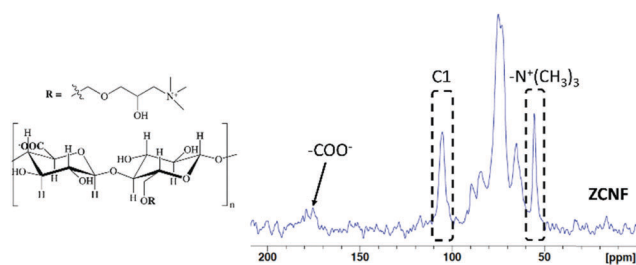


Fig. 1 $^{13}\text{C}\{^1\text{H}\}$ DP MAS NMR spectra for ZCNF powder (after thorough washing with acid solution (pH 2) and dialysed against DI water) after 512 scans, acquired on a 300 MHz spectrometer at a 10 kHz MAS rate and an 800 s relaxation delay.³³ A line broadening of 80 Hz was used. The peaks corresponding to the anomeric carbon and the cationic group are highlighted within dashed rectangles.

major radius, r_{maj} , of the cross-section were fitted variables while the fibril contour length, L_c , and the minor radius, r_{min} , were fixed. The parameter L_c could not be determined within the probed q -range, therefore it was fixed at an arbitrary value of 1000 nm, $L_c \gg (2\pi/q_{\text{min}})$ whereas r_{min} was fixed to 1 nm, based on the SANS data obtained for CNF.²⁷

Solid-state NMR experiments were performed at room temperature using a Bruker Avance III spectrometer equipped with a 4 mm triple resonance probe operating at frequencies of 300.13 MHz (^1H) and 75.47 MHz (^{13}C). Quantitative 1D $^{13}\text{C}\{^1\text{H}\}$ direct polarization (DP) NMR experiments were conducted at an MAS rate of 10 kHz for ZCNF and OCNF powders tightly packed in an 80 μL rotor (Fig. 1 and ESI† Fig. S3). It should be noted that to prove covalent grafting of the GTAMC to the OCNFs, excluding the hypothesis of ionic complexation between the negatively charged carboxyl group and the oppositely charged ammonium group, ^{13}C DP NMR spectra were collected for the freeze-dried powder before and after being thoroughly washed with acid solution (pH 2) and dialysed against DI water (Fig. 1 and ESI† Fig. S3). Relaxation delays of 200 (for 4096 scans) and 800 s (for 512 scans) were employed for the non-washed and washed ZCNF powder, respectively (Fig. 1 and ESI† Fig. S3). It should be noted that an 800 s recycle delay is sufficient for full relaxation of ^{13}C nuclei in cellulose samples.³³ All spectra were referenced with respect to TMS. The degree of cationic substitution (DS) of ZCNF was estimated using eqn (1).³⁴

$$\text{DS} = \frac{[\text{area of the methyl carbons resonance at 55 ppm}]}{3 \times (\text{area of C1 resonance at 105 ppm})} \quad (1)$$

Results and discussion

The amphoteric character of ZCNF was revealed by solid-state ^{13}C NMR and ζ -potential measurements. Quantitative solid-state ^{13}C NMR spectra confirmed the presence of the quaternary ammonium group on the ZCNFs (peak at 55 ppm),³⁴ and a DS (eqn (1)) of 23% was obtained (Fig. 1). In addition, comparison of the C4 chemical environments in the OCNF and ZCNF $^{13}\text{C}\{^1\text{H}\}$ DP NMR spectra (84 and 89 ppm for the amorphous and crystalline features, respectively³⁵) showed similar intensity

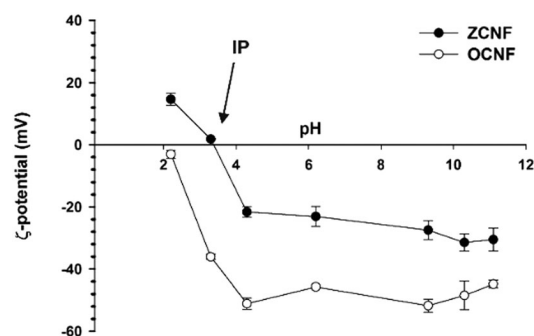


Fig. 2 The ζ -potential of ZCNF and OCNF dispersions as a function of pH. The average and standard deviation of values obtained for duplicate samples are reported.

peaks for the crystalline and amorphous components, indicating that no significant change was caused to the crystalline structure of ZCNF upon GTAMC functionalization (ESI† Fig. S3). $^{13}\text{C}\{^1\text{H}\}$ DP MAS NMR spectra of both OCNF and ZCNF showed the presence of the carboxyl group carbon atom at 175 ppm (ESI† Fig. S3).^{25,36} The $^{13}\text{C}\{^1\text{H}\}$ DP MAS NMR spectrum acquired with an 800 s relaxation delay (Fig. 1), in line with the previously reported estimate for the relaxation delay,³³ showed the same DS value as that obtained with a 200 s relaxation delay (ESI† Fig. S3).[‡]

The ζ -potential of ZCNF was measured across a wide pH range, from pH 2.2 to 11.1, and further compared with that of the precursor OCNF (Fig. 2). For the pH range investigated, the ζ -potential of ZCNF is confined between +30 and –30 mV. At pH < 3.3, the ZCNF dispersions show a positive ζ -potential, indicating that the positively charged ammonium group outweighs the charge contribution of the protonated carboxyl group. Conversely, at pH > 3.3, the net negative ζ -potential indicates that the negatively charged carboxyl group outweighs the positively charged ammonium group. The IP of ZCNF was estimated to be between pH 3.3 and 3.5. As previously reported, the ζ -potential of OCNF remains negative over the range of pH tested, approaching neutrality at pH values close to the pK_a of the carboxyl group.³⁷ The presence of oppositely charged moieties on the ZCNF surface strongly affected the stability of ZCNF aqueous dispersions at pH 6.8 upon addition of ionic and non-ionic surfactants. The stability of aqueous ZCNF dispersions was investigated upon addition of negatively charged SDS, positively charged DTAB and non-ionic TW80, referred to henceforth as ZCNF + SDS, ZCNF + DTAB and ZCNF + TW80, respectively. From visual observation, the 0.5 wt% ZCNF dispersions in the presence of 25 mM SDS, DTAB and TW80 showed different behaviours (Fig. 3a): 2 h after preparation, the ZCNF + DTAB dispersion shows similar turbidity to the ZCNF dispersion without surfactant, but ZCNF + SDS exhibits decreased turbidity, suggesting a noteworthy reduction in aggregate size. Although less

[‡] The DO of ca. 25% was obtained for OCNF by conductometric titration; however, titration was not considered a suitable method to calculate the DO of ZCNF due to the presence of oppositely charged moieties (ESI† Fig. S1 for conductometric titration of OCNF and ZCNF).

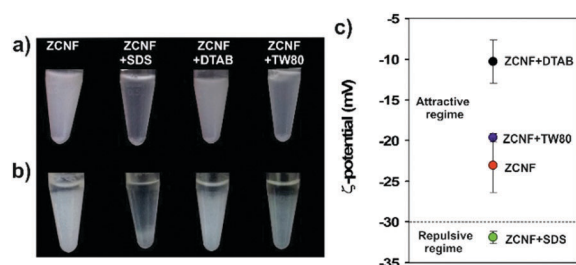


Fig. 3 Images of 0.5 wt% ZCNF dispersions upon addition of 25 mM SDS, 25 mM DTAB and 25 mM TW80 after (a) 2 hours and (b) 3 days after preparation. (c) The ζ -potential of ZCNF dispersions at 0.01 wt% upon addition of 25 mM SDS, 25 mM DTAB and 25 mM TW80 is presented as an average of measurements on duplicate samples.

pronounced than the case of ZCNF + SDS, the ZCNF + TW80 dispersion also shows a decrease in turbidity, suggesting the presence of smaller ZCNF aggregates following TW80 addition. After 3 days, all the dispersions show some sedimentation (Fig. 3b). The ZCNF + DTAB and ZCNF + TW80 samples show similar sedimentation to the surfactant-free dispersion, but the ZCNF + SDS sample shows a smaller quantity of more translucent sediment. Measurement of the particle surface charge has been used to investigate the electrostatic stabilization of CNF as a function of ionic strength,²³ pH,³⁷ and upon surfactant addition.³⁸ As such, the ζ -potential of ZCNF in the presence of 25 mM SDS, DTAB and TW80 was investigated (Fig. 3c).

The pure ZCNF dispersion has a ζ -potential of -23 mV, reflecting the net negative surface charge of the fibrils at pH 6.8. The ZCNF + SDS dispersion has a greater net negative surface charge compared to the pure ZCNF dispersion (-32 mV), indicating neutralization of the positively charged ZCNF moieties *via* electrostatic screening provided by the negatively charged SDS. In contrast, the ZCNF + DTAB dispersion shows a decrease in surface charge (-10 mV) due to screening of negatively charged ZCNF moieties by oppositely charged DTAB. Similarly, Hu *et al.* reported a decrease in the ζ -potential of negatively charged cellulose nanocrystals upon addition of positively charged surfactants.³⁹ It should be noted that for values of ζ -potential between ± 30 mV, attractive forces are dominant over the repulsive electrostatic forces, leading to flocculation and/or aggregation of the particles.⁴⁰ Thus, the ζ -potential measurements of the ZCNF dispersions suggest electrostatic stabilization upon SDS addition ($\zeta < -30$ mV) whereas a pronounced instability occurs upon DTAB addition ($-30 < \zeta < +30$ mV). Addition of neutral TW80 to the ZCNF dispersion results in an insignificant change in surface charge (-20 mV), as expected for the addition of a non-ionic surfactant, but non-electrostatic driven adsorption of TW80 onto the ZCNF surface could not be excluded by ζ -potential measurements.

In order to probe the non-electrostatic driven adsorption, surface tension measurements were performed. This experiment relies on the fact that the formation of a ZCNF–surfactant complex will exhibit different adsorption kinetics at the air–water interface compared to the individual components.

The γ_{aw} of the ZCNF dispersion did not deviate significantly from that of water (72 mN m^{-1} at 25°C), indicating a lack of

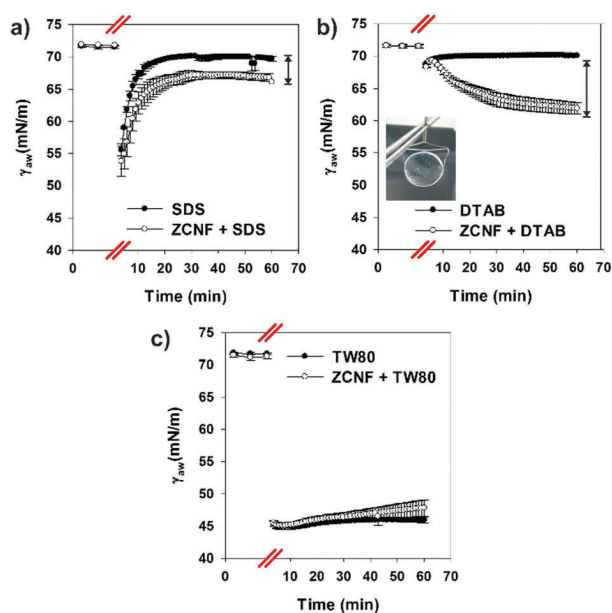


Fig. 4 Surface tension at the air–water interface (γ_{aw}) of 0.001 wt% ZCNF dispersions upon addition of (a) $125 \mu\text{M}$ SDS, (b) $125 \mu\text{M}$ DTAB and (c) $2.5 \mu\text{M}$ TW80. The breaks on the x axes indicate the addition of the surfactant to the dispersions. The average of duplicate measurements is reported. The insert in (b) shows the film formed in the Du Noüy ring at the end of the experiment.

surface active properties. Upon addition of SDS (dropwise at the air–water interface) to the ZCNF dispersion, the γ_{aw} decreases dramatically due to the direct addition of the surface active component at the air–water interface, which induces a surfactant and γ_{aw} gradient (Marangoni effect).¹⁰ Nevertheless, the concentration of surfactant distributed between the air–water interface and the bulk approaches equilibrium with time, reflected in the plateau of γ_{aw} versus time (Fig. 4). The γ_{aw} of ZCNF + SDS is significantly lower than the γ_{aw} of the pure surfactant in water. In agreement with ζ -potential measurements, this phenomenon suggests the formation of ZCNF–SDS complexes, which have greater surface activity compared to the individual ZCNF and SDS. The addition of DTAB to the ZCNF dispersion also leads to a distinct reduction in γ_{aw} compared to pure DTAB in water. The γ_{aw} of the ZCNF + DTAB dispersion does not reach equilibrium within 60 min and a thin film is slowly formed at the air–water interface (insert image Fig. 4b). This observation supports the hypothesis that the adsorption of the positively charged DTAB onto the negative moieties of ZCNF occurs, neutralising the charge, and rendering the particles more hydrophobic and thus likely to migrate to the air–water interface. Similar phenomena have been previously reported, for example, protein–gum arabic coacervates are more effective at reducing the γ_{aw} than the single components alone.⁴¹ Moreover, the slow change of γ_{aw} with time, for the ZCNF + DTAB dispersion, points to the presence of slowly migrating aggregates, compared to those occurring in the ZCNF + SDS dispersion, suggesting that larger aggregates are formed in this case. For the ZCNF + TW80 dispersion, the γ_{aw} lies within the standard deviation of the γ_{aw} of the pure surfactant, therefore, the hypothesis

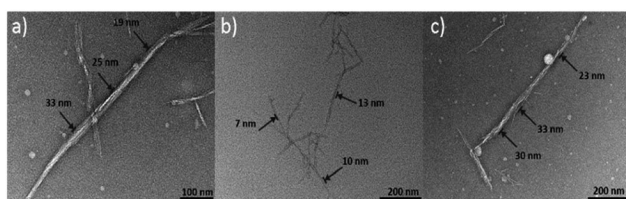


Fig. 5 TEM images of (a) 0.01 wt% ZCNF dispersion, (b) 0.01 wt% ZCNF with 50 mM SDS and (c) 0.01 wt% ZCNF with 50 mM DTAB. Arrows indicate the fibril or fibril aggregate diameters (nm).

of a non-electrostatically driven adsorption of TW80 onto ZCNF can be discarded.

In order to gain information about the shape, size and aggregation of the ZCNFs, TEM images were collected (Fig. 5). The ZCNF dispersion without surfactant shows a pronounced longitudinal fibril–fibril aggregation, resembling thick fibril-bundles with diameters of up to 30 nm, while the ZCNF + SDS dispersion shows individualised fibrils with diameters of ca. 5 nm, similar to the OCNF precursor of ZCNF.^{25,42,43}

The presence of individualized fibrils strongly suggests that SDS leads to defibrillation of the ZCNF bundles. The ZCNF + DTAB dispersion shows thick fibril-bundles, as observed for the ZCNF dispersion.

Overall, the TEM images agree with visual observation (Fig. 3) where thick fibril-bundles appear as more turbid dispersions compared to the translucent dispersions with SDS, reflecting individualized and well dispersed fibrils.

In order to gain information about the evolution of the ZCNF aggregates upon surfactant addition, the shear viscosity of 0.5 wt% ZCNF dispersions was measured at different SDS, DTAB and TW80 concentrations (Fig. 6). A significant reduction in η_r occurs even upon addition of 1 mM SDS, a concentration well below the surfactant CMC ($7 < \text{CMC} < 10 \text{ mM}^{30}$). A further decrease in η_r occurs upon addition of 25 mM SDS and the values of η_r remain similar up to 100 mM SDS, indicating that only a minimal quantity of SDS, between 1 and 25 mM, is needed to achieve a significant change in rheological properties. In contrast, the addition of different concentrations of DTAB (from 5 to 50 mM) and TW80 (from 10 to 100 mM) produces dispersions with similar rheological behaviour to the ZCNF alone dispersions.

The η_r of the 0.5 wt% ZCNF dispersions with 50 mM SDS, DTAB and TW80 were compared based on the severity of the shear thinning behaviour (Fig. 7a). A power law was fitted to the shear viscosity curves and the exponent, corresponding to the slope, was used as an indicator of the shear thinning intensity ($\eta_r \sim \text{shear rate}^m$). Upon addition of SDS, the ZCNF dispersion shows a clear transition from shear thinning to an almost shear independent fluid (with a slope change from -0.61 to -0.11) alongside a noteworthy decrease in η_r . These changes in the rheological properties of the ZCNF + SDS dispersion could be assigned to (i) the presence of individualized fibrils and/or thinner fibril-bundles, which easily follow the direction of the flow, supporting the defibrillation suggested by analysis of TEM images (Fig. 5) or (ii) the disruption of aggregates at shear rates below 25 s^{-1} . Conversely, the ZCNF + DTAB dispersion shows a more pronounced η_r decay upon

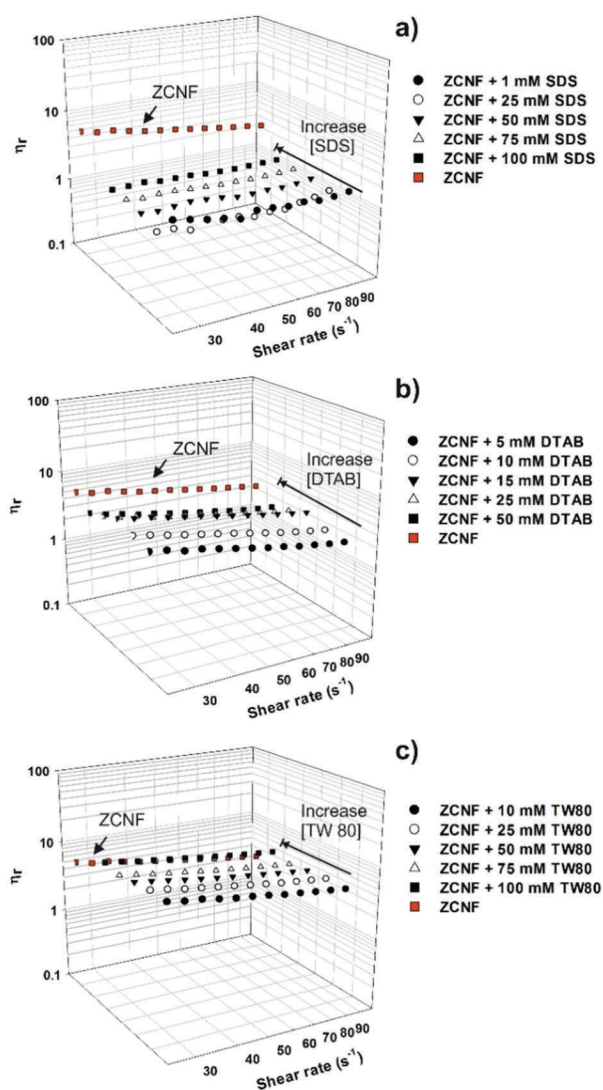


Fig. 6 Relative viscosity (η_r) as a function of shear rate (s^{-1}) for 0.5 wt% ZCNF dispersions containing (a) SDS, (b) DTAB and (c) TW80.

application of shear (slope = -0.71) than the ZCNF dispersion, indicating greater flocculation and the presence of aggregates that are readily disrupted by shear forces.⁴⁴ The ZCNF dispersion containing TW80 shows less pronounced shear thinning behaviour (slope = -0.50), suggesting less pronounced aggregation.⁴⁴

The weakly shear thinning behaviour of the 0.5 wt% ZCNF dispersion containing 50 mM SDS was qualitatively evaluated in terms of flow birefringence and compared to a dispersion of OCNF, the ZCNF precursor, as a positive control. Many studies have shown birefringence in cellulose dispersions and ascribed this phenomenon to the presence of nematic self-ordering of the fibrils.^{18,26,42,45} The 0.5 wt% ZCNF + SDS dispersion shows no flow induced birefringence, in contrast to the OCNF dispersion. Therefore, no flow induced alignment of ZCNF occurs in the presence of SDS, while a nematic self-ordering of the fibrils is observed for the OCNF dispersion, as previously reported.⁴⁵

The absence of flow induced self-ordering of the ZCNF + SDS dispersion could be ascribed to the presence of free micelles,

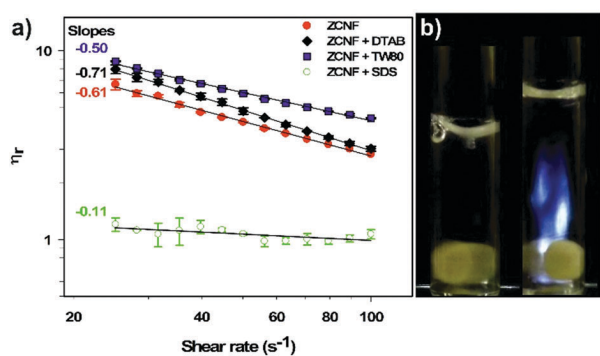


Fig. 7 (a) Relative viscosity (η_r) as a function of the shear rate for 0.5 wt% ZCNF containing 50 mM SDS, 50 mM DTAB and 50 mM TW80. The gradients of the curves (indicated to the left of the curves) are calculated from the values of the exponent of a power law fitting (black line). (b) Flow induced birefringence for a 0.5 wt% ZCNF dispersion containing 50 mM SDS (left) compared to 0.5 wt% OCNF (right). The stirred dispersions were photographed between two crossed polarised filters.

leading to steric hindrance, as well as weak hydrophobic interactions between the surfactant tails ionically grafted onto the ZCNF surface. Similar to the ZCNF + SDS dispersion, the pure ZCNF, ZCNF + DTAB and ZCNF + TW80 dispersions exhibited no flow induced birefringence.

SANS analysis provides non-invasive sample measurements, a good statistical overview and the ability to highlight only the ZCNF structure, by contrast matching the surfactant (d-SDS, d-DTAB) to the solvent (D_2O). Thus, analysis of SANS data provided the opportunity to compare the aggregation states of ZCNF in the presence of both SDS and DTAB. Data were collected for ZCNF + SDS and ZCNF + DTAB dispersions at surfactant concentrations of 1 and 5 mM, respectively. These concentrations were chosen in order to match the lowest surfactant concentrations used in this study. (As d-TW80 is not readily available, contrast matching experiments (surfactant-solvent) with this surfactant were not possible.)

None of the ZCNF dispersions, with or without surfactant, showed the presence of a Guinier region, indicating that the largest dimension of the fibril, the length, is not fully probed within the q -range used (Fig. 8). The minimum q probed is 0.005 \AA^{-1} , thus only features below 125 nm ($2\pi/q_{\min}$) in size are detected in this experiment. The best data fitting, for all the dispersions, was obtained using the model of flexible cylinders with an elliptical cross section based on the wormlike micelle model.³² In this fitting, the parameter b_{Kuhn} is descriptive of the polymer flexibility; the smaller the b_{Kuhn} , the more flexible the polymer. However, for particles, such as ZCNF, this definition of b_{Kuhn} is not necessarily the most appropriate. The values of b_{Kuhn} described from fitting a semi-flexible cylinder model could suggest a convolution of parameters such as mesh size and entanglement length rather than flexibility of the fibrils. The b_{Kuhn} values of the ZCNF and ZCNF + DTAB dispersions are similar (Table 1), while for the ZCNF + SDS dispersions, b_{Kuhn} approaches a value similar to L_c (hence fixed at 1000 nm, Table 1), indicating that the fibrils behave like isolated rigid rods, further supporting the non-interacting behaviour suggested from measurements of relative viscosity. The fitting parameter associated with the elliptical

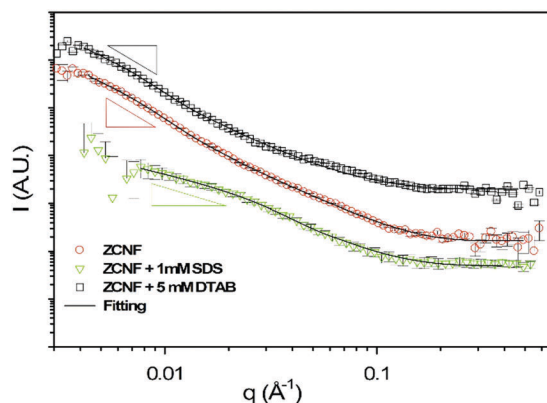


Fig. 8 SANS data for 0.5 wt% ZCNF dispersions in the presence of 1 mM d-SDS and 5 mM d-DTAB in D_2O . The black line corresponds to a model of a flexible cylinder with an elliptical cross section used to fit the data. The intensity (I) is shown in arbitrary units (A.U.). Triangles are shown to indicate the power law decay at low- q .

Table 1 Values of the parameters derived from fitting of SANS data for ZCNF and ZCNF plus d-SDS and d-DTAB, 1 and 5 mM, respectively, in D_2O . Data were fitted using a model of a flexible cylinder with an elliptical cross section

	r_{maj} (nm)	b_{Kuhn} (nm)	χ^2	D_m^b
ZCNF	27.9 ± 0.4	19.4 ± 0.2	2.1	2.6 ± 0.1
ZCNF + 1 mM SDS	7.51 ± 0.1	1000 ^a	2.7	1.3 ± 0.4
ZCNF + 5 mM DTAB	27.9 ± 0.5	23.8 ± 0.3	5.2	2.6 ± 0.1

^a b_{Kuhn} was fixed to the value of L_c . ^b D_m was calculated in the q -range $0.005\text{--}0.018 \text{ \AA}^{-1}$ for ZCNF and ZCNF + 5 mM DTAB, whereas it was $0.008\text{--}0.018 \text{ \AA}^{-1}$ for ZCNF + 1 mM SDS.

cross section, r_{maj} , is in agreement with the diameters obtained from measurements of the TEM images (Fig. 5). The power law decay at low- q indicates the fractal-like aggregation of the ZCNFs and the slope indicates the fractal dimension, D_m (Fig. 8).^{46,47} The ZCNF and the ZCNF + DTAB dispersions both yield a value of $D_m = 2.6 \pm 0.1$, indicative of dense aggregates. Similar to values derived from small angle X-ray scattering (SAXS)⁴⁸ and SANS⁴⁹ analysis of OCNF dispersions in the absence of surfactant, the ZCNF + SDS dispersion data give $D_m = 1.3 \pm 0.4$, indicative of open and less dense aggregates.⁴⁷ From the diffusion limited and reaction limited aggregation models, D_m would be expected to decrease with the increase of the net surface charge, due to the higher number of collisions needed to form the aggregates, until electrostatic stabilization is reached.⁵⁰ Therefore, the smaller value of D_m for ZCNF + SDS suggests that the ZCNF dispersion undergoes a transition from an unstable to a stable regime upon SDS addition. Overall, the difference in D_m between dispersions is in agreement with previous results, where dense ZCNF aggregates show pronounced turbidity, poor stability, and severe shear thinning behaviour compared to the open and less dense aggregates formed upon SDS addition.

Conclusion

The zwitterionic nature of ZCNF leads to the formation of fibril-bundles that further self-assemble into dense aggregates,

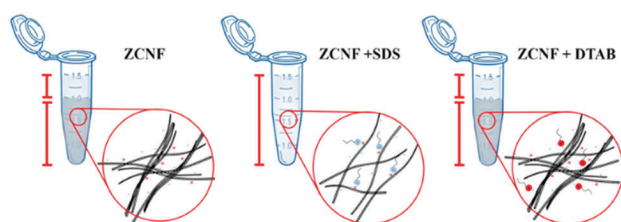


Fig. 9 Schematic of ZCNF dispersions alone and in the presence of negatively charged SDS and positively charged DTAB.

reflected in the fractal dimension $D_m = 2.6$, due to attractive electrostatic forces. Addition of negatively charged SDS to the ZCNF dispersion results in electrostatic complexation between SDS and the positively charged moieties present on ZCNF. The ZCNF–SDS complexes lead to electrostatically stabilized dispersions ($\zeta < -30$ mV), leading to the individualization of fibrils, which form less turbid, more stable, less viscous and weakly shear thinning dispersions (Fig. 9). Upon DTAB addition, the ZCNF negative charge is partially screened due to ZCNF–DTAB complex formation leading to greater charge symmetry ($\zeta = -10$ mV), usually associated with the formation of flocculated aggregates.¹¹ The more strongly flocculated nature of the DTAB containing dispersion is evidenced by the greater magnitude of the shear thinning behaviour (slope of the η_r curve). Moreover, the similarity in the scattering pattern between the ZCNF and DTAB containing dispersions indicates that the fibril-bundles assemble in a similar fashion. The addition of non-ionic TW80 to ZCNF leads to more translucent and less shear thinning dispersions, as expected for more stable, less flocculated, dispersions.⁴⁴ Therefore, the presence of free TW80 in the dispersion and the enhanced stabilization of ZCNF suggest a mechanism of depletion stabilization induced by the non-adsorbed TW80. Although still a topic of some debate, the depletion stabilization mechanism according to Fler and Vincent occurs at polymer concentrations beyond the polymer concentration required to induce depletion flocculation and is ascribed to the gain in configurational entropy of the particles over the osmotic attractive energy caused by the depletion layer.^{16,51} Nevertheless, it should be noted that the concentration threshold for a change between the depletion flocculation to depletion stabilization mechanism in ZCNF suspensions was not observed within the concentration range of TW80 investigated, probably due to its low CMC (12 μM).³⁰

Conflicts of interest

The authors declare no conflicts of interest.

Acknowledgements

The authors thank the EPSRC for funding this project (grant numbers EP/N033310/1 and EP/N033337/1). V. Calabrese thanks the University of Bath and V. Gabrielli thanks the BBSRC (BB/M011216/1) for PhD studentship funding. The authors would like to thank the ISIS Neutron and Muon Source for the award of

beam time (experiment no. RB1710159) and Dr N. Mahmoudi for assistance with the experiment on beamline SANS2D. We acknowledge the ISIS Deuteration Facility for provision of deuterated surfactants. TEM images were obtained at the Microscopy and Analysis Suite in Bath University with the assistance of Ursula Potter. This work benefited from the use of the SasView application, originally developed under the NSF award DMR-0520547. SasView contains code developed with funding from the European Union's Horizon 2020 research and innovation programme under the SINE2020 project, grant agreement No. 654000. Data supporting this article have been made freely available *via* the University of Bath Research Data Archive system at DOI: 10.15125/BATH-00538 and *via* the University of East Anglia Data Archive at [https://people.uea.ac.uk/en/datasets/data-for-surfactant-controlled-zwitterionic-cellulose-nanofibril-dispersions\(3c7b2b6e-42ee-41f5-bb95-97aece16ce6\).html](https://people.uea.ac.uk/en/datasets/data-for-surfactant-controlled-zwitterionic-cellulose-nanofibril-dispersions(3c7b2b6e-42ee-41f5-bb95-97aece16ce6).html).

References

- 1 V. Gold, *Compend. Chem. Terminol.*, IUPAC, 2014, pp. 1622–1622.
- 2 S. Kudaibergenov and A. Ciferri, *Macromol. Rapid Commun.*, 2007, **28**, 1953–1968.
- 3 A. Venault, W. Y. Huang, S. W. Hsiao, A. Chinnathambi, S. A. Alharbi, H. Chen, J. Zheng and Y. Chang, *Langmuir*, 2016, **32**, 4113–4124.
- 4 P. Liu, Q. Chen, L. Li, S. Lin and J. Shen, *J. Mater. Chem. B*, 2014, **2**, 7222–7231.
- 5 R. Yang, H. Jang, R. Stocker and K. K. Gleason, *Adv. Mater.*, 2014, **26**, 1711–1718.
- 6 T. Elschner, C. Lüdecke, D. Kalden, M. Roth, B. Löffler, K. D. Jandt and T. Heinze, *Macromol. Biosci.*, 2016, **16**, 522–534.
- 7 S. Liu, J. Liu, A. R. Esker and K. J. Edgar, *Biomacromolecules*, 2016, **17**, 503–513.
- 8 P. Trivedi, J. Trygg, T. Saloranta and P. Fardim, *Cellulose*, 2016, **23**, 1751–1761.
- 9 P. Zhang, F. Sun, C. Tsao, S. Liu, P. Jain, A. Sinclair, H.-C. Hung, T. Bai, K. Wu and S. Jiang, *Proc. Natl. Acad. Sci. U. S. A.*, 2015, **112**, 12046–12051.
- 10 P. Walstra, *Physical Chemistry of Foods*, CRC Press, 2004, pp. 182–221.
- 11 M. A. Dyakonova, N. Stavrouli, M. T. Popescu, K. Kyriakos, I. Grillo, M. Philipp, S. Jaksch, C. Tsitsilianis and C. M. Papadakis, *Macromolecules*, 2014, **47**, 7561–7572.
- 12 M. A. Dyakonova, A. V. Berezkin, K. Kyriakos, S. Gkermpoura, M. T. Popescu, S. K. Filippov, P. Štěpánek, Z. Di, C. Tsitsilianis and C. M. Papadakis, *Macromolecules*, 2015, **48**, 8177–8189.
- 13 R. M. Kramer, V. R. Shende, N. Motl, C. N. Pace and J. M. Scholtz, *Biophys. J.*, 2012, **102**, 1907–1915.
- 14 X. Zhang, M. R. Servos and J. Liu, *J. Am. Chem. Soc.*, 2012, **134**, 9910–9913.
- 15 S. Kim, K. Hyun, J. Y. Moon, C. Clasen and K. H. Ahn, *Langmuir*, 2015, **31**, 1892–1900.
- 16 G. J. Fler, J. H. M. H. Schetjens and B. Vincent, *ACS Symposium Series*, American Chemical Society, 1984, vol. 240, pp. 245–263.

- 17 D. da Silva Perez, S. Montanari and M. R. Vignon, *Biomacromolecules*, 2003, **4**, 1417–1425.
- 18 T. Saito, T. Uematsu, S. Kimura, T. Enomae and A. Isogai, *Soft Matter*, 2011, **7**, 8804–8809.
- 19 S. Tsuguyuki and A. Isogai, *Biomacromolecules*, 2004, **5**, 1983–1989.
- 20 J. C. Courtenay, M. A. Johns, F. Galembeck, C. Deneke, E. M. Lanzoni, C. A. Costa, J. L. Scott and R. I. Sharma, *Cellulose*, 2016, **24**, 253–267.
- 21 M. Zaman, H. Xiao, F. Chibante and Y. Ni, *Carbohydr. Polym.*, 2012, **89**, 163–170.
- 22 Y. Okita, T. Saito and A. Isogai, *Biomacromolecules*, 2010, **11**, 1696–1700.
- 23 H. Fukuzumi, R. Tanaka, T. Saito and A. Isogai, *Cellulose*, 2014, **21**, 1553–1559.
- 24 A. Isogai, T. Saito and H. Fukuzumi, *Nanoscale*, 2011, **3**, 71–85.
- 25 R. J. Crawford, K. J. Edler, S. Lindhoud, J. L. Scott and G. Unali, *Green Chem.*, 2012, **14**, 300–303.
- 26 M. Hasani, E. D. Cranston, G. Westman and D. G. Gray, *Soft Matter*, 2008, **4**, 2238–2244.
- 27 J. C. Courtenay, S. M. Ramalhete, W. J. Skuze, R. Soni, Y. Z. Khimyak, K. J. Edler and J. L. Scott, *Soft Matter*, 2018, **14**, 255–263.
- 28 T. Saito, Y. Nishiyama, J. L. Putaux, M. Vignon and A. Isogai, *Biomacromolecules*, 2006, **7**, 1687–1691.
- 29 M. A. Bahri, M. Hoebeke, A. Grammenos, L. Delanaye, N. Vandewalle and A. Seret, *Colloids Surf., A*, 2006, **290**, 206–212.
- 30 D. Linke, *Detergents. An Overview*, Elsevier Inc., 1st edn, 2009, ch. 34, vol. 463.
- 31 <http://www.sasview.org/contact.html>.
- 32 J. S. Pedersen and P. Schurtenberger, *Macromolecules*, 1996, **29**, 7602–7612.
- 33 K. Wickholm, P. T. Larsson and T. Iversen, *Carbohydr. Res.*, 1998, **312**, 123–129.
- 34 H. Kono, K. Ogasawara, R. Kusumoto, K. Oshima, H. Hashimoto and Y. Shimizu, *Carbohydr. Polym.*, 2016, **152**, 170–180.
- 35 D. L. VanderHart and R. H. Atalla, *Macromolecules*, 1984, **17**, 1465–1472.
- 36 C. Tahiri and M. R. Vignon, *Cellulose*, 2000, **7**, 177–188.
- 37 A. B. Fall, S. B. Lindstrom, O. Sundman, L. Sundman and L. W. Odberg, *Langmuir*, 2011, **27**, 11332–11338.
- 38 N. Quennouz, S. M. Hashmi, H. S. Choi, J. W. Kim and C. O. Osuji, *Soft Matter*, 2015, **12**, 157–164.
- 39 Z. Hu, S. Ballinger, R. Pelton and E. D. Cranston, *J. Colloid Interface Sci.*, 2015, **439**, 139–148.
- 40 L. L. Schramm, *Advances in chemistry*, 1996, vol. 251, pp. 21–22.
- 41 V. Duclé, J. Richard, Y. Popineau and F. Boury, *Biomacromolecules*, 2005, **6**, 790–796.
- 42 Y. Habibi, H. Chanzy and M. R. Vignon, *Cellulose*, 2006, **13**, 679–687.
- 43 T. Saito, S. Kimura, Y. Nishiyama and A. Isogai, *Biomacromolecules*, 2007, **8**, 2485–2491.
- 44 A. L. Ogden and J. A. Lewis, *Langmuir*, 1996, **7463**, 3413–3424.
- 45 R. K. Johnson, A. Zink-Sharp and W. G. Glasser, *Cellulose*, 2011, **18**, 1599–1609.
- 46 F. Cherhal, F. Cousin and I. Capron, *Langmuir*, 2015, **31**, 5596–5602.
- 47 B. Hammouda, *Probing Nanoscale Structures – The SANS toolbox*, National Institute of Standards and Technology Center for Neutron Research Gaithersburg, 2010, pp. 211–225.
- 48 Y. Su, C. Burger, B. S. Hsiao and B. Chu, *J. Appl. Crystallogr.*, 2014, **47**, 788–798.
- 49 Y. Mao, K. Liu, C. Zhan, L. Geng, B. Chu and B. S. Hsiao, *J. Phys. Chem. B*, 2017, **121**, 1340–1351.
- 50 S. Lazzari, L. Nicoud, B. Jaquet, M. Lattuada and M. Morbidelli, *Adv. Colloid Interface Sci.*, 2016, **235**, 1–13.
- 51 J. Peng, A. Kroes-Nijboer, P. Venema and E. van der Linden, *Soft Matter*, 2016, **12**, 3514.

CHAPTER 5

FILLER SIZE EFFECT IN AN ATTRACTIVE FIBRILLATED NETWORK: A STRUCTURAL AND RHEOLOGICAL PERSPECTIVE

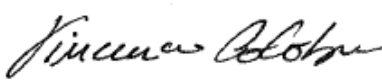
Following on from Chapter 4, we now describe how the addition of non-interacting colloidal particles, referred to as fillers, influence the mechanical properties of oxidised cellulose nanofibrils (OCNF)-based gels. In Chapter 4 we focused on the attractive electrostatic interactions between additives and zwitterionic cellulose nanofibrils (ZCNF) as a driving factor for tuning rheological properties of the dispersion. Contrarily, in the following Chapter we avoid strong filler-OCNF interactions and focus on the physical hindrance that the fillers impart to the OCNF network during breakage of the hydrogel (yielding). In this manner, it is possible to preserve the charge accessibility of OCNF for other reactions, as further described in Chapter 6, whilst tuning the rheological properties of the hydrogels. Although the literature regarding the rheological properties of cellulose-based hydrogels containing additives such as polymers^[52–54,57,58,162] and surfactants^[38,46–50] is vast, there is a current lack of knowledge on how colloidal fillers can be used as rheological modifiers. According to the work presented in the following Chapter, this may be justified by the fact that non-interacting fillers are not efficient rheological modifiers in terms of strengthening the gel. However, non-interacting fillers are efficient in modifying other rheological phenomena occurring at larger deformations such as yielding and flow. The in-depth investigation of these phenomena using oscillatory rheology is often avoided due to the lack of a common framework of analysis, although several have been proposed.^[103,104,128] Since commercial formulations are inevitably exposed to large deformations during industrial processing or customer usage, the understanding of the material response upon large deformations is essential. Furthermore, the rheological properties exhibited upon large deformations has only been recently linked with consumer appreciation.^[163]

On this ground, this study aims to understand how a non-interacting filler with two different sizes (a dimension similar and greater compared to the mesh size of the OCNF network) affect the mechanical properties of the hydrogel. Specifically, we use silica nanoparticles (SiNp) as non-interacting fillers. SiNp are broadly used to control the rheological properties of pastes and its use is approved as a food (E551) and animal ingredient.^[164] A recent study showed that common SiNp particles used in commercial products have dimensions in the nanoscale range similar to the ones used in the following study.^[164] A second reason directing us to use SiNp is that SiNp have been broadly studied, therefore, insights regarding their phase behaviour as a function of concentration and ionic strength are known.^[165–167] The SiNp phase behaviour is case-dependent, but in general follows a transition from stable dispersion to settling gels to

single-phase gels, upon the increase of the SiNp concentration.^[165] An increase of ionic strength has also been shown to promote aggregation and gelation of SiNp.^[165-167] However, to induce the sol-to-gel transition, longer time scales (hours to weeks) and NaCl concentrations typically above 1 wt% are required.^[165,166]

In this work, we demonstrate that, for non-interacting fillers, the filler-to-mesh size ratio is pivotal for tailoring the non-linear mechanical properties of the gel such as yielding and flow. The fundamental understanding provided in this Chapter contributes to industrially relevant information since the addition of fillers with different size, in a fibrillar matrix, can be used as a simple strategy to achieve specific mechanical properties.

Supporting information available in section 10.3.

This declaration concerns the article entitled:									
Filler size effect in an attractive fibrillated network: a structural and rheological perspective									
Publication status (tick one)									
draft manuscript	<input type="checkbox"/>	Submitted	<input checked="" type="checkbox"/>	In review	<input type="checkbox"/>	Accepted	<input type="checkbox"/>	Published	<input type="checkbox"/>
Publication details									
Candidate's contribution to the paper (detailed, and also given as a percentage).	<p>The candidate contributed to/ considerably contributed to/predominantly executed the...</p> <p>Formulation of ideas: -The initial idea was formulated by VC. 90%</p> <p>Design of methodology: -All the measurements were designed by VC with help of KJE, and MAS for the SANS experiment. 90%</p> <p>Experimental work: - The experimental work was conducted by VC (90%) and LP (10% who received the ready to be measured samples). - The data analysis was conducted by VC (100%).</p> <p>Presentation of data in journal format: -The first draft was written by VC with contribution of MAS, SB, KZH, JL and KJE. Subsequent drafts were reworked by VC following feedback from the authors. 90%</p>								
Statement from Candidate	This paper reports on original research I conducted during the period of my Higher Degree by Research candidature.								
Signed						Date	13/12/19		

Filler size effect in an attractive fibrillated network: a structural and rheological perspective

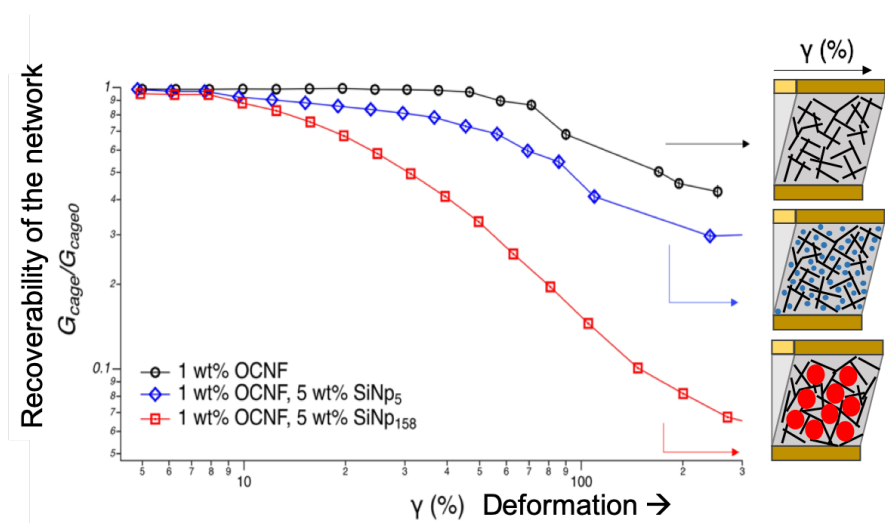
Vincenzo Calabrese,^{a*} Marcelo A. da Silva,^a Lionel Porcar,^b Saffron Bryant,^a

Kazi M. Zakir Hossain,^a Janet L. Scott,^{a,c} Karen J. Edler^{a*}

^a Department of Chemistry, University of Bath, Claverton Down, Bath, BA2 7AY, United Kingdom

^b Institut Laue-Langevin, 71 avenue des Martyrs, CS 20156, 38042 Grenoble cedex 9, France

^c Centre for Sustainable Chemical Technologies, University of Bath, Claverton Down, Bath, BA2 7AY, United Kingdom



Keywords: fibrillar network, hydrogel, filler, breakage mechanic.

Abstract

The effect of the filler size on the structural and mechanical properties of an attractive fibrillated network composed of oxidised cellulose nanofibrils (OCNF) in water was investigated. Silica nanoparticles, SiNp₅ and SiNp₁₅₈ which were ≈ 5 and ≈ 158 nm diameter, respectively, were chosen to be of a similar and a greater dimension of the network mesh size. Contrast matched Small Angle Neutron Scattering (SANS) experiments revealed that the presence of the fillers (SiNp₅ and SiNp₁₅₈) did not perturb the structural properties of the OCNF network at the nm-length scale. However, the filler size difference strongly affected the mechanical properties of the hydrogel upon large amplitude oscillatory shear. The presence of the smaller filler, SiNp₅, preserved the mechanical properties of the hydrogels while the larger filler, SiNp₁₅₈, allowed a smoother breakage of the network and low network recoverability after breakage. This study, show that the filler-to-mesh size ratio, for non-interacting fillers, is pivotal for tailoring the non-linear mechanical properties of the gel such as yielding and flow.

Introduction

The growing need for sustainable materials has promoted interest in the use of cellulose nanofibrils (CNF) as building blocks for renewable products. CNF belong to the colloidal domain and are usually characterized by a radius in the order of few nm and a length of 100-1000 nm depending on the preparation methods and source.¹ TEMPO-mediated oxidation of cellulose has been, for instance, a successful route for the production of oxidised cellulose nanofibrils (OCNF) on a large scale.^{2,3} Importantly, the carboxylate groups on the OCNF surface yield a surface negative charge which allows the preparation of stable aqueous dispersions.² Interfibrillar repulsive/attractive forces have been reported to be strongly dependent on the pH⁴ and ionic strength⁵⁻⁷ of the aqueous media.⁸ Charge screening due to counterion binding to the carboxylate group has been shown to be an effective gelation mechanism.^{5,7} Structural investigation of OCNF dispersions, via small angle X-ray scattering, revealed that, for concentrations above the overlap threshold,⁹ a clear transition from a repulsive to an attractive fibrillated network occurs upon increasing ionic strength.⁷ This finding is directly related to the sol-gel transition⁷ and to the theoretical expectations based on the Derjaguin–Landau–Verwey–Overbeek (DLVO) for two crossed cylindrical rods.⁵

To broaden the understanding of interfibrillar assembly in systems closer to industrially relevant scenarios, the use of additives, such as surfactant^{9,10} and polymers,^{11,12} in CNP-based hydrogels has

been explored.¹ Nevertheless, knowledge of the interplay between non-interacting colloidal fillers and a fibrillated network is lacking. The filler surface chemistry, size and volume fraction have been mainly investigated in protein-based hydrogels and referred to as “active” or “inactive” fillers based on their ability to strengthen or weaken the gel, respectively.^{13–15} In principle, fillers could be employed to modulate other mechanical properties such as structural breakage (yielding), flow, structural recoverability and plasticity; important parameters to account for processing operations and/or customer appreciation.¹⁶ Such mechanical properties often occur upon large deformations and high shear rates, where the mechanical response of the material depends on the applied strain and shear rate, identified as non-linear viscoelastic region (NLVR).

On this ground, we investigated the filler size effect on the linear and non-linear viscoelastic response of an attractive fibrillated network composed of OCNF. The interfibrillar attractive forces were promoted *via* addition of 100 mM NaCl, leading to an OCNF network with a mesh size, defined as the average distance between the nearest fibrillar junction zones, of 20–40 nm as recently reported by our group.⁷ Silica nanoparticles (SiNp) with an average dimension similar to the mesh size of the network and a SiNp larger (*ca.* by a factor of 5) than the network mesh size were chosen as non-interacting fillers in the OCNF-based gel. We show that the filler-to-mesh size ratio, for non-interacting fillers, is of pivotal importance for tailoring non-linear mechanical properties of the gel such as yielding and flow.

Materials and methods

An OCNF dispersion was prepared as previously described,¹⁷ using a TEMPO/NaOCl/NaBr oxidation.² A 2 wt% OCNF stock was re-dispersed from freeze-dried OCNF in ultrapure deionised (DI) water (18.2 M Ω ·cm) and stirred overnight, followed by a mild sonication process (Ultrasonic Processor FB-505, Fisher, 200 W·cm⁻², equipped with a 1 cm probe, using a series of 1 s on 1 s off in pulse mode for a net time of 120 s at 30% amplitude on *ca.* 45 mL dispersion contained in an ice bath). A 10 wt% SiNp₁₅₈ dispersion was prepared dispersing silica nanopowder (718483 Sigma Aldrich®) in ultrapure DI water (18.2 M Ω ·cm) followed by sonication (as for the OCNF indicated above) and used without further treatment. A *ca.* 9 wt% aqueous SiNp₅ dispersion, provided by Geo40™ (sodium stabilised Colloidal silica of geothermal origin), was dialysed using cellulose dialysis tubing (Sigma-Aldrich® cellulose dialysis tubing, molecular weight cut-off of 12,400 Da) against DI water for 3 days, refreshing the DI water twice per day. The dialysed SiNp₅ dispersion was pH adjusted to 7 using HCl (aq) and further dialysed against DI water, as previously described. Larger aggregates were removed

using a syringe filter unit with a cut-off size of 0.22 μm (Millex®-GS) and the solid content (wt%) of the filtered dispersion obtained gravimetrically. Specific OCNF, OCNF-SiNp₅ and OCNF-SiNp₁₅₈ concentrations were obtained via dilution of the stock dispersions described above, except where otherwise stated, followed by the addition of a 2 M NaCl solution to achieve a final NaCl concentration of 100 mM in all samples.

Small angle X-ray scattering (SAXS) measurements were performed on an Anton-Paar SAXSpoint 2.0 equipped with a copper source (Cu K- α , $\lambda=1.542 \text{ \AA}$) and a 2D EIGER R series Hybrid Photon Counting (HPC) detector. The sample-to-detector distance was 556 mm covering a q range of about $0.01 < q < 0.4 \text{ \AA}^{-1}$. Samples were loaded into 1 mm quartz capillaries and the scattering intensity collected in three frames, with 300 s exposure per frame. Temperature was kept at 25 °C via a Peltier unit ($\pm 0.1 \text{ }^\circ\text{C}$).

SANS experiments were conducted at the Institut Laue–Langevin (Grenoble, France) on the D22 SANS beamline using a wavelength of 6 \AA and a sample-to-detector distance of 2.8 and 17.6 m to yield a q -range of $0.003 < q < 0.4 \text{ \AA}^{-1}$. Temperature was kept at 25 °C via a Julabo circulating waterbath ($\pm 0.5 \text{ }^\circ\text{C}$). Particles which have the same scattering length density (SLD) as the continuous phase do not contribute to the scattering intensity ($I(q) = 0$) and they are said to be contrast matched.¹⁸ We determined the contrast match point of the SiNp particles, using different H₂O/D₂O ratios as the continuous phase. This is possible due to the different SLD between H₂O ($-0.5 \times 10^{-6} \text{ \AA}^{-2}$) and D₂O ($6.3 \times 10^{-6} \text{ \AA}^{-2}$) which allow tuning of the SLD of the continuous phase upon changing H₂O/D₂O ratios. Samples were prepared with a continuous phase composed of 60 vol% D₂O (99.9 atom % D, Sigma Aldrich®) and 40 vol% H₂O (DI water) which was experimentally determined to be the contrast match point for SiNp (Fig. S1) in agreement to what was previously reported.¹⁹ For this experiment, OCNF, OCNF-SiNp₅ and OCNF-SiNp₁₅₈ concentrations were obtained via dilution of a 2 wt% freeze-dried OCNF dispersed in pure D₂O (prepared as previously described) and SiNp stock dispersions described above (SiNp₅ and SiNp₁₅₈ (in H₂O)) with the required amount of H₂O/D₂O followed by the addition of a 2 M NaCl solution (in H₂O) to achieve a final NaCl concentration of 100 mM in all samples. Samples were measured in 2 cm wide optical quartz cells with 1 mm path-length. For SAXS and SANS measurements background subtraction and data treatment were performed using the Irena package²⁰ whilst data analysis was done using the NIST SANS Analysis package (models were used without further modification),²¹ both within IGOR Pro (Wavemetrics, Inc.).

Dynamic light scattering (DLS) was performed on diluted samples (0.01 wt% in 100 mM NaCl) using a Malvern Zetasizer Nano ZSP® (Malvern, UK). The samples were loaded in disposable polystyrene cells with a path length of 1 cm and measured as an average of 4 measurements from 100 scans each. The values are reported as normalised intensity and obtained from the average of three separate samples. Temperature was kept at 25 °C via a Peltier unit (± 0.1 °C).

The rheological measurements of the OCNF-based hydrogels were performed using a stress-controlled rheometer (Discovery HR3, TA instruments®) equipped with a sandblasted plate-plate geometry (40 mm). To avoid evaporation, the edge of the samples was covered with low viscosity mineral oil and further covered with a solvent trap to ensure constant temperature within the chamber (25 °C via a Peltier unit (± 0.1 °C)). After loading, the gel was exposed as following to *i*) 30 s pre-shear at 300 s^{-1} to ensure equal sample history, *ii*) time sweep employing small amplitudes ($\gamma = 0.05$ (%)) at constant angular frequency, $\omega = 1\text{ rad s}^{-1}$, for 50×10^3 s, *iii*) frequency sweep at constant strain $\gamma = 0.1$ %, being in the linear viscoelastic region (LVR) (Fig. S2) and *iv*) strain sweep at constant $\omega = 1\text{ rad s}^{-1}$. The storage and loss modulus, G' and G'' respectively, were computed by the TRIOS software and used to obtain the complex modulus $G^* = \sqrt{(G')^2 + (G'')^2}$, and $\tan\delta = G''/G'$. For *iv*), raw data were acquired as stress (σ) as function of intracycle shear rate $\dot{\gamma}$ (s^{-1}) and the intracycle strain (γ_0).

Results and discussion

Gelation of the 1 wt% OCNF was achieved upon addition of NaCl (100 mM), resulting in an attractive fibrillated network with a defined mesh size of 20-40 nm.⁷ Silica nanoparticles, with a dimension similar and greater than the mesh size of the network were incorporated in the 1 wt% OCNF gel and their effect on structural and mechanical properties of the OCNF-based gel investigated. At first, the filler sizes were evaluated via SAXS using conditions of ionic strength which induce gelation of OCNF (Fig. 1a). Contrarily to SiNp₁₅₈, the SiNp₅ displayed an approaching plateau at low- q , indicating that the characteristic size of the object is probed (radius of gyration). The data of the SiNp₅ were fitted to a model of spheres with a log-normal size distribution, yielding a particle mean size of 5.2 ± 0.2 nm and a size distribution as shown in Fig. 1b. Since SAXS measurements did not access the larger size of SiNp₁₅₈, DLS measurements were used to determine the hydrodynamic size of the particles (Fig. 1b). This accounts for the hydration shell of the particles which is expected to be in the order of few nm at this ionic strength. Overall, SiNp₁₅₈ displayed a greater mean size (158.0 ± 1.3 nm) and a narrower size distribution compared to SiNp₅.

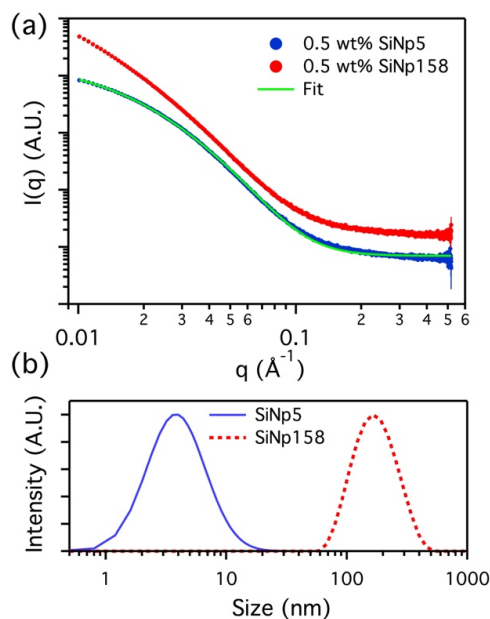


Fig. 1 (a) SAXS patterns for the 0.5 wt% SiNp₅ and SiNp₁₅₈ dispersions in 100 mM NaCl. A fit of spheres with log-normal size distribution is shown for SiNp₅. (b) Size distribution of 0.5 wt% SiNp₅, as obtained by the SAXS fitting in (a), and of 0.01 wt% SiNp₁₅₈, obtained via DLS, dispersions in 100 mM NaCl.

To explore the effect of the filler on the structural properties of the OCNF network, SANS measurements were performed under conditions where the SiNp scattering contribution was matched to the solvent. This results in a dominant OCNF scattering intensity, allowing us to probe, solely, the structural properties of the OCNF network in the presence of SiNp. In practice, this was achieved using a continuous phase composed of a mixture of 60 vol% D₂O and 40 vol% H₂O (see Fig S1 for contrast match point determination for SiNp). According to previous reports, the scattering pattern of 1 wt% OCNF at 100 mM NaCl (Fig. 2a) contains information regarding the shape of the fibrils in the high- q and intermediate- q region, which probe the radius and the larger dimension of the fibril, respectively.^{7,17,22} The upturn in the low- q region has been instead associated with the attractive interfibrillar interactions as described by Schmitt et al.⁷ The data were fitted, in the q -region where interfibrillar interactions are not detectable (high- q and intermediated- q range), to a model of non-interacting flexible cylinders with an elliptical cross-section from which the minor radius (R_{min}), major radius (R_{maj}) and the Kuhn length (b_{Kuhn}) were obtained; where the b_{Kuhn} is indicative of the OCNF mesh size.⁷ The data fitting was carried out using a fixed and arbitrary contour length of 500 nm as the average length was not accessible in the probed q -range, as indicated by the lack of a plateau in the

low- q region. In addition, the interfibrillar interactions, in the low- q region, would not allow extrapolation of the OCNF contour length (L). Since the lower threshold for the data fitting was $q_{\min} = 0.06 \text{ \AA}^{-1}$, using values of $L \gg 2\pi/q_{\min}$, kept the fitting unchanged. The model yielded values of $R_{\min} = 1.1 \pm 0.1 \text{ nm}$, $R_{\text{maj}} = 4.7 \pm 0.1 \text{ nm}$ and $b_{\text{Kuhn}} = 21.4 \pm 0.1 \text{ nm}$, in good agreement with previous SAXS measurements.^{7,17,22} Upon SiNp addition, the SANS patterns had a similar trend to that of the pure OCNF gel, indicating that, in the probed q -range, neither of these fillers strongly alter the structure of the fibrillated network. As such, the SiNp-containing samples were fitted using fixed values of $R_{\min} = 1.1$, $R_{\text{maj}} = 4.7$ and $b_{\text{Kuhn}} = 21.4 \text{ nm}$ as found for OCNF, allowing only scale and background to vary. The data were satisfactorily fitted using these constrained values with exception of the sample containing 2.5 wt% SiNp₅ which displayed some difference in the intermediate- q region as shown by the residual plot (Fig 2b). Analysis of the low- q region revealed a slope of ≈ 2.5 for all the samples, indicating that neither of the fillers alters the attractive interactions between OCNF at this length scales. Overall, both fillers preserved the structure of the fibrillated OCNF network at the nm length scale.

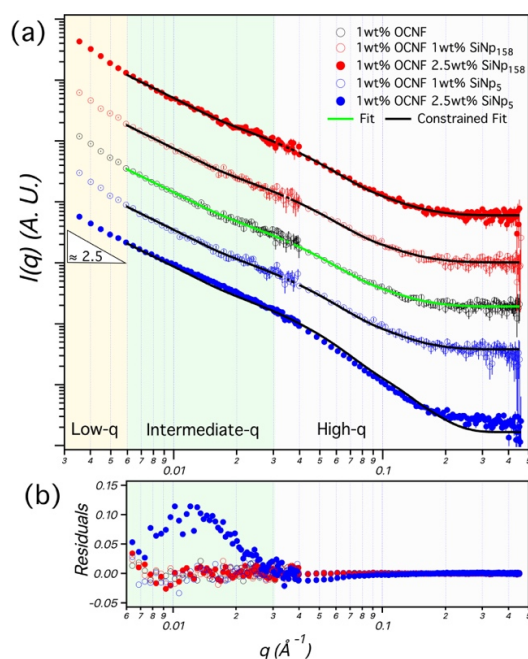


Fig. 2 (a) SANS patterns of the 1 wt% OCNF-based gels (in 100 mM NaCl). For all the samples, the continuous aqueous phase is composed by 60 vol% D₂O and 40 vol% H₂O. The green line describes the fitting of the variables R_{\min} , R_{maj} and b_{Kuhn} from a model of non-interacting flexible cylinders with an elliptical cross-section. The black lines display the fitting for constrained values of R_{\min} , R_{maj} and b_{Kuhn} as found from the fitting of 1 wt% OCNF. (b) Residual plot from the fits in (a).

Following the filler addition into the OCNF gel, the equilibration of the rheological behaviour of the OCNF-SiNp gels was evaluated post breakage (30 s at $\dot{\gamma} = 300 \text{ s}^{-1}$) (Fig. 3). After the imposed breakage, both G^* and $\tan\delta$ of the 1 wt% OCNF gel followed a rapid change (up to $ca. 10 \cdot 10^3 \text{ s}$) succeeded by a less pronounced evolution, indicating the dynamic nature of the OCNF network. Both filler-loaded gels showed greater values of G^* compared to the pure OCNF gel indicating an overall augmented toughness of the gels. Nevertheless, it must be noticed that the magnitude of G^* does not necessarily describe the elastic/viscous-like balance of materials, but, for instance, its increase may be simply due to the increase in volume fraction upon filler addition. On the other hand, $\tan\delta$ better correlates with the elastic/viscous-like contributions of materials despite changes in volume fraction. The $\tan\delta$ of the 1 wt% OCNF gel containing 2.5 and 5 wt% SiNp₅ displayed a very similar $\tan\delta$ profile to the 1 wt% OCNF gel up to $10 \cdot 10^3 \text{ s}$, whilst, at longer times, $\tan\delta$ showed greater values, indicating that the addition of SiNp₅ increases the viscous contribution of the gel without evident change of the elasticity. Contrarily, the gel containing the 2.5 and 5 wt% of SiNp₁₅₈ had a more pronounced decrease in $\tan\delta$ compared to the OCNF profile alone, indicating augmented elasticity of the gel.

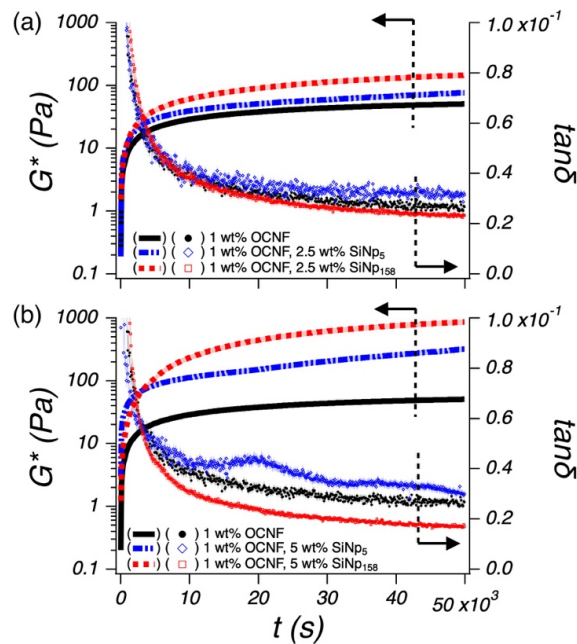


Fig. 3 Time sweep of the OCNF-based gels, starting after stoppage of the imposed breakage (shear at $\dot{\gamma} = 300 \text{ s}^{-1}$ for 30 s), in (a) containing 2.5 wt% SiNp₅ and SiNp₁₅₈ whilst in (b) containing 5 wt% SiNp₅ and SiNp₁₅₈. The 1 wt% OCNF gel (in black) is shown in both graphs as a reference.

A strain sweep spacing from small up to large deformation was employed to reveal how the filler size affects the OCNF network (Fig. 4). At small deformations, the 1 wt% OCNF gel showed a clear LVR whilst at higher deformation both G' and G'' showed a pronounced strain overshoot. Similar G' and G'' overshoots have been associated with the balance between breakage and regeneration of the network junctions.²³ Specifically, G' local maxima could arise by the increased connectivity between the fibrils occurring upon deformation, increasing the elastic contribution of the network. However, the presence of a local maxima in G'' would further indicate a cooccurring energy dissipation process, consequent to the network breakage. This is depicted by several network models as the balance between the formation and loss of the network junctions upon large deformations.^{24,25}

The G' and G'' overshoots have been classified by Hyun et. al as a *strong strain overshoot*, and to the best of our knowledge has never before been observed in CNF-based hydrogels.²³ When either 2.5 or 5 wt% SiNp₅ were added into the OCNF gel, G' overshoots were still appreciable suggesting that SiNp₅ has little influence on the gel mechanics. On the other hand, the G'' profile of the SiNp₅ containing gel, showed a similar overshoot as the pure OCNF gel although with an extra contribution appearing at lower values of γ . The G' overshoot for the OCNF gel containing 2.5 wt% SiNp₁₅₈ is strongly smoothed out, and was completely absent for the 5 wt% SiNp₁₅₈. The respective G'' overshoots became remarkably pronounced, indicating a pronounced energy dissipation process upon deformation due to the loss of network junctions. Both fillers, SiNp₅ and SiNp₁₅₈, showed a shift of the G'' overshoots towards lower values of γ at greater filler concentrations. This can be explained by the greater number of particles which would require less deformation to cage, allowing an earlier onset of the dissipative energy.

SiNp₅ and SiNp₁₅₈ belong respectively to a similar and a greater (*ca.* by a factor 5) length scale compared to the mesh size of the OCNF network.⁷ This information coupled with the herein described rheological measurements would suggest that, when strong attractive interactions between the network and the filler could be ruled out (e.g. electrostatic attraction, hydrophobic interactions), the filler-to-mesh size ratio is of great importance to induce specific rheological responses. Specifically, it is possible to attribute the unchanged elastic fingerprint of the OCNF-SiNp₅ gels to the possibility of the small filler particles to freely move within the aqueous phase of the OCNF network; only mildly affecting the breakage dynamics of the OCNF network upon oscillatory strain sweep. By contrast, the larger filler, SiNp₁₅₈, would not have available free space, leading to a completely different breakage dynamic where the G' overshoot disappears and the dissipative contribution displayed by G'' increases substantially. Moreover, in agreement with the lack of strong OCNF-SiNp interactions, the addition

of SiNP₁₅₈ in to the OCNF gel resulted into a transition from a strong strain overshoot behaviour (G' and G'' overshoots) to a weak strain overshoot (only G'' overshoot) due to the weakening of the associative forces between the network's building blocks, leading to a smoother structural breakage (yielding) upon deformation.²³

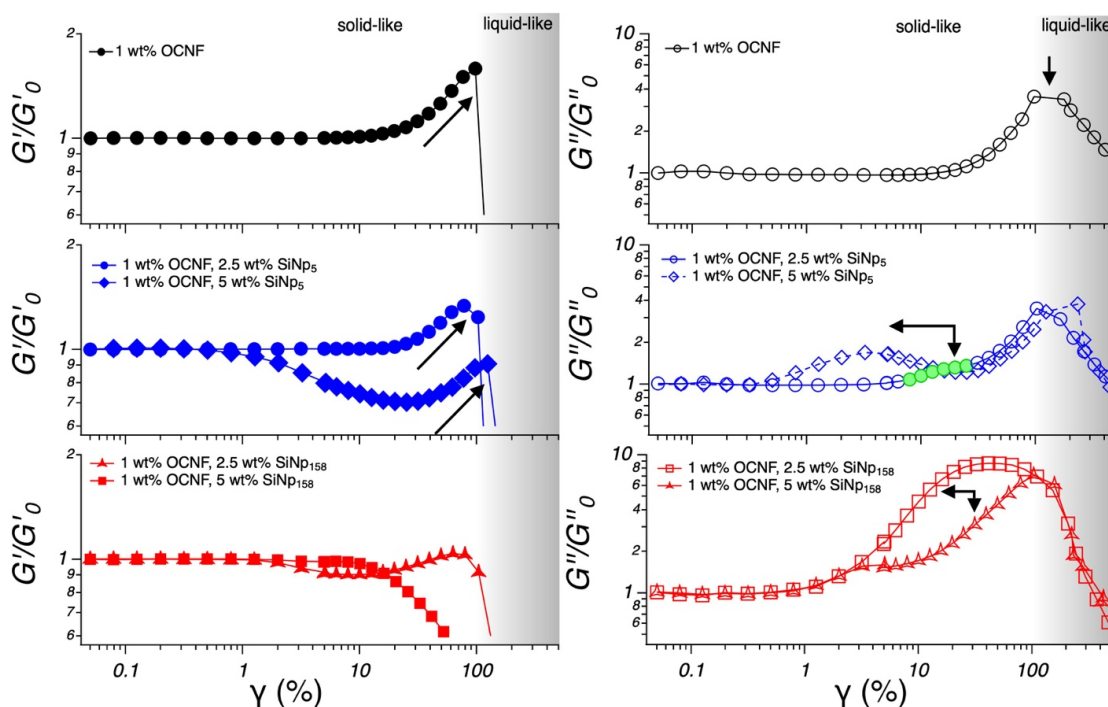


Fig. 4 Strain sweep for the OCNF-based hydrogels. G' and G'' normalized by the respective modulus in the LVR (G'_0 , G''_0) as a function of strain (γ). The darkening of the background refers to the transition from solid-like ($G' > G''$) to liquid-like ($G' < G''$) and is drawn to guide the eye. The green filled symbols are used to highlight the G'' overshoot. Non-normalized data are shown in Fig. S3.

The dynamic moduli, G' and G'' are calculated based on the assumption of the sinusoidal stress response of the material.^{26,27} Although G' and G'' provide a robust way to obtain structural information in the LVR, this assumption loses rigorous mathematical support in the NLVR, where the stress response deviates from being sinusoidal, as usually the case for large deformations.²⁶ In the case of the herein described gels, the richest rheological behaviour lies in the large deformation range, hence a waveform inspection was conducted via plotting the stress response (σ) as a function of the intracycle shear rate ($\dot{\gamma}$) and the intracycle strain (γ_0), commonly known as Lissajous-plots.²⁷

At low deformation, the Lissajous-plots of the gels showed a perfectly elliptical shape indicating the dominant linear response of the material (Fig. 5). By contrast, at greater deformations ($\gamma_0 \approx 35$ and 70

%) the Lissajous-plot acquired a more rhomboidal shape indicating the deviation of the stress signal from linearity. At the largest deformation ($\gamma_0 \approx 250\%$) the stress response was predominantly viscous and non-linear as indicated by the squared shape of the Lissajous-plot. For γ_0 values of *ca.* 35 and 70 % the stress response, starting at $\sigma = 0$, followed a linear increase with the strain (elastic straining), after which a more pronounced stress increase was observed, indicating strain-stiffening at greater intracycle deformations as captured by the G' overshoot displayed in Fig. 3. Similar strain-stiffening phenomena have been reported as ubiquitous in any network composed of semiflexible filamentous proteins²⁸ although found difficult to mimic using commercially available polymers.²⁹ The origin of strain-stiffening in fractal aggregates formed by a diffusion-limited cluster aggregation process, as expected for the OCNF network herein reported, has been proposed to arise from the intrinsic stiffness of the cluster backbone.³⁰

For $\gamma_0 < 100\%$, where the solid-like behaviour dominates ($G' > G''$), the shape of the Lissajous-plot of the pure OCNF and the 5 wt% SiNp₅ loaded gel showed similar features. In the presence of the 5 wt% SiNp₁₅₈ the Lissajous-plot displayed a more opened structure, indicating a pronounced energy dissipation (proportional to the area enclosed in the Lissajous-plot in the σ vs. γ_0 perspective), and a milder intracycle strain-stiffening, underpinning mechanical changes associated with the structural breakdown. At greater deformations, $\gamma_0 > 100\%$, the dominating liquid-like behaviour ($G' < G''$) was underlined by the appearance of the stress shoulder associated with yielding prior to flow.²⁶ At *ca.* 250% γ_0 , the stress shoulder became more pronounced for both filler loaded gels and, after yielding, displayed an abrupt stress decrease followed by an increase (indicated by the arrow). These similarities appeared solely in the Lissajous-plot of the filler-loaded gels, suggesting that at larger deformations, after yielding, the flow properties are characterised by the filler.

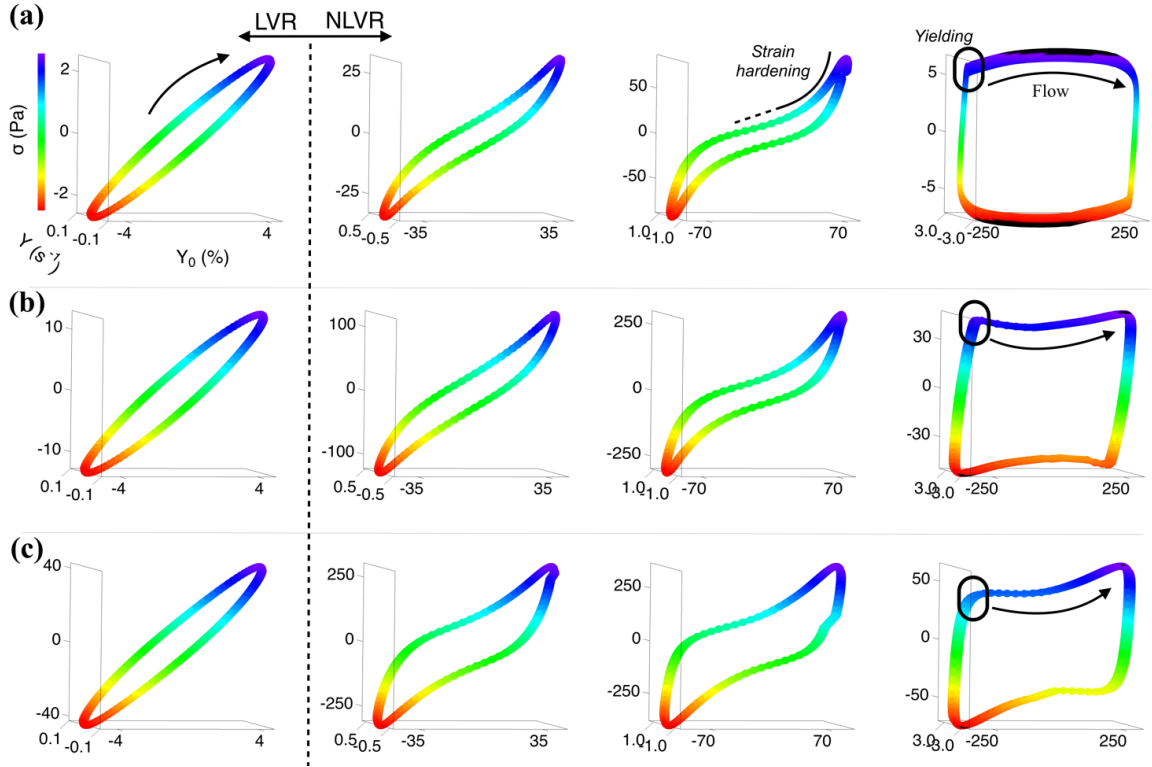


Fig. 5 Lissajous-plots of the (a) 1 wt% OCNF gel, (b) 1 wt% OCNF containing 5 wt% SiNp₅ and (c) 1 wt% OCNF containing 5 wt% SiNp₁₅₈ gels. The legend shown to the top-left Lissajous-plot applies to all. The colour scale is drawn as a function of the normalised value of σ and arrows indicate the direction of σ as a function of γ_0 .

To better interpret the non-linear behaviour, we employed the framework of Rogers et al.²⁶, which decomposes the whole amplitude cycle into separate sequences of events. Although different approaches have been developed to analyse Lissajous-plots, the one proposed by Rogers et al.²⁶ better links rheological events to structural properties. In particular, we characterize the linear stress response starting at $\sigma = 0$ by the local cage modulus G_{cage} as follows:

$$G_{\text{cage}} = \left. \frac{d\sigma}{d\gamma_0} \right|_{\sigma=0}$$

In the framework proposed by Rogers et al., starting at $\sigma = 0$, the Lissajous-plot at large deformations could be interpreted as a sequence of straining (where G_{cage} is calculated), yielding, flowing and structural reformation (labelled in Fig. 6 by 1, 2, 3 and 4, respectively).

At small amplitudes, in the LVR, G_{cage} reduces to G' (Fig. S3) whilst at greater deformations, G_{cage} diverges from G' due to the structural breakage which is not fully recovered upon yielding (2), flowing (3) and structural reformation (4) imposed by the sinusoidal cycle (Fig. 6).³¹ For the pure OCNF gel, a slight decrease in G_{cage} is displayed at greater deformations as expected by structural breakage which is not fully recovered within the sinusoidal cycle. The presence of the SiNp₅ did not substantially affect the rate of change of G_{cage} upon deformation, confirming that the structural recoverability of the gel is dominated by the OCNF network. However, the presence of SiNp₁₅₈ in the OCNF gel strongly affected the structural recoverability of the gel as displayed by the pronounced G_{cage} decrease. The onset of G_{cage} decrease, for the SiNp₁₅₈ containing gel, occurred at lower deformations than the OCNF gel, indicating that the network undergoes breakage at lower deformation and structural recoverability is not completed within the yielding (2), flowing (3) and structural reformation (4).

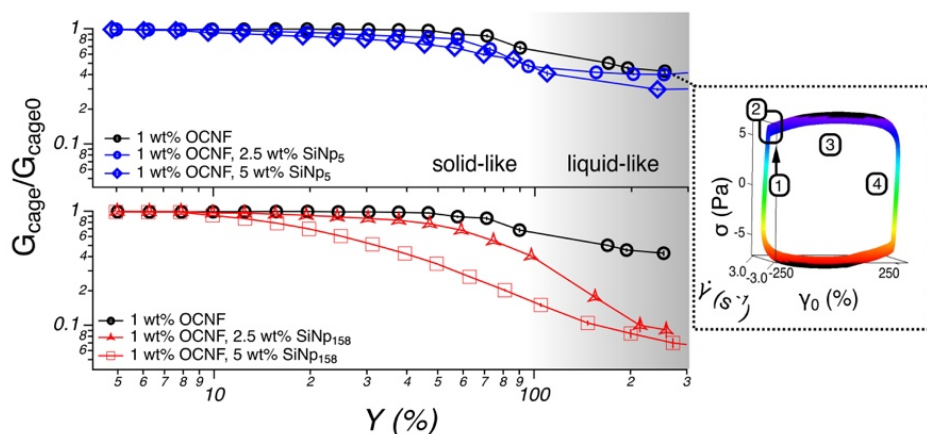


Fig. 6 G_{cage} normalised by the respective modulus in the LVR (G'_{cage0}) as a function of strain (γ) for the OCNF-based gels. The 1 wt% OCNF gel is shown in both graphs as a reference. The darkening of the background refers to the transition from solid-like ($G' > G''$) to liquid-like ($G' < G''$) and is drawn to guide the eye. The appended Lissajous-plot is drawn to depict the sequence of events which soft materials undergo upon LAOS: straining (1), yielding (2), flowing (3) and reformation (4) as suggested by Rogers et al.²⁶

Although structural properties of the hydrogels, at the nanoscale, are almost unaffected by the different filler size, the mechanical properties of the gel upon breakage change substantially. This indicates that the relation between mesh size of the network and filler are of great importance to modulate the rheological properties of the hydrogel. Specifically, we hypothesize that SiNp₁₅₈ – with a larger size compared to the mesh size of the OCNF network – could actively dislodge the physical junctions of

the network upon large deformations, leading to a smoother yielding (without G' overshoot). Contrarily, the smaller SiNp₅ could not actively dislodge the physical junctions of the network due to their ability to be accommodated within the mesh of the network upon large deformations, without disrupting the breakage dynamic of the network.

Conclusion

In this study we investigated the effect of the filler size on the structural and mechanical properties of an attractive fibrillated network composed of OCNF, in conditions where strong filler-filler and filler-fibril interactions are absent. The two fillers, SiNp₅ and SiNp₁₅₈ were chosen to be of a similar and a greater dimension of the gel network mesh size, respectively. Small angle neutron scattering revealed that the OCNF network preserved its nanoscale architecture in the presence of both fillers whilst oscillatory shear rheology captured clear rheological differences. Large amplitude oscillatory shear (LAOS) displayed the richest rheological behaviour and allowed to access the impact of the filler-to-mesh size ratio on the yielding behaviour of the hydrogel. Our findings indicate that the presence of the smaller filler, SiNp₅, in the OCNF network maintains the mechanics of the network almost unvaried. This phenomenon is associated with the ability of SiNp₅ to fit between the mesh size of the gel network without altering the dynamics of the network upon large amplitude oscillatory shear. In contrast, the presence of the larger filler, SiNp₁₅₈, resulted in a gradual structural breakage and a low network recoverability after breakage induced by large deformations, suggesting that the SiNp₁₅₈ could actively dislodge the junctions of the network. The fundamental understanding provided in this study has implications for industrially relevant formulations, where the efficacy of additives in primary matrixes is of main importance towards tunability of specific structural and mechanical properties on demand.

Acknowledgements: The authors thank the EPSRC for funding this project (grant number EP/N033310/1). V. Calabrese thanks the University of Bath for funding his PhD studentship. The authors thank Prof Roger Rother for the generous donation of SiNp₅ from Geo40™. The authors thank the Institut Laue-Langevin for the provision of neutron beam time on D22 instrument provided under the Easy Access System (the data set related to this beam time is archived at DOI: 10.5291/ILL-DATA.EASY-477). Data supporting this work is freely accessible in the Bath research data archive system at DOI: 10.15125/BATH-XXXX.

References

- (1) De France, K. J.; Hoare, T.; Cranston, E. D. Review of Hydrogels and Aerogels Containing Nanocellulose. *Chem. Mater.* **2017**, *29* (11), 4609–4631.
- (2) Saito, T.; Nishiyama, Y.; Putaux, J. L.; Vignon, M.; Isogai, A. Homogeneous Suspensions of Individualized Microfibrils from TEMPO-Catalyzed Oxidation of Native Cellulose. *Biomacromolecules* **2006**, *7* (6), 1687–1691.
- (3) Isogai, A.; Saito, T.; Fukuzumi, H. TEMPO-Oxidized Cellulose Nanofibers. *Nanoscale* **2011**, *3* (1), 71–85.
- (4) Saito, T.; Uematsu, T.; Kimura, S.; Enomae, T.; Isogai, A. Self-Aligned Integration of Native Cellulose Nanofibrils towards Producing Diverse Bulk Materials. *Soft Matter* **2011**, *7* (19), 8804–8809.
- (5) Fukuzumi, H.; Tanaka, R.; Saito, T.; Isogai, A. Dispersion Stability and Aggregation Behavior of TEMPO-Oxidized Cellulose Nanofibrils in Water as a Function of Salt Addition. *Cellulose* **2014**, *21* (3), 1553–1559.
- (6) Fneich, F.; Ville, J.; Seantier, B.; Aubry, T. Structure and Rheology of Aqueous Suspensions and Hydrogels of Cellulose Nanofibrils: Effect of Volume Fraction and Ionic Strength. *Carbohydr. Polym.* **2019**, *211* (February), 315–321.
- (7) Schmitt, J.; Calabrese, V.; Da Silva, M. A.; Lindhoud, S.; Alfredsson, V.; Scott, J. L.; Edler, K. J. TEMPO-Oxidised Cellulose Nanofibrils; Probing the Mechanisms of Gelation: Via Small Angle X-Ray Scattering. *Phys. Chem. Chem. Phys.* **2018**, *20* (23), 16012–16020.
- (8) Mendoza, L.; Batchelor, W.; Tabor, R. F.; Garnier, G. Gelation Mechanism of Cellulose Nanofibre Gels: A Colloids and Interfacial Perspective. *J. Colloid Interface Sci.* **2018**, *509*, 39–46.
- (9) Crawford, R. J.; Edler, K. J.; Lindhoud, S.; Scott, J. L.; Unali, G. Formation of Shear Thinning Gels from Partially Oxidised Cellulose Nanofibrils. *Green Chem.* **2012**, *14* (2), 300–303.
- (10) Tardy, B. L.; Yokota, S.; Ago, M.; Xiang, W.; Kondo, T.; Bordes, R.; Rojas, O. J. Nanocellulose–Surfactant Interactions. *Curr. Opin. Colloid Interface Sci.* **2017**, *29*, 57–67.
- (11) Chen, Y.; Xu, C.; Huang, J.; Wu, D.; Lv, Q. Rheological Properties of Nanocrystalline Cellulose Suspensions. *Carbohydr. Polym.* **2017**, *157*, 303–310.

-
- (12) Oguzlu, H.; Boluk, Y. Interactions between Cellulose Nanocrystals and Anionic and Neutral Polymers in Aqueous Solutions. *Cellulose* **2017**, *24* (1), 131–146.
- (13) Dickinson, E.; Chen, J. Heat-Set Whey Protein Emulsion Gels: Role of Active and Inactive Filler Particles. *J. Dispers. Sci. Technol.* **1999**, *20* (1–2), 197–213.
- (14) Vliet, T. Rheological Properties of Filled Gels. Influence of Filler Matrix Interaction. *Colloid Polym. Sci.* **1988**, *266* (6), 518–524.
- (15) Gravelle, A. J.; Barbut, S.; Marangoni, A. G. Influence of Particle Size and Interfacial Interactions on the Physical and Mechanical Properties of Particle-Filled Myofibrillar Protein Gels. *RSC Adv.* **2015**, *5* (75), 60723–60735.
- (16) Gillece, T.; McMullen, R. L.; Fares, H.; Senak, L.; Ozkan, S.; Foltis, L. Probing the Textures of Composite Skin Care Formulations Using Large Amplitude Oscillatory Shear. *J. Cosmet. Sci.* **2016**, *67*, 121–159.
- (17) Calabrese, V.; Muñoz-García, J. C.; Schmitt, J.; da Silva, M. A.; Scott, J. L.; Angulo, J.; Khimyak, Y. Z.; Edler, K. J. Understanding Heat Driven Gelation of Anionic Cellulose Nanofibrils: Combining Saturation Transfer Difference (STD) NMR, Small Angle X-Ray Scattering (SAXS) and Rheology. *J. Colloid Interface Sci.* **2019**, *535*, 205–213.
- (18) Grillo, I. Small-Angle Neutron Scattering and Applications in Soft Condensed Matter. In *Soft Matter Characterization*; Borsali, R., Pecora, R., Eds.; Springer Netherlands: Dordrecht, 2008; pp 27–30.
- (19) Adamo, M.; Poulos, A. S.; Miller, R. M.; Lopez, C. G.; Martel, A.; Porcar, L.; Cabral, J. T. Rapid Contrast Matching by Microfluidic SANS. *Lab Chip* **2017**, *17* (9), 1559–1569.
- (20) Ilavsky, J.; Jemian, P. R. *IT Irena*: Tool Suite for Modeling and Analysis of Small-Angle Scattering. *J. Appl. Crystallogr.* **2009**, *42* (2), 347–353.
- (21) Kline, S. R. Reduction and Analysis of SANS and USANS Data Using IGOR Pro. *J. Appl. Crystallogr.* **2006**, *39* (6), 895–900.
- (22) da Silva, M. A.; Calabrese, V.; Schmitt, J.; Celebi, D.; Scott, J. L.; Edler, K. J. Alcohol Induced Gelation of TEMPO-Oxidized Cellulose Nanofibril Dispersions. *Soft Matter* **2018**, *14* (45), 9243–9249.
- (23) K. Hyun; S. H Kim; K. H Ahn; S. J Lee. Large Amplitude Oscillatory Shear as a Way to

Classify the Complex Fluids. *J. Nonnewton. Fluid Mech.* **2002**, *107* (1–3), 51–65.

- (24) Ahn, K. H.; Osaki, K. A Network Model for Predicting the Shear Thickening Behavior of a Poly (Vinyl Alcohol)-Sodium Borate Aqueous Solution. *J. Nonnewton. Fluid Mech.* **1994**, *55* (3), 215–227.
- (25) Sim, H. G.; Ahn, K. H.; Lee, S. J. Large Amplitude Oscillatory Shear Behavior of Complex Fluids Investigated by a Network Model: A Guideline for Classification. *J. Nonnewton. Fluid Mech.* **2003**, *112* (2–3), 237–250.
- (26) Rogers, S. A.; Erwin, B. M.; Vlassopoulos, D.; Cloitre, M. A Sequence of Physical Processes Determined and Quantified in LAOS: Application to a Yield Stress Fluid. *J. Rheol.* **2011**, *55* (2), 435–458.
- (27) Hyun, K.; Wilhelm, M.; Klein, C. O.; Cho, K. S.; Nam, J. G.; Ahn, K. H.; Lee, S. J.; Ewoldt, R. H.; McKinley, G. H. A Review of Nonlinear Oscillatory Shear Tests: Analysis and Application of Large Amplitude Oscillatory Shear (LAOS). *Prog. Polym. Sci.* **2011**, *36* (12), 1697–1753.
- (28) Storm, C.; Pastore, J. J.; MacKintosh, F. C.; Lubensky, T. C.; Janmey, P. A. Nonlinear Elasticity in Biological Gels. *Nature* **2005**, *435* (7039), 191–194.
- (29) Ewoldt, R. H.; Clasen, C.; Hosoi, A. E.; McKinley, G. H. Rheological Fingerprinting of Gastropod Pedal Mucus and Synthetic Complex Fluids for Biomimicking Adhesive Locomotion. *Soft Matter* **2007**, *3* (5), 634–643.
- (30) Gisler, T.; Ball, R. C.; Weitz, D. A. Strain Hardening of Fractal Colloidal Gels. *Phys. Rev. Lett.* **1999**, *82* (5), 1064–1067.
- (31) van der Vaart, K.; Rahmani, Y.; Zargar, R.; Hu, Z.; Bonn, D.; Schall, P. Rheology of Concentrated Soft and Hard-Sphere Suspensions. *J. Rheol.* **2013**, *57* (4), 1195–1209.

CHAPTER 6

COMPOSITE HYDROGEL SPHEROIDS INCORPORATING CELLULOSE NANOFIBRILS AND CHIRAL COORDINATION POLYMER NANOFIBRES

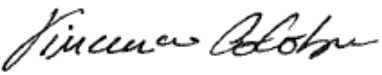
Building on findings of the previous Chapter, we added silica nanoparticles (SiNp) to oxidised cellulose nanofibrils (OCNF) hydrogels to modify the rheological properties of the hydrogel towards smoother breakage and yielding whilst preserving the charge accessibility of OCNF. Taking advantage of this rheological feature, the composite gel was uniformly extruded through a syringe needle into an aqueous solution containing salt. On the other hand, the charge accessibility of the OCNF enabled gelation of the extruded material and thus the formation of long-living spheroidal hydrogels in water. From here, we further advance, identifying key requirements for the fabrication of spheroidal hydrogels containing coordination polymer nanofibers^[168].

Coordination polymers are defined as structures formed by ligands, usually organic molecules, linked by metal ions. The supramolecular self-assembly of such structures leads to threads, sheets, or three-dimensional architectures; the latter of these are often referred to as metal-organic frameworks (MOF).^[169] Importantly, the myriad possible ligand-metal ion combinations enables the design of MOF with different structures and supramolecular assemblies, matching specific requirements. As such, MOF are the most studied class of coordination polymers due to their promising application in gas storage and separation, catalysis, pollutant removal and drug delivery.^[170,171] The combination of coordination polymers with cellulose has been proposed as an effective strategy to produce sustainable materials with functional properties.^[170] Solid cellulose substrates such as aerogels and films have been broadly investigated with the aim to remove specific components from water streams.^[170] For instance, the pellicles composed by bacterial cellulose and MOF prepared by Au-Duong et al.^[172] displayed high iodine uptake whilst filter papers incorporating MOF prepared by Part et al.^[173] presented selective dye capture. The incorporation of coordination polymers into gels has not been extensively reported, probably due to the antagonistic conditions required to obtain stable gels and MOF. To date, only Zhu et al. reported on the production of alginate hydrogels containing MOF.^[171] Zhu et al. prepared the composite in two steps: (i) fabrication of the alginate-based hydrogel containing metal ions and (ii) MOF self-assembly, which was achieved upon transferring the hydrogel to a solution of ligand in ethanol and incubating at 85°C for 18 h.^[171]

As an alternative to the approach of Zhu et al.^[171], in the following Chapter we take advantage of the metal ion to contemporaneously induce gelation of the OCNF-SiNp-ligand hydrogel while enabling conditions for the self-assembly of coordination polymer nanofibres within the hydrogel matrix. In addition, the gelation and the coordination polymer self-assembly occur

in aqueous medium without the use of high temperatures, adhering to the canonic principle of green chemistry. Although conceptually simple, this procedure allows incorporation and growth of the coordination polymer given specific rheological properties of the gel matrix and rate of self-assembly of the coordination polymer are satisfied. We demonstrate that the self-assembly rate of the coordination polymer and the rheological properties of the primary matrix are pivotal to achieving a high yield of the incorporated coordination polymer and a specific shape of the spheroidal hydrogel. Since a vast library of functional coordination polymers is available, especially metal-organic frameworks, the pieces of knowledge provided in this Chapter could guide the production of functional cellulose-based hydrogels through the incorporation of coordination polymers.

Supporting information available in section 10.4.

This declaration concerns the article entitled:			
Composite hydrogel spheroids incorporating cellulose nanofibrils and chiral coordination polymer nanofibres			
Publication status (tick one)			
draft manuscript	<input type="checkbox"/>	Submitted	<input checked="" type="checkbox"/> In review
	<input type="checkbox"/>	Accepted	<input type="checkbox"/> Published
Publication details			
Candidate's contribution to the paper (detailed, and also given as a percentage).	<p>The candidate contributed to/ considerably contributed to/predominantly executed the...</p> <p>Formulation of ideas: -The initial idea was formulated by ERE and VC based on preliminary rheological data obtained by VC and composite hydrogels obtained by ERE. 50%</p> <p>Design of methodology: -All the measurements were designed by ERE and VC.50%</p> <p>Experimental work: - The experimental work was conducted by ERE (50%) and VC (50% rheology and SAXS) - The data analysis was conducted by ERE (50%) and VC (50% rheology and SAXS). 50%</p> <p>Presentation of data in journal format: -The first draft was written by ERE with contribution of VC to the writing of the SAXS and rheology related sections. Subsequent drafts were reworked by ERE following feedback from VC, KJE, JLS. 25%</p>		
Statement from Candidate	This paper reports on original research I conducted during the period of my Higher Degree by Research candidature.		
Signed			Date 29/09/17

Composite hydrogel spheroids incorporating cellulose nanofibrils and chiral coordination polymer nanofibres

Emile R. Engel,*† Vincenzo Calabrese,† Karen J. Edler and Janet L. Scott

Received 00th January 20xx,
Accepted 00th January 20xx

DOI: 10.1039/x0xx00000x

Composite hydrogels of predictable spheroidal structure have been prepared, incorporating TEMPO-oxidised cellulose nanofibrils and a chiral Cu(II)-aspartate coordination polymer. The preparative procedure can be adapted for a variety of potential coordination polymers, provided such factors as rheological properties of the primary matrix and coordination polymer self-assembly rate are accounted for.

Cellulose- and other biopolymer-based hydrogels have received considerable attention as promising materials for tissue engineering as scaffolds and extracellular growth matrices.¹ Beyond tissue engineering, cellulose-based hydrogels have been explored for applications in water treatment,² drug delivery,³ agriculture⁴ and personal hygiene products.⁵ A recent review of structured macroporous hydrogels highlighted ongoing research challenges, including the creation of “anisotropy and directionality within the networks” and the development of “solvent-free or additive-free fabrication methods”.⁶

It is well-established that aqueous ionic solutions induce gelation of cellulose nanofibril dispersions.⁷ In the case of nanocrystalline cellulose bearing negatively-charged sulfate ester groups, ion-induced gelation has been attributed to a charge screening effect that promotes intermolecular attraction.⁸ A similar mechanism of gelation has been proposed for oxidised cellulose nanofibrils (OCNF) bearing carboxylate groups.⁹

Cellulose and coordination polymers, including the sub-class metal-organic frameworks, are attractive complementary materials for the fabrication of composites. Cellulose is a versatile structural material, useful for constructing films and membranes, packaging materials and, of course, hydrogels.

However, introducing certain functional properties, such as stimuli responsiveness,¹⁰ magnetism¹¹ and luminescence¹² to cellulose-based materials is challenging. Incorporating coordination polymers into cellulose-based materials is a strategy for introducing a wide range of properties, given the great diversity of existing and possible coordination polymers and the associated range of functional properties including chirality, porosity, selective sorption, magnetism, luminescence, fluorescence and catalytic activity.¹³ Zhu and co-workers prepared alginate hydrogels containing various metal-organic frameworks in a multi-step procedure involving metal-organic framework synthesis at elevated temperatures.¹⁴ However, cellulose is more naturally abundant and more structurally robust than alginate, making it preferable for large-scale applications. Moreover, a simpler one-step ambient temperature procedure based on cellulose and coordination polymers is conceivable.

Coordination polymer nanofibres combining Cu²⁺ and enantiomerically pure aspartic acid were first reported by Imaz and co-workers.¹⁵ The blue crystalline nanofibers of **Cu-Asp** are prepared by combining aqueous Cu(NO₃)₂ and an alkaline solution of L- or D-aspartate (L-Asp or D-Asp). Wu *et al.* later demonstrated that an alkaline solution of the aspartate racemate resolved in the presence of Cu²⁺, yielding a mixture of the L- and D- versions of **Cu-Asp**.¹⁶

We set out to prepare composite hydrogels from a 1 wt% OCNF dispersion containing 5 wt% silica nanoparticles (SiNP) and varying concentrations of aspartic acid and NaOH. SiNP as additive provided an elegant means of tuning the rheological properties of the primary matrix towards the formation of hydrogels with defined structures,¹⁷ such as spheroids and filaments. Video S1 shows the formation of filaments from a dispersion containing only OCNF and SiNP. OCNF, based on the well-established method of TEMPO-mediated oxidation,¹⁸ was obtained as an 8 wt% paste of solids in water with a degree of oxidation of 25% by conductometric titration.¹⁹ A 3 wt% stock dispersion of OCNF was prepared by dispersing the solids in water using a sonication probe (ca. 8000 J over 60 min of

Department of Chemistry, University of Bath, Claverton Down, Bath, BA2 7AY, UK.
E-mail: ee380@bath.ac.uk

† These authors contributed equally.

Electronic Supplementary Information (ESI) available: materials and methods, photographs of hydrogel spheroids, time-lapse optical microscopy and video file.
See DOI: 10.1039/x0xx00000x

processing time per batch of 40 mL). A 10 wt% SiNP stock dispersion was prepared using silica powder (Sigma Aldrich 718483), comprising SiNP of diameter 157.0 ± 1.3 nm (Z-average), was suspended in water, followed by sonication (240 J over 2 min of processing time per batch of 20 mL). The OCNF and SiNP dispersions were then combined in appropriate proportions and subjected to a short period of sonication (120 J over 1 min of processing time per 10 mL sample). Aspartic acid was added to dispersions as an alkaline solution of 1:2 aspartic acid/NaOH. NaOH served to deprotonate the ligand. The integrity of the matrix was preserved despite the addition of NaOH at relatively high concentrations; there were no indications of OCNF degradation. Additional details of sample preparation procedures are provided in the ESI. Further references to "OCNF dispersions" imply dispersions containing 1 % OCNF, 5 % SiNP and concentrations of aspartic acid and NaOH as specified.

Droplets of the dispersion were ejected from a syringe needle or micropipette into an aqueous solution of 100 mM $\text{Cu}(\text{NO}_3)_2$, to form hydrogel spheroids. It was hypothesised that Cu^{2+} and aspartate would self-assemble *in situ* to form **Cu-Asp** within the OCNF hydrogel matrix, and that **Cu-Asp** would interact with the OCNF via electrostatic or coordination interactions between Cu^{2+} and the OCNF carboxylate groups. For a series of OCNF dispersions containing L-Asp at different concentrations in the range 0-125 mM, representative examples of the resultant hydrogel spheroids are shown in Figure 1. The control sample formed a flattened structure with a depression in the middle. At 25 mM the spheroid is partially flattened. At 50 mM the structure is a tractable hydrogel with an elliptical shape. At 75 mM a conical shape results and at higher concentrations the structures are considerably elongated. The dispersion containing 50 mM L-Asp was determined to be favourable for preparing hydrogels of well-defined spheroidal structure and predictable sizes of 2-4 mm in diameter.

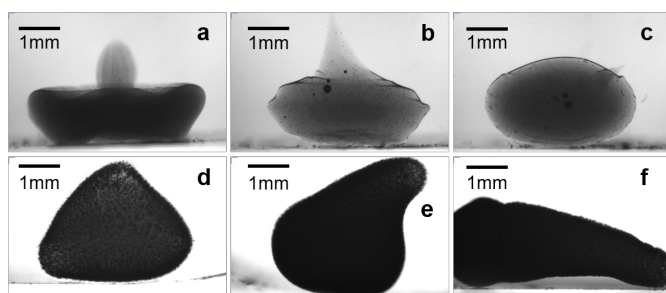


Figure 1. Hydrogel structures obtained by ejecting droplets of L-Asp-containing OCNF dispersions into 100 mM aqueous $\text{Cu}(\text{NO}_3)_2$. The concentrations of L-Asp are: a) 0 mM (control), b) 25 mM, c) 50 mM, d) 75 mM, e) 100 mM, f) 125 mM.

In Figure 2 combined SAXS and WAXS patterns for various samples of the composite hydrogels are compared with the reference pattern for pure **Cu-Asp**, which had been further characterised by powder X-ray diffraction (Figure S1). Considering WAXS length scales, at 50 mM L-Asp the scattering pattern is dominated by OCNF and SiNP. However, at concentrations of 75 mM and greater, peaks corresponding to

Cu-Asp are observed, confirming the presence and phase purity of the coordination polymer within the hydrogel matrix. Similar slopes are observed within the SAXS region for all patterns from OCNF containing solutions, confirming that no substantial structural changes occur at these length scales.

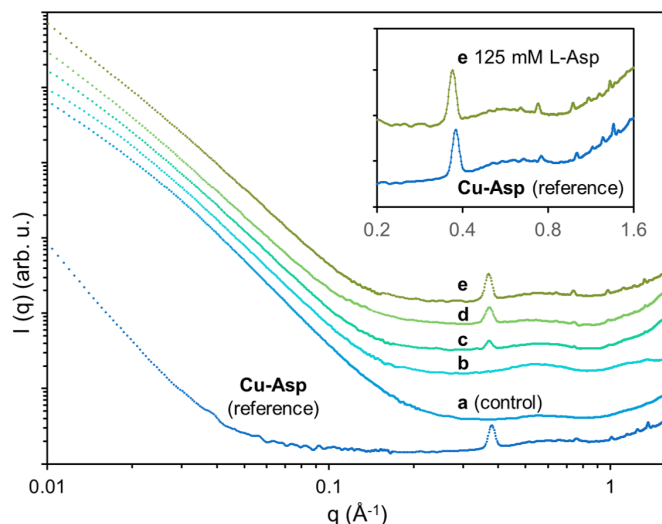


Figure 2. Combined SAXS and WAXS patterns for pure Cu-Asp as reference and OCNF dispersions containing L-Asp at the following concentrations: a) 0 mM (control sample), b) 50 mM, c) 75 mM, d) 100 mM and e) 125 mM.

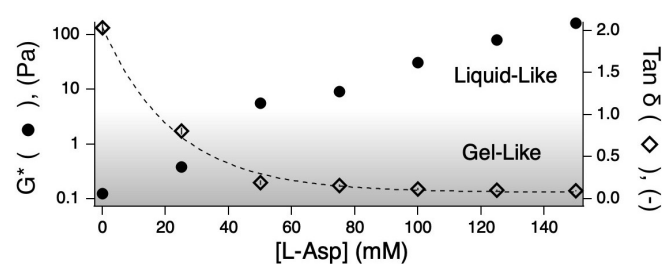


Figure 3. G^* and $\tan \delta$ for OCNF dispersions containing L-Asp at concentrations in the range 0-125 mM (in the absence of $\text{Cu}(\text{NO}_3)_2$). The dotted line is drawn as a guide, while darkening of the background indicates the liquid ($\tan \delta > 1$) to gel-like ($\tan \delta < 1$) transition.

Since the resistance to flow and elasticity of the OCNF dispersions (primary matrix) strongly dictate the shape of the spheroidal hydrogels generated by ejection from a syringe needle into the metal salt solution, we investigated the rheological properties of the OCNF dispersions at different L-Asp concentrations, (Figure 3). Opposing trends are observed for G^* and $\tan \delta$ as a function of L-Asp concentration, obtained from the linear viscoelastic region of a strain sweep at 1 rad s^{-1} . The increase in G^* as a function of L-Asp concentration indicates toughening of the dispersion. The decrease of $\tan \delta$ beyond $\tan \delta < 1$ points to enhanced elasticity of the dispersion and the formation of a material which is dominated by the solid (gel-like) contribution. Noticeably, at $[\text{L-Asp}] > 25$ mM the dispersions behave as gel-like materials, which correlates well with the variations in hydrogel structure represented in Figure 1. A transition occurs from concave edges at 0 mM L-Asp to distinctly convex edges at 50 mM L-Asp. At 50 mM L-Asp the

change in $\tan\delta$ approaches a constant value. At L-Asp concentrations beyond 50 mM, further toughening (i.e. an increase in G^*) results in more elongated hydrogel structures.

It had been previously demonstrated that racemic aspartic acid self-assembles with Cu^{2+} at a much slower rate than enantiomerically pure D- or L-Asp.¹⁶ To investigate the effect of this change in reaction rate, spheroids were prepared from a series of OCNF dispersions containing 50 mM L-Asp and doped with D-Asp at concentrations in the range 0-50 mM. Rheological analysis of this series of dispersions (Figure S2) revealed no considerable changes in elasticity as captured by $\tan\delta$. Figure 4 comprises photographs and optical micrographs of cross-sections of the hydrogel spheroids at various ratios of [L-Asp]:[D-Asp]. An anisotropic distribution of **Cu-Asp** crystallites within the hydrogel matrices is observed, as is a clear trend in the distribution of crystallites as a function of the ratio of [L-Asp]:[D-Asp]. In all cases the crystallites are located near the perimeter of the spheroid. For the sample containing L-Asp at 50 mM and no D-Asp (Figure 4a) a dense outer ring of crystallites is visible, along with a sparsely-populated secondary inner ring. Additional photographs of spheroids prepared from a dispersion containing L-Asp but no D-Asp are available in Figure S3. For the D-Asp-containing samples only a single ring of crystallites is visible. The density of crystallites declines with increasing D-Asp mole fraction. Evidently, the slower reaction rate, induced by increasing the concentration of D-Asp, allows aspartate ions to diffuse out of the OCNF matrix into the surrounding aqueous solution before crystallisation occurs. Thus, a sufficiently high rate of coordination polymer self-assembly is a necessary condition for *in situ* preparation of such composite hydrogels.

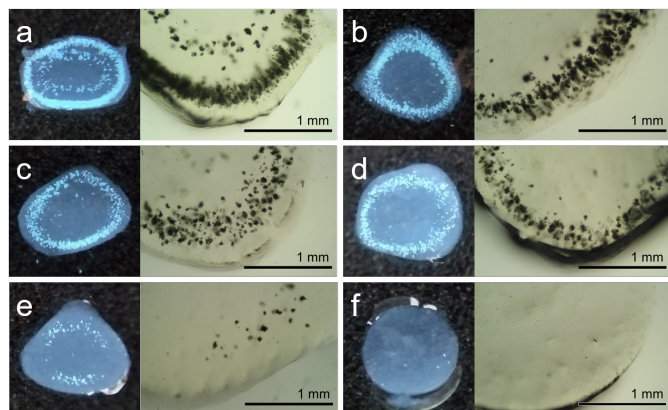


Figure 4. Photographs and photomicrographs of spheroids prepared from an OCNF dispersion containing 50 mM L-Asp doped with D-Asp at concentrations of: a) 0 mM (control), b) 5 mM, c) 10 mM, d) 15 mM, e) 20 mM and f) 50 mM (racemic mixture).

The kinetics of **Cu-Asp** self-assembly within the OCNF/SiNP hydrogel matrix were investigated in greater detail by image analysis. The experiment involved submerging 100 μL of the dispersion, containing OCNF, SiNP and ligand, in 100 mM aqueous $\text{Cu}(\text{NO}_3)_2$ and collecting photomicrographs at 10 s intervals. Further experimental details are provided in the ESI. Crystallite propagation and the increase in crystallite density with time are proportional to the darkening of greyscale

photomicrographs. Relative image darkness, d , as a function of time, t , was determined as an indicator of crystallite density. The value of d is the inverted 'mean grey value', measured by image analysis using ImageJ,²⁰ and converted to arbitrary units.

Figure 5 shows d for the OCNF dispersion containing L-Asp and varying amounts of D-Asp immediately after being submerged in aqueous $\text{Cu}(\text{NO}_3)_2$. For the control sample containing 50 mM L-Asp and 0 mM D-Asp (Figure 5a), the first crystallites are observable at 70 s after submersion in $\text{Cu}(\text{NO}_3)_2$ at $t = 0$ s (see Figure S4). The observation of macroscopic crystallites coincides with an inflection point in the Figure 5a plot. We propose that during 0 to 70 s metastable coordination complexes form, causing mild darkening of the solution, and nucleation of **Cu-Asp** occurs at ~ 70 s. In Figure 5b, for the sample containing 50 mM L-Asp and 15 mM D-Asp, the inflection at approximately 160 s also corresponds to the observation of microscopic crystallites via an optical microscope (Figure S5). For the Figure 5c plot an analogous broad inflection is observable in the range 1000-1200s, where macroscopic crystallites appear (Figure S6). These results confirm retardation of the onset of **Cu-Asp** crystallisation, which allows aspartate to diffuse from the hydrogel matrix into the surrounding aqueous medium during the preparation of spheroids.

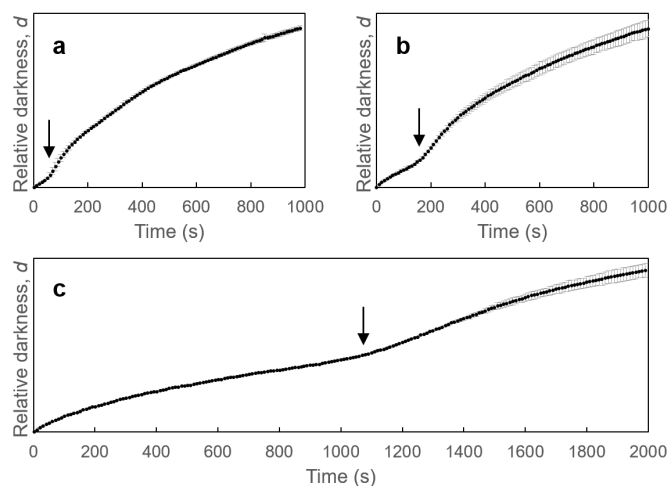


Figure 5. Relative image darkness (proportional to crystallite density), d , as a function of time for OCNF dispersions with the following ligand concentrations: a) 50 mM L-Asp only (measured in triplicate); b) 50 mM L-Asp + 15 mM D-Asp (measured in triplicate) and c) 50 mM L-Asp + 50 mM D-Asp (measured in duplicate). Arrows indicate the points at which crystallites of **Cu-Asp** were observed.

A facile method has been designed for the preparation of OCNF hydrogel spheroids incorporating coordination polymers. The present procedure is carried out in one step at ambient temperature with the coordination polymer self-assembly occurring *in situ*. In principle this method could be used to prepare analogous hydrogel structures incorporating a variety of coordination polymers provided a number of conditions are met, some of which have been established via the present investigation. Firstly, rheological parameters including elasticity and toughness, of the dispersion used to prepare the composite hydrogels must be carefully controlled to ensure the desired structures (e.g. concave/convex spheroids or elongated shapes)

can be achieved. The ligand and a deprotonating agent (NaOH) were found to have a strong influence on the mechanical properties of the dispersion. Therefore, the final dispersion, composed of the OCNF/SiNP primary matrix, ligand and deprotonating agents should be adjusted to achieve specific mechanical properties via, for instance, fine tuning the concentration of an additive such as SiNP. Importantly, the rate of coordination polymer self-assembly is key to achieving a high yield of entrapped crystallites. A high rate of self-assembly prevents diffusion of the free ligand out of the OCNF matrix. The understanding provided in this study could be rapidly exploited in other systems involving a divalent metal salt and ligand, where the coordination polymer or metal-organic framework self-assembles spontaneously. Provided that specific conditions are met, the preparation of composite hydrogels of well-defined structure could be extended to different combinations of matrixes, metal cations and ligands to tailor specific functional properties.

This research was supported by the Commonwealth Rutherford Fellowships Programme and the Centre for Sustainable Chemical Technologies at the University of Bath. V. Calabrese thanks the University of Bath for funding his PhD studentship. Data supporting this work is freely accessible in the Bath research data archive system at DOI: 10.15125/BATH-XXXX.

Conflicts of interest

There are no conflicts to declare.

Notes and references

‡ Footnotes relating to the main text should appear here. These might include comments relevant to but not central to the matter under discussion, limited experimental and spectral data, and crystallographic data.

§

§§

etc.

- 1 (a) S. Van Vlierberghe, P. Dubruel and E. Schacht, *Biomacromolecules*, 2011, **12**, 1387; (b) R. M. A. Domingues, M. E. Gomes and R. L. Reis, *Biomacromolecules*, 2014, **15**, 2327; (c) J. C. Courtenay, R. I. Sharma and J. L. Scott, *Molecules*, 2018, **23**, 654.
- 2 (a) N. Mohammed, N. Grishkewich and K. C. Tam, *Environ. Sci. Nano*, 2018, **5**, 623; (b) K. Bello, B. K. Sarojini and B. Narayana, *J. Polym. Res.*, 2019, **26**, 62; (c) J. Wang, N. Zhang, C. Jiang and C. Zhang, *J. Mater. Res.*, 2018, **33**, 3898.
- 3 (a) R. Rodríguez, C. Alvarez-Lorenzo and A. Concheiro, *J. Control. Release*, 2003, **86**, 253; (b) A. El-Hag Ali, H. A. Abd El-Rehim, H. Kamal and D. El-Sayed A. Hegazy, *J. Macromol. Sci. Pure Appl. Chem.*, 2008, **45**, 628; (c) C. C. Lin and A. T. Metters, *Adv. Drug Deliv. Rev.*, 2006, **58**, 1379.
- 4 M. Sarvas, P. Pavlenda and E. Takáčová, *J. Forest Sci.*, 2007, **53**, 204.
- 5 (a) A. Sannino, G. Mensitieri and L. Nicolais, *J. Appl. Polym. Sci.* 2004, **91**, 3791; (b) M. O. Haque and M. I. H. Mondal, in *Cellulose-Based Superabsorbent Hydrogels*, ed. M. I. H. Mondal, Springer, Cham, 2018, pp 1-21.
- 6 K. J. De France, F. Xu and T. Hoare, *Adv. Healthc. Mater.*, 2018, **7**, 1.
- 7 (a) M. Chau, S. E. Sriskandha, D. Pichugin, H. Thérien-Aubin, D. Nykypanchuk, G. Chauve, M. Méthot, J. Bouchard, O. Gang and E. Kumacheva, *Biomacromolecules*, 2015, **16**, 2455; (b) K. R. Peddireddy, I. Capron, T. Nicolai and L. Benyahia, *Biomacromolecules*, 2016, **17**, 3298.
- 8 P. Bertsch, S. Isabettoni and P. Fischer, *Biomacromolecules*, 2017, **18**, 4060.
- 9 (a) L. Mendoza, W. Batchelor, R. F. Tabor and G. Garnier, *J. Colloid Interface Sci.*, 2018, **509**, 39; (b) J. Schmitt, V. Calabrese, M. A. da Silva, S. Lindhoud, V. Alfredsson, J. L. Scott and K. J. Edler, *Phys. Chem. Chem. Phys.*, 2018, **20**, 16012; (c) H. Dong, J. F. Snyder, K. S. Williams and J. W. Andzelm, *Biomacromolecules*, 2013, **14**, 3338; (d) L. Geng, X. Peng, C. Zhan, A. Naderi, P. R. Sharma, Y. Mao and B. S. Hsiao, *Cellulose*, 2017, **24**, 5417.
- 10 Xiaoyun Qiu and Shuwen Hu, *Materials*, 2013, **6**, 738.
- 11 (a) X. Luo and L. Zhang, *J. Hazard. Mater.*, 2009, **171**, 340; (b) R. H. Marchessault, P. Rioux and L. Raymond, *Polymer*, 1992, **33**, 4024; (c) X. Sun, L. Yang, Q. Li, J. Zhao, X. Li, X. Wang and H. Liu, *Chem. Eng. J.*, 2014, **241**, 175.
- 12 (a) D. A. North, R. Harrop, G. O. Phillips and P. J. Baugh, *Polymer Photochemistry*, 1982, **2**, 309; (b) F. X. Redl, O. Köthe, K. Röckl, W. Bauer and J. Daub, *Macromol. Chem. Phys.*, 2000, **201**, 2091; (c) K. Junka, J. Guo, I. Filpponen, J. Laine and O. J. Rojas, *Biomacromolecules*, 2014, **15**, 876.
- 13 (a) S. Kitagawa and K. Uemura, *Chem. Soc. Rev.*, 2005, **34**, 109; (b) X. Zhang, W. Wang, Z. Hu, G. Wang and K. Uvdal, *Coord. Chem. Rev.*, 2015, **284**, 206.
- 14 H. Zhu, Q. Zhang and S. Zhu, *ACS Appl. Mater. Interfaces*, 2016, **8**, 17395.
- 15 I. Imaz, M. Rubio-Martínez, W. J. Saletta, D. B. Amabilino and D. Maspocho, *J. Am. Chem. Soc.*, 2009, **131**, 18222.
- 16 H. Wu, C. Tian, Y. Zhang, C. Yang, S. Zhang and Z. Jiang, *Chem. Commun.*, 2015, **51**, 6329.
- 17 V. Calabrese, M. A. da Silva, L. Porcar, S. Bryant, K. M. Z. Hossain, J. L. Scott and Karen J. Edler, "Filler size effect in an attractive fibrillated network investigated via small and large amplitude oscillatory shear rheology", manuscript in preparation.
- 18 (a) T. Saito and A. Isogai, *Biomacromolecules*, 2004, **5**, 1983; (b) T. Saito, S. Kimura, Y. Nishiyama and A. Isogai, *Biomacromolecules*, 2007, **8**, 2485; (c) A. Isogai, T. Saito, H. Fukuzumi, *Nanoscale*, 2011, **3**, 71.
- 19 (a) D. da Silva Perez, S. Montanari and M. R. Vignon, *Biomacromolecules*, 2003, **4**, 1417; (b) V. Calabrese, J. C. Muñoz-García, J. Schmitt, M. A. da Silva, J. L. Scott, J. Angulo, Y. Z. Khimyak and K. J. Edler, *J. Colloid Interface Sci.*, 2019, **535**, 205.
- 20 (a) C. A. Schneider, W. S. Rasband and K. W. Eliceiri, *Nat. Methods*, 2012, **9**, 671; (b) J. Schindelin, I. Arganda-Carreras and E. Frise, 2012, *Nat. Methods*, **9**, 676.

CHAPTER 7

CORE-SHELL SPHEROIDAL HYDROGELS PRODUCED VIA CHARGE-DRIVEN INTERFACIAL COMPLEXATION

In Chapter 6 we described the formation of spheroidal hydrogels through the enhancement of interfibrillar attractive interactions due to the ion induced charge screening of the fibrils as described in section 1.3.1. The resulting spheroidal hydrogels have a homogeneous structure due to the uniform diffusion of ions in the cellulose matrix. Contrarily, in the following Chapter we describe the fabrication of millimetre-sized core-shell spheroidal hydrogels through a charge-driven interfacial complexation process between a large Mw polymer and the oppositely charged cationic cellulose nanofibrils (CCNF).

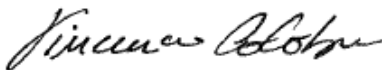
In the past decade, many reports focused on the production of alginate beads through the extrusion of sodium alginate in a divalent counterion-rich aqueous bath (commonly Ca^{2+}).^[174–177] This type of gelation has been often referred to as ionotropic gelation although it is in principle based on counterion charge screening as discussed in Chapter 1. Such alginate beads have thoroughly studied due to promising features for encapsulation and release of active components. Specifically, factors such as alginate concentration, pH and ionic strength enabled structural rearrangements of the porous gel matrix, tuning retention and release of the incorporated components.^[175] However, the lack of an outer membrane having a specific cut-off size does not make alginate beads perfect for applications where long-term storage of the incorporated components is desired. For instance the retention of emulsions droplets within alginate beads at different alginate concentration, ionic strength and pH was unsuccessful.^[176] Since the retention of μm -sized droplets in alginate beads is not effective, the long-term retention of smaller components as proteins and colloidal particles is not promising.

Core-shell capsules, produced through a targeted alginate gelation have been demonstrated to be valid materials for the retention of cells^[178] and yeasts^[179]. However, the dissolution of the alginate-based shell occurring in the presence of electrolytes in the water media is a limiting factor for potential applications.^[180] In addition, a combination of ionotropic gelation and charge-driven interfacial complexation process have been used to form more robust capsules, for instance, extruding a sodium alginate solution in an aqueous solution rich in both counterions and oppositely charged polymers.^[181–183] On the contrary, unstable and irregular capsules were reported by Lack et al. when the charge-driven interfacial complexation process was not coupled with the ionotropic gelation.^[181]

In this study, we use the charge-driven interfacial complexation between CCNF and negative charged polyacrylic acid (PAA) to form spheroidal hydrogels with a liquid-like core and a solid-like shell; this latest allowing inwards and outwards migration of (macro)molecules by analogy with a semi-permeable membrane. As such, the spheroidal hydrogels could swell or de-swell in according

to the osmotic pressure difference between the core and the surrounding media. Although the liquid-like core may represent a weakness of the spheroidal hydrogels, especially regarding their resilience, this feature is highly recommended for applications in bio-catalysis where a quick diffusion of targeted species is desired from and/or into the hydrogel. Common bio-microreactors are constituted by covalently immobilized enzymes on a substrate.^[184] However, this type of bio-microreactor often encounters drawbacks related to costs, laborious purification procedures (after covalent immobilization of the enzyme) and the reduction of the enzymatic activity due to their conformational change.^[184–186] As such, in the following Chapter, we demonstrate the ability of these spheroidal hydrogels to be valid enzymatic bio-microreactors for biocatalysis, where enzymes are physically entrapped in the core whilst substrate and product are freely able to migrate through the shell.

Supporting information available in section 10.5.

This declaration concerns the article entitled:									
Core-shell spheroidal hydrogels produced via charge-driven interfacial complexation									
Publication status (tick one)									
draft manuscript	<input type="checkbox"/>	Submitted	<input checked="" type="checkbox"/>	In review	<input type="checkbox"/>	Accepted	<input type="checkbox"/>	Published	<input type="checkbox"/>
Publication details									
Candidate's contribution to the paper (detailed, and also given as a percentage).	<p>The candidate contributed to/ considerably contributed to/predominantly executed the...</p> <p>Formulation of ideas: -The initial idea was formulated by VC based on preliminary observations conducted by AP and AMP. 85%</p> <p>Design of methodology: -All the measurements were designed by VC with exception of the enzymatic activity test designed by DC. 80%</p> <p>Experimental work: - The experimental work was conducted by VC (90%). - The data analysis was conducted by VC (95%)</p> <p>Presentation of data in journal format: -The first draft was written by VC with contribution of DC to the writing of the section regarding the enzymatic activity test. Subsequent drafts were reworked by VC following feedback from MS, JS, SB, KMZH, AMP, AP, JLS and KJE. 90%</p>								
Statement from Candidate	This paper reports on original research I conducted during the period of my Higher Degree by Research candidature.								
Signed						Date	13/12/19		

Core-shell spheroidal hydrogels produced *via* charge-driven interfacial complexation

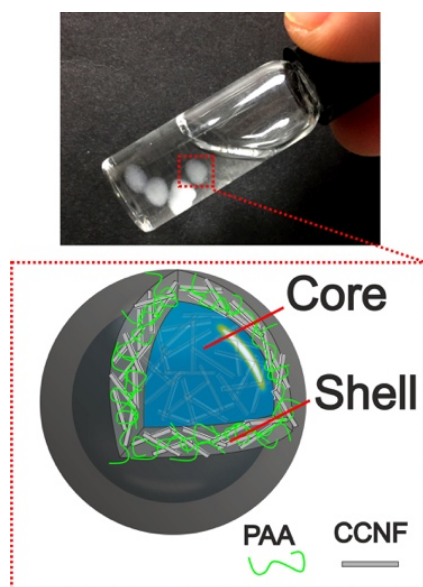
Vincenzo Calabrese,^a Davide Califano^{a,b}, Marcelo A. da Silva,^a Julien Schmitt,^{a,†} Saffron Bryant,^a Kazi M. Zakir Hossain,^a Ana M. Percebom,^c Aurora Pérez Gramatges,^c Janet L. Scott,^{a,b} Karen J. Edler^{a*}

^a Department of Chemistry, University of Bath, Claverton Down, Bath, BA2 7AY, United Kingdom

^b Centre for Sustainable Chemical Technologies, University of Bath, Claverton Down, Bath, BA2 7AY, United Kingdom

^c Department of Chemistry, Pontifical Catholic University of Rio de Janeiro (PUC-Rio), 22451-900 Rio de Janeiro, RJ, Brazil

[†] current address: LSFC Laboratoire de Synthèse et Fonctionnalisation des Céramiques, UMR 3080 CNRS / Saint-Gobain CREE, Saint-Gobain Research Provence, 550 avenue Alphonse Jauffret, Cavailon, France



Keywords: complex precipitate, cellulose, enzyme entrapment, glucose oxidase, biocatalysis.

Abstract

Through charge-driven interfacial complexation, we produced millimetre-sized spheroidal hydrogels (SH) with a core-shell structure allowing long term stability in aqueous media. The SH were fabricated by extruding, drop-wise, a cationic cellulose nanofibril (CCNF) dispersion into an oppositely charged polyacrylic acid (PAA) bath. The SH have a solid-like CCNF-PAA shell, acting as a semi-permeable membrane, and a liquid-like CCNF suspension in the core. Swelling behaviour of the SH was dependent on the osmotic pressure of the ageing media. Swelling could be suppressed by increasing the ionic strength of the media as this enhanced interfibrillar interactions and thus strengthened the outer gel membrane. We further validated a potential application of SH as re-usable matrixes for glucose oxidase (GOx) entrapment, where the SH work as “microreactors” from which substrate and product are freely able to migrate, through the SH shell whilst avoiding enzyme leakage.

Introduction

Segregative phase separation is a common phenomenon observed upon mixing of oppositely charged polyelectrolytes.¹ When two oppositely charged polyelectrolytes are mixed, they spontaneously form a polyelectrolyte-rich segregated phase, named a complex coacervate or complex precipitate, and a polyelectrolyte-poor coexisting phase containing mainly uncomplexed polyelectrolytes. This behaviour is the consequence of the favourable mixing enthalpy and increased entropy due to counterion release.^{2,3} Chollakup *et al.* established a phenomenological-based difference between complex coacervates and complex precipitates, the first being liquid-like whilst the second is solid-like.⁴ Since the first theoretical description of charge-driven polyelectrolyte complexation by Voorn and Overbeek,¹ many studies focused on the applicability of the theory for well-defined polyelectrolyte-based systems.^{2,5} Nevertheless, complex coacervates and complex precipitates produced by mixing of soluble polyelectrolytes with dispersed colloidal mixtures have also been reported.³ The formation of complex coacervates or precipitates depends on the molar ratio, $f = c^+/(c^+ + c^-)$, between the positively (c^+) and negatively (c^-) charged moieties; where $f = 0.5$ corresponds to a 1:1 stoichiometric ratio, whilst, $f > 0.5$ and $f < 0.5$ correspond to the excess of polycation or polyanion, respectively.^{5,6} Spruijt *et al.* showed that independent of the polycation/polyanion molar ratio, the coacervate maintains an equimolar ratio ($f \cong 0.5$), and the excess polyelectrolyte stays in the coexisting phase.⁶ Ionic strength and pH are also crucial factors in the formation and stability of coacervates or precipitates with the coexisting phase.^{2,4,5,7} For instance,

Hamad *et al.* demonstrated that by increasing the ionic strength, the coacervate exhibited a more liquid-like behaviour; they attributed this to the lowering of the electrostatic attraction between oppositely charged moieties, thus facilitating chain motion.⁵

The charge-driven complexation of polyelectrolytes and colloids has been broadly employed for the fabrication of capsules and drug carriers.^{8,9} This method exploits the labile nature of the physical cross-links to fabricate materials with mechanical properties that depend on external stimuli (e.g. pH and ionic strength). Charge-driven complexation has been successfully extended to two immiscible phases, often referred to as interfacial complexation.^{10,11} In this case, one charged species is solubilized or dispersed in one phase (e.g. water), with an oppositely charged species in the second immiscible phase (e.g. oil); the two species then complex across the liquid-liquid interface. This method has been shown to form strong interfaces, resulting in the formation of stable emulsions and microcapsules.^{10,11}

Analogously to the interfacial complexation method, we utilize the charge-driven complexation of cationic cellulose nanofibrils (CCNF) and polyacrylic acid (PAA) as a simple methodology to fabricate millimetric spheroidal hydrogels (SH) with long term stability in aqueous and saline media; this method relies on the formation of an irreversible complex precipitate at the SH/water interface, with a solid-like shell (SH-shell), and a liquid-like core (SH-core) composed of un-complexed particles. Similar core-shell structures have been previously reported, for instance by co-extruding an alginate solution around a second liquid phase (either water or oil) and precipitating the core-shell droplet into a divalent cation bath (sometimes referred to as ionotropic gelation¹²), leading to the gelation of the alginate around a liquid core.^{13,14} Although these structures have long-term stability in water, they have a limited life span in the range of just a few minutes when stored in a monovalent electrolyte solution, even at concentrations as low as 10 mM, due to alginate dissolution.¹³ The use of charge-driven complexation for the production of core-shell structures at the micro and nanoscale, has been broadly reported,¹⁵ whilst, to our knowledge, stable macroscopic core-shell porous hydrogels have only been reported using a combination of ionotropic gelation and charge-driven complexation of oppositely charged species.¹⁶⁻¹⁸ Macroscopic core-shell hydrogels offer applications in tissue engineering, cell culture, enzyme entrapment and controlled delivery of active excipients. Driven by the potential applications of SH in biotechnology applications, we investigated the structure-property relationship of cellulose-based SH in relevant conditions, providing a proof-of-concept application of SH as matrixes for enzyme entrapment.

Materials and methods

Preparation of the CCNF *via* grafting of the glycidyltrimethylammonium chloride (GTMAC) ($\geq 90\%$, Sigma-Aldrich®), was conducted as previously described,¹⁹ following the semi-dry protocol of Zaman *et al.*²⁰ resulting in a degree of substitution of 26% as measured by conductimetric titration.²¹

To fabricate the SH, a 2.0 wt% CCNF dispersion was extruded, drop-wise ($17.8 \pm 0.2 \mu\text{L}$), into a 0.1 wt% PAA (Sigma-Aldrich®, $M_v \sim 450 \text{ kDa}$) aqueous solution (50 mL), using a syringe equipped with a blunt end polypropylene dispensing tip (Fisnar Inc. – gauge 21 - inner diameter 0.513 mm, the tip positioned at *ca.* 2 cm from the PAA solution-air interface) and the SH aged for 5 min except where stated otherwise. A maximum of 50 SH were produced using the same PAA bath to ensure a large excess of the polyanion (estimation of f presented in the †ESI). The SH were thoroughly rinsed in deionised (DI) water ($18.2 \text{ M}\Omega \text{ cm}$) to remove any excess PAA before every experiment.

To image the SH-shell, the SH were fractured on a glass slide and images acquired using an optical microscope (Brunel Ltd SP200 equipped with a Canon EOS 1300D).

The retention of amphiphilic non-ionic species within the SH was probed *via* surface tension (Du Noüy ring method). A series of 2.0 wt% CCNF dispersions were loaded with 500 μM of Pluronic® F-127 ($M_w = 12.6 \text{ kDa}$) (F-127), 5 μM of 2-hydroxyethylcellulose ($M_w \sim 380 \text{ kDa}$, 2HEC-380, Sigma-Aldrich®) or 0.5 μM of 2-hydroxyethylcellulose ($M_v \sim 1300 \text{ kDa}$, 2HEC-1300, Sigma-Aldrich®). The SH were produced as previously described, and, a specific number of SH aged for three days in 50 mL of 100 mM NaCl solution (respectively 1, 3 and 3 SH for the F-127, 2HEC-380 and 2HEC-1300). The concentration of the amphiphilic species in the CCNF dispersion, as well as the number of SH aged in the same vial, was chosen to *i*) allow detection at the water-air (W/A) interface, *ii*) avoid saturation of the W/A interface, and, *iii*) be as low as possible to avoid significant change in the SH structure. The W/A surface tension (γ) of the ageing media was measured before and after SH breakage using the Du Noüy ring method (Sigma 701 instrument, Attension, Sweden, equipped with a 9.58 mm platinum ring and a vessel of 66 mm in diameter). Breakage of the SH was conducted employing a homogenizer (Ultra Turrax, IKA T25 digital, 30 s at 6500 rpm). Unloaded SH were employed as controls to ensure that the the SH on their own did not affect γ before or after breakage.

Immediately after the fabrication of the SH, their swelling was monitored by placing them in quartz cuvettes ($1 \times 1 \text{ cm}$) containing 1 mL of different continuous phases (DI water, 0.1 wt% PAA, and 1000 mM NaCl solution) and pictured over time (using a Drop Shape Analyzer – DSA30R). From the pictures, the area of the SH (A) was obtained *via* imaging analysis (ImageJ) and normalized as A_i/A_0 ,

where A_i is the area at time = i and A_0 the area at time = 0. The presented data were obtained from three separate experiments.

To study the effect of the osmotic pressure of the continuous media (Π_m) on the swelling properties of the SH, the swelling ratio (SR) of the SH aged in different media was obtained gravimetrically as $SR = W_{SH}/W_{droplet}$ where W_{SH} is the weight of a single SH and $W_{droplet}$ is the weight of a droplet of the CCNF dispersion used to fabricate SH. A SR of >1 , <1 , and $=1$ correspond to swelling, de-swelling and equilibrium, respectively. SH were separately aged in 2 mL solutions containing various concentrations of either NaCl or polyethylene glycol (PEG) ($M_n = 0.4$ kDa, Sigma-Aldrich®, Lot #BCBN5570V) for 3 days at room temperature. Concentrations of NaCl and PEG were chosen in order to match Π_m . The Π_m of NaCl solutions was calculated using the van't Hoff equation, $\Pi_m = MRT$, where M is the molarity (mol/L), R is the gas constant ($8.31 \cdot 10^3$ Pa L/mol K) and T is the temperature (K). The Π_m of PEG solutions was instead calculated using the empirical equation derived by Stanley and Strey²². The data shown are the average of 5 separate experiments.

The rheological measurements of 2.0 wt% CCNF hydrogels (prepared by diluting the CCNF stock dispersion with DI water and a 2.5 M NaCl solution) were performed using a stress-controlled rheometer (Discovery HR3, TA instruments®) equipped with a sandblasted stainless-steel plate-plate geometry (40 mm). Strain sweep experiments were conducted at 1 rad s^{-1} angular frequency and the $\tan \delta$ ($\tan \delta = G''/G'$, G' being the storage modulus and G'' the loss modulus) obtained from the linear viscoelastic region. The reported values are obtained from duplicate samples.

ζ -potential measurements were performed using a Malvern Zetasizer Nano ZSP® (Malvern, UK). CCNF hydrogels, prepared as for the rheological test, were diluted 100 fold using NaCl solutions at the same concentration as for the original sample, placed in the folded capillary electrode cell and the ζ -potentials measured as an average of 4 measurements from 100 scans each. The ζ -potential values reported here were obtained from the average of three separate samples.

Small angle X-ray scattering (SAXS) measurements on films of CCNF-PAA complexes which mimic the droplet interface were performed at Diamond Light Source (Didcot, Oxfordshire, UK), on the I22 beamline (beam energy $E = 12.4$ keV and wavelength $\lambda = 1 \text{ \AA}$). The data were collected using a Pilatus P3-2M (Silicon hybrid pixel detector, DECTRIS) with a total acquisition time of 7 s (as an average of multiple frames of 100 ms). The CCNF-PAA film was prepared by pouring, dropwise, 50 mL of 0.1 wt% PAA solution into 25 mL of 0.5 wt% CCNF dispersion under continuous stirring, allowing complete complexation of the oppositely charged moieties (and excess of un-complexed PAA ($f \cong$

0.19)). The complex precipitate was compressed between two stainless-steel plate with the aid of a rheometer (Discovery HR3, TA instruments®) to form a film of approximately 1 mm thickness and thoroughly rinsed with DI water, to remove any excess of un-complexed PAA, prior to ageing in a concentration series of NaCl solutions. After 48 h ageing SAXS measurements were performed. The wet films were removed from their media, placed in a film holder and measured in air. The time between sample loading and measurement was kept below 5 min (allowing for hutch search and motor movement), avoiding significant drying of the sample. The SAXS pattern of the 2.0 wt% CCNF dispersion was obtained after loading the suspension into glass capillary tubes (Capillary tube supplies Ltd®) of 1.5 mm external diameter. All the scattering data were background subtracted and transmission corrected; for the CCNF dispersion the SAXS pattern was corrected for the capillary and solvent contribution. CCNF-PAA films were modelled as fractal aggregates composed by cylindrical building blocks of radius R, length L corresponding to the characteristic node-to-node distance between cylinders, fractal dimension D, and a correlation length of the aggregate ξ , which defines the fractal length scale (i.e. aggregate size). This model couples the form factor of randomly oriented homogeneous cylinders, $P_{cyl}(q) = P_{cyl}(q, R, L)$, with a structure factor, $S(q) = S(q, \xi, D)$, describing a fractal structure as derived by Teixeira,²³ to compute the scattering intensity $I(q)$ (eqn. 1).^{24,25}

$$I(q) \propto P_{cyl}(q) S(q) \quad (1)$$

In order to reduce the number of fitting parameters, R was extracted from the fitting of the scattering pattern of CCNF dispersion at 2.0 wt% in the high-q region, using the $P_{cyl}(q)$ model (scattering pattern of CCNF in †ESI Fig. S1). It was then fixed to 2.0 nm for the study of the CCNF-PAA films; this length scale being in close agreement with our previous study.¹⁹ Background subtraction and data treatment were performed using the Irena package²⁶ whilst data analysis was done using the NIST SANS Analysis package from which the described model was used without further modification,²⁷ both within IGOR Pro (Wavemetrics, Inc.).

The enzyme retention within the SH matrix was studied using SH loaded with glucose oxidase (GOx) (EC 1.1.3.4, from *Aspergillus niger*, 100-250 units/mg). The SH were fabricated as previously described, employing 2.0 wt% CCNF dispersions containing GOx concentrations of 3.12, 6.25, 12.5, 25, 50 and 75 $\mu\text{g/mL}$. A GOx stock solution, prepared in phosphate buffer (100 mM, pH 6), was used to reach the specific concentrations required. The GOx loaded SH were thoroughly rinsed in DI water and immersed in a reaction well containing 125 μL of phosphate buffer. Afterwards, the well plate was placed on an orbital shaker, and, an aqueous glucose solution (D-(+)-Glucose 99% Sigma-Aldrich®)

added (final concentration of 44 mM in 500 μ L). To quantify the produced H_2O_2 , aliquots of the continuous media (20 μ L) were withdrawn every 5 min (for 25 min) and mixed with horseradish peroxidase, HRP, (EC Type II, EC 1.11.1.7, from Horseradish, 150-250 units/mg solid), phosphate buffer and AmplexTM Red (ThermoFisher Scientific), to reach final concentrations of 7.5 U/mL, 20 mM and 5 μ g/mL, respectively. The product of AmplexTM Red oxidation, resorufin, produced in a 1:1 stoichiometric ratio with H_2O_2 was quantified using fluorescence spectroscopy; the samples measured in a black 96 well plate using a plate reader (FLUOstar Omega, BMG-LABTECH, excitation and emission of 540 nm and 590 nm, respectively). H_2O_2 concentration was calculated using a standard curve employing known concentrations (provided by ThermoFisher Scientific and confirmed by titration against potassium permanganate). The GOx activity was determined by the conversion rate of the substrate (glucose) into the reaction product (H_2O_2) per unit time and per unit volume ($mU \cdot ml^{-1}$).

The reusability experiment was performed by cyclically monitoring the activity of the GOx-loaded SH upon repetitive catalytic cycles (4 cycles), over a time span of 8 days. Freshly prepared SH, utilizing the GOx-loaded CCNF dispersion made on day 1, were employed as control samples. All the samples were stored at 4°C, and the GOx-loaded SH were thoroughly rinsed before and after each catalytic cycle, and separately stored in 1.5 mL phosphate buffer (100 mM, pH 6). The reported values were obtained from the average of three independent samples.

Results and Discussion

The stability of the SH was found to be strongly dependent on the ageing media. The SH swell in DI water whilst acquiring long term stability (several months) in a media containing concentrations of NaCl greater than 10 mM. On this ground, the structure-to-stability relationship of the SH was evaluated as function of ageing media at different osmotic pressure Π_m .

At first, the morphological evidence of the core-shell structure of the SH was obtained upon breakage of the SH in DI water (Fig. 1a). The SH-shell showed characteristic wrinkles similar to water-in-oil capsules produced *via* interfacial complexation,²⁸ and it did not re-disperse over the probed time due to the irreversibility of the CCNF-PAA complexation. Contrarily, the gel structure within the SH-core slowly dispersed over time, indicating the presence of un-complexed CCNF. Microscope imaging of the SH-shell (Fig. 1b) displayed a thickness of *ca.* 1 μ m, confirming that the SH could be well depicted by a core-shell structure, containing un-complexed CCNF in the core and a CCNF-PAA complex across the SH/water interface, composing the SH-shell. On the basis of the phenomenological

characterization of Chollakup *et al.*, we define the CCNF-PAA complexation across the SH/water interface as a complex precipitate.⁴

Solutes can pass through the SH-shell if their size is similar or smaller than the typical mesh size of the SH-shell, this threshold is herein referred to as the cut-off size of the SH-shell. In order to qualitatively assess the cut-off size, the SH were loaded with surface active molecules and their leakage investigated by probing γ of the media containing unbroken or broken SH (Fig. 1c). However, it must be noticed that this technique does not probe the release kinetic of the loaded amphiphilic species, rather it enables evaluation their leakage or entrapment. F-127, having a Mw of 12.6 kDa, displayed complete release, as shown by almost superimposable γ curves before and after breakage, with, in both cases, a strong decrease of the air-water surface tension due to the presence of F127 at the interface. Contrarily, the probed amphiphilic molecules with Mw \geq 380 kDa (2HEC-380 and 2HEC-1300) did not leak from the SH matrix, as indicated by the unchanged $\gamma \approx 72$ mN/m before breakage, while a sudden drop is observed after breakage due to adsorption of the released amphiphilic molecules to the W/A interface. This experiment revealed the semi-permeable nature of the SH-shell and the ability of the SH to encapsulate large macromolecules while allowing small molecules to permeate through. Moreover, the unreleased molecules with Mw \geq 380 kDa from the SH, indicate that the PAA ($M_v \sim 450$ kDa) used to create the complex precipitate cannot migrate through the SH-shell after it has been formed.

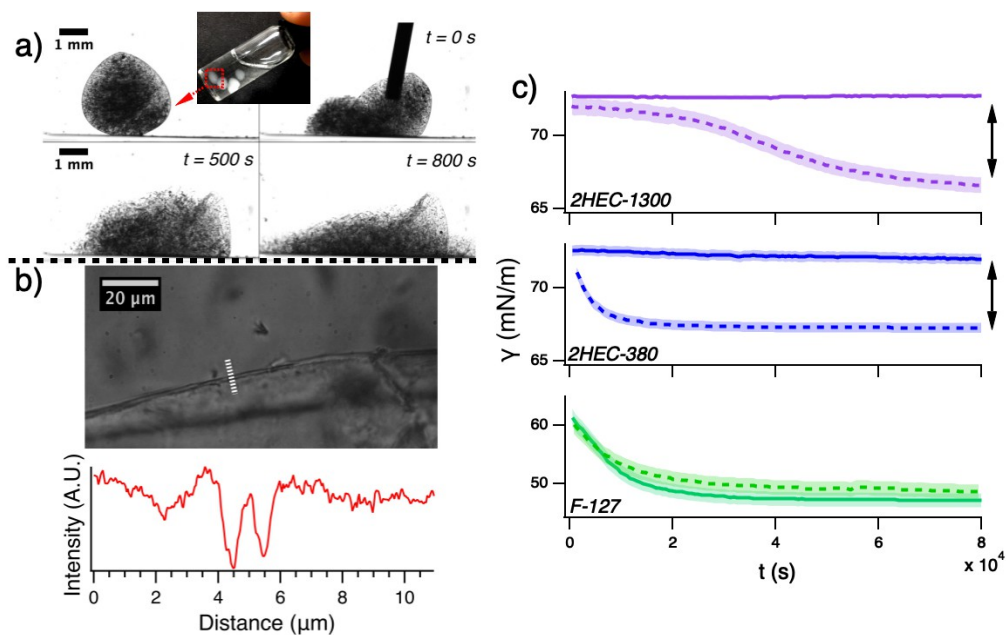


Fig. 1 (a) Images of the SH suspended in DI water before rupture, at the time of rupture, and after 500 and 800 s from rupture (top-left, top-right, bottom left and bottom right respectively). (b) Optical microscope image of the SH-shell (top) and the intensity profile of the SH-shell cross section as indicated by the white dotted line (bottom). (c) γ as a function of time of SH loaded with 2HEC-1300 (top), 2HEC-380 (center) and F-127 (bottom), before (filled line) and after rupture (dashed line). The standard deviation of duplicate samples is indicated by the shadow.

The SH swelling rate in media containing DI water, 1000 mM NaCl and 0.1 wt% PAA was monitored to gain information regarding the SH stability over time. The SH aged in DI water showed remarkable swelling over time (t) up to fracture, occurring at *ca.* 2400 s, clearly noticeable by the spillage of the CCFN dispersion from the SH, as well as scattered A_i/A_0 data points over time (Fig. 2a). This phenomenon suggests that the SH swelling occurs by stretching and thinning of the SH-shell up to formation of localized fracture points, from which the liquid-like CCFN dispersion present in the SH-core spills out. Moreover, the presence of a liquid-like SH-core supports the hypothesis that the CCFN-PAA complexation solely occurs across the SH-water interface, with the resulting SH-shell preventing PAA penetration into the SH-core.

The SH aged in 1000 mM NaCl solution showed minimal swelling up to *ca.* 1200 s, after which a steady state was reached (Fig. 2b). When SH were aged in the 0.1 wt% PAA solution, the swelling rate was constant over the experimental time, and no fracture of the SH-shell was observed up to 24 h (Fig.

2c inset). It is expected that upon swelling, the increase in stress along the SH-shell would induce fractures as previously described for DI water. However, the suppressed fracture of the SH-shell upon continuous SH swelling in 0.1 wt% PAA indicates that upon generation of new surface area, the uncomplexed CCNF of the SH-core is exposed to the SH/water interface and quickly complexes with PAA in the aging media; the PAA is acting as a “patch”.

Comparison of the three ageing media showed that the swelling rate of the SH, as captured by $k = \frac{d(A_i/A_0)}{dt}$, was substantially greater for DI water compared to the 0.1 wt% PAA and 1000 mM NaCl media, respectively (Fig. 2b inset). In principle, these dissimilarities could be justified by the mismatch of the osmotic pressure in the SH (Π_{SH}) and Π_m . Nevertheless, electrostatic interactions between the charged moieties of the SH and the electrolyte-rich media need to be accounted for.

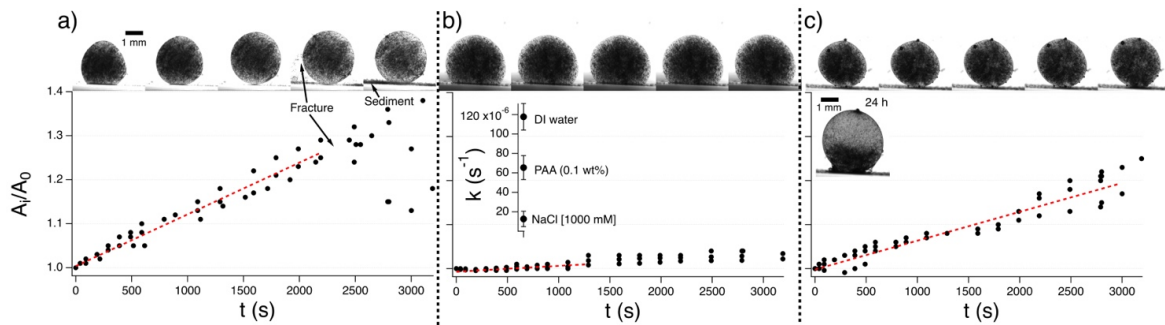


Fig. 2 Ageing of SH in (a) DI water, (b) 1000 mM NaCl and (c) 0.1 wt% PAA. SH images are shown on the top of the graphs in line with the time evolution indicated by the x-axis. Dotted lines indicated the region where the linear fittings were adopted to calculate the swelling rate, $k = \frac{d(A_i/A_0)}{dt}$, displayed as an inset in (b). Image of the 24 h SH aged in 0.1 wt% PAA solution shown as an inset in (c).

As such, to evaluate the role of the osmotic pressure of the media on the SH stability, a systematic study of the SH swelling behaviour was conducted in media containing different concentration ranges of NaCl and PEG at comparable values of Π_m . The use of non-ionic polyethylene glycol (PEG) allowed the investigation of the SH swelling behaviour due to changes in osmotic pressure, Π_m . Contrarily, the use of NaCl coupled changes in Π_m and charge screening of both CCNF and PAA. Both species are however small enough to pass unhindered through the interfacial membrane, allowing the system to reach an equilibrium swelling over time.

Surprisingly, the SH did not exhibit substantial swelling or de-swelling over a large span of NaCl concentrations, and consequently Π_m , tested; the $SR \cong 1$ (Fig. 3a, top). Since different swelling behaviours are expected upon changes in Π_m , we hypothesise, based on the swelling theory of ionic polymeric networks, that the increase of ionic strength would gradually enhance CCNF interactions, augmenting the elasticity of the network and suppressing both swelling and de-swelling.²⁹ To test the hypothesis, a concentration series of a non-ionic polymer, PEG, solutions were prepared to match the Π_m of the NaCl solutions. The use of PEG revealed a clear transition from a swelling (Π_m below $\cong 5 \times 10^5$ Pa, $\cong 6.26$ PEG wt%) to a de-swelling regime upon increasing Π_m above 5×10^5 Pa (Fig. 3a, bottom), a missing feature for the case of the NaCl containing media. The lack of further swelling at the lower PEG concentrations (≤ 1.74 wt%) and the sedimented CCNF at the bottom of the vial indicated that swelling occurred up to the SH-shell fracture. As such, this experiment revealed that the swelling and de-swelling of the SH could be either modulated via the osmotic pressure of the uncharged medium, or even strongly suppressed through modulation of the ionic strength in the media, confirming our hypothesis.

The strength of the SH arises from both the shell and the core, hence, the two contributions must be considered separately. Since the SH-core is PAA-free, the effect of NaCl on the SH-core was probed through ζ -potential and oscillatory rheology measurements of the 2.0 wt% CCNF hydrogels (not in the SH form) to gain information on interfibrillar interactions within the SH-core (Fig. 3b). ζ -potential of CCNF was found to decrease upon NaCl addition, indicating neutralization of the positively charged moieties *via* electrostatic screening. Noticeably, addition of 10 mM NaCl was sufficient to overcome the repulsive electrostatic regime, leading to enhancement of short-ranged interfibrillar attractions.³⁰ The $\tan \delta$ of the CCNF hydrogels followed a similar trend as for ζ -potential, indicating the formation of a more pronounced gel-like interconnected network upon addition of NaCl, as previously observed for similar systems.³¹ These results support the hypothesis of network strengthening in the SH-core, although the properties of the solid precipitated SH-shell upon NaCl addition were not directly assessed.

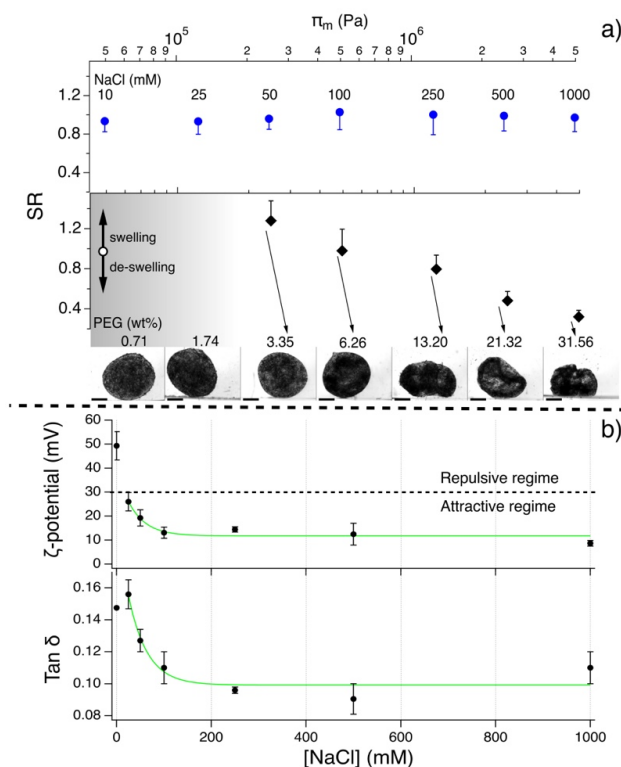


Fig. 3 (a) Swelling Ratio (SR) as a function of Π_m for NaCl (top) and PEG (bottom) solutions, along with images of SH with PEG. Data points are labelled with concentration of NaCl (mM) and PEG (wt%). Data points for the SH at PEG concentrations ≤ 1.74 wt% were not acquired due to the pronounced swelling and fracture of the SH-shell as displayed by the gray background. (b) ζ -potential measurements and (c) $\tan \delta$ of the 2.0 wt% CCNF hydrogels shown as a function of NaCl concentration. The lines are drawn to guide the eye.

Since insights into the SH-shell structure at the nm length scale are very complicated to obtain *in situ*, we mimicked the SH-shell structure by preparing CCNF-PAA films aged at different NaCl concentrations and probing their microstructure *via* SAXS (Fig. 4a). All the SAXS patterns displayed similar high-q patterns, associated with the CCNF cross-section, as for the pure CCNF (\dagger ESI Fig. S1), confirming the main contribution of CCNF to the scattering intensity in the CCNF-PAA films, as well as unvaried CCNF cross-section upon addition of NaCl.

A pronounced difference between samples was noticeable in the intermediate-q and low-q range. In these ranges, greater length scales than the CCNF cross-section are probed (*e.g.* persistence length). The SAXS patterns did show the absence of a Guinier region (a plateau in the low-q region), indicating

that the characteristic dimension of the object is not fully probed. Moreover, the low- q slopes substantially diverged from a q^{-1} slope which is associated with scattering from dilute solutions of elongated objects, indicating a pronounced level of interactions between CCNF.³¹

In order to better compare the SAXS patterns, the CCNF-PAA were modelled as fractal aggregates composed of cylinders as building-blocks (as schematically represented in Fig. 4a, inset). The L yielded by the model did not show a pronounced variation in the 50-1000 mM NaCl range, indicating that the characteristic node-to-node distance of the fractal network is constant, whilst a smaller value of L was obtained in the absence of NaCl (Fig. 4b, top). It is noted that the value of ξ was found to be much greater (at least by one order of magnitude) than the values of radius of gyration, R_g , of the cylindrically shaped CCNF ($R_g^2 = (R^2/2) + (L^2/12)$)³², indicating that both L and D are independent of the value of ξ (values of ξ in †ESI Fig. S2).²⁷

The values of D obtained from the fractal model followed a gradual increase with increasing NaCl concentration from 50 to 1000 mM, indicating a densification of the aggregates (Fig. 4b, bottom). In the literature, the response of oppositely charged polyelectrolytes to subsequent addition of salt has been reported to, *i*) reduce aggregation up to dissolution, *ii*) induce additional aggregation or *iii*) have a negligible effect depending on the characteristic of the polyelectrolytes.^{4,5,7,33-35} Specific instances of *i*), were provided by Hamad *et al.*⁵ and Spruijt *et al.*⁷ who found an increase in mesh size and a more pronounced liquid-like behaviour in polyelectrolyte mixtures upon increase of ionic strength due to diminishing polycation-polyanion attractive forces. The case of additional aggregation (*ii*) upon addition of NaCl has been reported by Dautzenberg and coworkers,³³⁻³⁵ referred to as secondary aggregation, and mainly attributed to the presence of strongly ionic groups and a mismatch in charge density between the oppositely charged polyelectrolytes. Chollakup *et al.* reported on the secondary aggregation of PAA-Poly(allylamine) coacervates upon NaCl addition and this behaviour was assigned to the polyelectrolyte charge screening and/or a diminished solvent quality.⁴ Similarly, it is possible that for the CCNF-PAA complexation, the enhanced aggregation of the fibrillar particles upon NaCl addition arises due to the charge screening of neighbouring, un-complexed, charged moieties of CCNF allowing these to aggregate further. It is noted that the pattern of increasing D upon NaCl addition does not apply to the case of 0 mM NaCl where D displayed a greater value than in the 50-500 mM NaCl range. This may be addressed by the substantially smaller building-blocks of the network, as captured by the characteristic node-to-node distance between fibrils, L , in the absence of NaCl, which would allow better packing and consequently a denser network.

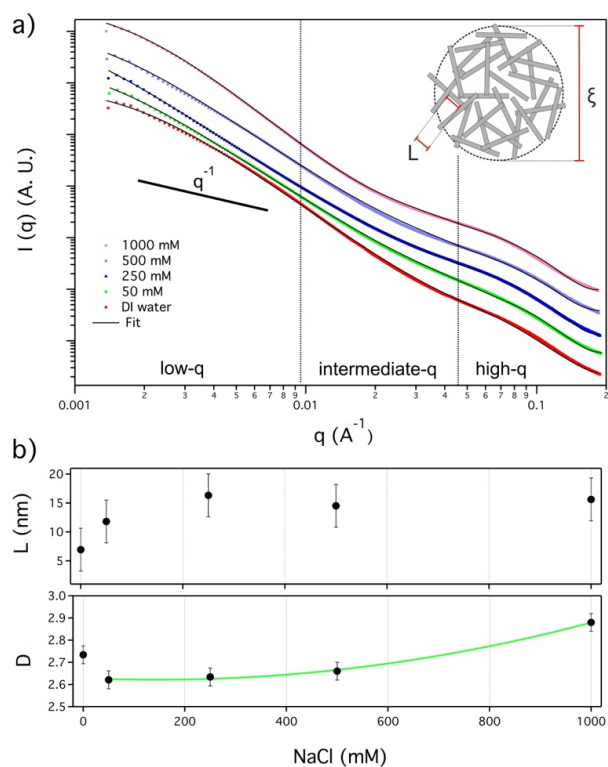


Fig. 4 (a) SAXS patterns of the CCNF-PAA films at different NaCl concentration fitted using a model of fractal cylinders.²³ (b) L (top) and D (bottom) values obtained by fitting of the fractal model to the SAXS data. The line is drawn to guide the eye.

Hydrogel beads have been broadly exploited for the encapsulation and release of active components.³⁶ Nonetheless, the long-term entrapment of macromolecules has been stressed as an outstanding challenge, limiting their application and reusability.^{37,38} On this ground, we investigated the entrapment of a model enzyme, GOx, within SH by monitoring its catalytic activity. As expected, the GOx activity increased as a function of the concentration loaded into the SH. More interestingly, the activity of the GOx-loaded SH approached a plateau at higher concentrations, suggesting limited substrate diffusion into the SH matrix (Fig. 5). The 50 $\mu\text{g/mL}$ GOx-loaded SH were employed to test their reusability over a time span of 8 days (Fig. 5 inset). The GOx activity showed excellent retention of activity upon storage and catalytic cycles with only a minimal decay on the 5th day. The GOx activity measured on the 8th day was compared to a control sample of freshly prepared GOx-loaded SH, fabricated utilizing an 8 day vintage GOx-loaded CCNF dispersion. The GOx activity in the control sample showed a similar value to the GOx-loaded SH on the 8th day, indicating that no significant GOx leakage occurred upon storage or catalytic cycles. Moreover, the control sample showed a slightly

lower value compared to the GOx-loaded SH on day 1, suggesting that the long term GOx storage in aqueous media may be an influencing factor on its activity. The ability of the SH to retain enzymes for several days is a feature which differs from the previously reported alginate beads where substantial enzyme leakage occurred within a few hours.^{36–38} Moreover, the SH resilience in saline solutions, as demonstrated here by storage in phosphate buffer and NaCl differs from, for instance, alginate beads which undergo dissolution under similar conditions.^{13,14,36} This highlights the potential of these SH in biotechnological applications.

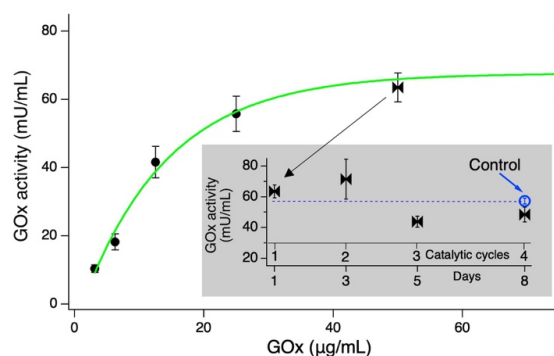


Fig. 5 The catalytic activity of GOx-loaded SH as a function of the initial GOx concentration in the CCNF dispersion (employed for the production of the SH); the line is drawn to guide the eye. Inset displays the activity of GOx-loaded SH upon catalytic cycles and as a function of storage time (4 °C).

Conclusion

This work aimed to characterise SH produced by a charge-driven interfacial complexation process. We found that *via* extruding, dropwise, a dispersion of positively charged cellulose nanofibrils, CCNF, into an aqueous bath containing negatively charged polymer, PAA, SH were formed. The SH were characterised by a liquid-like core, composed of un-complexed CCNF and a solid-like shell formed by the CCNF-PAA complexation. The SH-shell did not redisperse in pure water and saline environments, due to the irreversible CCNF-PAA complexation, and possessed characteristic features of a semipermeable membrane, allowing the release of small macromolecules (≤ 12.6 kDa) whilst retaining larger ones. Moreover, the semipermeable nature of the SH-shell allowed a tunable swelling behaviour of the SH according to the osmotic pressure of the continuous media. We found that insensitivity to swelling was achieved in saline media, associated with the enhancement of interfibrillar interactions in both the SH-core and the SH-shell. Furthermore, we validated the applicability of SH as suitable

matrixes for physical enzyme entrapment, allowing the use and re-use of SH as “microreactors” from which substrate and product are freely able to migrate through the SH whilst avoiding enzyme leakage.

Acknowledgements: The authors thank the EPSRC for funding parts of this project (grant number EP/N033310/1). V. Calabrese and D. Califano thank the University of Bath for funding their PhD studentships. We thank the Diamond Light Source for access to beamline I22 (SM20409-1) that contributed to the results presented here, and we would like to thank Dr N. Terrill, Dr. T. Snow and Dr A. Smith for their assistance with the experiment on beamline I22. Data supporting this work is freely accessible in the Bath research data archive system at DOI: 10.15125/BATH-XXXX.

References

- (1) Overbeek, J. T. G.; Voorn, M. J. Phase Separation in Polyelectrolyte Solutions. Theory of Complex Coacervation. *Philos. Stud.* **1957**, *49*, 7–26.
- (2) Evan Spruijt, Adrie H. Westphal, Jan Willem Borst, Martien A. Cohen Stuart, J. van der G. Binodal Compositions of Polyelectrolyte Complexes. *Macromolecules* **2010**, *43*, 6476–6484.
- (3) Kizilay, E.; Kayitmazer, A. B.; Dubin, P. L. Complexation and Coacervation of Polyelectrolytes with Oppositely Charged Colloids. *Adv. Colloid Interface Sci.* **2011**, *167* (1–2), 24–37.
- (4) Chollakup, R.; Smitthipong, W.; Eisenbach, C. D.; Tirrell, M. Phase Behavior and Coacervation of Aqueous Poly(Acrylic Acid)-Poly(Allylamine) Solutions. *Macromolecules* **2010**, *43* (5), 2518–2528.
- (5) Fawzi G. Hamad, Quan Chen, R. H. C. Linear Viscoelasticity and Swelling of Polyelectrolyte Complex Coacervates. *Macromolecules* **2018**, *51*, 5547–5555.
- (6) Spruijt, E.; Cohen Stuart, M. A.; Van Der Gucht, J. Linear Viscoelasticity of Polyelectrolyte Complex Coacervates. *Macromolecules* **2013**, *46* (4), 1633–1641.
- (7) Spruijt, E.; Leermakers, F. A. M.; Fokkink, R.; Schweins, R.; Van Well, A. A.; Cohen Stuart, M. A.; Van Der Gucht, J. Structure and Dynamics of Polyelectrolyte Complex Coacervates Studied by Scattering of Neutrons, X-Rays, and Light. *Macromolecules* **2013**, *46* (11), 4596–4605.

-
- (8) De Geest, B. G.; Sanders, N. N.; Sukhorukov, G. B.; Demeester, J.; De Smedt, S. C. Release Mechanisms for Polyelectrolyte Capsules. *Chem. Soc. Rev.* **2007**, *36* (4), 636–649.
- (9) De Geest, B. G.; Sukhorukov, G. B.; Möhwald, H. The Pros and Cons of Polyelectrolyte Capsules in Drug Delivery. *Expert Opin. Drug Deliv.* **2009**, *6* (6), 613–624.
- (10) Kaufman, G.; Boltyanskiy, R.; Nejati, S.; Thiam, A. R.; Loewenberg, M.; Dufresne, E. R.; Osuji, C. O. Single-Step Microfluidic Fabrication of Soft Monodisperse Polyelectrolyte Microcapsules by Interfacial Complexation. *Lab Chip* **2014**, *14* (18), 3494–3497.
- (11) Monteillet, H.; Hagemans, F.; Sprakel, J. Charge-Driven Co-Assembly of Polyelectrolytes across Oil–Water Interfaces. *Soft Matter* **2013**, *9* (47), 11270.
- (12) Segale, L.; Giovannelli, L.; Mannina, P.; Pattarino, F. Calcium Alginate and Calcium Alginate-Chitosan Beads Containing Celecoxib Solubilized in a Self-Emulsifying Phase. *Scientifica (Cairo)*. **2016**, No. ID 5062706, 1–8.
- (13) Rolland, L.; Santanach-Carreras, E.; Delmas, T.; Bibette, J.; Bremond, N. Physicochemical Properties of Aqueous Core Hydrogel Capsules. *Soft Matter* **2014**, *10* (48), 9668–9674.
- (14) Bremond, N.; Santanach-Carreras, E.; Chu, L. Y.; Bibette, J. Formation of Liquid-Core Capsules Having a Thin Hydrogel Membrane: Liquid Pearls. *Soft Matter* **2010**, *6* (11), 2484–2488.
- (15) Johnston, A. P. R.; Cortez, C.; Angelatos, A. S.; Caruso, F. Layer-by-Layer Engineered Capsules and Their Applications. *Curr. Opin. Colloid Interface Sci.* **2006**, *11* (4), 203–209.
- (16) Lacík, I.; Briššová, M.; Anilkumar, A. V.; Powers, A. C.; Wang, T. New Capsule with Tailored Properties for the Encapsulation of Living Cells. *J. Biomed. Mater. Res.* **1997**, *39* (1), 52–60.
- (17) Briššová, M.; Lacík, I.; Powers, A. C.; Anilkumar, A. V.; Wang, T. Control and Measurement of Permeability for Design of Microcapsule Cell Delivery System. *J. Biomed. Mater. Res.* **1997**, *39* (1), 61–70.
- (18) Krajčovič, T.; Bučko, M.; Vikartovská, A.; Lacík, I.; Uhelská, L.; Chorvát, D.; Neděla, V.; Tihlaříková, E.; Gericke, M.; Heinze, T.; et al. Polyelectrolyte Complex Beads by Novel Two-Step Process for Improved Performance of Viable Whole-Cell Baeyer-Villiger Monooxygenase by Immobilization. *Catalysts* **2017**, *7* (11), 1–12.

-
- (19) Calabrese, V.; Muñoz-García, J. C.; Schmitt, J.; da Silva, M. A.; Scott, J. L.; Angulo, J.; Khimyak, Y. Z.; Edler, K. J. Understanding Heat Driven Gelation of Anionic Cellulose Nanofibrils: Combining Saturation Transfer Difference (STD) NMR, Small Angle X-Ray Scattering (SAXS) and Rheology. *J. Colloid Interface Sci.* **2019**, *535*, 205–213.
- (20) Zaman, M.; Xiao, H.; Chibante, F.; Ni, Y. Synthesis and Characterization of Cationically Modified Nanocrystalline Cellulose. *Carbohydr. Polym.* **2012**, *89* (1), 163–170.
- (21) Hasani, M.; Cranston, E. D.; Westman, G.; Gray, D. G. Cationic Surface Functionalization of Cellulose Nanocrystals. *Soft Matter* **2008**, *4* (11), 2238–2244.
- (22) Stanley, C. B.; Strey, H. H. Measuring Osmotic Pressure of Poly(Ethylene Glycol) Solutions by Sedimentation Equilibrium Ultracentrifugation. *Macromolecules* **2003**, *36* (18), 6888–6893.
- (23) Teixeira, J. Small-Angle Scattering by Fractal Systems. *J. Appl. Crystallogr.* **1988**, *21* (6), 781–785.
- (24) Golosova, A. A.; Adelsberger, J.; Sepe, A.; Niedermeier, M. A.; Lindner, P.; Funari, S. S.; Jordan, R.; Papadakis, C. M. Dispersions of Polymer-Modified Carbon Nanotubes: A Small-Angle Scattering Investigation. *J. Phys. Chem. C* **2012**, *116* (29), 15765–15774.
- (25) Chen, C.-Y.; Chan, S.-H.; Li, J.-Y.; Wu, K.-H.; Chen, H.-L.; Chen, J.-H.; Huang, W.-Y.; Chen, S.-A. Formation and Thermally-Induced Disruption of Nanowhiskers in Poly(3-Hexylthiophene)/Xylene Gel Studied by Small-Angle X-Ray Scattering. *Macromolecules* **2010**, *43*, 7305–7311.
- (26) Ilavsky, J.; Jemian, P. R. Irena : Tool Suite for Modeling and Analysis of Small-Angle Scattering. *J. Appl. Crystallogr.* **2009**, *42* (2), 347–353.
- (27) Kline, S. R. Reduction and Analysis of SANS and USANS Data Using IGOR Pro. *J. Appl. Crystallogr.* **2006**, *39* (6), 895–900.
- (28) Kaufman, G.; Nejati, S.; Sarfati, R.; Boltyanskiy, R.; Loewenberg, M.; Dufresne, E. R.; Osuji, C. O. Soft Microcapsules with Highly Plastic Shells Formed by Interfacial Polyelectrolyte-Nanoparticle Complexation. *Soft Matter* **2015**, *11* (38), 7478–7482.
- (29) Flory, P. J. Principle of Polymer Chemistry; Press, Cornell University, 1953; pp 576–594.
- (30) Schramm, L. L. Suspensions : Basic Principles. In *Advances in chemistry*; 1996; Vol. 251, pp

21–22.

- (31) Schmitt, J.; Calabrese, V.; Da Silva, M. A.; Lindhoud, S.; Alfredsson, V.; Scott, J. L.; Edler, K. J. TEMPO-Oxidised Cellulose Nanofibrils; Probing the Mechanisms of Gelation: Via Small Angle X-Ray Scattering. *Phys. Chem. Chem. Phys.* **2018**, *20* (23), 16012–16020.
- (32) Hammouda, B. Part A, B, C, D, E, F, G. In *Probing Nanoscale Structures - The SANS toolbox*; National Institute of Standards and Technology Center for Neutron Research Gaithersburg, 2010; pp 1–326.
- (33) Dautzenberg, H.; Karibyants, N. Polyelectrolyte Complex Formation in Highly Aggregating Systems. 1. Effect of Salt: Polyelectrolyte Complex Formation in the Presence of NaCl. *Macromol. Chem. Phys.* **1999**, *200* (1), 118–125.
- (34) Dautzenberg, H.; Jaeger, W. Effect of Charge Density on the Formation and Salt Stability of Polyelectrolyte Complexes. *Macromol. Chem. Phys.* **2002**, *203* (14), 2095–2102.
- (35) Dautzenberg, H.; Kriz, J. Response of Polyelectrolyte Complexes to Subsequent Addition of Salts with Different Cations. *Langmuir* **2003**, *19* (13), 5204–5211.
- (36) Gombotz, W. R.; Wee, S. F. Protein Release from Alginate Matrices. *Adv. Drug Deliv. Rev.* **2012**, *64*, 194–205.
- (37) Zhang, Z.; Zhang, R.; Chen, L.; McClements, D. J. Encapsulation of Lactase (β -Galactosidase) into κ -Carrageenan-Based Hydrogel Beads: Impact of Environmental Conditions on Enzyme Activity. *Food Chem.* **2016**, *200*, 69–75.
- (38) Zhang, Z.; Zhang, R.; Zou, L.; McClements, D. J. Protein Encapsulation in Alginate Hydrogel Beads: Effect of PH on Microgel Stability, Protein Retention and Protein Release. *Food Hydrocoll.* **2016**, *58*, 308–315.

CHAPTER 8

CHARGE-DRIVEN INTERFACIAL GELATION OF CELLULOSE NANOFIBRILS ACROSS THE WATER/OIL INTERFACE

In Chapter 7, the interfacial complexation between two oppositely charged species was used as a strategy to induce a rapid assembly of cellulose nanofibrils (CNF), allowing the formation of a solid-like shell able to trap a liquid-core. In the following study, we aim to form solid-like interfaces across two immiscible fluids (at the water/oil (W/O) interface) using a conceptually similar method. However, contrarily from Chapter 7, polymers in the oil phase are not ionized, hence do not exhibit charge. To overcome this problem, we exploit the amphiphilicity of an oil-soluble surfactant with an ionizable head group, oleylamine (OA). In this manner, the spontaneous diffusion of the OA to the W/O interface and the partitioning of the ionizable head group towards the aqueous media enables decoration of the W/O interface with positively charged OA head groups (NH_3^+). The positively charged W/O interface was coupled with the oppositely charged and water-dispersible oxidised cellulose nanofibrils (OCNF) in order to trigger a targeted charge-driven gelation at the interface. To date, similar systems have been investigated with the aim to produce resilient capsules. Kaufman et al. reported the formation of stiff and elastic microcapsules produced using an aqueous media containing negatively charged cellulose nanofibrils (CNF) and an oil-soluble and positively charged polymer.^[187] Interestingly, the addition of polyacrylic acid (PAA) in the aqueous phase enabled tuning of the mechanical properties of the capsule. This behaviour was associated with the greater number of binding sites provided by the PAA for complexation with the oppositely charged species.^[187] This principle has been further used to structure liquids at interfaces, allowing the formation of "liquid letters"^[79] and "liquid tubules"^[78]. These materials have in common a stress-bearing interface which can constrain the bulk liquid in nonequilibrium shapes. As such, controlling the rheological properties at the interface allows improvement of the resilience and shelf-life of capsules and similar interface-dominated structures. Wu et al. have recently investigated through *in situ* atomic force microscopy (AFM) the interactions between cellulose nanocrystals (CNC) and an oppositely charged species at the W/O interface as a function of the pH.^[83] However, using this methodology, Wu et al. could not assess information regarding the rupture and yielding of the interfacial layer, important features to foresee suitable applications for capsules produced using a similar approach.^[83] The maximum stress which a capsule can hold is related to the magnitude of the applied force and to the intrinsic properties of the capsules such as geometry, bulk properties (e.g. Newtonian or viscoelastic fluid) and interfacial properties.^[188] Although the geometries and bulk properties of capsules fabricated using a charge-driven interfacial assembly have been assessed, the rheological properties of the

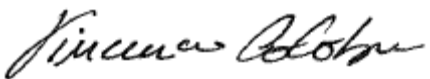
interfacial structure at the W/O interface have yet not been clarified.

In this context, we demonstrate the interfacial gelation of OCNF mediated by an oil-soluble and oppositely charged surfactant, focusing on *how* and *why* such interfacial gels can be modulated in terms of rheological properties. We describe how the interplay between the OCNF adsorption at W/O interface and the co-occurring interfibrillar interactions dictate the strength of the interfacial gel. The understanding provided in the following study could be promptly exploited for the fabrication of capsules with tailored surface roughness as further discussed in section 9.

Supporting information available in section 10.6.

The publication included here is reproduced under the Creative Commons License.



This declaration concerns the article entitled:			
Charge-driven interfacial gelation of cellulose nanofibrils across the water/oil interface			
Publication status (tick one)			
draft manuscript	<input type="checkbox"/>	Submitted	<input type="checkbox"/>
	<input type="checkbox"/>	In review	<input type="checkbox"/>
	<input type="checkbox"/>	Accepted	<input type="checkbox"/>
	<input type="checkbox"/>	Published	<input checked="" type="checkbox"/>
Publication details	Calabrese, V.; Da Silva, M. A.; Schmitt, Zakir Hossain, K. M.; Scott, J. L.; Edler, K. J. Charge-driven interfacial gelation of cellulose nanofibrils across the water/oil interface. <i>Soft Matter</i> 2019.		
Candidate's contribution to the paper (detailed, and also given as a percentage).	<p>The candidate contributed to/ considerably contributed to/predominantly executed the...</p> <p>Formulation of ideas: -The initial idea was formulated by VC based on preliminary observations conducted using water-soluble positively charged surfactants. 90%</p> <p>Design of methodology: -All the measurements were designed by VC. 100%</p> <p>Experimental work: - The experimental work was conducted by VC (100%). - The data analysis was conducted by VC (100%)</p> <p>Presentation of data in journal format: -The first draft was written by VC with contribution of the authors. Subsequent drafts were reworked by VC following feedback from MS, JS, SB, KMZH, JLS and KJE. 90%</p>		
Statement from Candidate	This paper reports on original research I conducted during the period of my Higher Degree by Research candidature.		
Signed			Date 13/12/19



Charge-driven interfacial gelation of cellulose nanofibrils across the water/oil interface†

Cite this: DOI: 10.1039/c9sm01551e

 Vincenzo Calabrese,^a Marcelo A. da Silva,^a Julien Schmitt,^a Kazi M. Zakir Hossain,^a Janet L. Scott^{ab} and Karen J. Edler^{*,a}

Interfacial gels, obtained by the interaction of water-dispersible oxidised cellulose nanofibrils (OCNF) and oil-soluble oleylamine (OA), were produced across water/oil (W/O) interfaces. Surface rheology experiments showed that the complexation relies on the charge coupling between the negatively-charged OCNF and OA. Complexation across the W/O interface was found to be dependent on the ζ -potential of the OCNF (modulated by electrolyte addition), leading to different interfacial properties. Spontaneous OCNF adsorption at the W/O interface occurred for particles with ζ -potential more negative than -30 mV, resulting in the formation of interfacial gels; whilst for particles with ζ -potential of ca. -30 mV, spontaneous adsorption occurred, coupled with augmented interfibrillar interactions, yielding stronger and tougher interfacial gels. On the contrary, charge neutralisation of OCNF (ζ -potential values more positive than -30 mV) did not allow spontaneous adsorption of OCNF at the W/O interface. In the case of favourable OCNF adsorption, the interfacial gel was found to embed oil-rich droplets – a spontaneous emulsification process.

Received 2nd August 2019,
Accepted 6th November 2019

DOI: 10.1039/c9sm01551e

rsc.li/soft-matter-journal

Introduction

Over the last decade rod-like cellulose nanoparticles (CNP), such as cellulose nanofibrils (CNF) and cellulose nanocrystals (CNC), have received much attention due to the combined biocompatibility and tuneable self-assembly of these particles, which allows the production of eco-friendly materials with tailored properties.¹ The relationship between CNP assembly and bulk properties has been widely explored, through the combination of surface modification and tuning of environmental conditions (e.g., pH,² ionic strength,^{3,4} presence of surfactants,^{5,6} and heat⁷). Stable CNP dispersions have been successfully produced by introducing charged moieties onto cellulose nanoparticle surfaces.⁸ For example, oxidised cellulose nanofibrils (OCNF) produced *via* 2,2,6,6-tetramethylpiperidine-1-oxyl radical (TEMPO)-mediated oxidation of cellulose, bear carboxylate groups on the surface of the cellulose fibrils, allowing for negatively charged surfaces at appropriate pHs.^{9–11} OCNF self-assembly has been found to be strongly dependent on electrostatic interfibrillar interactions; specifically, charge screening of the fibrils has been shown to be the main driving

factor in enhancing interfibrillar interactions due to the associative forces outweighing repulsive charge interactions.^{3,12}

CNP assembly across water/oil (W/O) interfaces has been broadly investigated in the context of Pickering emulsions, since CNP are good emulsion stabilizers.^{13,14} The physico-chemical properties of such emulsions are dictated by the coupled bulk (e.g., droplet–droplet interactions) and W/O interfacial properties (e.g., interfacial binding and rigidity). Although information regarding the bulk properties of emulsions can be obtained using several techniques (e.g., rheology, scattering techniques), probing the interfacial properties of microscopic droplets can be a challenge. Due to this, the study of planar liquid–liquid interfaces *via*, for example, surface shear rheology or reflectometry, or of interfaces generated on macroscopic droplets (e.g., *via* pendant drop tensiometric measurements) have been employed as model systems to yield insights into CNP assembly at the interface between two immiscible liquid phases. Recently, Bertsch *et al.* reported on the spontaneous adsorption of CNC at water/air (W/A) interface without the addition of any chemical modification or additional species (e.g., surfactants).¹⁵ In this field, three main approaches have been broadly employed to tune the wettability of CNP, favouring their adsorption to the interface: (i) electrostatic complexation between oppositely charged CNP and water-soluble amphiphilic species (e.g., surfactants),^{16–18} (ii) covalent hydrophobization of the CNP interface,^{19–21} and, (iii) interfacial polyelectrolyte–CNP charge complexation between a polyelectrolyte, which is largely soluble in the organic phase (e.g., oil),

^a Department of Chemistry, University of Bath, Claverton Down, Bath, BA2 7AY, UK.
E-mail: k.edler@bath.ac.uk

^b Centre for Sustainable Chemical Technologies, University of Bath,
Claverton Down, Bath, BA2 7AY, UK

† Electronic supplementary information (ESI) available: CMC of OA, strain sweep experiments, microscopy images, and further details on the interfacial shear rheology setup. See DOI: 10.1039/c9sm01551e

and an oppositely charged water-dispersible CNP. This last approach relies on the use of two immiscible liquids as scaffolds, delivering two oppositely-charged species and directing assembly across the liquid–liquid interface, analogously to the more extensively studied complex coacervates.^{22,23} Recently, interfacial polyelectrolyte–CNP charge complexes, also called nanoparticle-surfactants,^{24,25} have received great attention due to their synergistic effect in reducing surface tension across the liquid–liquid interface as well as their ability to form structured interfaces which allowed the production of capsules,²⁶ liquid tubules²⁷ and all-liquid objects.²⁸ In these systems, harnessing the 2D assembly of CNP across the immiscible phases is crucial for the formation of long-lived structures as well as to impart specific mechanical properties. On this ground, we have assessed the mechanical properties of the W/O interface upon complexation of negatively-charged water-dispersible CNP with an oppositely-charged oil-soluble species under conditions where bulk contributions are negligible, allowing exploration of the interfacial phenomena alone. A combination of surface shear rheology and microscopic analyses have been used to successfully probe the spontaneous interfacial complexation of the negatively charged OCNF with the oil-soluble and positively charged surfactant, oleylamine (OA) (which is protonated at values of pH lower than its pK_a of ~ 10.6 ²⁹) and establish the link between the rheological and morphological properties of the resulting interfacial gel. We demonstrate that modulation of OCNF surface charge, *via* tuning of ionic strength in the aqueous phase, leads to interfacial gels *via* adsorption and interfibrillar interactions. This work has implications for, for example, single-step fabrication of capsules with tailored shell properties, offering opportunities for fine control of mechanical properties.

Materials and methods

OCNF, prepared by TEMPO/NaOCl/NaBr oxidation³⁰ of wood pulp followed by high-pressure homogenization, were provided by Croda[®] International Plc (Goole, UK) as an 8 wt% slurry and purified as previously described¹⁶ to achieve stable OCNF dispersions. The degree of oxidation of the OCNF (as the % of primary C6 hydroxyl groups oxidised to carboxylate groups) was measured to be 25% by conductometric titration.³¹ Ultra-pure DI water (18 M Ω cm) and hexadecane oil (Sigma-Aldrich[®], 99%) were used, respectively, as the water and oil phases, except where stated otherwise. An OA stock solution (30 mM) was prepared by dissolving OA (Sigma-Aldrich[®], primary amine >98%) in the oil and was subsequently diluted to yield a 4.25 mM OA in oil solution (above the herein reported critical micellar concentration (CMC) value of $\cong 2.7$ mM (Fig. S1, ESI[†]), in close agreement with the previously reported value of $\cong 3.7$ mM calculated for OA dissolved in Miglyol[®] 812 oil).³² OA is almost insoluble in the aqueous phase. A 100 ppm OCNF dispersion was prepared by dilution of a 1 wt% OCNF in DI water dispersion, vortexed thoroughly and degassed using a bath sonicator (10 min). The OCNF concentration in water was

chosen to ensure low viscosity of the aqueous phase, yet to provide a quantity of OCNF much greater than that required to saturate the O/W interface with an OCNF monolayer (calculation for the interfacial shear rheology experiments can be found in the ESI[†]). The 100 ppm OCNF dispersion and the 4.25 mM OA solution were used throughout, except where stated otherwise.

The interfacial properties of the OCNF–OA complex were measured using a stress-controlled rheometer (Discovery HR-3, TA Instruments[®]) at 25 °C equipped with a double wall ring (DWR) and a Couette cell geometry, following previously described methodology.^{33,34} After loading of the aqueous phase into the cell (18.2 mL), the DWR was carefully positioned at the water/air interface. Briefly, the DWR was lowered to the water interface while measuring the axial force (N) as a function of distance. The distance corresponding to the water–DWR first contact was obtained by the drop in axial force (example provided in the Fig. S2, ESI[†]). The DWR was further immersed into the water phase by 500 μm , corresponding to 1/2 of the DWR thickness (calculated from the distance corresponding to the water–DWR first contact), to achieve accurate positioning of the DWR across the two phases (W/A). The oil phase (6 mL) was then gently added onto the water phase and, after 5 min allowed for equilibration, OA stock solution (30 mM) was added in order to reach a final OA concentration of 4.25 mM in the oil phase. The system was immediately subjected to the following sequence of experiments (Fig. 1): (TS1) 3 h time sweep at 1 rad s^{-1} angular frequency and 0.5% strain (γ_0); (SSC1) strain sweep cycle composed of two separate strain sweeps (0.05–100 $\gamma_0(\%)$) at 1 rad s^{-1} separated by a 1 min rest time; (TS2) time sweep as in TS1; and, (SSC2) strain sweep cycle as in SSC1. The SSC1 and SSC2 segments were employed to induce a controlled breakage of the interfacial gel. When *in situ* NaCl solution injection was performed, an adapted Couette cell geometry (picture provided in the Fig. S3, ESI[†]) and a customized syringe pump (KD Scientific[®]), were employed, allowing the coupled injection and withdrawal of water phase at a constant rate of 0.1 mL min^{-1} thus maintaining the positioning of the DWR at the W/O interface. Specifically, the 100 ppm OCNF suspension was aged for 0.3 h below the OA-doped oil phase and following this an NaCl solution was added into the bottom of the aqueous phase to reach the final concentration of 55 mM. ζ -Potential measurements were conducted using a Malvern

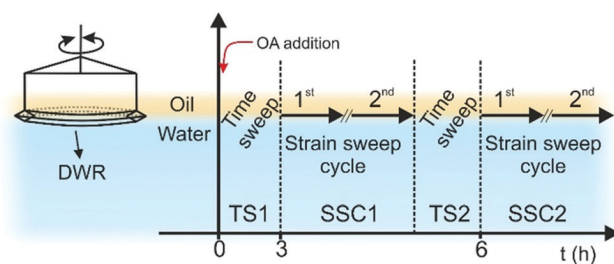


Fig. 1 Sketch of the double wall ring (DWR) at the W/O interface and the experimental sequences employed for the rheological study of the structures evolving at the W/O interface. TS1 and TS2 are time sweeps whilst, SSC1 and SSC2 are strain sweep cycles.

Zetasizer Nano ZSP[®] (Malvern, UK). Samples of OCNF 100 ppm dispersion in water at specific NaCl concentrations were placed in the capillary electrode cell and the ζ -potentials measured as an average of 4 measurements from 100 scans each. Macroscopic observation of formed interfacial gels was conducted after immersion of an OCNF-containing water droplet (10 μ L) into 2 mL of OA-doped oil in a quartz cuvette (1 \times 1 cm). Prior to imaging (USB camera equipped with a Kowa[®] LM75JC objective), the droplets were aged for *ca.* 24 h (at 25 $^{\circ}$ C) followed by gentle tilting.

To image the W/O interface using conventional optical microscopy (Brunel Ltd SP200 equipped with a Canon EOS 1300D), the water phase was loaded into 1 mm thick quartz cells, filling 2/3 of the volume, followed by gentle addition of the oil phase into the remaining 1/3 followed by aging in a vertical position for *ca.* 24 h (at 25 $^{\circ}$ C). The cell was then placed parallel to the focal plane of the microscope (rotation through 90 $^{\circ}$) and the interface imaged.

Confocal laser scanning microscopy (CLSM) analysis was performed at room temperature on a Zeiss LSM880 microscope (Zeiss, Germany). The oil phase was dyed with 0.1 wt% Nile Red (Sigma-Aldrich[®]): dye was added to the oil phase dispersed with stirring for 1 h and insoluble residues removed *via* centrifugation before OA was added to give a final concentration of 4.25 mM. In the case of double staining, the 100 ppm OCNF dispersion in 25 mM aqueous NaCl was prepared with Na-Fluorescein (Sigma-Aldrich[®]) added to a final concentration of 1 μ M. The water droplets (10 μ L) were aged for 24 h (at 25 $^{\circ}$ C) in the stained OA-doped oil. Prior to imaging, the water droplets, including shells, were pipetted onto a confocal microscope slide (25.4 \times 76.2 mm) and covered with a coverslip.

To visualize the W/O interface using scanning electron microscopy (SEM, JEOL JSM6480LV, USA; at an operating voltage of 10 kV), styrene (Sigma-Aldrich[®], 99%) was employed as the oil phase and polymerised using a modified protocol after Perrin *et al.*³⁵ In brief, prior to use, the styrene was passed through an inhibitor remover column and loaded with 1 wt% of a radical initiator (azobisisobutyronitrile, Sigma-Aldrich[®]) and pure OA to obtain a 4.25 mM OA solution, except where stated otherwise. The aqueous phase (1.5 mL) was loaded into a standing plastic syringe (NORM-JECT[®], internal diameter 12.45 mm) followed by addition of 1.5 mL of the OA-doped styrene solution (gently placed on top of the water phase). The W/styrene interface was aged for 24 h and then the syringe placed into a pre-heated oven (55 $^{\circ}$ C for 24 h) to effect styrene polymerisation. After polymerisation, the polymerised styrene (polystyrene) was sliced, washed thoroughly with DI water, mounted on adhesive carbon tape and gold sputter-coated, prior to imaging.

Surface tension (γ) of the oil/air interface was measured using a surface tensiometer (Kibron, Ez-Pi+) equipped with a Dyne probe and γ determined as an average of 4 measurements of duplicate samples. The oil phase was titrated with an OA stock solution (30 mM) and allowed to equilibrate for 15 min, ensuring a time independent γ . The CMC was estimated as the point of change in slope of the domains above and below the CMC (Fig. S1, ESI[†]).

Results and discussion

Examination of the interfacial rheological behaviour of OCNF dispersions showed pronounced adsorption at the W/O interface and interfacial gel formation only when coupled with OA in the oil phase. Tuning of OCNF charge screening was found to be a key parameter, allowing enhancement of interfibrillar interactions at the W/O interface up to a point, where suppression of OCNF interfacial adsorption occurs.

Interfacial shear rheology

To probe the formation of the interfacial gel at the W/O interface with time (TS1), as well as the rheological response upon strain-induced breakage (SSC1) followed by recovery (TS2), *in situ* oscillatory rheology was conducted. Since fluid–fluid interfaces are governed by the contribution of both interfacial and bulk phenomena we ensured that the rheological measurements performed at the W/O interface effectively capture interfacial phenomena only (see ESI[†] for estimation of the bulk contribution to the interfacial rheology).

At first, the rheological properties of the separated components were investigated over time (TS1). When only OA was present, spontaneous adsorption of the amphiphilic OA at the W/O interface occurred,^{32,36} although values of the interfacial complex modulus ($|G_i^*|$) are below the limit of detectability of the instrument (Fig. 2a). Similarly, the sample containing only 100 ppm OCNF, in the absence of OA in the oil phase, did not show any structuring of the interface over 3 h, with values of $|G_i^*|$ of the order of 10^{-5} – 10^{-4} Pa m (Fig. S4, ESI[†]). When OA in the oil phase was coupled with 100 ppm OCNF in the aqueous phase, a remarkable increase of $|G_i^*|$ occurred (Fig. 2a), as expected if there is a strong charge-driven adsorption of the negatively-charged OCNF onto the positively-charged W/O interface (induced by the positively-charged head group of OA; NH_3^+ for values of $\text{pH} < \text{pK}_a$ of OAH^+ , which is $\sim 10.6^{29}$). Bertsch *et al.* reported that for unmodified CNC, a diffusion limited time lag is observed before adsorption occurs,¹⁵ whilst, similarly to the results herein described, Scheuble *et al.* showed that the kinetic of adsorption for methylated CNP is not delayed by a time lag.²¹ This suggests that CNP hydrophobization or interfacial polyelectrolyte–CNP charge complexation (as herein described) are effective strategies to decrease the energy barrier for CNP adsorption at the W/O interface.³⁷

The W/O interface behaved elastically, as denoted by the $\tan(\delta_i) = G_i''/G_i' < 1$ (Fig. 2b), with $G_i' > G_i''$ suggesting rapid formation of an elastic-like structure at the interface (G_i' being the interfacial storage modulus and G_i'' the interfacial loss modulus). The samples containing 100 ppm OCNF plus NaCl at 25 and 55 mM gave the largest values for $|G_i^*|$ and the lowest values of $\tan(\delta_i)$, indicating that, at these NaCl concentrations, stronger and more elastic interfacial gels formed. At even higher NaCl concentrations, 130 and 250 mM, the weakly structured interfaces point to a less favourable adsorption of OCNF at the W/O interface. This phenomenon is supported by the strong charge screening of OCNF (ζ -potential above -30 mV) at high NaCl concentrations where the electrostatic forces,

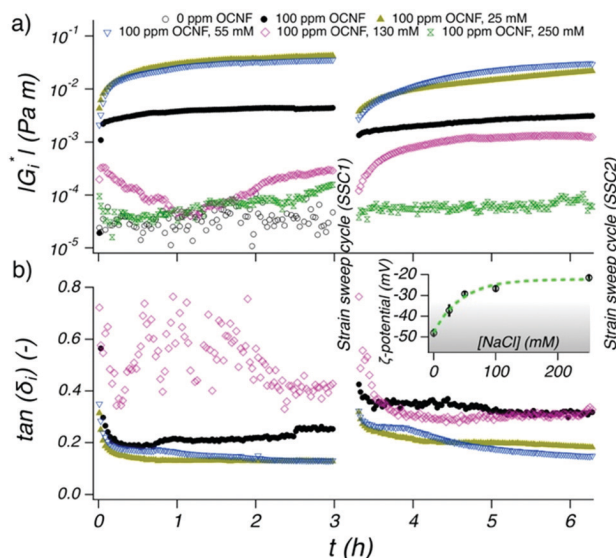


Fig. 2 Evolution of (a) $|G_i^*|$ and (b) $\tan(\delta_i)$ at the W/O interface composed of a OA-doped oil phase and a water phase containing 100 ppm OCNF with 0, 25, 55, 130 and 250 mM NaCl (0 ppm OCNF was used as a control sample). Measurements taken during TS1 and TS2 are displayed on the left and right respectively. ζ -Potential measurements of 100 ppm OCNF suspensions as a function of NaCl concentration, are shown in the inset. The grey shaded region denotes the ζ -potential regime where the repulsive electrostatic forces between fibrils outweigh the attractive forces and a line is drawn to guide the eye.

the driving factor for the OCNF adsorption at the W/O interface, are outweighed by forces such as van der Waals and hydrogen bonds (inset Fig. 2b, see Fig. S5 (ESI \dagger) for Debye length as function of NaCl concentration). Charge-driven polyelectrolyte assembly across W/O interfaces has previously been shown to have an increased surface tension, γ , with increasing ionic strength, indicating that co-adsorption of the polyelectrolytes decreases with increased charge screening.²²

The rheological properties of the interface reached equilibrium ($|G_i^*|$ plateau) for the 100 ppm OCNF suspensions in the presence of 0, 25 and 55 mM NaCl within 3 h, indicating that both adsorption and rearrangement of OCNF at the W/O interface was complete within this time. After breakage of the structured interface, using a cycle of two oscillatory amplitude sweeps (SSC1), its recovery was followed (TS2). It is important to note that during the TS2 segment, the OCNF are already adsorbed at the interface (contrary to the TS1 segment), hence, the evolution of $|G_i^*|$ can be assigned solely to OCNF rearrangement across the W/O interface after disruption (assuming that the W/O surface area is constant). After breakage, the W/O interface formed in presence of 100 ppm OCNF at 0, 25 and 55 mM NaCl almost fully recovered their initial structure within 3 h, due to the reversible physical forces driving interfibrillar interactions. However, the 100 ppm OCNF at 130 mM NaCl, showed an increase in $|G_i^*|$ in the second sweep compared to the first sweep, suggesting incomplete OCNF adsorption within the first 3h of aging (during TS1). The strain sweep cycles (SSC1 and SSC2), composed of two amplitude sweeps separated by a 1 min resting time, were used to induce breakage of the

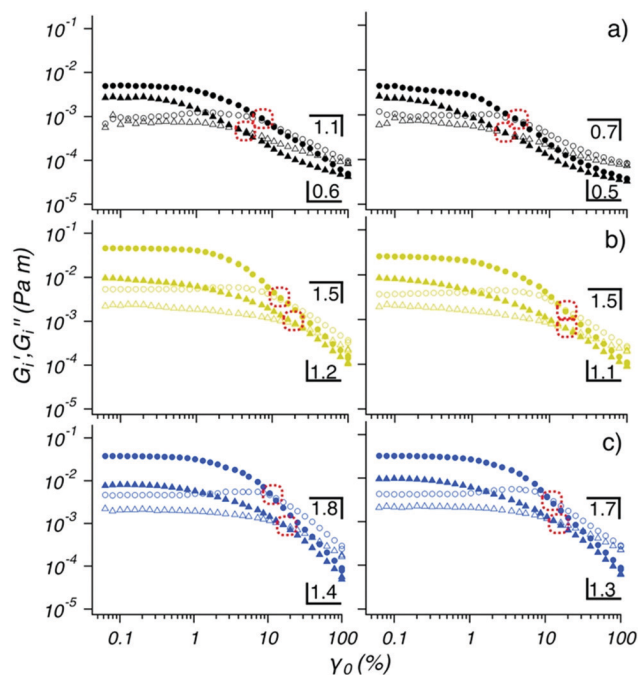


Fig. 3 Measurements conducted during SSC1 (left) and SSC2 (right) segments at the W/O interface for an aqueous phase containing 100 ppm OCNF in (a) 0, (b) 25 and (c) 55 mM NaCl solutions and an OA-doped oil phase. G_i' and G_i'' displayed as filled and empty symbols respectively. Circles and triangles indicate the first and second strain sweep, respectively. Dotted red circles show the yield point ($G_i' = G_i''$). The slope of the fitted G_i' power law decay ($R^2 > 97\%$), at large amplitude strains (10–100 γ_0 (%)), is given for the first (above the data) and second (below the data) strain sweep.

structured interface and to allow extraction of information regarding the structural properties of the interface (Fig. 3). The samples at 0, 25 and 55 mM of NaCl showed $G_i' > G_i''$ at low strains ($\gamma_0 < 1\%$) and $G_i' < G_i''$ at larger strains; characteristic features of a gel-like structure, which behave as solids that yield and flow at higher strain values (illustrated for the strain sweep cycle of 100 ppm OCNF at 130 and 250 mM NaCl in Fig. S6, ESI \dagger). This information, coupled with the film observed at the W/O interface presented in Fig. 6 suggest the gel-like nature of the interface.

In the SSC1 and SSC2 measurements, the moduli were observed to shift to lower values during the second amplitude sweep, which indicated incomplete network regeneration within the short 1 min resting period between the two amplitude sweeps.

This was expected as the previously described time sweeps showed that longer times are needed (>1 h) to achieve a complete recovery of the interfacial gel properties (Fig. 2).

The interfacial gels were compared at large strains (10–100 γ_0 (%)) where G_i' follows a power law scaling behaviour, $G_i'(\gamma_0) \propto \gamma_0^{-\mu}$, with the exponent μ being the slope. The weakly-structured interfacial gel formed by the 100 ppm OCNF suspension without salt was marked by a shallow μ (1.1) and by a yield strain, (chosen here as the strain value at which $G_i' = G_i''$) shifting toward lower values of strain with the second

amplitude sweep. On the other hand, the gel layers formed by a 100 ppm OCNF suspension at 25 and 55 mM NaCl exhibited tougher and stronger interfacial gels, as displayed by greater moduli and yield strain, respectively, and as expected for a firm interface, gave a greater value of μ (1.5 and 1.8 for 25 and 55 mM NaCl, respectively) indicative of a more abrupt breakage of the network. The yield strain associated with the second amplitude sweep, for both 25 and 55 mM NaCl, shifts toward larger values due to the fast regeneration of the interfacial properties. The SSC2 segment, performed after TS2, showed very similar features to the SSC1 segment, indicating that, especially for the 100 ppm OCNF suspension at 25 and 55 mM, interfacial structure was fully recovered.

To understand how electrostatic interactions affect the interfacial gel properties, an increase in ionic strength was induced after the initial formation of an interfacial gel prepared with 100 ppm OCNF in pure water *via* subsequent addition of NaCl solution to the subphase (Fig. 4a), thus allowing for charge screening of the OCNF only after initial OCNF adsorption at the W/O interface. Injection of the NaCl solution was made into the base of the cell, without stirring, to avoid disturbance to the interfacial region, meaning that some time was required for the ions to diffuse to the interface. Approximately 0.5 h after the NaCl injection, $|G_i^*|$ increased significantly while $\tan(\delta_i)$, after an overshoot, decreased, demonstrating that the interfacial gel became stronger (higher G_i')

and more elastic (smaller G_i''/G_i' ratio) upon NaCl addition. The effect of ionic strength on the bulk rheology of OCNF dispersions has been widely exploited and charge screening effects have been associated with shorter interfibrillar distances leading to greater aggregation and gel formation.^{3,12} A similar conclusion was suggested for the polyelectrolyte–CNC system investigated by Wu *et al.* who reported densification of the CNC interfacial layers across the W/O interface upon protonation of the sulfate groups.³⁸ For unmodified CNC across the W/A interface, a similar gain in viscoelasticity has been observed upon increase of ionic strength, in good agreement with the interfacial rheology described herein which strongly suggests enhanced interfibrillar aggregation at the W/O interface upon NaCl addition.³⁹

Following the previously described protocol, SSC1 and SSC2 segments were performed interposed by TS2 (Fig. 4b). The first strain sweep in SSC1 showed values of G_i' greater than any other interfacial gel aged in presence of NaCl (from time = 0 h), and, the presence of a slight overshoot in G_i'' (before the moduli crossover) indicating that the interfacial gel yields plastically, a phenomenon which is usually associated with an interconnected network structure.^{40,41} The effective disruption of the network at larger strain was highlighted by a value of $\mu = 1.7$ and by a second amplitude sweep which did not recover a linear domain at low value of strains ($\gamma_0 < 1\%$). The moduli measured in the SSC2 segment performed after TS2 (Fig. 4b (right)) highlighted the limited recoverability of the interfacial structure even after TS2, where no linear domain was observed.

Morphology

The OA-OCNF complexation, at the macroscopic level, was investigated for different concentrations of NaCl in the aqueous phase (Fig. 5a). Droplets of the 100 ppm OCNF suspension in water at different NaCl concentrations were aged for *ca.* 24 h in an OA-doped oil solution and imaged after gentle tilting of the droplet. A ‘hairy’ structure at the W/O interface is weakly visible at 0 mM, while a pronounced folded interfacial layer, which is easily peeled off by gentle tilting of the droplets, appears at 25 and 55 mM NaCl. On the contrary, no substantial shell formation appeared for the droplets containing OCNF at 130 and 250 mM NaCl, in agreement with rheological results which showed stronger W/O interfaces at 25 and 55 mM NaCl. The macroscopic droplet shape however appears to be driven by the effects of OA and NaCl on interfacial tension since the droplets have similar shapes in the presence and absence of OCNF (for images see Fig. S7, ESI†).

The W/O interface of the 100 ppm OCNF suspension at 25 mM NaCl was analysed *via* optical microscopy by placing the two phases in a thin cuvette cell, as sketched in Fig. 5b, and imaged after *ca.* 24 h aging. In this case, the undisturbed interfacial gel showed a dendritic structure covering the whole layer formed at the W/O interface. A similar structure was present for the sample at 55 mM NaCl, although the structure appeared to be significantly less dense (for images of samples at other NaCl concentrations see Fig. S8, ESI†).

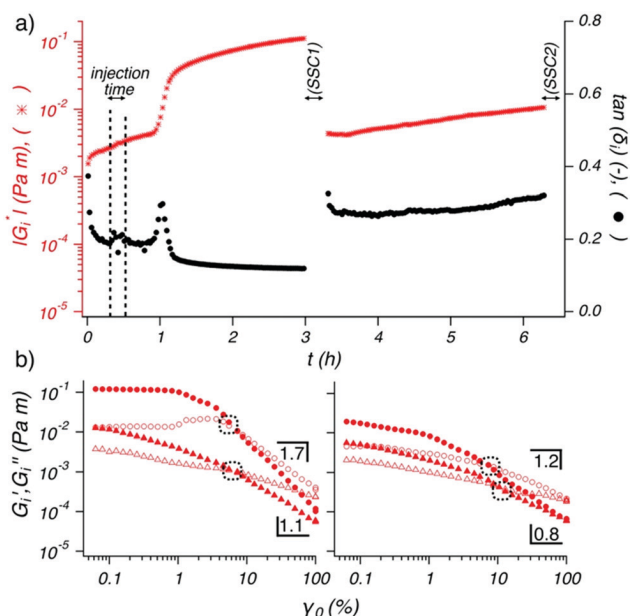


Fig. 4 Evolution of (a) $|G_i^*|$, in red, and $\tan(\delta_i)$, in black, at the W/O interface of an aqueous phase containing 100 ppm OCNF and OA-doped oil phase. At 0.3 h, an injection of NaCl solution was conducted over 10 min (indicated by dotted lines) to yield a final concentration of 55 mM NaCl in the aqueous phase. (b) G_i' and G_i'' are displayed as filled and empty symbols respectively, for the (left) SSC1 and (right) SSC2. Circles and triangles indicate the first and second strain sweep, respectively. Dotted circles show the yield point ($G_i' = G_i''$). The slope of the G_i' power law decay ($R^2 > 99\%$), at large strains (10–100 γ_0 (%)), is given for the first and second strain sweep above and below the data, respectively.

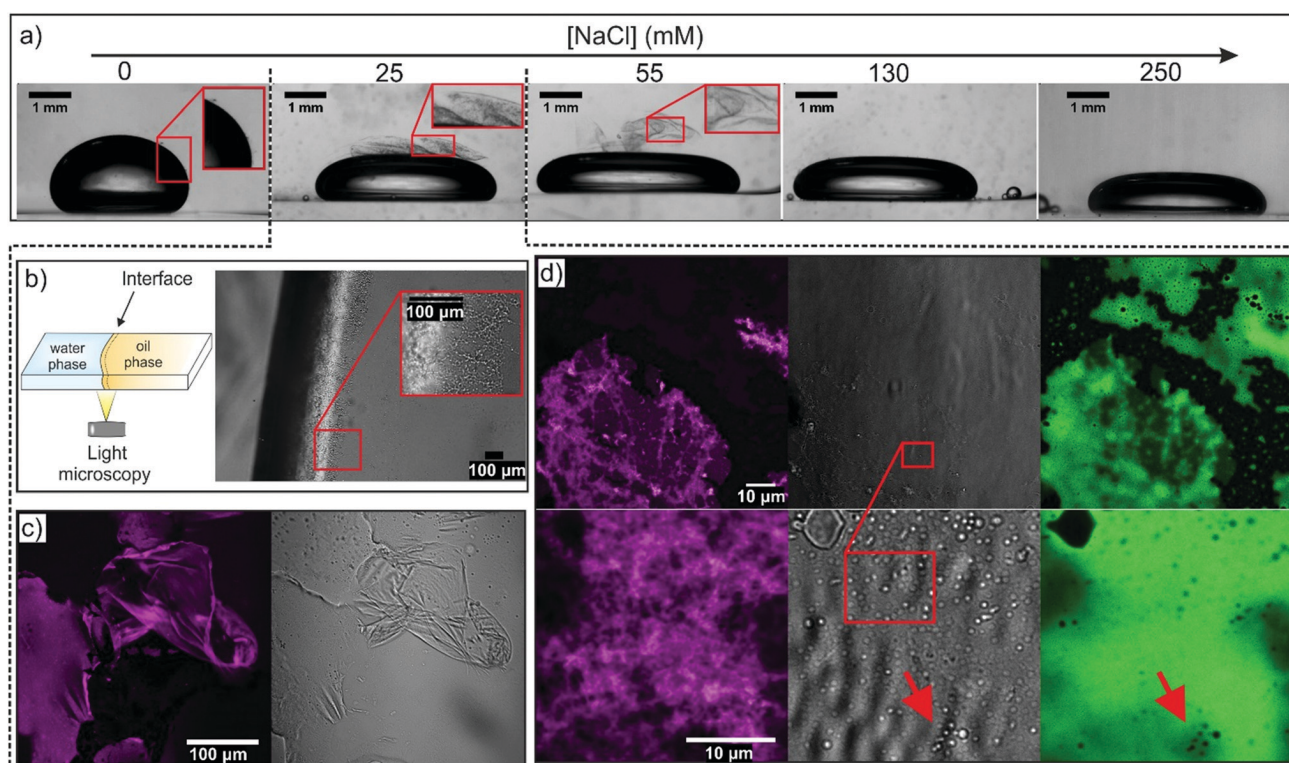


Fig. 5 (a) Images of 24 h aged OCNF-containing water droplets in OA-doped oil containing 100 ppm OCNF at various NaCl concentrations. (b) Optical micrograph of an undisturbed W/O interface between 100 ppm OCNF in 25 mM aqueous NaCl and OA-doped oil. The W/O interface was formed in a thin cuvette cell as depicted schematically. (c) CLSM images of the interfacial gel formed at the interface between 100 ppm OCNF in 25 mM aqueous NaCl and OA-doped oil; excitation channel for the oil-soluble dye (Nile red, depicted in magenta) and transmitted light displayed on the left and right respectively. (d) CLSM images at higher magnification collected with both oil-soluble and water-soluble dye (Na-Fluorescein, shown in green) for the sample as in (c); excitation channel for the oil-soluble dye, transmitted light and excitation channel for the water-soluble dye displayed on the left, centre and right respectively.

The interfacial gel morphology produced from a 100 ppm OCNF suspension in 25 mM aqueous NaCl was probed by CLSM using oil soluble Nile Red (Fig. 5c). The structure of the interfacial layer, at this magnification, displays wrinkles and sharp cuts, caused by the disruptive sample preparation. The gel resembled a shell-like structure, similar to the microcapsule shells produced by polyelectrolyte-nanoparticle complexation reported by Kaufman *et al.*⁴² Homogeneous staining of the interfacial gel (shown in magenta, Fig. 5c) confirmed the presence of embedded oil. Surprisingly, at higher magnifications (Fig. 5d), a layer of jammed droplets was visible in the gel, similarly to that observed by Huang *et al.* employing nanoparticle-surfactant complexes (see ESI of Huang *et al.*).⁴³ The image of the film containing both the water-soluble dye, Na-Fluorescein, and the oil-soluble Nile Red showed that the droplets observed in the transmitted light configuration were not visible in the Nile red excitation channel, whilst non-fluorescent droplets were visible in the Na-Fluorescein excitation channel, indicating that the embedded droplets were oil-rich. Droplets of similar size are seen in the interfacial gels formed at 50 mM aqueous NaCl (shown in Fig. S9, ESI†). We also note that the number of droplets in the interfacial gel initially grows over time and a few hours are required to achieve

saturation of the interfacial gel with oil droplets as observed in Fig. 5 and in Fig. 6b. After 24 h ageing, the W/O interface did not display substantial changes. Samples aged for several weeks also showed unchanged features, as visualized using confocal microscopy, suggesting that the embedded droplets are stable against coalescence.

To demonstrate the presence of oil-rich droplets within the interfacial layer, SEM analysis of the W/polystyrene interface was conducted for interfacial gels formed at 100 ppm OCNF and varying NaCl concentrations (Fig. 6). Since a different organic phase is used in this experiment, interface morphology was solely evaluated to observe the presence or absence of droplets at the interface, with the aim to further validate the CLSM observation. Flocs of droplets appeared at a low density across the entire W/polystyrene interface at 0 mM NaCl whilst at 25 mM NaCl, the droplets densely populated the interface, protruding into the aqueous phase. Surprisingly, higher magnification of the floc-free areas clearly revealed an interfacial layer of jammed droplets, analogous to the CLSM images. At 55 mM NaCl, the W/polystyrene interface showed an absence of flocs, although a “textured pattern” appeared, different from the smooth interface obtained from the control samples (W/OA-doped polystyrene,

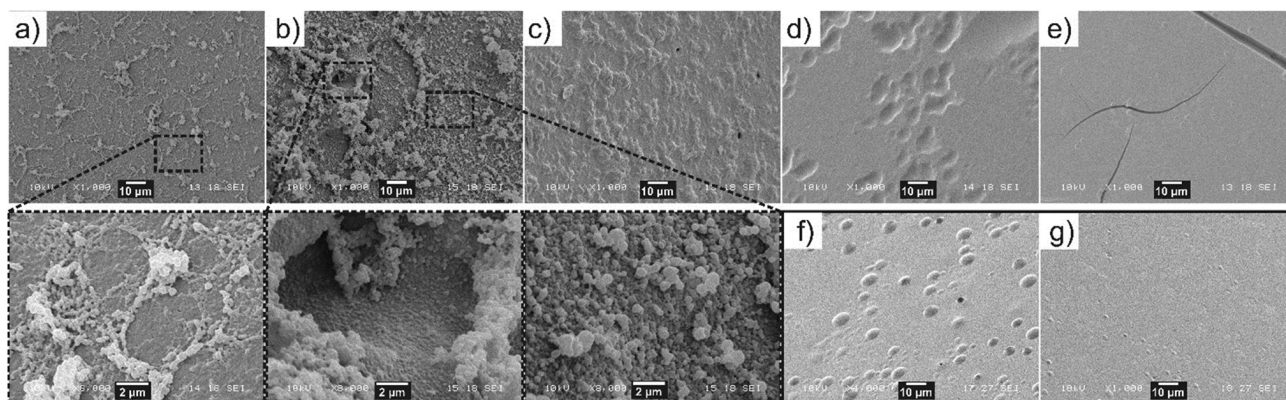


Fig. 6 SEM images of W/polystyrene interface from the aqueous "side", normal to the oil phase. The water phase was composed of 100 ppm OCNF at (a) 0, (b) 25, (c) 55, (d) 130 and (e) 250 mM NaCl, while the oil phase (polystyrene) was OA-doped. Control samples are (f) W/OA-doped polystyrene, in the absence of OCNF and (g) water-OCNF/polystyrene in the absence of OA. Zoomed areas are indicated by black rectangles.

in absence of OCNF (Fig. 6f), and water-OCNF/polystyrene in absence of OA (Fig. 6g)).

This suggests that at 55 mM, the interfacial gel at the W/polystyrene interface did not withstand the procedure required to induce polymerisation of the styrene (*i.e.*, heating and slicing of the polystyrene). However, at the highest NaCl concentrations, 130 and 250 mM, the W/polystyrene interfaces are as featureless as the control samples, indicating that, at these NaCl concentrations, there is no appreciable development of the droplet containing interfacial gel. The formation of oil-rich droplets at the W/O interface, observed at low NaCl concentrations, suggests that spontaneous emulsification occurs.⁴⁴ Similar phenomena have been recently observed for other oil-soluble surfactants across W/O interfaces.^{40,45} This phenomenon is associated with a drastic decrease in γ , compensating for the increase in surface area associated with droplet formation, which favours negative Gibbs free energy values leading to spontaneous droplet formation.⁴⁴ It is possible, qualitatively, to relate both γ and $|G_i^*|$ to the particle volume fractions at the interface (ϕ_i) as $\gamma \propto 1/\phi_i$ and $|G_i^*| \propto \phi_i$. This implies that $\gamma \propto 1/|G_i^*|$, indicating that the greatest values of $|G_i^*|$ for OCNF–OA complexes are concurrent with a strong

decrease in γ , a prerequisite for spontaneous emulsification to occur. It is worth noting that the spontaneous formation of an oil-in-water emulsion across the interface also suggests that the OCNF–OA complexes have a three-phase contact angle $< 90^\circ$, implying a favourable partitioning of the OCNF–OA complex into the water phase.⁴⁶ As such, we propose that the OCNF adsorption is essential for inducing self-emulsification, as well as stabilization of the oil-rich droplet at the interface. Specifically, the stabilization of the oil droplets within the interfacial gel suggests that the OCNF–OA complexes adsorb at the W/O interface of the oil droplets, acting as a physical barrier against coalescence, as previously reported for CNP in the context of Pickering emulsions.¹³ Moreover, the interfacial gel across the planar W/O interface would allow droplet entrapment and bridging as shown by CLSM. On this basis, we suggest that the 2D assembly of OCNF across the W/O interface exists in three different regimes defined by the ζ -potential of OCNF particles (Fig. 7, top): (a) at ζ -potential more negative than -30 mV (0 mM NaCl), the highly negatively-charged OCNF spontaneously adsorbs to the W/O interface forming a weak interfacial gel due to complexation with the oppositely-charged OA; (b) at ζ -potential approximately equal to -30 mV (25 and 55 mM NaCl)

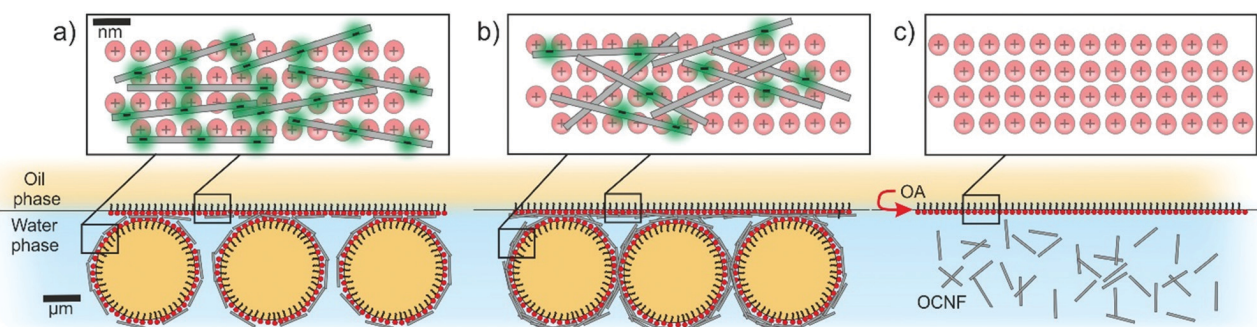


Fig. 7 (top) Schematic representation of the 2D OCNF–OA assembly (grey rectangles and red circle respectively, negative charges highlighted in green) across the W/O interface from a normal perspective upon three different regimes according to the NaCl concentration and thus the $|\zeta$ -potential| of the OCNF: (a) > 30 mV, (b) ~ 30 mV and (c) < 30 mV of the OCNF. (bottom) A zoomed-out representation from the parallel perspective. For clarity, components are not drawn to scale.

spontaneous OCNF adsorption at the W/O interface, coupled with some degree of charge screening, results in the formation of the strongest and toughest interfacial gels due to augmented interfibrillar interactions, and (c) at ζ -potential more positive than -30 mV (130 and 250 mM NaCl), little or no OCNF adsorption occurs, as the fibrils bear insufficient net charge to promote adsorption. At the micrometre length scale (Fig. 7, bottom), in the case of favourable OCNF adsorption, the interfacial gel embeds oil-rich droplets bridged by the salt-responsive OCNF.

Conclusions

The electrostatically-driven complexation of negatively-charged water-dispersible OCNF with positively-charged oil-soluble OA at W/O interface was investigated to elucidate the effect of ionic strength on OCNF adsorption and arrangement across the liquid-liquid interface. It was found that the ζ -potential of OCNF, modulated by changes in NaCl concentration, dictated OCNF adsorption and arrangement across the oppositely-charged W/O interface. Although absolute limits have yet to be established, the spontaneous formation of oil-rich droplets at the W/O interface suggests that spontaneous emulsification takes place upon OCNF-OA complexation. The utility of interfacial rheology combined with careful observation of 2D interfaces to discern the development of complex structures has been illustrated. The observations of interfacial gels embedding oil droplets, dependent on charge screening and adsorption to interfaces in bulk biphasic systems containing charged components, have implications for the production of hybrid gel-emulsion materials, capsule formation and tuning in O/W emulsions – systems where interfacial rheology studies are extremely challenging, yet where tuneability is key to utility.

Conflicts of interest

The authors declare no conflicts of interest.

Acknowledgements

The authors thank the EPSRC for funding this project (grant numbers EP/N033310/1). V. Calabrese thanks the University of Bath for PhD funding, Dr Andrea Pensado-Lopez for the useful discussions and Dr Giovanni Vorraro for the help provided in the customisation of the rheological apparatus. Data supporting this article have been made freely available *via* the University of Bath Research Data Archive system at DOI: 10.15125/BATH-00662.

References

- 1 S. J. Eichhorn, *Soft Matter*, 2011, 7, 303–315.
- 2 T. Saito, T. Uematsu, S. Kimura, T. Enomae and A. Isogai, *Soft Matter*, 2011, 7, 8804–8809.
- 3 H. Fukuzumi, R. Tanaka, T. Saito and A. Isogai, *Cellulose*, 2014, 21, 1553–1559.
- 4 H. Dong, J. F. Snyder, K. S. Williams and J. W. Andzelm, *Biomacromolecules*, 2013, 14, 3338–3345.
- 5 R. J. Crawford, K. J. Edler, S. Lindhoud, J. L. Scott and G. Unali, *Green Chem.*, 2012, 14, 300–303.
- 6 N. Quennouz, S. M. Hashmi, H. S. Choi, J. W. Kim and C. O. Osuji, *Soft Matter*, 2015, 12, 157–164.
- 7 V. Calabrese, J. C. Muñoz-García, J. Schmitt, M. A. da Silva, J. L. Scott, J. Angulo, Y. Z. Khimyak and K. J. Edler, *J. Colloid Interface Sci.*, 2019, 535, 205–213.
- 8 K. J. De France, T. Hoare and E. D. Cranston, *Chem. Mater.*, 2017, 29, 4609–4631.
- 9 D. da Silva Perez, S. Montanari and M. R. Vignon, *Biomacromolecules*, 2003, 4, 1417–1425.
- 10 Y. Okita, T. Saito and A. Isogai, *Biomacromolecules*, 2010, 11, 1696–1700.
- 11 S. Tsuguyuki and A. Isogai, *Biomacromolecules*, 2004, 5, 1983–1989.
- 12 J. Schmitt, V. Calabrese, M. A. Da Silva, S. Lindhoud, V. Alfredsson, J. L. Scott and K. J. Edler, *Phys. Chem. Chem. Phys.*, 2018, 20, 16012–16020.
- 13 I. Kalashnikova, H. Bizot, B. Cathala and I. Capron, *Langmuir*, 2011, 27, 7471–7479.
- 14 V. Calabrese, J. C. Courtenay, K. J. Edler and J. L. Scott, *Curr. Opin. Green Sustainable Chem.*, 2018, 12, 83–90.
- 15 P. Bertsch, M. Diener, J. Adamcik, N. Scheuble, T. Geue, R. Mezzenga and P. Fischer, *Langmuir*, 2018, 34, 15195–15202.
- 16 V. Calabrese, M. A. Da Silva, J. Schmitt, J. C. Muñoz-García, V. Gabrielli, J. L. Scott, J. Angulo, Y. Z. Khimyak and K. J. Edler, *Soft Matter*, 2018, 14, 7793–7800.
- 17 N. Dhar, D. Au, R. C. Berry and K. C. Tam, *Colloids Surf., A*, 2012, 415, 310–319.
- 18 Z. Hu, R. Xu, E. D. Cranston and R. H. Pelton, *Biomacromolecules*, 2016, 17, 4095–4099.
- 19 M. E. H. van den Berg, S. Kuster, E. J. Windhab, L. M. C. Sagis and P. Fischer, *Phys. Fluids*, 2018, 30, 072103.
- 20 M. E. H. van den Berg, S. Kuster, E. J. Windhab, J. Adamcik, R. Mezzenga, T. Geue, L. M. C. Sagis and P. Fischer, *Langmuir*, 2018, 34, 10932–10942.
- 21 N. Scheuble, T. Geue, E. J. Windhab and P. Fischer, *Biomacromolecules*, 2014, 15, 3139–3145.
- 22 H. Monteillet, F. Hagemans and J. Sprakel, *Soft Matter*, 2013, 9, 11270.
- 23 H. Monteillet, J. M. Kleijn, J. Sprakel and F. A. M. Leermakers, *Adv. Colloid Interface Sci.*, 2017, 239, 17–30.
- 24 M. Cui, T. Emrick and T. P. Russell, *Science*, 2013, 342, 460–463.
- 25 Y. Chai, A. Lukito, Y. Jiang, P. D. Ashby and T. P. Russell, *Nano Lett.*, 2017, 17, 6453–6457.
- 26 G. Kaufman, S. Mukhopadhyay, Y. Rokhlenko, S. Nejati, R. Boltyanskiy, Y. Choo, M. Loewenberg and C. O. Osuji, *Soft Matter*, 2017, 13, 2733–2737.
- 27 X. Liu, S. Shi, Y. Li, J. Forth, D. Wang and T. P. Russell, *Angew. Chem., Int. Ed.*, 2017, 56, 12594–12598.
- 28 S. Shi, X. Liu, Y. Li, X. Wu, D. Wang, J. Forth and T. P. Russell, *Adv. Mater.*, 2018, 30, 1–5.

- 29 M. A. Scrociapino, R. Sanna, A. Ardu, F. Orr, M. Casu, A. Musinu and C. Cannas, *J. Colloid Interface Sci.*, 2013, **407**, 67–75.
- 30 T. Saito, Y. Nishiyama, J. L. Putaux, M. Vignon and A. Isogai, *Biomacromolecules*, 2006, **7**, 1687–1691.
- 31 T. Saito and A. Isogai, *Biomacromolecules*, 2004, **5**, 1983–1989.
- 32 N. G. Eskandar, S. Simovic and C. A. Prestidge, *Phys. Chem. Chem. Phys.*, 2007, **9**, 6313–6318.
- 33 A. Franck, *5th Int. Symp. Food Rheol.*, 1997, vol. 8, pp. 242–244.
- 34 S. Vandebril, A. Franck, G. G. Fuller, P. Moldenaers and J. Vermant, *Rheol. Acta*, 2010, **49**, 131–144.
- 35 E. Perrin, H. Bizot, B. Cathala and I. Capron, *Biomacromolecules*, 2014, **15**, 3766–3771.
- 36 W. Wu, H. Fang, F. Yang, S. Chen, X. Zhu, Q. Yuan and W. Gan, *J. Phys. Chem. C*, 2016, **120**, 6515–6523.
- 37 K. Du, E. Glogowski, T. Emrick, T. P. Russell and A. D. Dinsmore, *Langmuir*, 2010, **26**, 12518–12522.
- 38 X. Wu, Q. Yuan, S. Liu, S. Shi, T. P. Russell and D. Wang, *ACS Macro Lett.*, 2019, **8**, 512–518.
- 39 P. Bertsch and P. Fischer, *Langmuir*, 2019, **35**, 7937–7943.
- 40 S. Bochner De Araujo, M. Merola, D. Vlassopoulos and G. G. Fuller, *Langmuir*, 2017, **33**, 10501–10510.
- 41 L. M. C. Sagis and P. Fischer, *Curr. Opin. Colloid Interface Sci.*, 2014, **19**, 520–529.
- 42 G. Kaufman, S. Nejati, R. Sarfati, R. Boltyanskiy, M. Loewenberg, E. R. Dufresne and C. O. Osuji, *Soft Matter*, 2015, **11**, 7478–7482.
- 43 C. Huang, J. Forth, W. Wang, K. Hong, G. S. Smith, B. A. Helms and T. P. Russell, *Nat. Nanotechnol.*, 2017, **12**, 1060–1063.
- 44 C. Solans, D. Morales and M. Homs, *Curr. Opin. Colloid Interface Sci.*, 2016, **22**, 88–93.
- 45 P. S. Silva, S. Zhdanov, V. M. Starov and R. G. Holdich, *Colloids Surf., A*, 2017, **521**, 141–146.
- 46 B. P. Binks, L. Isa and A. T. Tyowua, *Langmuir*, 2013, **29**, 4923–4927.

The exploratory research undertaken herein led to the insightful understanding of new phenomena and, as usual, the development of further research questions seeking answers. As such, in the following section, a summary of the main finding is reported with relevant recommendations for further research.

The work aimed to study different avenues for the assembly of cellulose nanoparticles (CNP) in industrially relevant conditions to produce capsules and hydrogels able to incorporate targeted components following the principles of green chemistry. This thesis began with a fundamental study on how CNP are affected by ageing and temperature; two factors which dictate the processability and the shelf-life of CNP-based end products. The investigation aims to respond *how* and *why* heat and time affect the structural properties, and thus the mechanical properties, of oxidised cellulose nanofibrils (OCNF) and cationic cellulose nanofibrils (CCNF)-based hydrogels (Chapter 3). Although often disregarded, this study demonstrates that the OCNF assembly is dramatically influenced by the temperature, especially at concentrations close to that required for the sol-to-gel transition. Contrarily, CCNF did not show any structural evolution upon heating. The underpinning reason was associated with the decreased polarizability of the water media upon the increase in temperature, leading to a less effective interfibrillar repulsion. Nonetheless, the heat sensitivity of the fibrils was strictly dependent on their aggregation state. For instance, in the case where fibrils displayed some level of aggregation, such as CCNF and OCNF at high concentration (e.g. 5 wt%) the heat responsiveness diminished. Despite the new insightful results, a clearer picture of this phenomenon is demanded. Specifically, the establishment of a direct link between interfibrillar interactions and the heat-responsiveness may provide further insights applicable to a broader range of colloidal particles.

Since the pronounced aggregation state of CCNF yielded heat insensitive hydrogels, OCNF were covalently grafted with a quaternary ammonium group, yielding electrostatically interacting zwitterionic cellulose nanofibrils (ZCNF). The ZCNF did not display heat responsiveness and ageing, two essential features for its potential application as a rheological modifier in formulated products where a long shelf-life is desired. Since surfactants are the core of formulated products, the assessment of the structure-property relationship of ZCNF in the presence of common surfactants was investigated (Chapter 4). It was found that the addition of small amounts of charged surfactants leads to a drastic change in the structural and rheological properties of the ZCNF-based dispersions. As such, the distinct rheological behaviour of the ZCNF in the presence of neutral and charged surfactant would make ZCNF a versatile rheological modifier. Although several pathways for the synthesis of zwitterionic celluloses have been proposed,^[155–158,161] their colloidal stability has not yet been elucidated. Thus, this research adds valuable pieces of knowl-

edge to foresee the use of ZCNF in functional materials where control of the assembly is key to utility. Remaining research questions include (i) what is the effect of ionic strength on the structure-property relationship of ZCNF dispersions? (ii) How to stabilize a ZCNF dispersion without the use of charged surfactants? The information provided could (i) establish the potential of ZCNF in formulated products, often containing salts, and (ii) enable the use of ZCNF as a versatile carrier of ionic drugs.

Nonetheless ionic species are efficient rheological modulators of dispersions composed of charged CNP, the binding of oppositely charged species on the CNP surface hinders the use of the charged moieties for further reactions. On this ground, Chapter 5 describes the effect of non-interacting colloidal particles (fillers) on the rheological properties of an OCNF-based hydrogel. Based on the ability to strengthen the gel, non-interacting fillers have been described as inefficient rheological modifiers.^[189] However, the physical hindrance that the fillers impart on the primary matrix (OCNF) is evident upon large deformations, where breakage and yielding occur. Although often ignored, knowledge regarding the rheological properties of materials upon large deformations are pivotal in industrial processes and to match customer appreciation.^[163] On this ground, the influence of the filler size on the structural and mechanical properties of an OCNF-based hydrogel was evaluated. Our study demonstrates that a filler larger than the mesh size of the network leads to a more gradual breakage of the hydrogel. This feature was exploited in the work described in Chapter 6 where the filler was used with the aim to smoothly eject through a syringe needle the composite OCNF-filler hydrogels. The presence of non-interacting fillers did not hinder aggregation of the OCNF-based hydrogel when the hydrogel was placed in an aqueous bath containing a metal counterion. These features allowed the composite OCNF-filler hydrogels to incorporate coordination polymers nanofibers. To date, only the work of Zhu et al. described a route for the incorporation of coordination polymers in hydrogels, although using a multi-step procedure involving high temperatures.^[171] Contrarily, in this study, we identify a single step and ambient temperature preparative procedure which allows incorporation of coordination polymers into cellulose-based hydrogels. Specifically, we identify rheological properties of the precursor hydrogels and the rate of coordination polymer self-assembly required to successfully incorporate coordination polymers into cellulose-based hydrogels. As such, this procedure could be used for a variety of coordination polymers with unique properties such as stimuli responsiveness, magnetism and luminescence, offering an easy approach to add functional properties to cellulose-based hydrogels. From the fundamental side, it is possible to propose further research focusing on the incorporation of coordination polymers which display different supramolecular structures, such as sheets or three-dimensional architectures. The incorporation of coordination polymers with different shape and size could enable tuning of the rheological properties of the hydrogel, hence, opening a new strategy to impart desired mechanical properties to cellulose-based hydrogels. Contrarily, from the application side, it is possible to propose proof-of-concept studies, where functional coordination polymers are used to impart specific functional properties.

The homogeneous and dense structure of the hydrogels described in Chapter 6 enables the incorporation of large structures (typically larger than the network mesh size) whilst allowing nm -sized components to freely diffuse away. To ensure physical entrapment of nm -sized components into the hydrogels we described the fabrication of core-shell spheroidal hydrogels (SH) produced through the charge-driven interfacial complexation of CCFNF and an oppositely charged polymer (Chapter 7). Since the shell of the SH performed as a semi-permeable membrane, the stability of the SH was strongly dependent by the osmotic pressure. In this regard, this study aims to elucidate the effect of the ionic strength and osmotic pressure on the SH stability. Furthermore, we demonstrated the applicability of SH as bioreactors - where enzymes are physically entrapped in the core whilst substrate and product are freely able to migrate through the shell. Contrarily to common microreactors, SH enable the entrapment of enzymes without the use of a covalent immobilization.^[184] As such, SH allow to overcome problems related

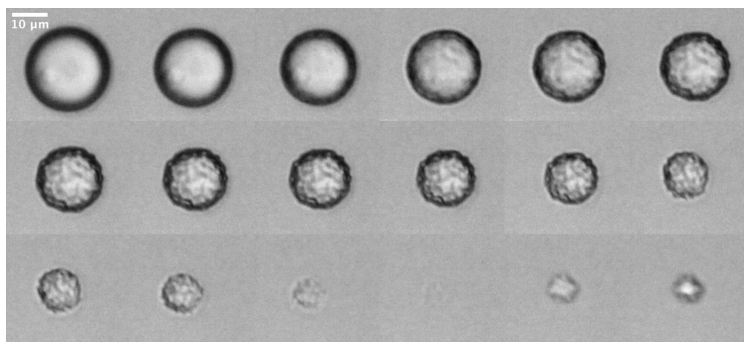


Figure 9.1 Water-in-oil droplet upon ambient drying (from left to right) on a microscope slide. The aqueous phase containing 1.5 wt% OCNF and the oil phase containing 4.25 mM OA as discussed in Chapter 8. The emulsions were produced through handshaking and imaged immediately after preparation. Pictures were collected each 60 s.

with the conformational change of the enzyme upon covalent immobilization, reduce costs for enzymatic immobilization and remove the burden of intensive purification procedures required with the covalent immobilization of enzymes. Besides these beneficial features for biocatalysis applications, the poor mechanical resilience of core-shell structures, which mainly relies on the shell, can represent a drawback. To improve the mechanical resilience of the SH, we propose the incorporation of non-ionic polymers which undergo a heat-induced sol-to-gel transition into the CCNF matrix (precursor of the SH). This recommendation is based on preliminary results which confirmed that the incorporation of non-ionic polymers into the CCNF matrix did not drastically alter the production of the SH and that the integrity of the SH was preserved up to 80°C when the SH was kept in an aqueous media containing mM quantity of NaCl.

Ultimately, in Chapter 8 the charge-driven assembly of two oppositely charged species was used to form solid-like interfaces across two immiscible fluids (at the water/oil (W/O) interface). Since polymers in the oil phase are not ionized, we took advantage from the amphiphilicity of an oil-soluble surfactant with an ionizable head group, to decorate the W/O interface with positive charged moieties. Similar mechanisms have been explored for the production of capsules, providing information regarding the mechanical properties of the whole capsule. However, for similar systems, information regarding the rheological properties at the interface are absent. In this study, we explored the rheological properties at the W/O interface, focussing on how the ionic strength affects the interplay between spontaneous adsorption and assembly of OCNF at the W/O interface. Although very fundamental, this study elucidates key parameters to produce core-shell droplets with tailored interfacial mechanical properties. The production of capsules with solid-like interfaces would allow tuning of their roughness. This can be achieved through a controlled removal of the liquid core from the capsule, for instance via evaporation as shown in Figure 9.1. Since the water removal from the capsules can be easily tuned, this could represent a simple and convenient strategy to increase the roughness of the capsules, a recommendable feature in catalysis and drug delivery.

Overall, in this work we explored different strategies for the CNP assembly in aqueous media, providing insights on the structure-property relationship and contributing towards the production of functional materials using renewable sources.

BIBLIOGRAPHY

- [1] J. van der Gucht, *Grand Challenges in Soft Matter Physics*, *Frontiers in Physics*, **6**, p. 87 (2018).
- [2] P. G. De Gennes, *Nobel Lecture*, Nobel Media AB 2019 (1991).
- [3] P. G. De Gennes, *Soft matter: More than words*, *Soft Matter*, **1**, p. 16 (2005).
- [4] E. Board, *The future of plastic*, *Nature communications*, **9**, p. 2157 (2018).
- [5] <https://www.ncbi.nlm.nih.gov/pubmed/>.
- [6] Z. Hu and M. G. Gänzle, *Challenges and opportunities related to the use of chitosan as a food preservative*, *Journal of Applied Microbiology*, **126**, pp. 1318–1331 (2019).
- [7] A. K. Zetzl, A. G. Marangoni, and S. Barbut, *Mechanical properties of ethylcellulose oleogels and their potential for saturated fat reduction in frankfurters*, *Food and Function*, **3**, pp. 327–337 (2012).
- [8] M. Henchion, M. Hayes, A. Mullen, M. Fenelon, and B. Tiwari, *Future Protein Supply and Demand: Strategies and Factors Influencing a Sustainable Equilibrium*, *Foods*, **6**, p. 53 (2017).
- [9] L. Monaci, V. Tregoat, A. J. Van Hengel, and E. Anklam, *Milk allergens, their characteristics and their detection in food: A review*, *European Food Research and Technology*, **223**, pp. 149–179 (2006).
- [10] D. J. Gardner, G. S. Oporto, R. Mills, and M. A. S. Azizi Samir, *Adhesion and surface issues in cellulose and nanocellulose*, *Journal of Adhesion Science and Technology*, **22**, pp. 545–567 (2008).
- [11] R. Jonas and L. F. Farah, *Production and application of microbial cellulose*, *Polymer Degradation and Stability*, **59**, pp. 101–106 (1998).
- [12] J. Peng, V. Calabrese, S. J. Veen, P. Versluis, K. P. Velikov, P. Venema, and E. van der Linden, *Rheology and microstructure of dispersions of protein fibrils and cellulose microfibrils*, *Food Hydrocolloids*, **82**, pp. 196–208 (2018).
- [13] A. Isogai, T. Saito, and H. Fukuzumi, *TEMPO-oxidized cellulose nanofibers*, *Nanoscale*, **3**, pp. 71–85 (2011).
- [14] P. Bertsch, M. Diener, J. Adamcik, N. Scheuble, T. Geue, R. Mezzenga, and P. Fischer, *Adsorption and Interfacial Layer Structure of Unmodified Nanocrystalline Cellulose at Air/Water Interfaces*, *Langmuir*, **34**, pp. 15195–15202 (2018).
- [15] S. J. Eichhorn, *Cellulose nanowhiskers: Promising materials for advanced applications*, *Soft Matter*, **7**, pp. 303–315 (2011).
- [16] D. da Silva Perez, S. Montanari, and M. R. Vignon, *TEMPO-mediated oxidation of cellulose III*, *Biomacromolecules*, **4**, pp. 1417–1425 (2003).
- [17] Y. Okita, T. Saito, and A. Isogai, *Entire surface oxidation of various cellulose microfibrils by TEMPO-mediated oxidation*, *Biomacromolecules*, **11**, pp. 1696–1700 (2010).
- [18] M. Zaman, H. Xiao, F. Chibante, and Y. Ni, *Synthesis and characterization of cationically modified nanocrystalline cellulose*, *Carbohydrate Polymers*, **89**, pp. 163–170 (2012).

- [19] M. Hasani, E. D. Cranston, G. Westman, and D. G. Gray, *Cationic surface functionalization of cellulose nanocrystals*, *Soft Matter*, **4**, pp. 2238–2244 (2008).
- [20] J. C. Courtenay, S. M. Ramalheite, W. J. Skuze, R. Soni, Y. Z. Khimyak, K. J. Edler, and J. L. Scott, *Insights into cationic cellulose nanofibril hydrogel structure through NMR spectroscopy and small angle neutron scattering*, *Soft Matter*, **14**, pp. 255–263 (2018).
- [21] J. Schmitt, V. Calabrese, M. A. Da Silva, S. Lindhoud, V. Alfredsson, J. L. Scott, and K. J. Edler, *TEMPO-oxidised cellulose nanofibrils; Probing the mechanisms of gelation: Via small angle X-ray scattering*, *Physical Chemistry Chemical Physics*, **20**, pp. 16012–16020 (2018).
- [22] S. Montanari, M. Roumani, L. Heux, and M. R. Vignon, *Topochemistry of carboxylated cellulose nanocrystals resulting from TEMPO-mediated oxidation*, *Macromolecules*, **38**, pp. 1665–1671 (2005).
- [23] Y. Nishiyama, *Structure and properties of the cellulose microfibril*, *Journal of Wood Science*, **55**, pp. 241–249 (2009).
- [24] K. Wickholm, P. T. Larsson, and T. Iversen, *Assignment of non-crystalline forms in cellulose I by CP/MAS ^{13}C NMR spectroscopy*, *Carbohydrate Research*, **312**, pp. 123–129 (1998).
- [25] O. A. Battista, *Hydrolysis and Crystallization of Cellulose*, *Industrial & Engineering Chemistry*, **42**, pp. 502–507 (1950).
- [26] I. Usov, G. Nyström, J. Adamcik, S. Handschin, C. Schötz, A. Fall, L. Bergström, and R. Mezzenga, *Understanding nanocellulose chirality and structure-properties relationship at the single fibril level*, *Nature Communications*, **6** (2015).
- [27] J. Y. Park, C. W. Park, S. Y. Han, G. J. Kwon, N. H. Kim, and S. H. Lee, *Effects of pH on nanofibrillation of TEMPO-oxidized paper mulberry bast fibers*, *Polymers*, **11** (2019).
- [28] J. L. S. James C. Courtenay, Yun Jin, Julien Schmitt, Karen J. Edler, *Salt responsive Pickering emulsions stabilized by functionalised cellulose nanofibrils*, In preparation (2018).
- [29] T. Saito, T. Uematsu, S. Kimura, T. Enomae, and A. Isogai, *Self-aligned integration of native cellulose nanofibrils towards producing diverse bulk materials*, *Soft Matter*, **7**, pp. 8804–8809 (2011).
- [30] M. Nordenström, A. Fall, G. Nyström, and L. Wågberg, *Formation of Colloidal Nanocellulose Glasses and Gels*, *Langmuir*, **33**, pp. 9772–9780 (2017).
- [31] H. Tanaka, J. Meunier, and D. Bonn, *Nonergodic states of charged colloidal suspensions: Repulsive and attractive glasses and gels*, *Physical Review E - Statistical, Nonlinear, and Soft Matter Physics*, **69**, pp. 1–6 (2004).
- [32] B. Hammouda, *Part A, B, C, D, E, F, G*, in *Probing Nanoscale Structures - The SANS toolbox*, pp. 1–326, National Institute of Standards and Technology Center for Neutron Research Gaithersburg (2010).
- [33] M. Uhlig, A. Fall, S. Wellert, M. Lehmann, S. Prévost, L. Wågberg, R. von Klitzing, and G. Nyström, *Two-Dimensional Aggregation and Semidilute Ordering in Cellulose Nanocrystals*, *Langmuir*, **32**, pp. 442–450 (2016).
- [34] P. Bertsch, S. Isabettini, and P. Fischer, *Ion-Induced Hydrogel Formation and Nematic Ordering of Nanocrystalline Cellulose Suspensions*, *Biomacromolecules*, **18**, pp. 4060–4066 (2017).
- [35] P. Bertsch, A. Sánchez-Ferrer, M. Bagnani, S. Isabettini, J. Kohlbrecher, R. Mezzenga, and P. Fischer, *Ion-Induced Formation of Nanocrystalline Cellulose Colloidal Glasses Containing Nematic Domains*, *Langmuir*, **35**, pp. 4117–4124 (2019).
- [36] A. D. Haywood, K. M. Weigandt, P. Saha, M. Noor, M. J. Green, and V. A. Davis, *New insights into the flow and microstructural relaxation behavior of biphasic cellulose nanocrystal dispersions from RheoSANS*, *Soft Matter*, **13**, pp. 8451–8462 (2017).
- [37] D. Celebi, R. H. Guy, K. J. Edler, and J. L. Scott, *Ibuprofen delivery into and through the skin from novel oxidized cellulose-based gels and conventional topical formulations*, *International Journal of Pharmaceutics*, **514**, pp. 238–243 (2016).

- [38] R. J. Crawford, K. J. Edler, S. Lindhoud, J. L. Scott, and G. Unali, *Formation of shear thinning gels from partially oxidised cellulose nanofibrils*, *Green Chemistry*, **14**, pp. 300–303 (2012).
- [39] P. Mohammadi, M. S. Toivonen, O. Ikkala, W. Wagermaier, and M. B. Linder, *Aligning cellulose nanofibril dispersions for tougher fibers*, *Scientific Reports*, **7**, pp. 1–10 (2017).
- [40] M. J. Lundahl, A. G. Cunha, E. Rojo, A. C. Papageorgiou, L. Rautkari, J. C. Arboleda, and O. J. Rojas, *Strength and Water Interactions of Cellulose i Filaments Wet-Spun from Cellulose Nanofibril Hydrogels*, *Scientific Reports*, **6**, pp. 1–13 (2016).
- [41] H. Fukuzumi, R. Tanaka, T. Saito, and A. Isogai, *Dispersion stability and aggregation behavior of TEMPO-oxidized cellulose nanofibrils in water as a function of salt addition*, *Cellulose*, **21**, pp. 1553–1559 (2014).
- [42] H. Dong, J. F. Snyder, K. S. Williams, and J. W. Andzelm, *Cation-induced hydrogels of cellulose nanofibrils with tunable moduli*, *Biomacromolecules*, **14**, pp. 3338–3345 (2013).
- [43] K. Sim, J. Lee, H. Lee, and H. J. Youn, *Flocculation behavior of cellulose nanofibrils under different salt conditions and its impact on network strength and dewatering ability*, *Cellulose*, **22**, pp. 3689–3700 (2015).
- [44] V. Calabrese, M. A. Da Silva, J. Schmitt, J. C. Muñoz-Garcia, V. Gabrielli, J. L. Scott, J. Angulo, Y. Z. Khimyak, and K. J. Edler, *Surfactant controlled zwitterionic cellulose nanofibril dispersions*, *Soft Matter*, **14**, pp. 7793–7800 (2018).
- [45] L. Mendoza, W. Batchelor, R. F. Tabor, and G. Garnier, *Gelation mechanism of cellulose nanofibre gels: A colloids and interfacial perspective*, *Journal of Colloid and Interface Science*, **509**, pp. 39–46 (2018).
- [46] N. Quennouz, S. M. Hashmi, H. S. Choi, J. W. Kim, and C. O. Osuji, *Rheology of cellulose nanofibrils in the presence of surfactants*, *Soft Matter*, **12**, pp. 157–164 (2016).
- [47] N. Dhar, D. Au, R. C. Berry, and K. C. Tam, *Interactions of nanocrystalline cellulose with an oppositely charged surfactant in aqueous medium*, *Colloids and Surfaces A: Physicochemical and Engineering Aspects*, **415**, pp. 310–319 (2012).
- [48] R. Prathapan, R. Thapa, G. Garnier, and R. F. Tabor, *Modulating the zeta potential of cellulose nanocrystals using salts and surfactants*, *Colloids and Surfaces A: Physicochemical and Engineering Aspects*, **509**, pp. 11–18 (2016).
- [49] E. K. Oikonomou, F. Mousseau, N. Christov, G. Cristobal, A. Vacher, M. Airiau, C. Bourgaux, L. Heux, and J. F. Berret, *Fabric Softener-Cellulose Nanocrystal Interaction: A Model for Assessing Surfactant Deposition on Cotton*, *Journal of Physical Chemistry B*, **121**, pp. 2299–2307 (2017).
- [50] S. Alila, S. Boufi, M. N. Belgacem, and D. Beneventi, *Adsorption of a cationic surfactant onto cellulosic fibers I. Surface charge effects*, *Langmuir*, **21**, pp. 8106–8113 (2005).
- [51] T. D. Jakobsen, S. Simon, E. B. Heggset, K. Syverud, and K. Paso, *Interactions between Surfactants and Cellulose Nanofibrils for Enhanced Oil Recovery*, *Industrial and Engineering Chemistry Research*, **57**, pp. 15749–15758 (2018).
- [52] M. S. Reid, M. Villalobos, and E. D. Cranston, *The role of hydrogen bonding in non-ionic polymer adsorption to cellulose nanocrystals and silica colloids*, *Current Opinion in Colloid and Interface Science*, **29**, pp. 76–82 (2017).
- [53] H. Oguzlu and Y. Boluk, *Interactions between cellulose nanocrystals and anionic and neutral polymers in aqueous solutions*, *Cellulose*, **24**, pp. 131–146 (2017).
- [54] Y. Chen, C. Xu, J. Huang, D. Wu, and Q. Lv, *Rheological properties of nanocrystalline cellulose suspensions*, *Carbohydrate Polymers*, **157**, pp. 303–310 (2017).
- [55] Q. Beuguel, J. R. Tavares, P. J. Carreau, and M.-C. Heuzey, *Rheological behavior of cellulose nanocrystal suspensions in polyethylene glycol*, *Journal of Rheology*, **62**, pp. 607–618 (2018).
- [56] C. D. Edgar and D. G. Gray, *Influence of Dextran on the Phase Behavior of Suspensions of Cellulose Nanocrystals*, *Macromolecules*, **35**, pp. 7400–7406 (2002).
- [57] Z. Hu, E. D. Cranston, R. Ng, and R. Pelton, *Tuning Cellulose Nanocrystal Gelation with Polysaccharides and Surfactants*, *Langmuir*, **30**, pp. 2684–2692 (2014).

- [58] G. Lenfant, M. C. Heuzey, T. G. van de Ven, and P. J. Carreau, *Gelation of crystalline nanocellulose in the presence of hydroxyethyl cellulose*, Canadian Journal of Chemical Engineering, **95**, pp. 1891–1900 (2017).
- [59] K. D. Danov and P. A. Kralchevsky, *The standard free energy of surfactant adsorption at air/water and oil/water interfaces: Theoretical vs. empirical approaches*, Colloid Journal, **74**, pp. 172–185 (2012).
- [60] *Liquid-Gas and Liquid-Liquid interfaces*, in *Introduction to colloid and surface chemistry*, pp. 60–107 (1966).
- [61] M. S. Manga, T. N. Hunter, O. J. Cayre, D. W. York, M. D. Reichert, S. L. Anna, L. M. Walker, R. A. Williams, and S. R. Biggs, *Measurements of Submicron Particle Adsorption and Particle Film Elasticity at Oil-Water Interfaces*, Langmuir, **32**, pp. 4125–4133 (2016).
- [62] H. Vatanparast, F. Shahabi, A. Bahramian, A. Javadi, and R. Miller, *The role of electrostatic repulsion on increasing surface activity of anionic surfactants in the presence of hydrophilic silica nanoparticles*, Scientific Reports, **8**, pp. 1–11 (2018).
- [63] E. Vignati, R. Piazza, and T. P. Lockhart, *Pickering emulsions: Interfacial tension, colloidal layer morphology, and trapped-particle motion*, Langmuir, **19**, pp. 6650–6656 (2003).
- [64] K. Du, E. Glogowski, T. Emrick, T. P. Russell, and A. D. Dinsmore, *Adsorption Energy of Nano- and Microparticles at Liquid-Liquid Interfaces*, Langmuir, **26**, pp. 12518–12522 (2010).
- [65] D. J. McClements, *Emulsion science in the food industry*, in *Food Emulsions: Principles, Practices, and Techniques*, pp. 1–26 (2005).
- [66] C. Solans, D. Morales, and M. Homs, *Spontaneous emulsification*, Current Opinion in Colloid and Interface Science, **22**, pp. 88–93 (2016).
- [67] C. Huang, J. Forth, W. Wang, K. Hong, G. S. Smith, B. A. Helms, and T. P. Russell, *Bicontinuous structured liquids with sub-micrometre domains using nanoparticle surfactants*, Nature Nanotechnology, **12**, pp. 1060–1063 (2017).
- [68] W. Ramsden, *Separation of Solids in the Surface-Layers of Solutions and 'Suspensions' (Observations on Surface-Membranes, Bubbles, Emulsions, and Mechanical Coagulation)*, Proceedings of the Royal Society of London, **72**, pp. 156–164 (1903).
- [69] S. U. Pickering, *Emulsions*, Journal of the Chemical Society, Transaction, **91**, pp. 2001–2021 (1907).
- [70] S. Lam, K. P. Velikov, and O. D. Velev, *Pickering stabilization of foams and emulsions with particles of biological origin*, Current Opinion in Colloid and Interface Science, **19**, pp. 490–500 (2014).
- [71] M. Zanini and L. Isa, *Particle contact angles at fluid interfaces: Pushing the boundary beyond hard uniform spherical colloids*, Journal of Physics Condensed Matter, **28** (2016).
- [72] P. A. Kralchevsky, I. B. Ivanov, K. P. Ananthapadmanabhan, and A. Lips, *On the thermodynamics of particle-stabilized emulsions: Curvature effects and catastrophic phase inversion*, Langmuir, **21**, pp. 50–63 (2005).
- [73] S. K. R. Adhikari, I. Pagonabarraga, D. J.-C., and M. E. Cates, *Chemistry: Colloidal jamming at interfaces: A route to fluid-bicontinuous gels*, Science, **309**, pp. 2198–2201 (2005).
- [74] E. M. Herzig, K. A. White, A. B. Schofield, W. C. Poon, and P. S. Clegg, *Bicontinuous emulsions stabilized solely by colloidal particles*, Nature Materials, **6**, pp. 966–971 (2007).
- [75] J. H. Thijssen and J. Vermant, *Interfacial rheology of model particles at liquid interfaces and its relation to (bicontinuous) Pickering emulsions*, Journal of Physics Condensed Matter, **30**, p. aa9c74 (2018).
- [76] I. Kalashnikova, H. Bizot, B. Cathala, and I. Capron, *New pickering emulsions stabilized by bacterial cellulose nanocrystals*, Langmuir, **27**, pp. 7471–7479 (2011).
- [77] V. Calabrese, J. C. Courtenay, K. J. Edler, and J. L. Scott, *Pickering emulsions stabilized by naturally derived or biodegradable particles*, Current Opinion in Green and Sustainable Chemistry, **12**, pp. 83–90 (2018).

- [78] X. Liu, S. Shi, Y. Li, J. Forth, D. Wang, and T. P. Russell, *Liquid Tubule Formation and Stabilization Using Cellulose Nanocrystal Surfactants*, *Angewandte Chemie - International Edition*, **56**, pp. 12594–12598 (2017).
- [79] S. Shi, X. Liu, Y. Li, X. Wu, D. Wang, J. Forth, and T. P. Russell, *Liquid Letters*, *Advanced Materials*, **30**, pp. 1–5 (2018).
- [80] G. Kaufman, S. Nejati, R. Sarfati, R. Boltyanskiy, M. Loewenberg, E. R. Dufresne, and C. O. Osuji, *Soft microcapsules with highly plastic shells formed by interfacial polyelectrolyte-nanoparticle complexation*, *Soft Matter*, **11**, pp. 7478–7482 (2015).
- [81] M. E. van den Berg, S. Kuster, E. J. Windhab, J. Adamcik, R. Mezzenga, T. Geue, L. M. C. Sagis, and P. Fischer, *Modifying the contact angle of anisotropic cellulose nanocrystals: Effect on interfacial rheology and structure*, *Langmuir*, **34**, pp. 10932–10942 (2018).
- [82] M. E. van den Berg, S. Kuster, E. J. Windhab, L. M. Sagis, and P. Fischer, *Nonlinear shear and dilatational rheology of viscoelastic interfacial layers of cellulose nanocrystals*, *Physics of Fluids*, **30**, p. 072103 (2018).
- [83] X. Wu, Q. Yuan, S. Liu, S. Shi, T. P. Russell, and D. Wang, *Nanorod Surfactant Assemblies and Their Interfacial Behavior at Liquid-Liquid Interfaces*, *ACS Macro Letters*, **8**, pp. 512–518 (2019).
- [84] E. Spruijt, M. A. Cohen Stuart, and J. Van Der Gucht, *Linear viscoelasticity of polyelectrolyte complex coacervates*, *Macromolecules*, **46**, pp. 1633–1641 (2013).
- [85] Z. Hu, S. Ballinger, R. Pelton, and E. D. Cranston, *Surfactant-enhanced cellulose nanocrystal Pickering emulsions*, *Journal of Colloid and Interface Science*, **439**, pp. 139–148 (2015).
- [86] F. Cherhal, F. Cousin, and I. Capron, *Structural Description of the Interface of Pickering Emulsions Stabilized by Cellulose Nanocrystals*, *Biomacromolecules*, **17**, pp. 496–502 (2016).
- [87] M. Gestranus, P. Stenius, E. Kontturi, J. Sjöblom, and T. Tammelin, *Phase behaviour and droplet size of oil-in-water Pickering emulsions stabilised with plant-derived nanocellulosic materials*, *Colloids and Surfaces A: Physicochemical and Engineering Aspects*, **519**, pp. 60–70 (2017).
- [88] Y. Jia, X. Zhai, W. Fu, Y. Liu, F. Li, and C. Zhong, *Surfactant-free emulsions stabilized by tempo-oxidized bacterial cellulose*, *Carbohydrate Polymers*, **151**, pp. 907–915 (2016).
- [89] L. Bai, S. Lv, W. Xiang, S. Huan, D. J. McClements, and O. J. Rojas, *Oil-in-water Pickering emulsions via microfluidization with cellulose nanocrystals: 1. Formation and stability*, *Food Hydrocolloids*, **96**, pp. 699–708 (2019).
- [90] F. Niu, B. Han, J. Fan, M. Kou, B. Zhang, Z. J. Feng, W. Pan, and W. Zhou, *Characterization of structure and stability of emulsions stabilized with cellulose macro/nano particles*, *Carbohydrate Polymers*, **199**, pp. 314–319 (2018).
- [91] L. Bai, S. Huan, W. Xiang, and O. J. Rojas, *Pickering emulsions by combining cellulose nanofibrils and nanocrystals: Phase behavior and depletion stabilization*, *Green Chemistry*, **20**, pp. 1571–1582 (2018).
- [92] R. Aaen, F. W. Brodin, S. Simon, E. B. Heggset, and K. Syverud, *Oil-in-water emulsions stabilized by cellulose nanofibrils: The effects of ionic strength and pH*, *Nanomaterials*, **9**, pp. 1–14 (2019).
- [93] C. Tang, S. Spinney, Z. Shi, J. Tang, B. Peng, J. Luo, and K. C. Tam, *Amphiphilic Cellulose Nanocrystals for Enhanced Pickering Emulsion Stabilization*, *Langmuir*, **34**, pp. 12897–12905 (2018).
- [94] A. Häberle, *Concentrating solar technologies for industrial process heat and cooling*, in K. Lovegrove and W. Stein (editors), *Concentrating Solar Power Technology*, Woodhead Publishing Series in Energy, pp. 602–619, Elsevier (2012).
- [95] D. Silva, *Elastic Scattering*, in *Elementary Scattering Theory*, pp. 61–160, Oxford University Press (2011).
- [96] Y. S. Heimo Schnablegger, *Basic of SAXS*, in *The SAXS guide*, pp. 13–30, Anton Paar GmbH (2013).

- [97] I. Grillo, *Small-Angle Neutron Scattering and Applications in Soft Condensed Matter*, in R. Borsali and R. Pecora (editors), *Soft Matter Characterization*, January, pp. 27–30, Springer Netherlands, Dordrecht (2008).
- [98] R. Phyn, *Neutron scattering a primer*, volume 27, Los Alamos Science (2017).
- [99] A. J. Jackson, *Introduction to Small-Angle Neutron Scattering and Neutron Reflectometry*, NIST Center for Neutron Research, pp. 1–24 (2008).
- [100] S. Lazzari, L. Nicoud, B. Jaquet, M. Lattuada, and M. Morbidelli, *Fractal-like structures in colloid science*, *Advances in Colloid and Interface Science*, **235**, pp. 1–13 (2016).
- [101] T. L. Moore, L. Rodriguez-Lorenzo, V. Hirsch, S. Balog, D. Urban, C. Jud, B. Rothen-Rutishauser, M. Lattuada, and A. Petri-Fink, *Nanoparticle colloidal stability in cell culture media and impact on cellular interactions*, *Chemical Society Reviews*, **44**, pp. 6287–6305 (2015).
- [102] S. Kynde, K. Hewitt Klenø, G. Nagy, K. Mortensen, K. Lefmann, J. Kohlbrecher, and L. Arleth, *A compact time-of-flight SANS instrument optimised for measurements of small sample volumes at the European Spallation Source*, *Nuclear Instruments and Methods in Physics Research, Section A: Accelerators, Spectrometers, Detectors and Associated Equipment*, **764**, pp. 133–141 (2014).
- [103] S. A. Rogers, B. M. Erwin, D. Vlassopoulos, and M. Cloitre, *A sequence of physical processes determined and quantified in LAOS: Application to a yield stress fluid*, *J. Rheol.*, **55**, pp. 435–458 (2011).
- [104] K. Hyun, S. H Kim, K. H Ahn, and S. J Lee, *Large amplitude oscillatory shear as a way to classify the complex fluids*, *Journal of Non-Newtonian Fluid Mechanics*, **107**, pp. 51–65 (2002).
- [105] J. Mewis, N. J. Wagner, J. Mewis, and N. J. Wagner, *Introduction to colloid science and rheology*, *Colloidal Suspension Rheology*, pp. 1–35 (2011).
- [106] I. T. Norton, F. Spyropoulos, and P. Cox, *Practical Food Rheology An Interpretive Approach*, in *Chemical Engineering*, pp. 10–15, Wiley-Blackwell (2011).
- [107] H. M. Laun, *Rheological properties of aqueous polymer dispersions*, *Die Angewandte makromolekulare Chemie Applied macromolecular chemistry and physics*, **123**, pp. 335–359 (1984).
- [108] A. M. Philippe, C. Baravian, M. Imperor-Clerc, J. De Silva, E. Paineau, I. Bihannic, P. Davidson, F. Meneau, P. Levitz, and L. J. Michot, *Rheo-SAXS investigation of shear-thinning behaviour of very anisometric repulsive disc-like clay suspensions*, *Journal of Physics Condensed Matter*, **23** (2011).
- [109] I. W. Hamley, S. Burholt, J. Hutchinson, V. Castelletto, E. R. Da Silva, W. Alves, P. Gutfreund, L. Porcar, R. Dattani, D. Hermida-Merino, G. Newby, M. Reza, J. Ruokolainen, and J. Stasiak, *Shear Alignment of Bola-Amphiphilic Arginine-Coated Peptide Nanotubes*, *Biomacromolecules*, **18**, pp. 141–149 (2017).
- [110] M. Takeda, T. Kusano, T. Matsunaga, H. Endo, M. Shibayama, and T. Shikata, *Rheo-SANS studies on shear-thickening/thinning in aqueous rodlike micellar solutions*, *Langmuir*, **27**, pp. 1731–1738 (2011).
- [111] M. A. da Silva, V. Calabrese, J. Schmitt, D. Celebi, J. L. Scott, and K. J. Edler, *Alcohol induced gelation of TEMPO-oxidized cellulose nanofibril dispersions*, *Soft matter*, **14**, pp. 9243–9249 (2018).
- [112] E. Van Der Linden, L. Sagis, and P. Venema, *Rheo-optics and food systems*, *Current Opinion in Colloid and Interface Science*, **8**, pp. 349–358 (2003).
- [113] R. G. Larson, *Particulate Suspensions*, in *The structure and rheology of complex fluids*, pp. 263–324 (1999).
- [114] N. C. Crawford, L. B. Popp, K. E. Johns, L. M. Caire, B. N. Peterson, and M. W. Liberatore, *Shear thickening of corn starch suspensions: Does concentration matter?*, *Journal of Colloid and Interface Science*, **396**, pp. 83–89 (2013).
- [115] J. M. Brader, *Nonlinear rheology of colloidal dispersions*, *Journal of Physics: Condensed Matter*, **22**, p. 363101 (2010).

- [116] A. L. Ogden and J. A. Lewis, *Effect of Nonadsorbed Polymer on the Stability of Weakly Flocculated Suspensions*, *Langmuir*, **7463**, pp. 3413–3424 (1996).
- [117] H. A. Barnes, *Thixotropy - a review*, *Journal of Non-Newtonian Fluid Mechanics*, **70**, pp. 1–33 (1997).
- [118] J. Mewis and N. J. Wagner, *Thixotropy*, *Advances in Colloid and Interface Science*, **147**, pp. 214–227 (2009).
- [119] V. Calabrese, J. C. Muñoz-García, J. Schmitt, M. A. da Silva, J. L. Scott, J. Angulo, Y. Z. Khimiyak, and K. J. Edler, *Understanding heat driven gelation of anionic cellulose nanofibrils: Combining saturation transfer difference (STD) NMR, small angle X-ray scattering (SAXS) and rheology*, *Journal of Colloid and Interface Science*, **535**, pp. 205–213 (2019).
- [120] I. Masalova, M. Taylor, E. Kharatiyan, and A. Y. Malkin, *Rheopexy in highly concentrated emulsions*, *Journal of Rheology*, **49**, pp. 839–849 (2005).
- [121] J. Mewis and N. J. Wagner, *Hydrodynamic Effects*, in *Colloidal Suspension Rheology*, pp. 36–78 (2011).
- [122] A. Einstein, *Eine neue Bestimmung der Moleküldimensionen*, *Annalen der Physik*, **19**, pp. 289–306 (1906).
- [123] A. Einstein, *Berichtigung zu meiner Arbeit: "Eine neue Bestimmung der Moleküldimensionen"*, *Annalen der Physik*, **34**, pp. 591–592 (1911).
- [124] R. G. Larson, *Polymers*, in *The structure and rheology of complex fluids*, pp. 107–179 (1999).
- [125] G. K. Batchelor and J. T. Green, *of Spherical Particles To Order C2*, *Journal of Fluid Mechanics*, **56**, pp. 401–427 (1972).
- [126] I. M. Krieger and T. J. Dougherty, *A Mechanism for NonNewtonian Flow in Suspensions of Rigid Spheres*, *Transactions of the Society of Rheology*, **3**, pp. 137–152 (1959).
- [127] J. S. Chong, E. B. Christiansen, and A. D. Baer, *Rheology of Concentrated Suspensions*, *Journal of Applied Polymer Science*, pp. 2007–2021 (1971).
- [128] K. Hyun, M. Wilhelm, C. O. Klein, K. S. Cho, J. G. Nam, K. H. Ahn, S. J. Lee, R. H. Ewoldt, and G. H. McKinley, *A review of nonlinear oscillatory shear tests: Analysis and application of large amplitude oscillatory shear (LAOS)*, *Progress in Polymer Science*, **36**, pp. 1697–1753 (2011).
- [129] R. H. Ewoldt, C. Clasen, A. E. Hosoi, and G. H. McKinley, *Rheological fingerprinting of gastropod pedal mucus and synthetic complex fluids for biomimicking adhesive locomotion*, *Soft Matter*, **3**, pp. 634–643 (2007).
- [130] L. M. C. Sagis and P. Fischer, *Current Opinion in Colloid & Interface Science Nonlinear rheology of complex fluid fluid interfaces*, *Current Opinion in Colloid & Interface Science*, **19**, pp. 520–529 (2014).
- [131] S. H. Kim, H. G. Sim, K. H. Ahn, and S. J. Lee, *Large amplitude oscillatory shear behavior of the network model for associating polymeric systems*, *Korea-Australia Rheology Journal*, **14**, pp. 49–55 (2002).
- [132] J. C.-W. Lee, L. Porcar, and S. A. Rogers, *Unveiling Temporal Nonlinear Structure Rheology Relationships under Dynamic Shearing*, *Polymers*, **11**, p. 1189 (2019).
- [133] J. C.-W. Lee, K. M. Weigandt, E. G. Kelley, and S. A. Rogers, *Structure-Property Relationships via Recovery Rheology in Viscoelastic Materials*, *Physical Review Letters*, **122**, p. 248003 (2019).
- [134] S. Vandebril, A. Franck, G. G. Fuller, P. Moldenaers, and J. Vermant, *A double wall-ring geometry for interfacial shear rheometry*, *Rheologica Acta*, **49**, pp. 131–144 (2010).
- [135] J. Drelich, *Measurement of Interfacial Tension in Fluid-Fluid Systems*, *Encyclopedia of Surface and Colloid Science*, pp. 3152–3166 (2002).
- [136] V. A. Hackley and J. D. Clogston, *Measuring the Hydrodynamic Size of Nanoparticles in Aqueous Media Using Batch-Mode Dynamic Light Scattering*, in *Characterization of Nanoparticles Intended for Drug Delivery*, pp. 35–52 (2011).

- [137] R. Finsy, *Particle sizing by quasi-elastic light scattering.*, Advances in Colloid and Interface Science, **52**, pp. 79–143 (1994).
- [138] J. Stetefeld, S. A. McKenna, and T. R. Patel, *Dynamic light scattering: a practical guide and applications in biomedical sciences*, Biophysical Reviews, **8**, pp. 409–427 (2016).
- [139] Y. Boluk and C. Danumah, *Analysis of cellulose nanocrystal rod lengths by dynamic light scattering and electron microscopy*, Journal of Nanoparticle Research, **16** (2014).
- [140] J. G. De La Torre and V. A. Bloomfield, *Hydrodynamic properties of complex, rigid, biological macromolecules: Theory and applications*, Quarterly Reviews of Biophysics, **14**, pp. 81–139 (1981).
- [141] M. Kaszuba, J. Corbett, F. M. N. Watson, and A. Jones, *High-concentration zeta potential measurements using light-scattering techniques*, Philosophical Transactions of the Royal Society A: Mathematical, Physical and Engineering Sciences, **368**, pp. 4439–4451 (2010).
- [142] J. D. Clogston and A. K. Patri, *Zeta potential Measurements*, in *Characterization of Nanoparticles Intended for Drug Delivery*, pp. 63–70 (2011).
- [143] I. M. Tucker, J. C. Corbett, J. Fatkin, R. O. Jack, M. Kaszuba, B. MacCreath, and F. McNeil-Watson, *Laser Doppler Electrophoresis applied to colloids and surfaces*, Current Opinion in Colloid and Interface Science, **20**, pp. 215–226 (2015).
- [144] A. Nwaneshiudu, C. Kuschal, F. H. Sakamoto, R. Rox Anderson, K. Schwarzenberger, and R. C. Young, *Introduction to confocal microscopy*, Journal of Investigative Dermatology, **132**, pp. 1–5 (2012).
- [145] S. W. Paddock and K. W. Eliceiri, *Laser Scanning Confocal Microscopy: History, Applications, and Related Optical Sectioning Techniques*, in *Confocal Microscopy Methods and Protocols*, pp. 9–48 (2014).
- [146] J. S. Cannell, *Review paper Fundamentals of stability testing*, International Journal of Cosmetic Science, **7**, pp. 291 – 303 (1984).
- [147] R. Nigmatullin, V. Gabrielli, J. C. Muñoz-García, A. E. Lewandowska, R. Harniman, Y. Z. Khimiyak, J. Angulo, and S. J. Eichhorn, *Thermosensitive supramolecular and colloidal hydrogels via self-assembly modulated by hydrophobized cellulose nanocrystals*, Cellulose, **26**, pp. 529–542 (2019).
- [148] J. C. Muñoz-garcia, K. R. Corbin, H. Hussain, V. Gabrielli, T. Koev, D. Iuga, A. N. Round, D. Mikkelsen, P. A. Gunning, F. J. Warren, and Y. Z. Khimiyak, *High molecular weight mixed-linkage glucan as a mechanical and hydration modulator of bacterial cellulose : characterisation by advanced NMR spectroscopy* (2019).
- [149] S. M. C. Silva, F. V. Pinto, F. E. Antunes, M. G. Miguel, J. J. S. Sousa, and A. a. C. C. Pais, *Aggregation and gelation in hydroxypropylmethyl cellulose aqueous solutions*, Journal of Colloid and Interface Science, **327**, pp. 333–340 (2008).
- [150] L. Weng, L. Zhang, D. Ruan, L. Shi, and J. Xu, *Thermal Gelation of Cellulose in a NaOH/Thiourea Aqueous Solution*, Langmuir, **20**, pp. 2086–2093 (2004).
- [151] L. Li, *Thermal gelation of methylcellulose in water: Scaling and thermoreversibility*, Macromolecules, **35**, pp. 5990–5998 (2002).
- [152] P. A. Cornwell, *A review of shampoo surfactant technology: consumer benefits, raw materials and recent developments*, International Journal of Cosmetic Science, **40**, pp. 16–30 (2018).
- [153] X. Zhang, M. R. Servos, and J. Liu, *Ultrahigh nanoparticle stability against salt, pH, and solvent with retained surface accessibility via depletion stabilization*, Journal of the American Chemical Society, **134**, pp. 9910–9913 (2012).
- [154] H. Sun, M. Y. Z. Chang, W. I. Cheng, Q. Wang, A. Commisso, M. Capeling, Y. Wu, and C. Cheng, *Biodegradable zwitterionic sulfobetaine polymer and its conjugate with paclitaxel for sustained drug delivery*, Acta Biomaterialia, **64**, pp. 290–300 (2017).
- [155] P. Liu, Q. Chen, L. Li, S. Lin, and J. Shen, *Antibiofouling ability and cytocompatibility of the zwitterionic brushes-modified cellulose membrane*, Journal of Materials Chemistry B, **2**, pp. 7222–7231 (2014).
- [156] Y. Liu, H. Huang, P. Huo, and J. Gu, *Exploration of zwitterionic cellulose acetate antifouling ultrafiltration membrane for bovine serum albumin (BSA) separation*, Carbohydrate Polymers, **165**, pp. 266–275 (2017).

- [157] T. Elschner, C. Lüdecke, D. Kalden, M. Roth, B. Löffler, K. D. Jandt, and T. Heinze, *Zwitterionic Cellulose Carbamate with Regioselective Substitution Pattern: A Coating Material Possessing Antimicrobial Activity*, *Macromolecular Bioscience*, **16**, pp. 522–534 (2016).
- [158] S. Liu, J. Liu, A. R. Esker, and K. J. Edgar, *An Efficient, Regioselective Pathway to Cationic and Zwitterionic N-Heterocyclic Cellulose Ionomers*, *Biomacromolecules*, **17**, pp. 503–513 (2016).
- [159] P. Trivedi, J. Trygg, T. Saloranta, and P. Fardim, *Synthesis of novel zwitterionic cellulose beads by oxidation and coupling chemistry in water*, *Cellulose*, **23**, pp. 1751–1761 (2016).
- [160] H. Huang, Y. Shen, J. Yu, H. Guo, F. Yang, J. Gu, and Y. Liu, *A Spherical Zwitterionic Cellulose Acetate/ Graphene Oxide Composite Adsorbent for Efficient Removal of Cu²⁺ and Cd²⁺ from Aqueous Solution*, *BioResources*, **13**, pp. 3642–3658 (2018).
- [161] J. Rostami, A. P. Mathew, and U. Edlund, *Zwitterionic Acetylated Cellulose Nanofibrils*, *Molecules*, **24**, p. 3147 (2019).
- [162] E. Gicquel, C. Martin, Q. Gauthier, J. Engström, C. Abbattista, A. Carlmark, E. D. Cranston, B. Jean, and J. Bras, *Tailoring Rheological Properties of Thermoresponsive Hydrogels through Block Copolymer Adsorption to Cellulose Nanocrystals*, *Biomacromolecules*, **20**, pp. 2545–2556 (2019).
- [163] T. Gillece, R. L. McMullen, H. Fares, L. Senak, S. Ozkan, and L. Foltis, *Probing the textures of composite skin care formulations using large amplitude oscillatory shear*, *Journal of cosmetic science*, **67**, pp. 121–159 (2016).
- [164] J. Athinarayanan, V. S. Periasamy, M. A. Alsaif, A. A. Al-Warthan, and A. A. Alshatwi, *Presence of nanosilica (E551) in commercial food products: TNF-mediated oxidative stress and altered cell cycle progression in human lung fibroblast cells*, *Cell Biology and Toxicology*, **30**, pp. 89–100 (2014).
- [165] C. O. Metin, K. M. Rankin, and Q. P. Nguyen, *Phase behavior and rheological characterization of silica nanoparticle gel*, *Applied Nanoscience (Switzerland)*, **4**, pp. 93–101 (2014).
- [166] X. J. Cao, H. Z. Cummins, and J. F. Morris, *Structural and rheological evolution of silica nanoparticle gels*, *Soft Matter*, **6**, p. 5425 (2010).
- [167] M. Kobayashi, F. Juillerat, P. Galletto, P. Bowen, and M. Borkovec, *Aggregation and charging of colloidal silica particles: Effect of particle size*, *Langmuir*, **21**, pp. 5761–5769 (2005).
- [168] I. Imaz, M. Rubio-Martínez, W. J. Saletta, D. B. Amabilino, and D. Maspocho, *Amino acid based metal-organic nanofibers*, *Journal of the American Chemical Society*, **131**, pp. 18222–18223 (2009).
- [169] K. Biradha, A. Ramanan, and J. J. Vittal, *Coordination polymers versus metal-organic frameworks*, *Crystal Growth and Design*, **9**, pp. 2969–2970 (2009).
- [170] M. L. Kim, E. H. Ota, and J. P. Hinestroza, *Cellulose meets reticular chemistry: interactions between cellulosic substrates and metalorganic frameworks*, *Cellulose*, **26**, pp. 123–137 (2019).
- [171] H. Zhu, Q. Zhang, and S. Zhu, *Alginate Hydrogel: A Shapeable and Versatile Platform for in Situ Preparation of Metal-Organic Framework-Polymer Composites*, *ACS Applied Materials and Interfaces*, **8**, pp. 17395–17401 (2016).
- [172] A.-N. Au-Duong and C.-K. Lee, *Flexible MetalOrganic Framework-Bacterial Cellulose Nanocomposite for Iodine Capture*, *Crystal Growth & Design*, **18**, pp. 356–363 (2018).
- [173] J. Park and M. Oh, *Construction of flexible metal-organic framework (MOF) papers through MOF growth on filter paper and their selective dye capture*, *Nanoscale*, **9**, pp. 12850–12854 (2017).
- [174] L. Segale, L. Giovannelli, P. Mannina, and F. Pattarino, *Calcium Alginate and Calcium Alginate-Chitosan Beads Containing Celecoxib Solubilized in a Self-Emulsifying Phase*, *Scientifica*, pp. 1–8 (2016).
- [175] B. Zeeb, A. H. Saberi, J. Weiss, and D. J. McClements, *Retention and release of oil-in-water emulsions from filled hydrogel beads composed of calcium alginate: impact of emulsifier type and pH*, *Soft matter*, pp. 2228–2236 (2015).

- [176] B. Zeeb, A. H. Saberi, J. Weiss, and D. J. McClements, *Formation and characterization of filled hydrogel beads based on calcium alginate: Factors influencing nanoemulsion retention and release*, *Food Hydrocolloids*, **50**, pp. 27–36 (2015).
- [177] Z. Zhang, R. Zhang, L. Zou, and D. J. McClements, *Protein encapsulation in alginate hydrogel beads: Effect of pH on microgel stability, protein retention and protein release*, *Food Hydrocolloids*, **58**, pp. 308–315 (2016).
- [178] C. Lamaze, B. Sinha, S. Scheuring, L. Fetler, F. Rico, P. Nassoy, S. Geraldo, K. Alessandri, L. Rolland, A. Simon, V. V. Gurchenkov, T. R. Kiessling, H. Domejean, D. Vignjevic, J. Bibette, N. Bremond, A. Funfak, and B. R. Sarangi, *Cellular capsules as a tool for multicellular spheroid production and for investigating the mechanics of tumor progression in vitro*, *Proceedings of the National Academy of Sciences*, **110**, pp. 14843–14848 (2013).
- [179] N. Bremond, E. Santanach-Carreras, L. Y. Chu, and J. Bibette, *Formation of liquid-core capsules having a thin hydrogel membrane: Liquid pearls*, *Soft Matter*, **6**, pp. 2484–2488 (2010).
- [180] L. Rolland, E. Santanach-Carreras, T. Delmas, J. Bibette, and N. Bremond, *Physicochemical properties of aqueous core hydrogel capsules*, *Soft Matter*, **10**, pp. 9668–9674 (2014).
- [181] I. Lacík, M. Briššová, A. V. Anilkumar, A. C. Powers, and T. Wang, *New capsule with tailored properties for the encapsulation of living cells*, *Journal of Biomedical Materials Research*, **39**, pp. 52–60 (1997).
- [182] M. Briššová, I. Lacík, A. C. Powers, A. V. Anilkumar, and T. Wang, *Control and measurement of permeability for design of microcapsule cell delivery system*, *Journal of Biomedical Materials Research*, **39**, pp. 61–70 (1997).
- [183] T. Krajčovič, M. Bučko, A. Vikartovská, I. Lacík, L. Uhelská, D. Chorvát, V. Neděla, E. Tihlařková, M. Gericke, T. Heinze, and P. Gemeiner, *Polyelectrolyte complex beads by novel two-step process for improved performance of viable whole-cell baeyer-villiger monooxygenase by immobilization*, *Catalysts*, **7**, pp. 1–12 (2017).
- [184] E. Laurenti and A. dos Santos Vianna Jr., *Enzymatic microreactors in biocatalysis: history, features, and future perspectives*, *Biocatalysis*, **1**, pp. 148–165 (2016).
- [185] R. C. Rodrigues, C. Ortiz, Á. Berenguer-Murcia, R. Torres, and R. Fernández-Lafuente, *Modifying enzyme activity and selectivity by immobilization*, *Chemical Society Reviews*, **42**, pp. 6290–6307 (2013).
- [186] F. Secundo, *Conformational changes of enzymes upon immobilisation*, *Chemical Society Reviews*, **42**, pp. 6250–6261 (2013).
- [187] G. Kaufman, S. Mukhopadhyay, Y. Rokhlenko, S. Nejati, R. Boltyanskiy, Y. Choo, M. Loewenberg, and C. O. Osuji, *Highly stiff yet elastic microcapsules incorporating cellulose nanofibrils*, *Soft Matter*, **13**, pp. 2733–2737 (2017).
- [188] D. Barthés-Biesel, *Role of interfacial properties on the motion and deformation of capsules in shear flow*, *Physica A: Statistical Mechanics and its Applications*, **172**, pp. 103–124 (1991).
- [189] E. Dickinson and J. Chen, *Heat-set whey protein emulsion gels: Role of active and inactive filler particles*, *Journal of Dispersion Science and Technology*, **20**, pp. 197–213 (1999).

CHAPTER 10

APPENDIX

10.1 Supporting information for Chapter 3

Understanding heat driven gelation of anionic cellulose nanofibrils: combining STD NMR, SAXS and rheology

Vincenzo Calabrese,^{a‡} Juan C. Muñoz-García,^{b‡} Julien Schmitt,^a Marcelo A. da Silva,^a Janet L. Scott,^{a,c} Jesús Angulo,^b Yaroslav Z. Khimyak,^{b*} Karen J. Edler^{a*}

^a Department of Chemistry, University of Bath, Claverton Down, Bath, BA2 7AY, UK. E-mail: k.edler@bath.ac.uk;
Tel: 01225 384192

^b School of Pharmacy, University of East Anglia, Norwich Research Park, Norwich, NR4 7TJ, UK

^c Centre for Sustainable Chemical Technology, University of Bath, Claverton Down, Bath, BA2 7AY, UK. E-mail:
j.l.scott@bath.ac.uk University of Bath Tel: 01225 386307

‡ These authors contributed equally

* Corresponding authors: Y.Khimyak@uea.ac.uk, k.edler@bath.ac.uk

Supplementary information

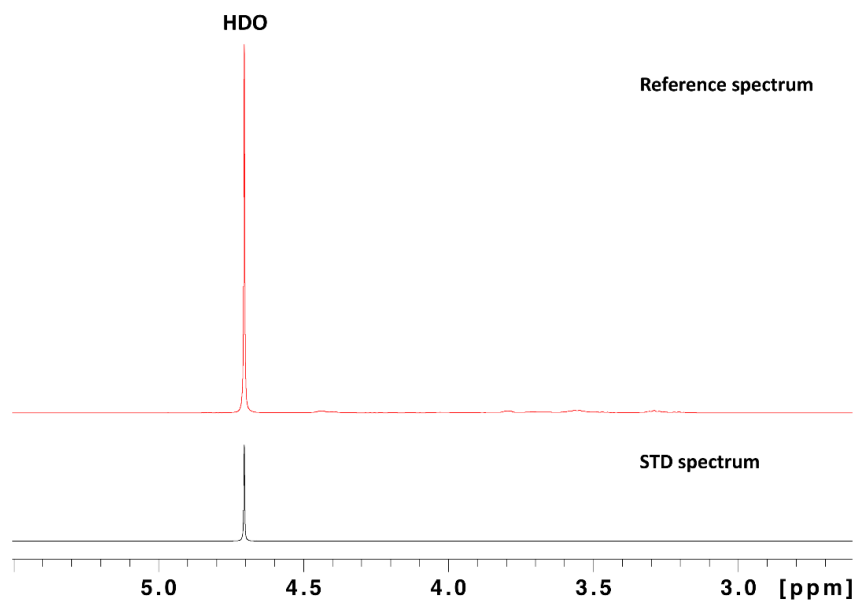


Figure S1. Overlay of the ^1H STD (black) and off-resonance (red) spectra of 1 wt% OCNF at 80 °C.

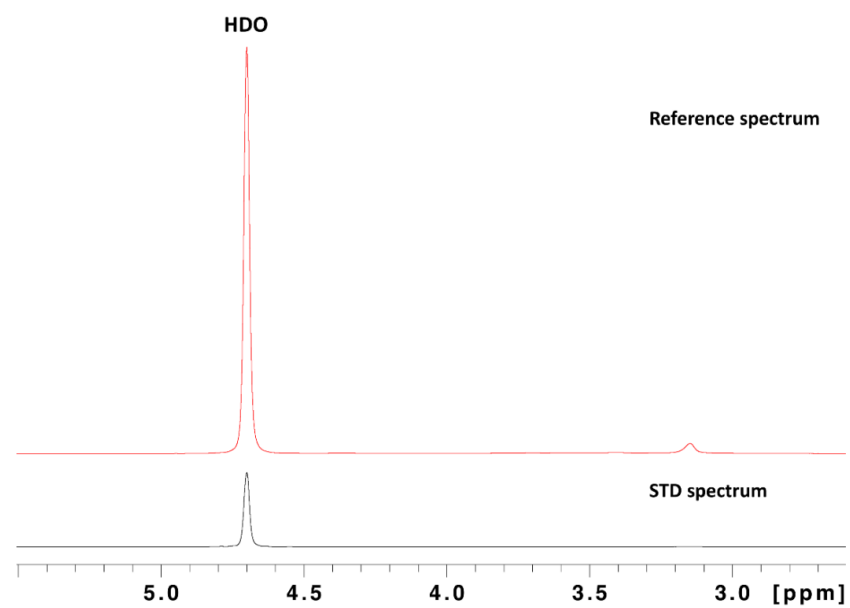


Figure S2. Overlay of the ^1H STD (black) and off-resonance (red) spectra of CCNF 1 wt% at 80 °C.

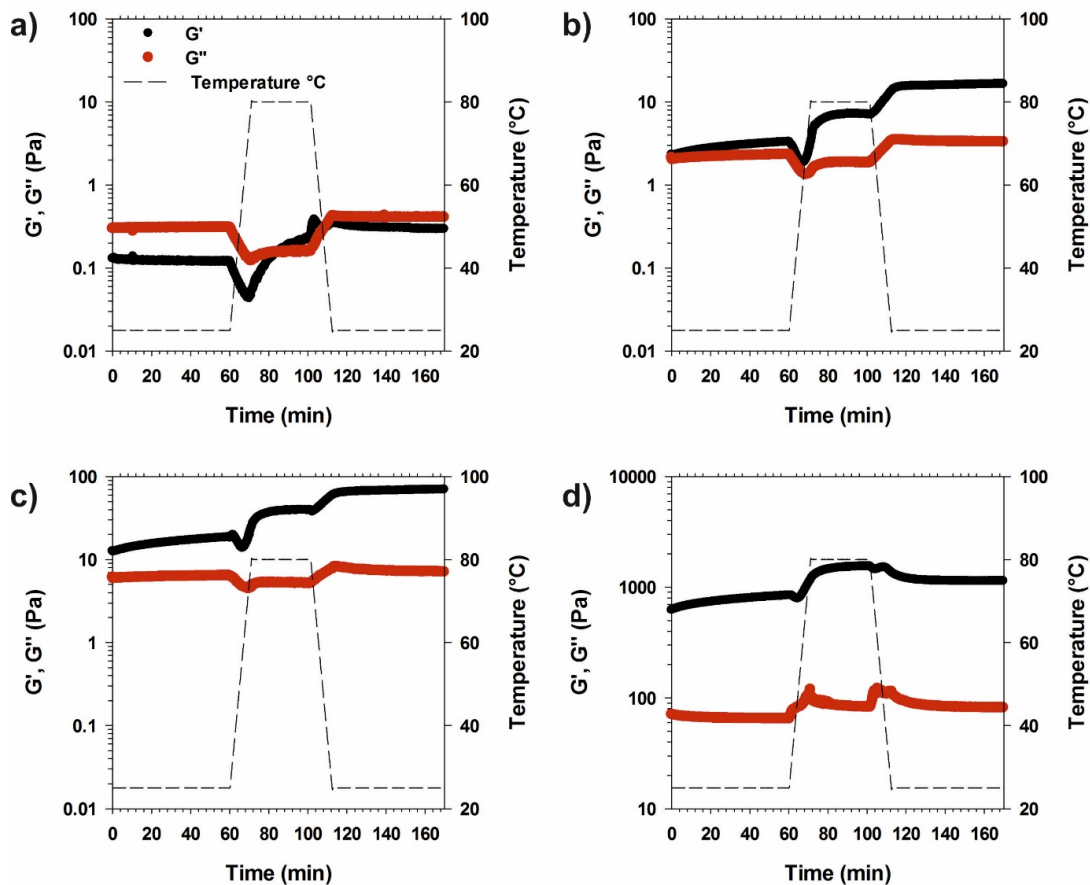


Figure S3. Storage (G') and loss (G'') moduli as function of temperature and time of OCNF dispersions at 1.00, 1.50, 1.75 and 4 wt%, respectively a), b), c) and d). Error for intrinsic limitation of sample loading and equipment of ca. 5%. This is within the size of the symbols used on the graphs.

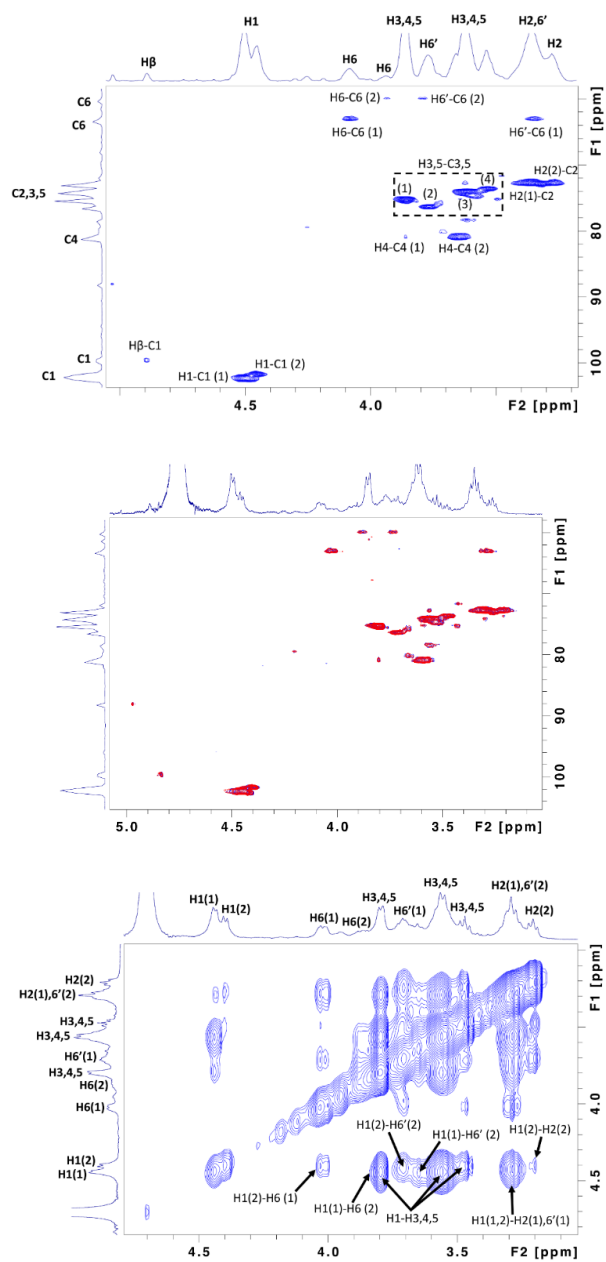


Figure S4. (Top) ^1H ^{13}C HSQC spectra of OCNF 1 wt% acquired at 25 °C. (Central) Overlay of ^1H ^{13}C HSQC spectra of OCNF 1 wt% acquired at 25 °C before (blue) and after (red; 3X zoomed in) heating the sample at 80 °C for an hour. No chemical shift differences are observed. (Bottom) NOESY spectrum of a dispersion of OCNF 1 wt% at 25 °C and 300 ms mixing time.

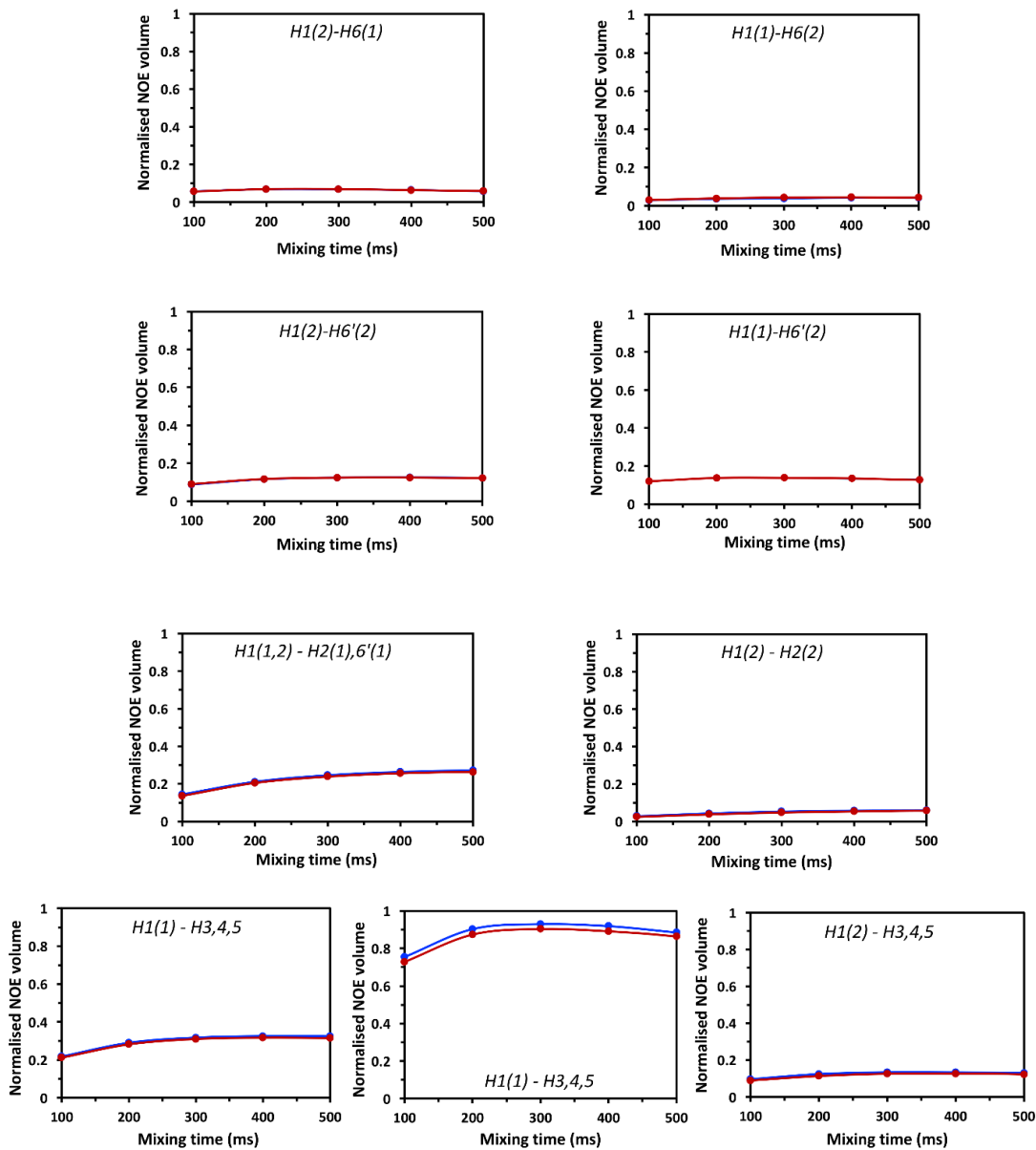


Figure S5. NOESY build up curves acquired at 25 °C for OCNF 1 wt% dispersion before (blue line dots) and after (red line dots) heating at 80 °C for an hour. The corresponding cross peaks are indicated in each graph as shown in figure S4. No significant differences are observed between heated and non-heated samples, thus indicating no conformational change at the surface of OCNF fibrils upon heating.

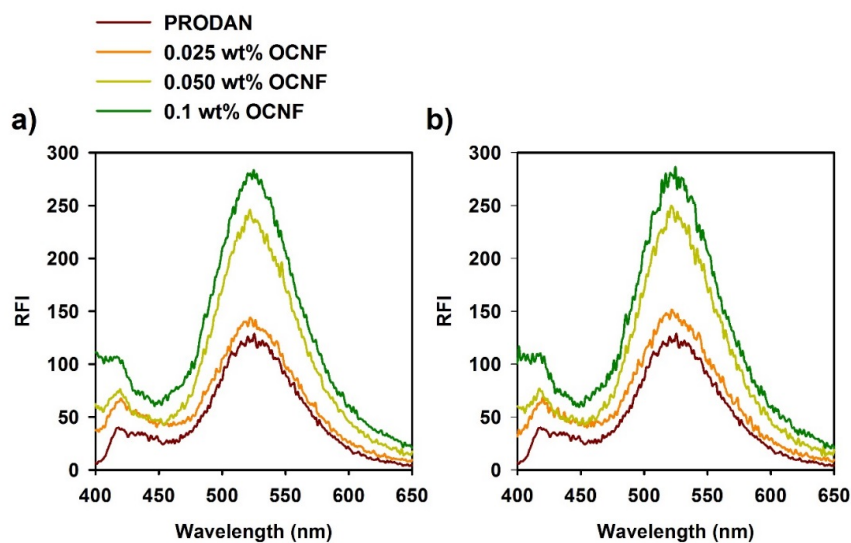


Figure S6. Relative fluorescent intensity (RFI) of non-heated (a) and heated (b) OCNF dispersions. The sample containing pure PRODAN shows a peak between 500 and 550 nm as previously reported.⁵ Nevertheless, a second peak occurring at ca. 450 nm associated to the grafted PRODAN was absent before and after heating (80 °C for 30min) of the samples. Therefore, it indicates the absence of strong hydrophobic interactions in both non-heated and heated OCNF.

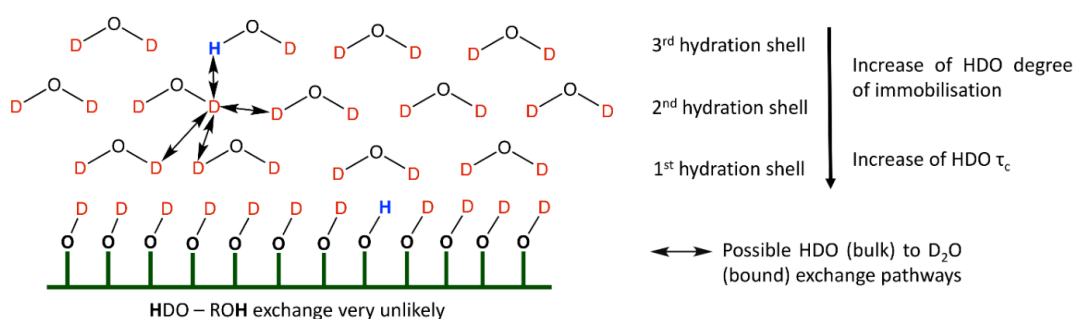


Figure S7. Scheme showing the contribution to the STD signal of the chemical exchange between the exchangeable protons (OH groups) of cellulose and deuterated water. This contribution is strongly reduced when the sample is prepared in D₂O. In other words, the STD factor observed for the HDO peak is mostly reporting on the fraction of cellulose bound HDO, as the vast majority of STD signal comes from inter molecular NOE of HDO with the non-exchangeable protons of cellulose. On the other hand, the relaxation time T₂ of HDO is largely affected by the HDO D₂O exchange.

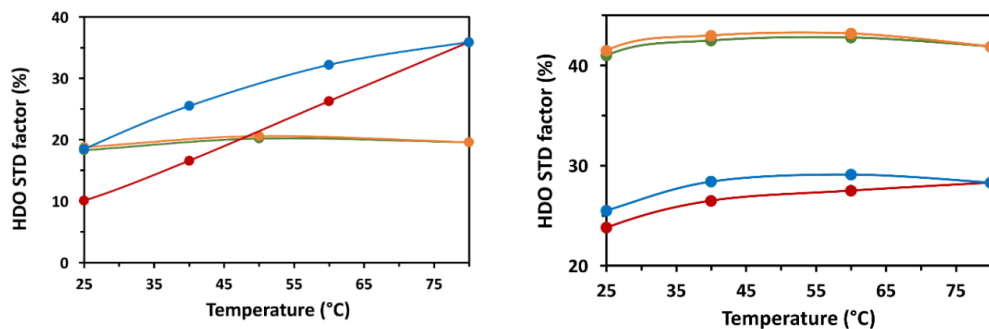


Figure S8. Temperature evolution of the ^1H STD factor (%) for the HDO peak in 1 wt% (left) and 4 wt% (right) OCNF (red heating and blue cooling dots) and CCNF (green heating and orange cooling dots) gels. The error of the measurement of STD factors is ca. 10%, in line with the previous reports.

Additional Nuclear Magnetic Resonance (NMR) characterisation

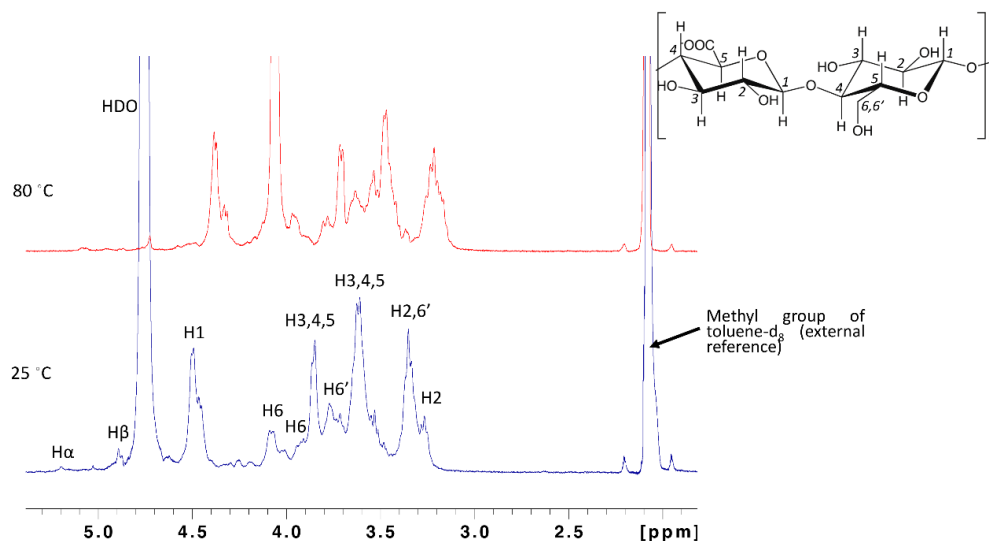


Figure S9. Overlay of the ^1H NMR spectra of OCNF 1 wt% dispersion at 25 °C (blue) and 80 °C (red). The spectra are referenced to the methyl peak of toluene- d_8 (2.08 ppm at 25 °C), used as external reference in a coaxial tube.

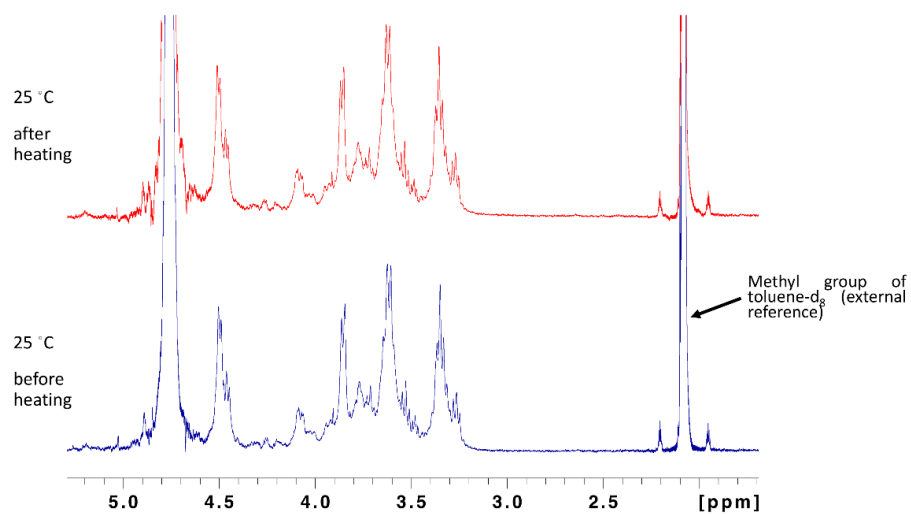


Figure S10. Overlay of the ^1H NMR spectra of OCNF 1 wt% dispersion at 25 °C, before (blue) and after (red) heating at 80 °C for an hour. The spectra are referenced to the methyl peak of toluene d_8 (2.08 ppm at 25 °C), used as external reference in a coaxial tube. No chemical shift differences are observed for the heated sample.

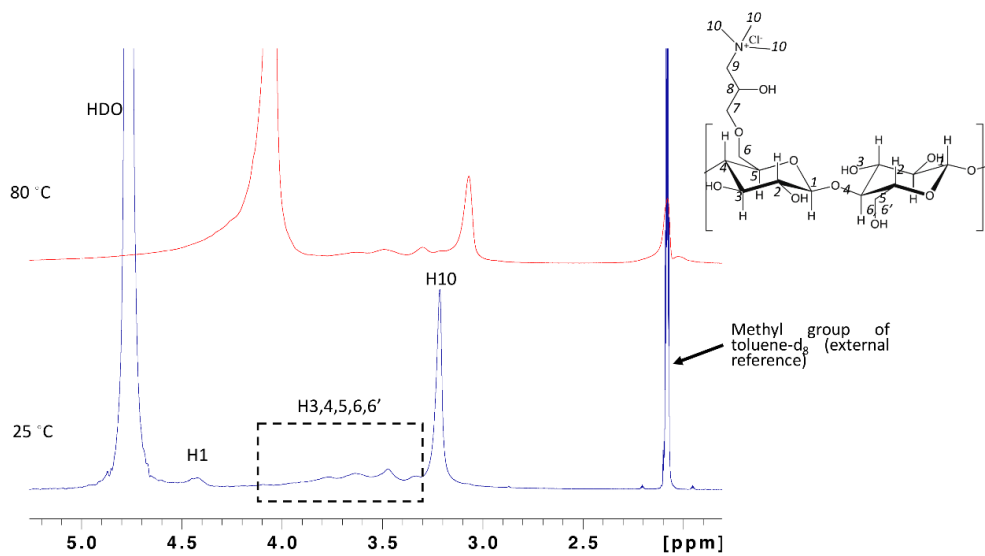


Figure S11. Overlay of the ^1H NMR spectra of CCNF 1 wt% gel at 25 °C (blue) and 80 °C (red).

T₁ and T₂ relaxation of water (HDO) in OCND and CCNF hydrogels

¹H longitudinal relaxation times (T₁) were measured using a standard inversion recovery pulse sequence with a recycle delay of 5 s. 16 or 64 points were acquired at variable delay time after the inversion pulse, ranging from 100 ms to 20 s, or 25 ms to 50 s. The evolution of intensities of the HDO peak was fitted to the inversion-recovery monoexponential equation in TopSpin 3.5

$$M_z(\tau) = M_0 \left[1 - 2e^{\left(\frac{-\tau}{T_1}\right)} \right] \quad (1)$$

where M_z is the z component of magnetisation, M_0 the equilibrium magnetisation (at τ_∞), and τ the variable delay time.⁶ The additional factor of two arises as the recovery starts from inverted magnetization.

The Carr-Purcell-Meiboom-Gill (CPMG) experiment was carried out to determine the transverse relaxation time (T₂), using a recycle delay of 5 s. 16 points were acquired at variable *spin echo* period repetitions (20 ms per *spin echo*), so that the total evolution time ranged from 40 ms to 9 s. The decrease of the intensity of the HDO resonance over the evolution time was fitted in to the monoexponential decay function

$$M_z(\tau) = M_0 \left[e^{\left(\frac{-\tau}{T_2}\right)} \right] \quad (2)$$

where τ is the refocusing time.⁷ The data were analysed using TopSpin 3.5 software.

¹H relaxation times (T₁ and T₂) are traditionally used to investigate solvation in hydrogels.^{8,9} We carried out the ¹H T₁ and T₂ study of the HDO peak for both OCNF and CCNF gels at variable temperatures (from 25 to 80 °C). A significant increase of ¹H T₁ times of HDO was observed for CCNF gels upon heating, this effect being more acute at 1 wt% compared to 4 wt% CCNF concentration (Fig. S12, S13). As in the rheological study the parameters G' and G'' of CCNF gels were barely affected by temperature (Fig. 1), the behaviour of T₁ times upon heating should be related to the increase of mobility (rotational diffusion) of water. This effect is more significant for CCNF 1 wt% gels due to the higher fraction of water molecules in the bulk-like free state at lower concentration of the particle. This is deduced from the longer T₁ values of water in CCNF 1 wt% compared to 4 wt% gels (Fig. S12, S13).

On the other hand, ¹H T₁ of HDO in OCNF dispersions showed a hysteretic behaviour during the heat-cooling cycle (Fig. S13), in agreement with rheology (Fig. 1, Fig. S3). Interestingly, ¹H T₁ times of HDO did not change significantly in OCNF 1 wt% dispersions upon heating, while in 4 wt% gels the temperature effect was more acute although still lower than in CCNF 4wt% gels (Fig. S12, S13). Although it is tempting to relate the lower impact of temperature on OCNF T₁ times to an increase in the fraction of OCNF-confined water compared to CCNF gels, the data are not conclusive. This is because (i) the solid-like component (G') measured by rheology increased significantly upon heating in OCNF gels, this effect being more pronounced at 1 wt% compared to 4 wt% gels (Fig. 1, Fig. S12, S13), and (ii) T₁ relaxation time is characterized by a parabolic-like dependence with molecular motion, so that both a tightly confined and a bulklike free water molecule could contribute to increased T₁ times. Therefore,

the measured T_1 values of water are reporting on different organizations of the gel network at low and high temperature (different rheology). However, they represent an average over all different contributions, ranging from bulk-like free to tightly confined water molecules, along with all possible intermediate dynamic ranges at the different solvation shells of cellulose. For that reason, we can conclude that T_1 is not a convenient NMR parameter to assess the role of water in temperature triggered gelation mechanisms.

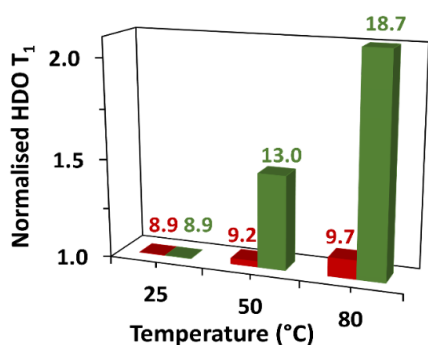


Fig. S12 Normalised ^1H HDO T_1 relaxation time at increasing temperatures (25, 40 and 80 °C) for OCNF (red bars) and CCNF (green bars) 1 wt% dispersions. The evolution of the intensity of the HDO peak at different delay times in the inversion-recovery experiments was fitted to a one component mono-exponential equation, and the calculated values were normalized against the smallest one (arbitrary value of 1). Absolute T_1 values (in seconds) are included above each bar (negligible error bars, within the 10^{-2} - 10^{-3} range, thus not shown).

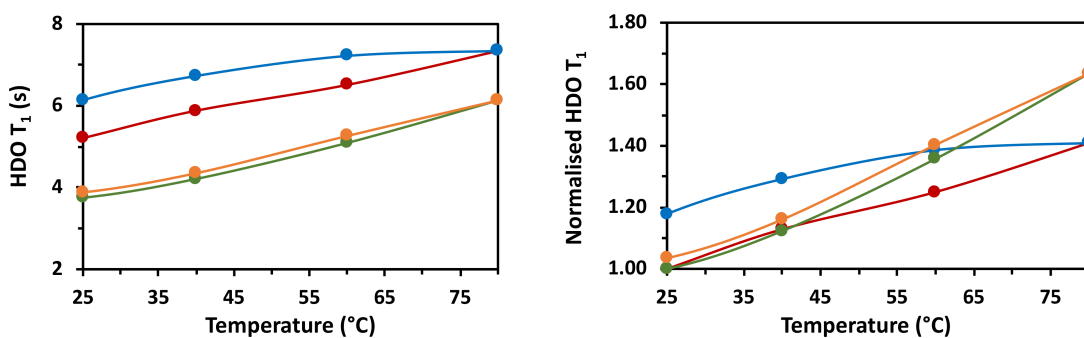


Figure S13. HDO T_1 relaxation times over temperature for OCNF (red heating and blue cooling dots) and CCNF (green heating and orange cooling dots) 4 wt% gels, obtained from the fit to one T_1 component. The absolute and normalised (against the lowest T_1 value obtained for each gel) values are shown on the left and right graph, respectively.

To resolve the complexity of ^1H T_1 data interpretation of OCNF hydrogels, ^1H T_2 relaxation time measurements for HDO were carried out at increasing temperatures. It should be noted that T_2 relaxation is characterised by a monotonic dependence with molecular motion, with more restricted mobility resulting in shorter T_2 times.⁶ In addition, unlike T_1 , T_2 relaxation can be affected by chemical

exchange. The CCNF 1 wt% gels were used as control samples. HDO ^1H T_2 times increased for the CCNF 1wt% gel at high temperature (Fig. S14b), confirming its bulk-like free state behaviour. On the other hand, as shown above for ^1H T_1 , the ^1H T_2 times of HDO in OCNF dispersions showed a hysteretic behaviour during the heat-cooling-cycle (Fig. S14a, S15), in agreement with our rheological observations (Fig. 1, Fig. S3). Importantly, ^1H T_2 times decreased significantly in OCNF gels upon heating (Fig. S14a), thus suggesting an increased fraction of OCNF-confined water molecules at elevated temperatures. Nevertheless, we cannot discard a contribution of chemical exchange (from the free to bound water exchange), which depends on the fraction of OCNF-bound water and the kinetics of exchange. To elucidate which of these mechanisms were contributing to relaxation, ^1H T_2 times were measured for water in 4 wt% OCNF gels.

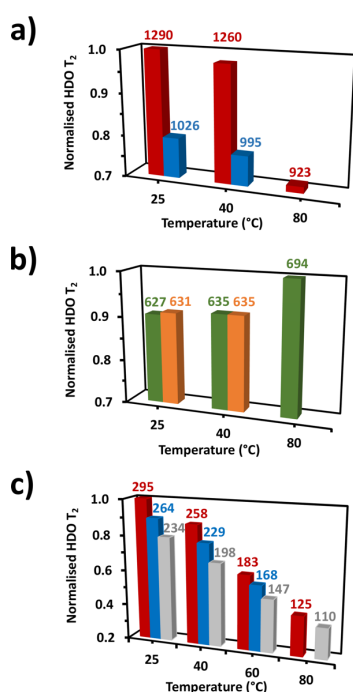


Figure S14. Evolution of the ^1H HDO T_2 relaxation time with temperature for a) 1 wt% OCNF, during heating (red bars, 25, 40 and 80 $^{\circ}\text{C}$) and subsequent cooling (blue bars, 40 and 80 $^{\circ}\text{C}$), b) 1 wt% CCNF, during heating (green bars, 25, 40 and 80 $^{\circ}\text{C}$) and subsequent cooling (orange bars, 40 and 80 $^{\circ}\text{C}$) and c) 4 wt% OCNF during heating (red bars, 25, 40, 60 and 80 $^{\circ}\text{C}$), subsequent cooling (blue bars, 25, 40 and 60 $^{\circ}\text{C}$), and cooling 48 h after the first annealing (grey bars, 25, 40, 60 and 80 $^{\circ}\text{C}$). The absolute T_2 values, in ms, are shown next to each data point or bar. The error bars are not shown as the standard deviation was negligible in all cases (within the 10^{-2} - 10^{-3} range).

As expected for the stiffer 4 wt% gels, ^1H T_2 times were significantly lower for 4 wt% compared to 1 wt% OCNF and CCNF dispersions (Fig. S14, S15). From the rheological measurements it would be expected, in the absence of chemical exchange, a rather small impact of temperature on T_2 times of water at 4

wt% compared to 1 wt% OCNF gels (Fig. S3), as the interfibrillar overlap is close to saturation in 4 wt% gels already at room temperature. However, the effect of heating on ^1H T_2 times was higher at 4 wt% for both CCNF and OCNF gels (Fig. S14c, S15). This indicated that ^1H T_2 values are not only reporting on the increase of the fraction of OCNF-confined water, but they show a very significant contribution of chemical exchange to T_2 relaxation, which is higher at increased particle concentration. Therefore, although T_2 times reported qualitatively on the different rheological behaviour of OCNF and CCNF at 1wt%, they did not allow discrimination between the contribution of kinetics of chemical exchange and the fraction of confined water to T_2 relaxation. This hinders the detailed understanding of the specific role of water during heat induced gelation of OCNF. Interestingly, when HDO ^1H T_2 times were measured again for 4 wt% OCNF gels after 48 h ageing (at 25 °C in static conditions) since the first heating loop, a further decrease of T_2 over the temperature range was observed (Fig. S14c, grey bars), indicating that both heating and ageing strongly influence the water structure within the OCNF network, in very good agreement with rheology (Fig. 1a, Fig. S3).

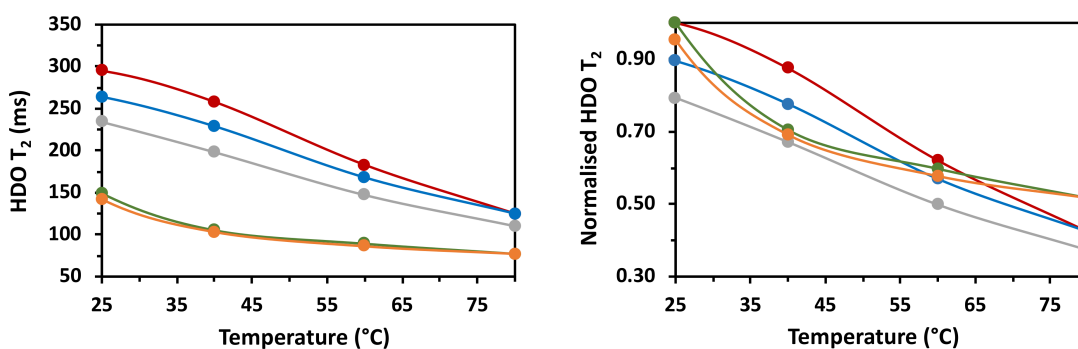


Figure. S15 HDO T_2 relaxation over temperature for OCNF (red dots for heating, blue dots for cooling, and grey dots for cooling after 48h) and CCNF (green dots for heating and orange dots for cooling) 4 wt% gels, obtained from the fit to 1 T_2 component. The absolute and normalised (against the highest T_2 value obtained for each gel) values are shown on the left and right graph, respectively.

T₁ and T₂ relaxation times: additional notes

The longitudinal relaxation time T_1 depends on the frequency distribution of the motion of a randomly tumbling molecule. Briefly, a constrained water molecule would show a more efficient longitudinal relaxation than a bulk one, therefore a shorter T_1 .

Once disturbed from equilibrium, the magnetisation will have components in the xy plane that will also relax back to equilibrium following a first order kinetics characterised by the transverse relaxation time, T_2 , which is affected by molecular motion and chemical exchange. It should be noted that T_2 can be smaller or equal, but can never be greater than T_1 relaxation.

The main differences between the relaxation mechanisms contributing to T_1 and T_2 are (i) the spectral density function at zero frequency ($J(0)$), which only contributes to T_2 relaxation (making T_2 decrease for reduced molecular tumbling, or slow motion), and (ii) the chemical exchange, which again only participates in T_2 relaxation. Therefore, under conditions of slow motion (e.g. a constrained or polymer bound water molecule), $J(0)$ becomes predominant, and thus, T_2 becomes shorter than T_1 .

References

- 1 I. W. Y. Cheung, A. M. Liceaga and E. C. Y. Li-Chan, *J. Food Sci.*, 2009, **74**, C588–C594.
- 2 A. Moro, C. Gatti and N. Delorenzi, *J. Agric. Food Chem.*, 2001, **49**, 4784–4789.
- 3 N. Alizadeh-Pasdar and E. C. Y. Li-Chan, *J. Agric. Food Chem.*, 2000, **48**, 328–334.
- 4 T. Hiratsuka, *Biochemistry*, 1998, **37**, 7167–7176.
- 5 C. A. Haskard and E. C. Y. Li-Chan, *J. Agric. Food Chem.*, 1998, **46**, 2671–2677.
- 6 T.D.W. Claridge, Elsevier, 2008, p. 30.
- 7 H. Y. Carr and E. M. Purcell, *Phys. Rev.*, 1954, **94**, 630–638.
- 8 D. Capitani, V. Crescenzi, A. A. De Angelis and A. L. Segre, *Macromolecules*, 2001, **34**, 4136–4144.
- 9 C. L. Cooper, T. Cosgrove, J. S. van Duijneveldt, M. Murray and S. W. Prescott, *Soft Matter*, 2013, **9**, 7211.

10.2 Supporting information for Chapter 4

Electronic Supplementary Information

Surfactant controlled zwitterionic cellulose nanofibril dispersions

Vincenzo Calabrese,^a Marcelo A. da Silva,^a Julien Schmitt,^a Juan C. Muñoz-Garcia,^b Valeria Gabrielli,^b Janet L. Scott,^{a,c} Jesus Angulo,^b Yaroslav Z. Khimyak,^b Karen J. Edler^{a*}

^a Department of Chemistry, University of Bath, Claverton Down, Bath, BA2 7AY, UK. E-mail: k.edler@bath.ac.uk; Tel: 01225 384192

^b School of Pharmacy, University of East Anglia, Norwich Research Park, Norwich, NR4 7TJ, UK

^c Centre for Sustainable Chemical Technology, University of Bath, Claverton Down, Bath, BA2 7AY, UK. E-mail: j.l.scott@bath.ac.uk University of Bath Tel: 01225 386307

* Corresponding author: E-mail: k.edler@bath.ac.uk; Tel: 01225 384192

Conductimetric titration (Fig. S1) of the oxidised cellulose nanofibril (OCNF) and the zwitterionic cellulose nanofibril (ZCNF) were performed in according to the protocol of da Silva Perez *et. al* using the following equation:¹

$$DO = \frac{162 C (V_2 - V_1)}{w - 37 C (V_2 - V_1)}$$

where C is NaOH concentration (mol/l), V₁ and V₂ the volume of NaOH (l) based on the plateau of the curves, w the dry weight of OCNF (g). The value of 162 is the molecular weight of the anhydroglucose unit (AGU, 162 (g/mol)) whilst 36 corresponds to the difference in molecular weight between the AGU and that of the sodium salt of the glucuronic acid (162-199=37 (g/mol)).

The ZCNF did not show a well defined region where conductivity is weakly dependent on NaOH addition, hence, the DO of oxidation was not evaluated using conductimetric titration.

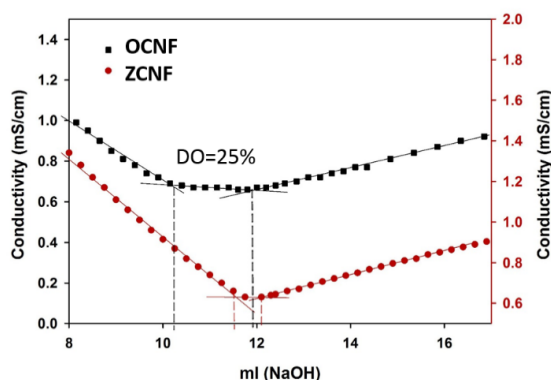


Fig. S1 Conductimetric titration of OCNF and ZCNF.

Attenuated total reflection Fourier transform infrared (ATR-FTIR) spectroscopy was performed using a Perkin Elmer Frontier. The samples were freeze dried in order to remove all the water and the spectra collected in the range 600 to 4000 cm⁻¹. The spectra of OCNF and ZCNF are similar except

for a small difference at 1479 cm^{-1} in the ZCNF spectra (Fig. S2). Zaman *et. al* associated this peak with the CH_2 band arising from the cationic substituent.²

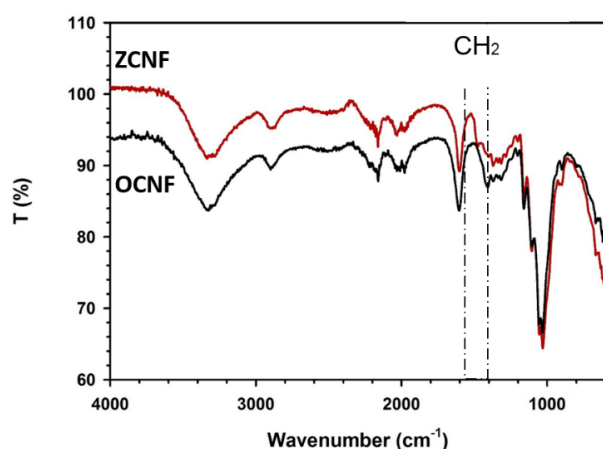


Fig. S2. FTIR spectra of OCNF and ZCNF.

The degree of oxidation (DO) derived from $^{13}\text{C}\{^1\text{H}\}$ DP NMR, calculated as the ratio between the peak areas of the carboxyl group (indicated by an arrow) and the anomeric carbon (peak at 105 ppm), kept constant (*ca.* 25 %) between OCNF and ZCNF samples using 200 s relaxation delay (†ESI Fig. S3). The assessment of DO using the spectra acquired with 800 s relaxation delay is hampered due to poor S/N for the carboxylate peak after 512 scans (Figure 1, †ESI Fig. S4), in spite of 5 days of experimental time. The DO obtained from the experiments with 200 s relaxation delay demonstrates the absence of impact of GTMAC coupling on the degree of oxidation.

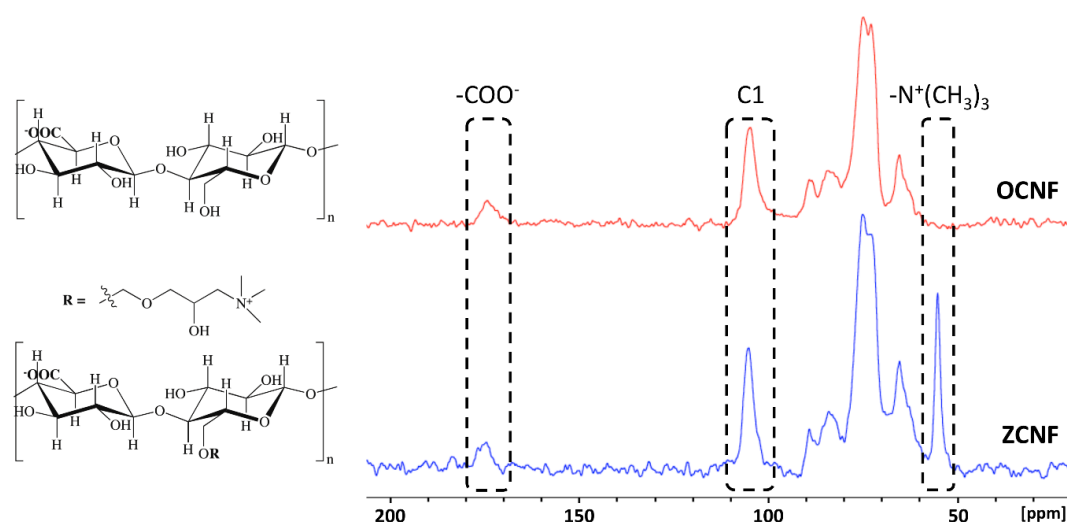


Fig. S3. ^{13}C DP MAS NMR spectra for non-washed ZCNF (blue line) and washed OCNF (red line), after 4k and 8k scans, respectively, acquired at 10 kHz MAS rate and 200 s relaxation delay. The

peaks corresponding to the anomeric carbon and the functionalisation groups are highlighted within dashed rectangles. A degree of oxidation (DO = ratio between the peak area of the carboxyl group and the anomeric carbon) of *ca.* 25 % was obtained for both powders.

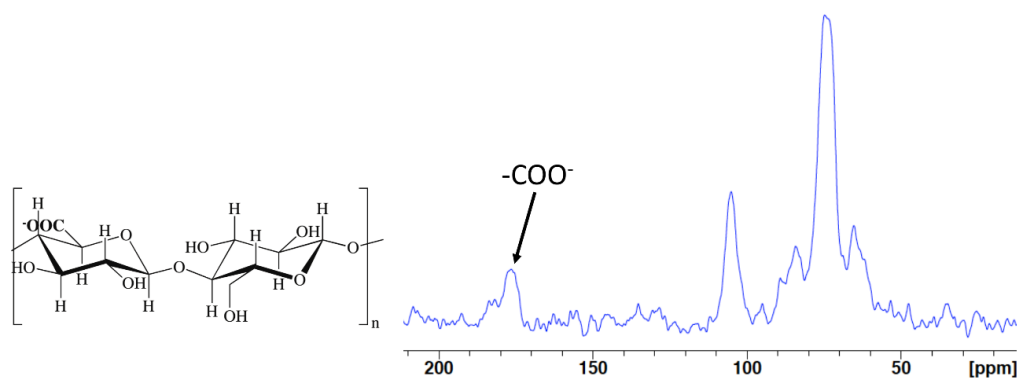


Fig. S4. $^{13}\text{C}\{^1\text{H}\}$ DP MAS NMR spectra for washed OCNF powder after 512 scans, acquired on a 300 MHz spectrometer at 10 kHz MAS rate and 800 s relaxation delay to allow for complete ^{13}C relaxation.³ A line broadening of 80 Hz was used.

References

- 1 D. da Silva Perez, S. Montanari and M. R. Vignon, *Biomacromolecules*, 2003, **4**, 1417–1425.
- 2 M. Zaman, H. Xiao, F. Chibante and Y. Ni, *Carbohydr. Polym.*, 2012, **89**, 163–170.
- 3 K. Wickholm, P. T. Larsson and T. Iversen, *Carbohydr. Res.*, 1998, **312**, 123–129.

10.3 Supporting information for Chapter 5

Filler size effect in an attractive fibrillated network: a structural and rheological perspective

Vincenzo Calabrese,^{a*} Marcelo A. da Silva,^a Lionel Porcar,^b Saffron Bryant,^a

Kazi M. Zakir Hossain,^a Janet L. Scott,^{a,c} Karen J. Edler^{a*}

^a Department of Chemistry, University of Bath, Claverton Down, Bath, BA2 7AY, United Kingdom

^b Institut Laue-Langevin, 71 avenue des Martyrs, CS 20156, 38042 Grenoble cedex 9, France

^c Centre for Sustainable Chemical Technologies, University of Bath, Claverton Down, Bath, BA2 7AY, United Kingdom

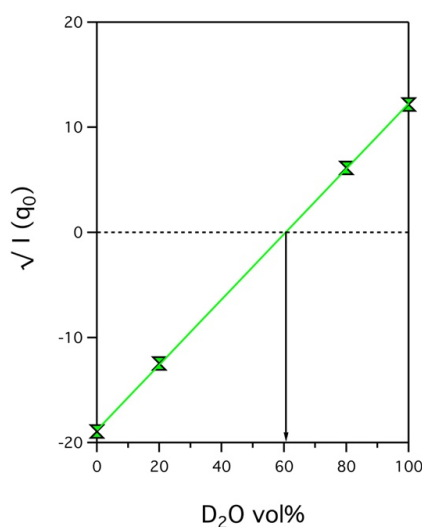


Fig. S1 Contrast match experiment performed for 2.5 wt% SiNp₁₅₈ at different H₂O/D₂O ratios. The scattering Intensity at low-q ($I(q_0)$) for samples at different concentration of D₂O vol% is plotted as the $\sqrt{I(q_0)}$ vs %D₂O. A linear fit, indicated by the green line, was used to determine the point where $\sqrt{I(q_0)} = 0$.

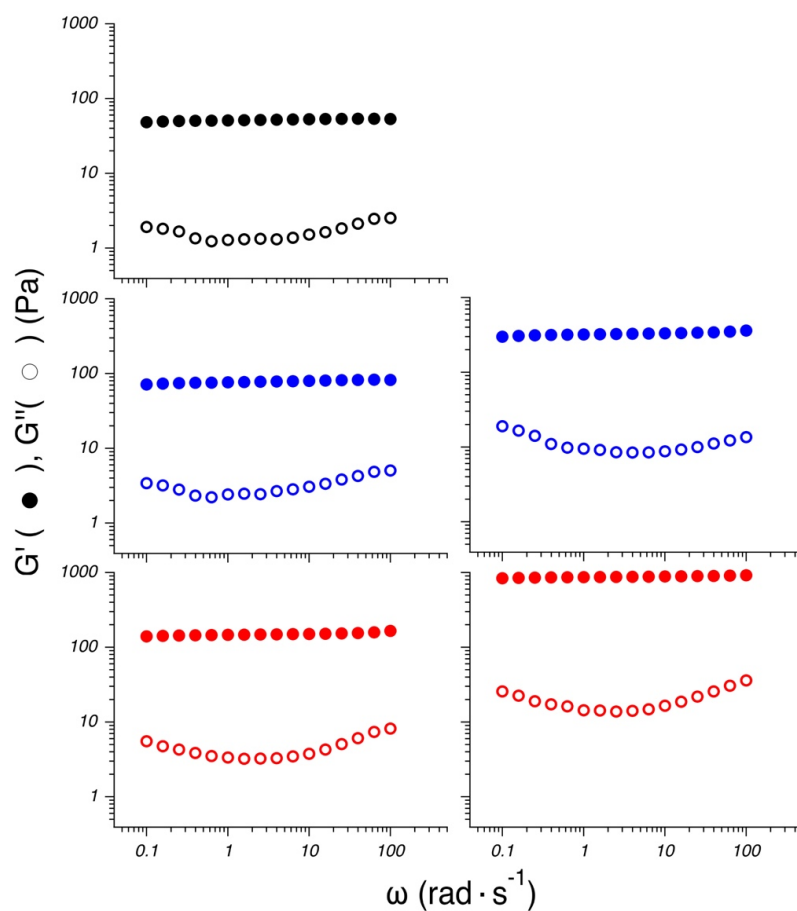


Fig. S2 Frequency sweep performed at constant $\gamma = 0.1\%$, after the time sweep described in the main manuscript, for (top) 1 wt% OCNF, (centre-left) 1 wt% OCNF containing 2.5 wt% SiNp₅, (centre-right) 1 wt% OCNF containing 5 wt% SiNp₅, (bottom-left) 1 wt% OCNF containing 2.5 wt% SiNp₁₅₈, (bottom-right) 1 wt% OCNF containing 5 wt% SiNp₁₅₈. All samples contain 100 mM NaCl.

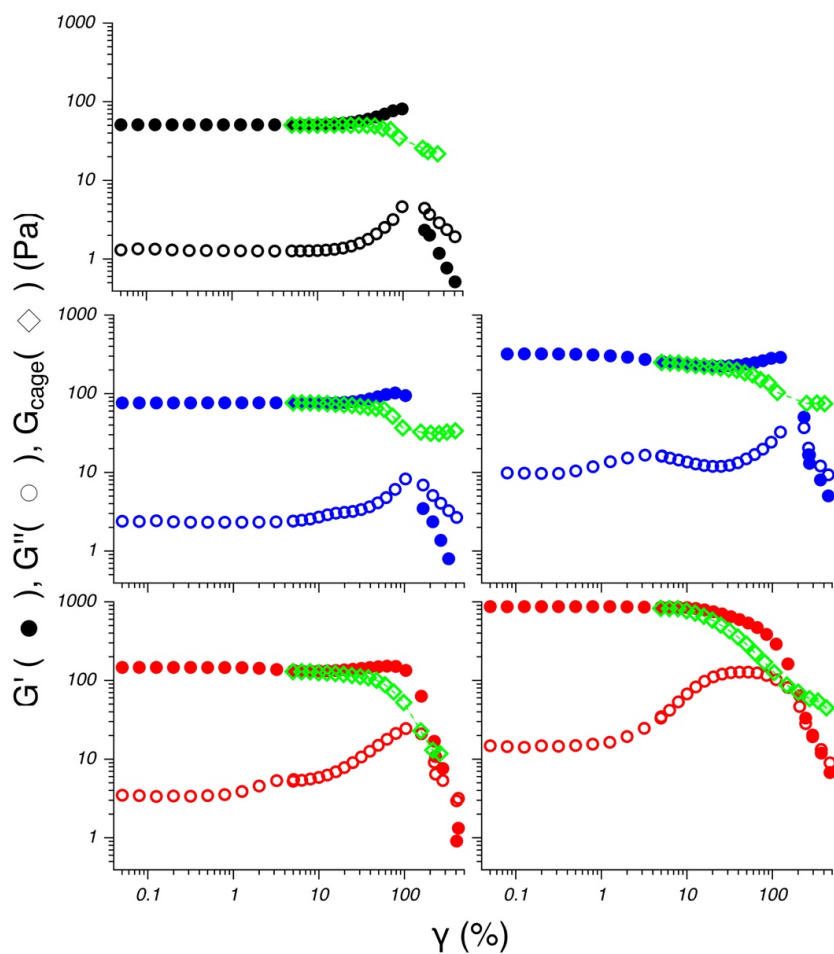


Fig. S3 Strain sweep performed at constant $\omega = 1 \text{ rad s}^{-1}$ for (top) 1 wt% OCNF, (centre-left) 1 wt% OCNF containing 2.5 wt% SiNP₅, (centre-right) 1 wt% OCNF containing 5 wt% SiNP₅, (bottom-left) 1 wt% OCNF containing 2.5 wt% SiNP₁₅₈, (bottom-right) 1 wt% OCNF containing 5 wt% SiNP₁₅₈. All samples contain 100 mM NaCl.

10.4 Supporting information for Chapter 6

Supplementary information

Composite hydrogel spheroids incorporating cellulose nanofibrils and chiral coordination polymer nanofibres

Emile R. Engel, Vincenzo Calabrese, Karen J. Edler and Janet L. Scott

Department of Chemistry, University of Bath, Bath BA2 7AY, UK

E-mail: ee380@bath.ac.uk

Materials

TEMPO-oxidised cellulose nanofibrils (OCNF)¹ were provided by Croda® as a ca. 8 wt% paste of solids in water. The degree of oxidation, with respect to number of anhydroglucose units, is 25% by conductometric titration.² The OCNF was acidified to pH 3 using 1 M HCl (aq) and purified by dialysis against deionised water using Sigma-Aldrich® cellulose dialysis tubing with a molecular weight cut-off of 12,400 Da. Dialysis was carried out for 3 days, with daily replacement of deionised water, after which the pH of the OCNF suspension was adjusted to 7 using 0.1 M NaOH (aq). A stock dispersion of 3.01(6) wt% OCNF was prepared by mechanical shearing for 30 min at 10,000 rpm using an IKA T18 digital Ultra-Turrax, followed by sonication. Batches of 40 mL 3.01(6) wt% OCNF were dispersed by sonication (instrument details and method provided below) for a total processing time of 60 min (ca. 7500 J) per batch.

Silica nanoparticles (SiNP) of diameter 157 ± 1 nm (Z-average) and DLS polydispersity index (intensity distribution) of 0.14 (DLS instrument details provided below) were purchased as silica powder from Sigma-Aldrich (product number 718483). A 10.04(1) wt% stock dispersion was prepared by suspending SiNP in water and dispersing by sonication, using the method below, in 20 mL batches for a total processing time of 2 min (240 J) per batch.

L-Aspartic acid (L-Asp), D-Aspartic acid (D-Asp), $\text{Cu}(\text{NO}_3)_2 \cdot 3\text{H}_2\text{O}$ and NaOH were purchased from Sigma-Aldrich® and used as received.

Primary matrix: The 3.01(6) wt% OCNF and 10.04(1) wt% SiNP stock dispersions were combined in appropriate proportions with water to prepare the primary (ligand-free) matrix comprising 1.00(6) wt% OCNF and 5.02(1) wt% SiNP. This dispersion was homogenised in batches of 10 mL by the sonication method below for a total processing time of 60 s (120 J) per batch.

Ligand-containing matrix: The 3.01(6) wt% OCNF and 10.04(1) wt% SiNP stock dispersions were combined in appropriate proportions with water, aspartic acid and NaOH to prepare the ligand-containing matrix comprising 1.00(6) wt% OCNF, 5.02(1) wt% SiNP and specific concentrations of L-Asp and D-Asp. These dispersions were homogenised in batches of 10 mL by the sonication method below for a total processing time of 60 s (120 J) per batch.

Sonication

All methods involving sonication employed an Ultrasonic Processor FB-505, Fisher, 200 W cm^{-2} , equipped with a 6 mm probe. The instrument was operated at 30% amplitude in the “1 s on 1 s off” pulse mode.

Dynamic Light Scattering (DLS)

DLS measurements were carried out on dilute samples of SiNP (0.01 wt%) using a Malvern Zetasizer Nano ZSP®. Samples were measured as an average of 4 measurements from 100 scans each. All DLS data were collected within 48 h of sample preparation.

Powder X-ray diffraction

Powder X-ray diffraction data were collected at ambient temperature using a STOE STADI P diffractometer, equipped with germanium monochromator and STOE IP-PSD image plate. The instrument was operated in transmission mode with Cu $K_{\alpha 1}$ ($\lambda = 1.5406 \text{ \AA}$) radiation. Data were collected in the 2θ range 2-75° (4893 data points) and processed using WinXPOW.

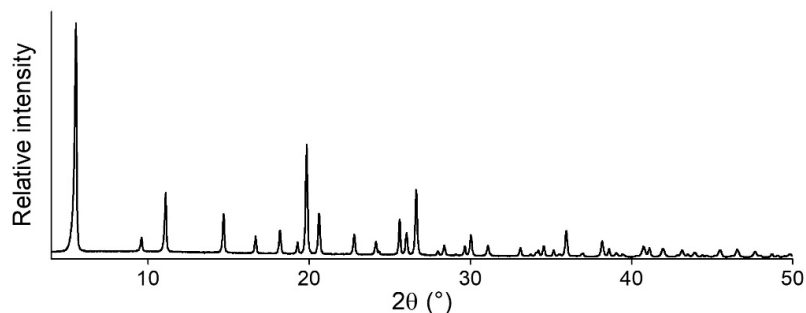


Figure S1. Powder X-ray diffractogram for Cu-Asp prepared from $\text{Cu}(\text{NO}_3)_2$ and L-Asp.

Small-angle X-ray scattering (SAXS) and wide-angle X-ray scattering (WAXS)

SAXS and WAXS data were collected on a SAXSpoint 2.0 (Anton Paar) equipped with Primux 100 micro Cu and Mo X-ray sources and a 2D EIGER R 1M hybrid photon counting detector (Dectris). Cu K_{α} radiation ($\lambda = 1.542 \text{ nm}$) was used. Samples were loaded in PasteCell (Anton Paar) sample holders. Background data were collected using an empty sample cell and this background was subtracted from each sample dataset. Data were processed using SAXSanalysis (Anton Paar).

Rheology

Rheological measurements were performed on the OCNF-based primary and ligand-containing matrices using a stress-controlled rheometer (Discovery HR3, TA instruments) equipped with sandblasted plate-plate geometry (40 mm). To avoid evaporation, the edges of samples were covered with low viscosity mineral oil and further covered with a lid to minimise temperature fluctuations around the set temperature of 25 °C. After loading, the gel was exposed to: i) 30 s of pre-shearing at 300 s^{-1} to ensure consistent sample history, followed by ii) a strain sweep at constant $\omega = 1 \text{ rad s}^{-1}$. The storage and loss modulus, G' and G'' respectively, were computed using the software programme TRIOS. The values for G' and G'' were used to calculate the complex modulus $G^* = \sqrt{G'^2 + G''^2}$, and $\tan\delta = G''/G'$. The values reported for G^* and $\tan\delta$ are obtained from the linear viscoelastic region. All rheological data were collected within 48 h of sample preparation.

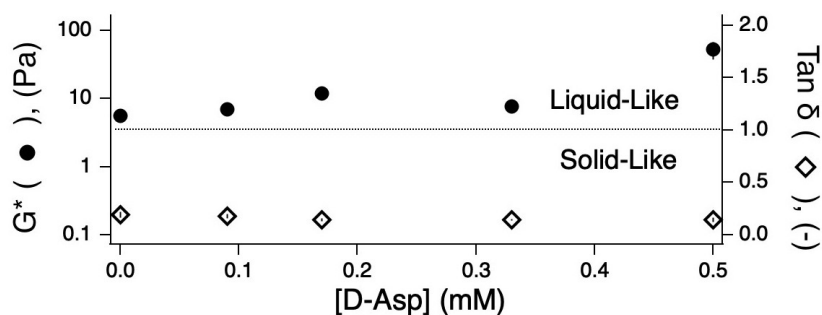


Figure S2. G^* and $\tan \delta$ for OCNF dispersions containing 50 mM L-Asp and doped with D-Asp at concentrations of 0 mM to 50 mM showing no considerable changes with increasing D-Asp concentration.

Composite hydrogel spheroids

Droplets of 20 μ L of the primary matrix or ligand-containing matrix were ejected via micropipette or syringe needle into a bath of 100 mM $\text{Cu}(\text{NO}_3)_2$ to produce hydrogel spheroids.

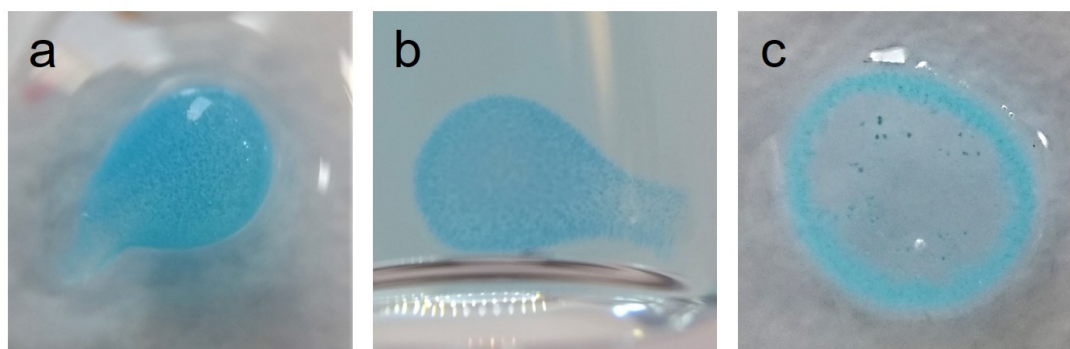


Figure S3. Photographs of composite hydrogel spheroid samples generated from OCNF-based dispersions containing: (a) 65 mM L-Asp, (b) 50 mM L-Asp and (c) 50 mM L-Asp (cross-section).

Video S1

Hydrogel filaments are prepared from a dispersion of 1.00(6) wt% OCNF and 5.02(1) wt% SiNP (primary matrix) by ejecting the dispersion, via syringe needle, directly into a solution of 100 mM $\text{Cu}(\text{NO}_3)_2$ (aq).

Qualitative analysis of the rate of Cu-Asp self-assembly

Time lapse optical microscopy was used to investigate the rate of Cu-Asp self-assembly. Dispersions were prepared containing 1.00(6) wt% OCNF, 5.02(1) wt% SiNP, 50 mM L-Asp and:

- 1) 0 mM D-Asp (measured in triplicate)
- 2) 15 mM D-Asp (measured in triplicate)
- 3) 50 mM D-Asp (measured in duplicate)

NaOH was incorporated at 2 molar equivalents per 1 molar equivalent of aspartic acid. Each dispersion was immersed in aqueous 100 mM $\text{Cu}(\text{NO}_3)_2$ solution at $t = 0$ s and optical micrographs were collected at a rate of 1 image per 10 s. Image analysis was carried out using ImageJ. For each set of images, 'mean grey values', as an indicator of Cu-Asp crystallite density, were determined for a rectangular

subregion of the image with consistent background and even crystallite distribution. The 'mean grey value' was inverted and converted to arbitrary units to yield a value for relative image darkness, d , as a function of time.

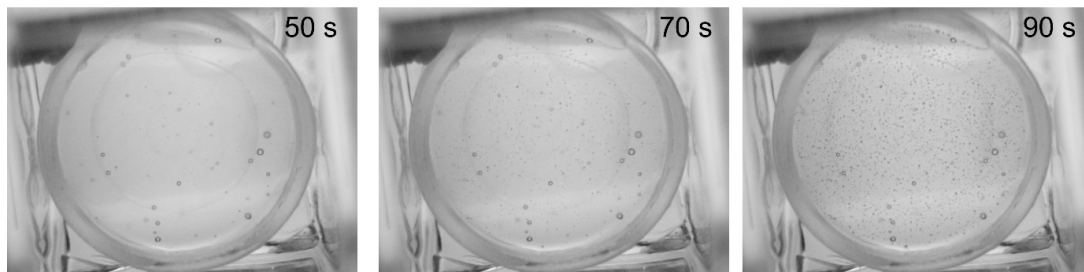


Figure S4. Optical micrographs for the reaction of 100 mM $\text{Cu}(\text{NO}_3)_2$ with a dispersion of 1.00(6) wt% OCNF, 5.02(1) wt% SiNP, containing 50 mM L-Asp and 0 mM D-Asp and showing the emergence of macroscopic crystallites at approximately $t = 70$ s.

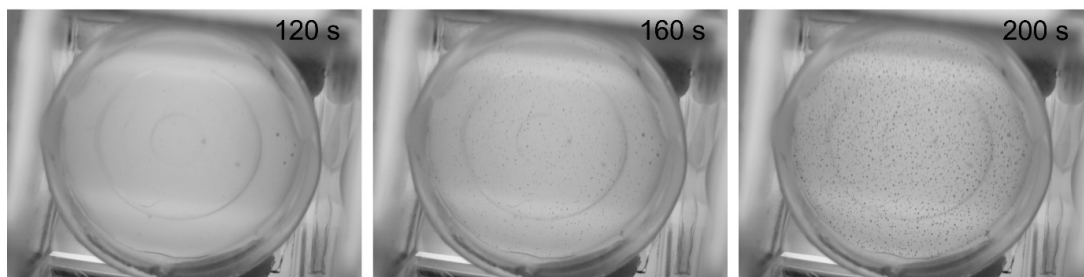


Figure S5. Optical micrographs for the reaction of 1100 mM $\text{Cu}(\text{NO}_3)_2$ with a dispersion of 1.00(6) wt% OCNF, 5.02(1) wt% SiNP, containing 50 mM L-Asp and 15 mM D-Asp showing the emergence of macroscopic crystallites at approximately $t = 160$ s.

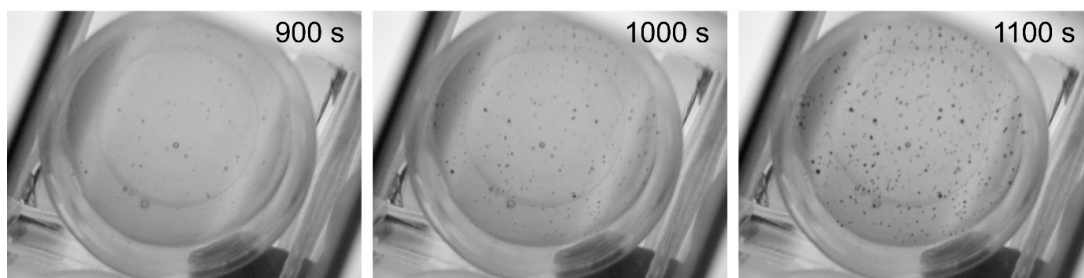


Figure S6. Optical micrographs for the reaction of 100 mM $\text{Cu}(\text{NO}_3)_2$ with a dispersion of 1.00(6) wt% OCNF, 5.02(1) wt% SiNP, containing 50 mM L-Asp and 50 mM D-Asp showing the emergence of macroscopic crystallites at approximately $t = 1000$ s.

References

1. (a) T. Saito and A. Isogai, *Biomacromolecules*, 2004, **5**, 1983; (b) T. Saito, S. Kimura, Y. Nishiyama and A. Isogai, *Biomacromolecules*, 2007, **8**, 2485; A. Isogai, T. Saito, H. Fukuzumi, *Nanoscale*, 2011, **3**, 71.
2. (a) D. da Silva Perez, S. Montanari and M. R. Vignon, *Biomacromolecules*, 2003, **4**, 1417; (b) V. Calabrese, J. C. Muñoz-García, J. Schmitt, M. A. da Silva, J. L. Scott, J. Angulo, Y. Z. Khimyak and K. J. Edler, *J. Colloid Interface Sci.*, 2019, **535**, 205.

10.5 Supporting information for Chapter 7

Core-shell spheroidal hydrogels produced via charge-driven interfacial complexation

Vincenzo Calabrese,^a Davide Califano^{a,b} Marcelo A. da Silva,^a Julien Schmitt,^{a,†} Saffron Bryant,^a

Kazi M. Zakir Hossain,^a Ana M. Percebom,^c Aurora Pérez Gramatges,^c Janet L. Scott,^{a,b} Karen J. Edler^{a*}

^a Department of Chemistry, University of Bath, Claverton Down, Bath, BA2 7AY, United Kingdom

^b Centre for Sustainable Chemical Technologies, University of Bath, Claverton Down, Bath, BA2 7AY, United Kingdom

^c Department of Chemistry, Pontifical Catholic University of Rio de Janeiro (PUC-Rio), 22451-900 Rio de Janeiro, RJ, Brazil

[†] current address: LSFC Laboratoire de Synthèse et Fonctionnalisation des Céramiques, UMR 3080 CNRS / Saint-Gobain CREE, Saint-Gobain Research Provence, 550 avenue Alphonse Jauffret, Cavaillon, France

Notes on the estimation of f

The mole fraction of the oppositely charged moieties, f , needs to be in a range which allows full complexation of the CCNF with the PAA across the SH/water interface with no excess of free CCNF. The f was estimated as described by eqn 1.

$$f \equiv \frac{m_{CCNF} \alpha_{CCNF}}{m_{CCNF} \alpha_{CCNF} + \frac{m_{PAA}}{M_{PAA}} \alpha_{PAA}} \quad (1)$$

Where m_{CCNF} is the mass (g) of CCNF employed and α_{CCNF} the mol/g of trimethylammonium chloride functionalisation on the CCNF surface, as determined by conductometric titration (1.3×10^{-3} mol/g).¹ The m_{PAA} is the mass (g) of PAA in the bath, M_{PAA} the molecular weight of the repeating unit (g/mol) and $\alpha_{PAA} = \frac{N}{N'}$, where N is the number of monomers and N' the number of monomers bearing the negatively charged moiety; for PAA $\alpha_{PAA} = 1$ since all the repeating units present a carboxyl groups as the negatively charged moiety. Eqn. 1 reduces to a mole fraction, where, for $f = 0.5$, CCNF and PAA are perfectly charge balanced, for $f > 0.5$ there is excess of the positively charged moieties from CCNF, and, for $f < 0.5$ there is excess of the negatively charged moieties from PAA. Eqn. 1 yielded for $f = 0.5$, a CCNF/PAA ratio of 10.5 on dry basis and allowed an estimation that the 50 mL bath of 0.1 wt% PAA would ensure a large excess of PAA ($f = 0.05$), and, full CCNF-PAA complexation for *ca.* 80 SH (each made up of 17.8 ± 0.2 μ L).

It is noted that the f parameter herein calculated assumes that the whole CCNF composing the SH complexes with the PAA, hence underestimating the number of SH which could be produced with a single 50 mL bath of 0.1 wt% PAA (since in the main manuscript we explain that the CCNF-PAA complexation occurs solely at the SH/water interface).

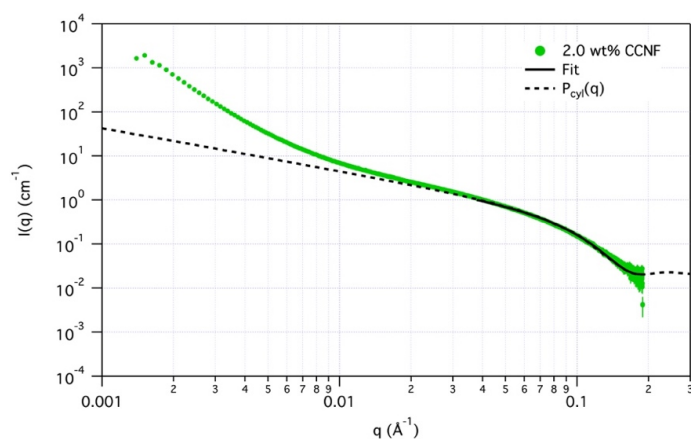


Fig. S1 SAXS pattern of the 2.0 wt% CCNF dispersion. Fitting of the form factor of randomly oriented homogeneous cylinders, $P_{cyl}(q)$, at high- q is displayed by the filled line. The pattern at low- q displayed a strong divergence from the slope of q^{-1} indicating strong aggregation, as previously reported,² hence omitted for the fitting of the $P_{cyl}(q)$. Regardless, fitting of the high- q region was sufficient to extrapolate the average radius, R , of the CCNF although from this analysis the interactions between fibrils and fibril length cannot be accessed. Dotted line shows the $P_{cyl}(q)$ across the whole q -range, employing the same parameter as the one obtained by the fitting.

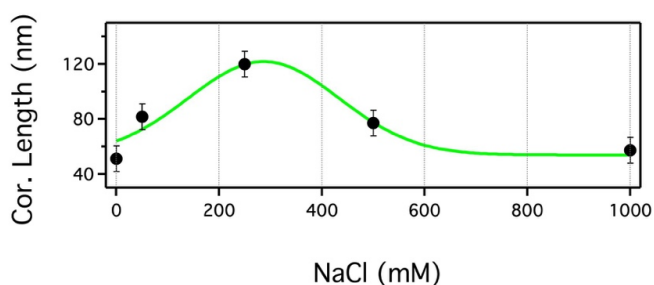


Fig. S2 Correlation Length (ξ) obtained by the fitting of the fractal model to the SAXS data of the CCNF-PAA films. The line is drawn to guide the eye.

References

- 1 M. Hasani, E. D. Cranston, G. Westman and D. G. Gray, *Soft Matter*, 2008, **4**, 2238–2244.
- 2 V. Calabrese, J. C. Muñoz-García, J. Schmitt, M. A. da Silva, J. L. Scott, J. Angulo, Y. Z. Khimyak and K. J. Edler, *J. Colloid Interface Sci.*, 2019, **535**, 205–213.

10.6 Supporting information for Chapter 8

Charge-driven interfacial gelation of cellulose nanofibrils across the water/oil interface

Vincenzo Calabrese,^a Marcelo A. da Silva,^a Julien Schmitt,^a Kazi M. Zakir Hossain,^a Janet L. Scott,^{a,b} Karen J. Edler^{a*}

^a Department of Chemistry, University of Bath, Claverton Down, Bath, BA2 7AY, UK. E-mail: k.edler@bath.ac.uk; Tel: 01225 384192

^b Centre for Sustainable Chemical Technology, University of Bath, Claverton Down, Bath, BA2 7AY, UK. E-mail: j.l.scott@bath.ac.uk University of Bath Tel: 01225 386307

* Corresponding author: E-mail: k.edler@bath.ac.uk; Tel: 01225 384192

OCNF coverage at W/O interface

Assuming a single oxidised cellulose nanofibril (OCNF) as a perfect cylinder, its volume (V_f) is

$$V_f = \pi r^2 L = 616 \text{ nm}^3 = 6.16 \cdot 10^{-24} \text{ m}^3$$

where r and L are respectively the radius (3.5 nm) and the length (160 nm) of OCNF. (DOI:10.1039/C8CP00355F)

The mass of a single OCNF (g_f) is

$$g_f = \rho \cdot V_f = 9.24 \cdot 10^{-18} \text{ g}$$

Where ρ is the OCNF density (*ca.* 1500 Kg/m³). (10.1002/jps.20459)

Since the total mass of the fibrils (g_t) is known (for the case of interfacial shear rheology experiments 18.2 ml of 100 ppm OCNF were employed $g_t = 1.82 \cdot 10^{-3}$ g), it is possible to calculate the total number of fibrils (N_f) as:

$$N_f = \frac{g_t}{g_f} = 1.97 \cdot 10^{14}$$

Assuming a perfect single layer 2D packing of OCNF at the W/O interface, it is possible to consider OCNF as a 2D object, hence, the surface area at W/O interface occupied by a single OCNF (Si_f) can be estimated as for a rectangular object.

$$Si_f = (2r) \cdot L = 1120 \text{ nm}^2 = 1.12 \cdot 10^{-11} \text{ cm}^2$$

and the total surface area occupied by N_f (Si) calculated as

$$Si = N_f \cdot Si_f = 2.21 \cdot 10^3 \text{ cm}^2$$

For the case of interfacial shear rheology experiments, Si for the concentration of OCNF used was much greater than the W/O interface generated in the Couette cell geometry (18.81 cm²).

Bulk contribution at the W/O interface

The bulk contribution to the surface stress needs to be estimated. The Boussinesq number, Bo , estimated using the following equation, allows decoupling of these two effects.^{1,2}

$$Bo = \frac{|G_i^*|}{(\eta_1 + \eta_2)\omega r}$$

Where $|G_i^*|$ ($\text{Pa}\cdot\text{m}$) is the interfacial complex modulus, defined as

$$|G_i^*| = \sqrt{G_i'^2 + G_i''^2}$$

(G_i' being the interfacial storage modulus and G_i'' the interfacial loss modulus), η_1 and η_2 are the viscosities of the bulk phases ($\text{Pa}\cdot\text{s}$), ω is the angular frequency ($\text{rad}\cdot\text{s}^{-1}$) and r is a characteristic distance of the flow geometry (7×10^{-4} m).³ For $Bo \gg 1$, the contribution of the bulk phase can be neglected, whilst for $Bo \sim 1$ the bulk contribution must be considered. For $|G_i^*| > 10^{-3}$ $\text{Pa}\cdot\text{m}$, the low viscosity of the 100 ppm OCNF dispersion (similar to that of pure water) and the low value of ω employed in this study generated a value of $Bo \gg 1$ (e.g., $Bo > 1000$ after 1000 s in TS1 measurements), ensuring a negligible bulk contribution. On these grounds, we assert that the rheological measurements performed at the W/O interface effectively capture interfacial phenomena only.

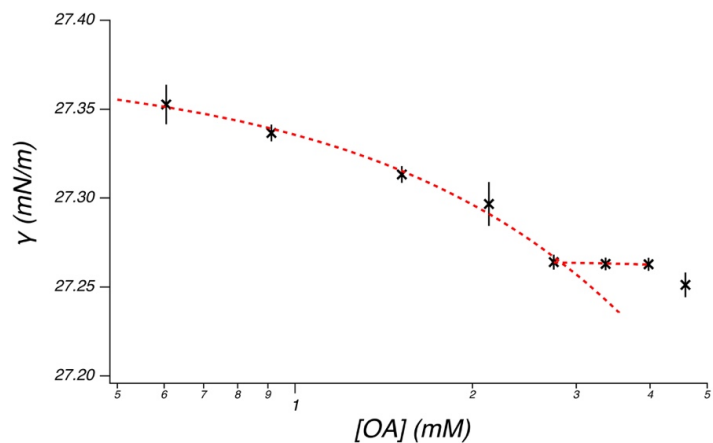


Fig. S1 Surface tension (γ) vs OA concentration (mM) measured at Oil-Air interface. The change in slope, considered as the CMC, was obtained by fitting the data to two linear equations.

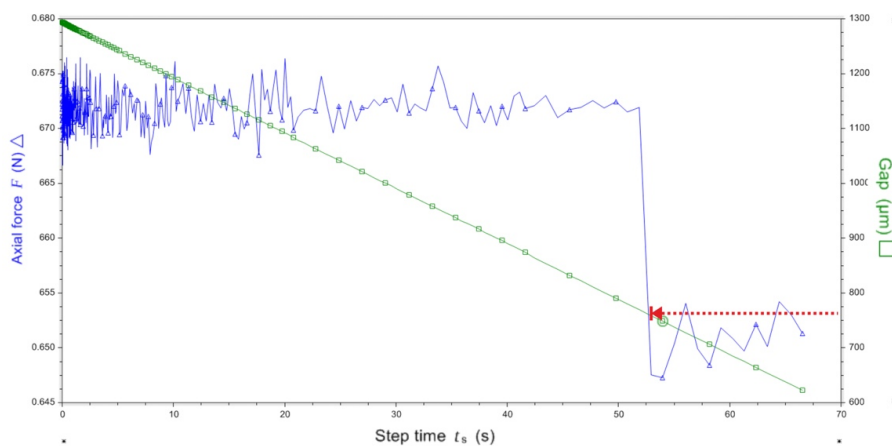


Fig. S2 Axial force (N) as a function of DWR Gap distance (μm). The distance corresponding to the water-DWR first contact is observed by the drop in axial force (arrow).

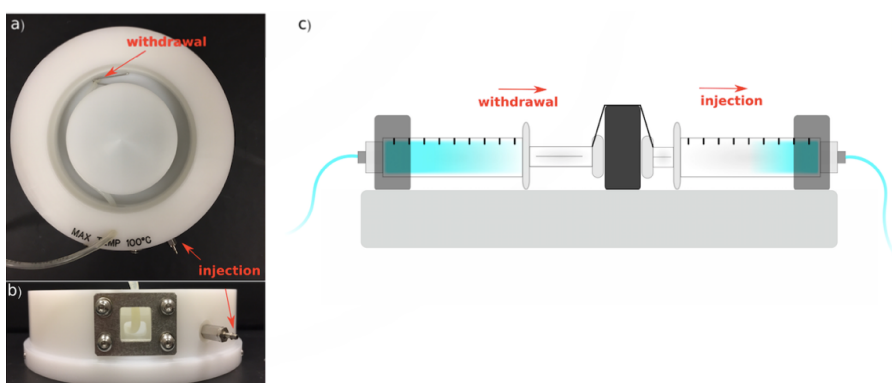


Fig. S3 Customised cuvette cell geometry displayed in (a) top view and (b) side view. Sketch of the customised syringe pump (KD Scientific®) displayed in (c).

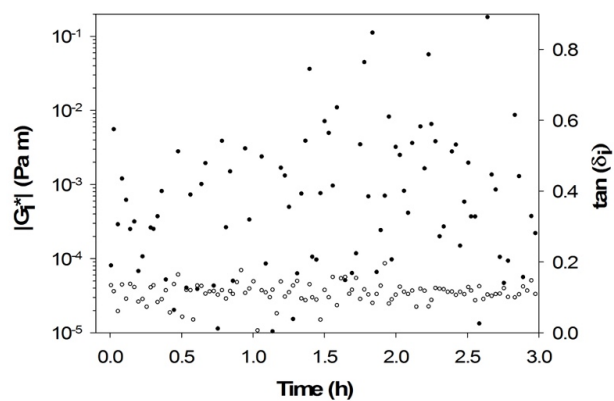


Fig. S4 Evolution of $|G_i^*|$ (empty symbol) and $\tan(\delta_i)$ (filled symbol) at the W/O interface composed by a water phase of 100 ppm OCNF and a pure oil phase (in the absence of OA in the oil phase).

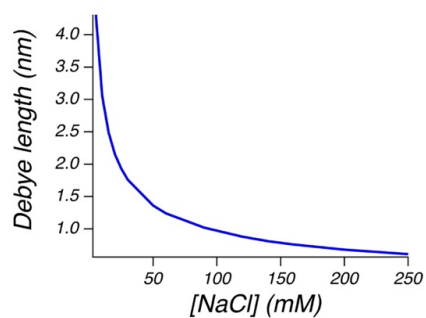


Fig. S5 Debye length (nm) as function of NaCl calculated as described by Fukuzumi et al.⁴

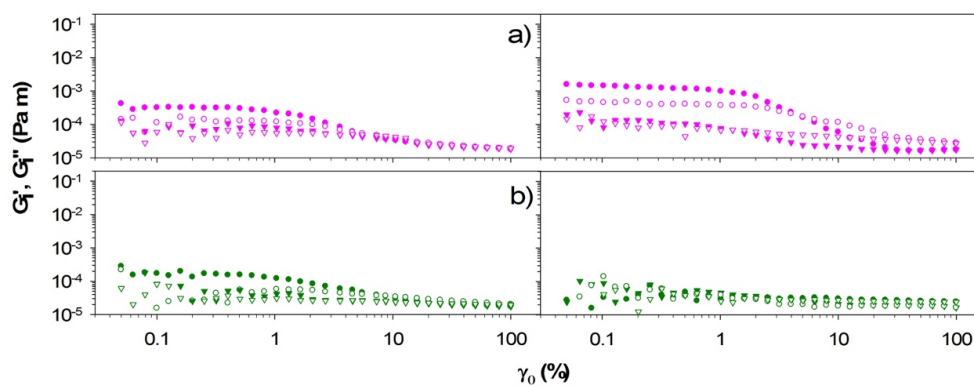


Fig. S6 Strain sweep cycle at the W/O interface composed by a water phase of 100 ppm OCNF with (a) 130 and (b) 250 mM NaCl and an OA-doped oil phase. SSC1 and SSC2 shown on the left and right, respectively.



Fig. S7 Images of 24 h aged water droplets containing 0, 55 and 250 mM NaCl, from left to right respectively, in OA-doped oil.

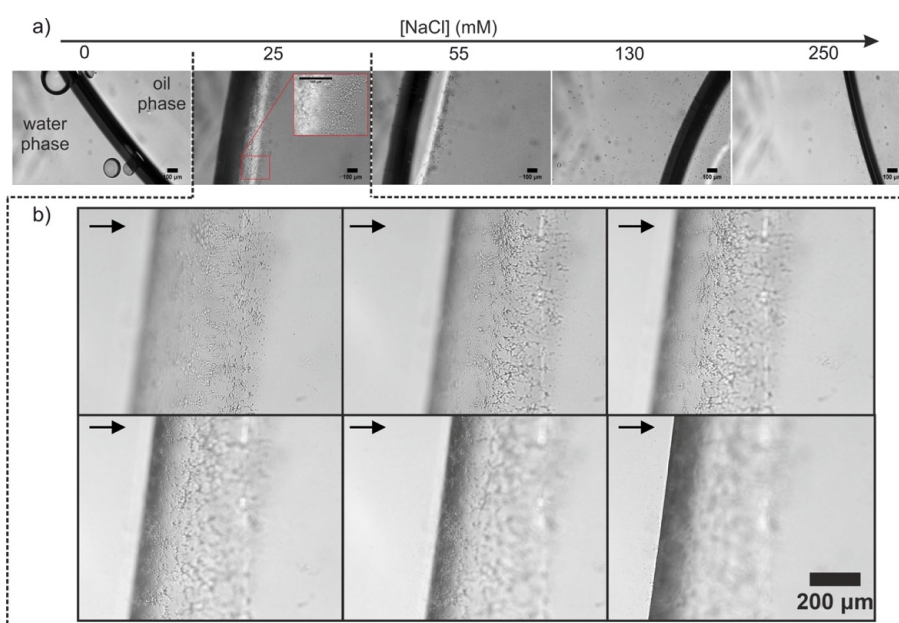


Fig. S8 (a) Optical micrographs of 24 h aged W/O interface assembled from 100 ppm OCNF suspensions at different NaCl concentrations and the OA-doped oil phase. The left-hand side of the meniscus shows the water phase. (b) Gradual change in focal plane, displayed by the direction of the arrow, for the sample containing 100 ppm OCNF with 25 mM NaCl as the water phase.

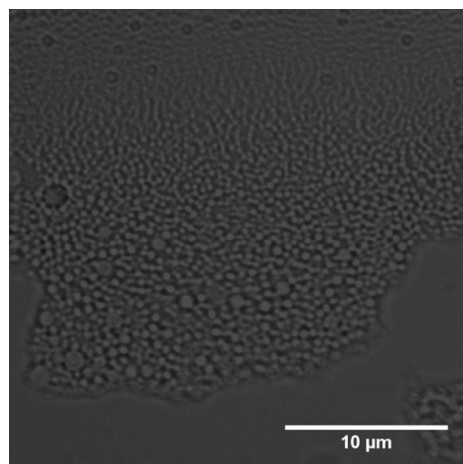


Fig. S9 Optical micrograph of the interfacial gel formed at the interface between 100 ppm OCNF in 55 mM aqueous NaCl and OA-doped oil.

References

- 1 P. Erni, P. Fischer, E. J. Windhab, V. Kusnezov, H. Stettin and J. Läger, *Rev. Sci. Instrum.*, 2003, **74**, 4916–4924.
- 2 J.-M. Jung, D. Z. Gunes and R. Mezzenga, *Langmuir*, 2010, **26**, 15366–15375.
- 3 A. Franck, *5th Int. Symp. Food Rheol.*, 1997, **8**, 242–244.
- 4 H. Fukuzumi, R. Tanaka, T. Saito and A. Isogai, *Cellulose*, 2014, **21**, 1553–1559.